Quantum Error Correction using cat qubits

Antoine Marquet

▶ To cite this version:

Antoine Marquet. Quantum Error Correction using cat qubits. Quantum Physics [quant-ph]. Ecole normale supérieure de lyon - ENS LYON, 2023. English. ⟨NNT : 2023ENSL0125⟩. ⟨tel-04524858⟩

HAL Id: tel-04524858

https://theses.hal.science/tel-04524858v1

Submitted on 28 Mar 2024

Thèse
en vue de l'obtention du grade de docteur, délivrée par
L'ÉCOLE NORMALE SUPÉRIEURE DE LYON

École Doctorale N°52
Physique et Astrophysique de Lyon (PHAST)

Discipline : Physique

Soutenue publiquement le 12/12/2023, par

Antoine Marquet

Quantum Error Correction using cat qubits

Correction d'Erreurs Quantiques avec des qubits de chats

Devant le jury compomposé de

Kirchmair Gerhard, Professeur, université d'Innsbruck	Rapporteur
Steele Gary, Professeur, TU Delft	Rapporteur
Fawzi Omar, Directeur de recherche, Inria Lyon	Examinateur
Le Jeannic Hanna, Chargée de recherche, LKB	Examinatrice
Lescanne Raphaël, CTO Alice & Bob	Examinateur
Bienfait Audrey, Chargée de recherche, ENS de Lyon	Examinatrice
Huard Benjamin, Professeur, ENS de Lyon	Directeur

QUANTUM ERROR CORRECTION USING CAT QUBITS

3 YEARS OF PLAYING WITH FLUFFY QUANTUM STATES

ANTOINE MARQUET

Directed by Benjamin HUARD & Audrey BIENFAIT
Co-directed by Raphaël LESCANNE
ENS de Lyon, Alice & Bob
December 2023

ABSTRACT

Over the past two decades, superconducting circuits have emerged as a promising platform for building a quantum computer. However, they remain limited by their coherence time which is still insufficient to demonstrate a practical quantum advantage.

Quantum error correction (QEC) offers an approach to counter these errors. Its fundamental principle consists of introducing redundancy in order to define a so-called logical qubit. Thus, if an isolated physical qubit suffers an error, it can be detected and corrected without affecting the information stored within the logical qubit. One of the most intuitive approaches, and one that comes closest to conventional error correction, is to use an array of physical qubits to achieve the desired redundancy.

This thesis explores an alternative approach, based on encoding quantum information in superconducting cavities, where the redundancy is provided by the infinite dimension of the Hilbert space. Specifically, we use cat qubits for which the logical $|0\rangle$ and $|1\rangle$ states are coherent states $|\pm\alpha\rangle$ of a harmonic oscillator. These states are stabilized by leveraging dissipation to our advantage so that photon exchanges between the harmonic mode and its environment predominantly occur in pairs. In this way, "bit-flip" errors are exponentially suppressed as a function of the number of photons contained by the mode, at the modest cost of a linear increase in "phase-flip" errors. These errors could then be corrected by an additional layer of correction, such as a repetition code of cat qubits.

At the heart of this thesis work is the introduction of a self-parametric superconducting circuit that non-linearly couples a mode containing the cat qubit to a dissipative mode whose frequency is set to twice that of the cat mode. Unlike previous implementations, this passive coupling does not require a parametric pump and achieves a high two-photon dissipation rate $\kappa_2/2\pi$ of around 2 MHz. Bit-flip errors are then avoided for a characteristic period of up to 0.3 s, with a moderate impact on phase-flip errors. In addition, we demonstrate universal control of this qubit using the two-photon dissipation to implement $\hat{X}$, $\hat{Y}$ and $\hat{Z}$ logic gates of arbitrary θ angle.

RÉSUMÉ

Au cours des deux dernières décennies, les circuits supraconducteurs se sont imposés comme une plateforme prometteuse pour la construction d'un ordinateur quantique. Cependant, ils demeurent limités par leur temps de cohérence qui reste insuffisant pour démontrer un avantage quantique pratique.

La correction d'erreur quantique offre une approche pour contrer la décohérence, le principe fondamental étant d'introduire de la redondance afin de définir un qubit dit logique. Ainsi, si un qubit physique isolé subit une erreur, celle-ci peut être détectée et corrigée sans affecter l'information contenue dans le qubit logique. L'une des approches les plus intuitives, se rapprochant le plus de la correction d'erreur classique, consiste à utiliser une multitude de qubits physiques pour réaliser la redondance recherchée.

Cette thèse explore une approche alternative, basée sur l'encodage de l'information quantique dans des cavités supraconductrices, la redondance étant alors simplement fournie par la dimension infinie de l'espace de Hilbert. Nous utilisons des qubits de chat pour lesquels les états logiques $|0\rangle$ et $|1\rangle$ sont des états cohérents $|\pm\alpha\rangle$ d'un oscillateur harmonique. Ces états sont stabilisés en utilisant la dissipation à notre avantage, de sorte que les échanges de photons entre le mode harmonique et son environnement se fassent principalement par paires. Ainsi, les erreurs de type « bit-flip » sont supprimées exponentiellement avec le nombre de photons contenus dans le mode, au prix d'une augmentation linéaire des erreurs de type « phase-flip ». Ces erreurs pourraient alors être corrigées par une couche supplémentaire de correction, tel qu'un code de répétition de qubits de chats.

Le coeur de ce travail de thèse consiste à introduire un circuit supraconducteur autoparamétrique qui couple de manière non-linéaire un mode contenant le qubit de chat à un mode dissipatif dont la fréquence est réglée au double de celle du mode du chat. Contrairement à de précédentes réalisations, ce couplage passif ne nécessite pas de pompe paramétrique et atteint un fort taux de dissipation $\kappa_2/2\pi$ d'environ 2 MHz. Les erreurs de bit-flip sont alors évitées pendant une période caractéristique pouvant aller jusqu'à 0.3 s, avec un impact modéré sur les erreurs de phase-flip. De plus, nous démontrons un contrôle universel de ce qubit en utilisant la dissipation à 2 photons pour réaliser des portes logiques $\hat{X}$, $\hat{Y}$ et $\hat{Z}$ d'un angle θ arbitraire.

REMERCIEMENTS

Extérieurement, une thèse peut ressembler à une aventure solitaire où un étudiant lutte quotidiennement contre des calculs qui ne veulent pas aboutir, ou une expérience refusant désespérément de donner le résultat tant espéré. Il y a un peu de vérité dans cette vision, il faut l'admettre. Cependant, et heureusement, une thèse ne se fait pas complètement seul, et j'ai eu la chance tout au long de ces presque 4 années de thèse d'être accompagné de personnes sans qui cette thèse n'aurait pas pu voir le jour.

C'est naturellement vers mon directeur de thèse Benjamin Huard que se tournent mes premiers remerciements. Je t'ai d'abord connu dans le rôle de professeur lors d'un cours de M1 portant sur la supraconductivité, puis en M2 pour une introduction à l'ingénierie quantique. Il faut croire que ces cours ont éveillé ma curiosité puisque j'allais rapidement te voir concernant mon stage de fin d'études... que j'ai finalement effectué à Paris dans le groupe de Zaki. Tu m'as cependant proposé une thèse après cette première rencontre et peu de temps après, malgré quelques déboires lors d'un retour d'Australie et un confinement covid, j'ai finalement eu la chance de découvrir le Quantum Circuit Group. Je te remercie pour la patience et la compréhension dont tu as fait preuve tout au long de cette thèse, m'encourageant pendant les moments où rien ne marchait et partageant mon excitation quand les résultats arrivaient finalement. Je te remercie également pour ta curiosité constante qui, je l'espère, a déteint sur moi. Les séances passées dans ton bureau à gribouiller au tableau en imaginant une nouvelle expérience resteront des souvenirs marquants de ces années passées. Plus que tout, je veux te remercier pour la bienveillance dont tu as toujours fait preuve, ne t'intéressant pas simplement à l'aspect scientifique de la recherche mais aussi à son caractère humain. L'intérêt que tu portes à chacun, allant jusqu'à ramener un pauvre étudiant boitillant dans les Alpes jusqu'à sa voiture, fait de ce groupe un endroit où l'on a envie d'aller travailler tous les matins. Pour tout cela je te remercie, et je m'estime chanceux que tu m'aies proposé cette thèse il y a de cela presque 5 ans.

J'ai eu la chance durant cette thèse d'avoir Audrey Bienfait comme co-encadrante. Je te remercie tout d'abord pour toute l'aide que tu m'as apportée au quotidien dans mes expériences, que ce soit pour designer le câblage du frigo, le montage de ma table optique, le tutoriel SolidWorks dont j'ai maintenant à peu près tout oublié, les relectures d'abstract et d'articles, et tant d'autres choses que je n'ai pas la place de lister. Je te remercie également pour les discussions que nous avons pu avoir, que ce soit sur des aspects scientifiques où ton point de vue m'a souvent apporté un nouvel éclairage sur la manière d'aborder un problème, ou concernant le métier de chercheur en général. Finalement, je voudrais te remercier pour l'aspect humain dont tu as toujours fait preuve, ton support constant, et la motivation que tu insuffles à tes étudiants.

J'ai également eu l'opportunté durant ma thèse d'être accompagné par tous les autres membres du groupe. Je voudrais remercier ceux qui m'ont accueilli et m'ont inculqué l'esprit du Quantum Circuit Group à coup de pichets du Ninkasi : Antoine Essig et Jeremy Stevens que j'aurais la joie de retrouver à Alice et Bob, Alexis Jouan, Daniel Szombati, Rémy Dassonneville et Réouven Assouly. Vous côtoyer au quotidien, bien qu'impressionnant quand on arrive à peine et qu'on ne comprend pas grand-chose à son premier TLS, m'a montré ce vers quoi je devais aspirer.

J'ai une pensée spéciale pour mes partenaires de promo avec qui nous avons formé le « basement crew », admirant la superbe vue sur les Alpes et cachant les objets compromettants quand des étudiants venaient visiter le labo. J'ai maintenant une impressionnante collection de très petites cuillères grâce à Arne Babahr, et beaucoup trop d'anecdotes de spéléologie alors même que ce sport me terrifie profondément. Je remercie également Hector Hutintin, notre maintenant super méga stagiaire sénior, de m'avoir supporté toutes ces années. Je retiendrai les longues discussions où tu t'arrachais les cheveux alors même que tu t'aventurais dans un énième délire théorique, les références de mangas et manhwa toujours intéressantes, et les fous rires que nous avons eus quotidiennement avec Arne et toi. Je me souviendrai longtemps de ce basement, qu'il soit au -1 ou au 1er étage, et du plaisir d'avoir partagé mon quotidien avec vous.

Je remercie également ceux arrivés dans le groupe pendant ma thèse, déjà partis vers un nouveau poste pour certains : Matteo Boselli, Cyril Elouard, Camille Lombard Latune, Yannick Seis, Ambroise Peugeot, Adria Rospars, Simon Dupouy et Tristan Lorriaux. Le groupe a de beaux jours devant lui et je serai heureux de pouvoir à nouveau parler d'expériences avec vous maintenant que la rédaction de ce manuscrit se conclut.

J'ai également eu la chance durant cette thèse de travailler pour la compagnie Alice & Bob. Tout d'abord, je tiens à remercier Theau Peronnin et Raphaël Lescanne de m'avoir donné cette opportunité alors que la société n'avait que quelques mois et que nous n'étions qu'une petite équipe de 10 employés. Merci d'avoir fait ce pari de me prendre en thèse CIFRE, et d'avoir créé cette structure où des projets de recherche ambitieux peuvent être menés de front. Observer l'évolution réalisée en 3 ans, les nouveaux locaux, et le nombre de personnes brillantes travaillant maintenant chez A&B, est vraiment impressionnant. Je suis réellement heureux de savoir que je pourrai continuer de jouer avec des qubits de chat dans un tel environnement. Je tiens particulièrement à remercier Sébastien Jezouin qui a été mon premier interlocuteur au début de cette thèse, alors que nous essayions de mettre en place une stabilisation de parité. Tes inputs et conseils lors des expériences menées pendant cette thèse ont toujours été d'une grande aide.

Je voudrais également remercier certaines personnes qui m'ont soutenus durant toutes ces années de thèse. Tout d'abord Hugo avec qui j'ai vécu les confinements successifs à manger du fromage, brasser notre bière maison, et manger de la pizza pendant nos parties de D&D. Mes colocataires actuels ensuite, François et Hervé, qui en quelques années sont devenus des amis et des soutiens précieux. La couverture de cette thèse est notamment due aux talents de graphiste de François. Enfin, je tiens à remercier ma famille. Merci d'avoir toujours cru en moi et de m'avoir toujours soutenus dans mes projets, même lorsque maman me voyait partir loin à l'étranger pour des stages. Merci de m'avoir transmis la fibre scientifique et de m'avoir toujours encouragé à demander « pourquoi » quand quelque chose de nouveau et d'étonnant se présente.

CONTENTS

I Cat qubits and their use for Quantum Error Correction

II Stabilization and control of a cat qubit using the Auto-cat design

III Appendix

IV Bibliography

1

INTRODUCTION

The theoretical framework of quantum mechanics emerged at the dawn of the 20th century, originally as an attempt to explain experiments on blackbody radiation, the photoelectric effect, or solar emission spectra. This framework gave physicists a new understanding of the microscopic world[1], and paved the way for what's known as the *first quantum revolution*. This revolution resulted in the emergence of new technologies that have since become widely adopted and an integral part of our society, with notable advancements such as lasers or transistors. The latter was invented at Bell Labs as a replacement for the vacuum tube [2], exploiting the wave function associated with electrons in a semiconductor. Through decades of refinement, as these components shrank in size and increased in efficiency, they became the cornerstone of modern computing and can be found in the billions in any processor.

The breakthroughs of this first quantum revolution relied on the collective behavior of an ensemble of quantum systems, as opposed to isolated systems and the precise control of their degrees of freedom. This was actually thought to be impossible until the second half of the 20th century, with Erwin Schrödinger writing in 1952 "[...] we *never* experiment with just *one* electron or atom or (small) molecule. In thought-experiments we sometimes assume that we do; this invariably entails ridiculous consequences [...]" [3]. Only in the 1980's did experiments on Rydberg atoms and trapped ions demonstrate the measurement and manipulation of individual quantum systems, resulting in 2012 to the Physics Noble Prize being awarded to Serge Haroche and David Wineland [4]. This paved the way to the *second quantum revolution*, where effects such as superposition or entanglement[2] are now exploited in

---

[1] The world of *isolated objects* would be more accurate. While originally thought of as a description of molecules, atoms, or subatomic particles, the framework of quantum mechanics actually applies to any object isolated from its environment whose properties can be quantized. For instance, despite weighting nearly 40 kg, the mirrors in the LIGO and VIRGO experiments present degrees of freedom which are described by Quantum mechanics [1].

[2] Experiments on entanglement led to the attribution in 2022 of the Physics Nobel Prize to Alain Aspect, John Clauser, and Anton Zeilinger. These experiments notably proved the violation of Bell's inequalities [5, 6], disproving local hidden-variable theories as an interpretation of quantum mechanics.

the fields of quantum sensing, metrology, communication, cryptography, and quantum computing.

This thesis focuses on the field of quantum computing, whose origin can be traced back to an article from Richard Feynman in 1982 [7]. In this work, Feynman postulates that a quantum computer would be the optimal tool for simulating the behaviors of large quantum systems, a task that classical computers struggle with due to the size of the Hilbert spaces. Other applications for quantum computers later emerged, including Shor's [8] or Grover's [9] algorithms which could offer exponential speed-up for challenges such as integer factorization and unstructured searches. These developments sparked the interest of physicists who took on the challenge of building such a quantum computer, with industrial players becoming increasingly involved in recent years.

The concept of what constitutes an ideal quantum computer was formalized in 2000 by David DiVincenzo [10], consisting of the 5 DiVincenzo's criteria.

A scalable physical system with well-characterized qubits. At the heart of a quantum computer are its qubits, the quantum analog of classical bits. It corresponds to a two-level system, used to store and manipulate the quantum information, whose state is described as the superposition of a ground state $|g\rangle$ and excited state $|e\rangle$ (also symbolized as $|0\rangle$ and $|1\rangle$). The notion of scalability is associated with the ability to add more and more of these qubits to the quantum computer, without incurring an exponential cost in physical resources. This scalability allows a quantum computer composed of N qubits to operate within a Hilbert space of dimension 2^N, a stark contrast to the linear scaling of classical bits, which is what makes quantum computers so appealing.

The ability to initialize the state of these qubits. At the beginning of each algorithm, a quantum computer comprising N qubits is initialized into a known state, usually its ground state $|g\rangle \otimes |g\rangle \otimes |g\rangle \otimes ... = |ggg...\rangle$.

Long relevant decoherence times. Qubits in a quantum computer are susceptible to errors that corrupt the quantum information, with the decoherence time characterizing the time during which this information remains intact. In order to perform accurate operations that do not suffer from decoherence, the decoherence time must significantly exceed the duration of any operation performed.

A universal set of quantum gates. Similar to classical computers, a minimal set of universal gates can be defined which allows the execution of any multi-qubit gate on a quantum computer. The experimental implementation of these gates depends on the specific physical realization of the quantum computer.

A qubit-specific measurement capability. Because performing operations without having access to the result can be quite infuriating, experimenters need to have access to the state of these N qubits.

Building such a device proves extremely challenging, particularly when it comes to conciliating the need for long coherence times and the ability to measure and manipulate qubits. The dilemma arises from the necessity to access quantum information for manipulation and readout, which entails a coupling of the N qubits with their surrounding environment, resulting in decoherence. Striking a balance between minimizing this coupling to preserve coherence times and achieving efficient operations and measurements is a complex task.

1.1 SUPERCONDUCTING CIRCUITS FOR QUANTUM COMPUTING

Despite being investigated for more than two decades, no clear consensus emerged among the scientific community regarding the most suitable platform for quantum computing. As a consequence, several technologies are currently being developed in a race to build the first quantum computer, such as Rydberg atoms [11], trapped ions [12], quantum dots [13], nuclear spins [14, 15] or photonic qubits [16, 17]. These technologies rely on existing two-level systems to encode the quantum information, achieving coherence times as high as 40 ms using nuclear spins [18] or 1 h with trapped ions [19]. However, their operations are typically slow, and scalability remains a challenge. Moreover, since these qubits rely on naturally occurring physical objects, their Hamiltonian and energy spectrum are more or less fixed and cannot be freely adjusted to meet specific requirements.

These issues can be mitigated using superconducting circuits that behave as an *artificial* atoms when cooled under a critical temperature T_c[3]. At such temperatures, electrons in the superconducting metal bind to form Cooper pairs [20] due to an attractive interaction, for instance mediated by phonons. These Cooper pairs, composed of two spin 1/2 particles, obey a bosonic statistic which allows them to occupy the same fundamental state and exhibit a collective behavior. This Cooper-pair condensate is described by a single degree of freedom [21, 22] whose potential can be controlled by macroscopically defined inductances and capacitances. Harmonic potentials can be realized using superconducting circuits with microwave resonators or cavities, while qubits are fabricated using Josephson junctions [23].

---

[3] Superconductors such as tantalum and aluminum, routinely used in superconducting circuits, have a respective critical temperature of $T_\mathrm{c}(\mathrm{Ta}) = 4.5$ K and $T_\mathrm{c}(\mathrm{Al}) = 1.2$ K

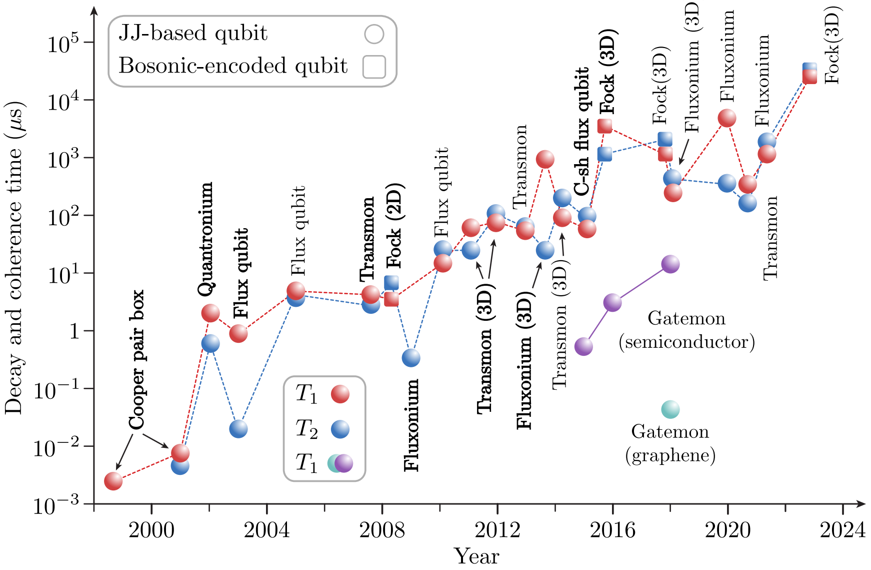

Figure 1.1: Evolution of lifetimes (T_1) and coherence times (T_2) of superconducting qubits. Bold fonts indicate the first demonstration of a given design. JJ-based qubits correspond to qubits where the quantum information is stored in a qubit made out of one or several Josephson junctions. On the opposite, bosonic qubits encode the information in the multiple energy levels of a quantum harmonic oscillator, with Josephson junctions being used to control and read this information. Figure adapted from [24], adding the realizations of [25, 26, 27, 28].

In comparison to alternative quantum computing platforms, superconducting circuits offer distinct advantages, notably in terms of scalability. Multiple qubits can be manufactured and interconnected on the same chip, making it an easily scalable approach. Initialization of these qubits to their ground state is ensured by working at a low temperature $T \ll T_c$ such that thermal noise does not induce unwanted excitations, resulting in the condition $\hbar\omega \gg k_b T$ where $\hbar\omega$ represents the energy difference between the qubit's two energy states. Considering the typical frequencies of superconducting qubits, which are around $\omega/2\pi \approx 0.1 - 10$ GHz[4], these qubits are operated at temperatures $T \approx 10$ mK within dilution fridges. Furthermore, a universal set of gates can be tailored to the specific type of qubits in use, with operations that can

---

[4] Frequencies exceeding 10 GHz can be impractical due to microwave sources and components being outside their usual operational range. Additionally, the maximum frequency is constrained to a few 10s of GHz due to the bound imposed by the superconducting gap and the plasmon frequency of Josephson junctions.

be performed in just a few nanoseconds due to the large dipole exhibited by these artificial qubits. Lastly, the readout of superconducting qubits has been demonstrated in a quantum-non-demolition (QND) manner by coupling them to a microwave mode [29, 30].

The primary drawback of superconducting qubits is their limited coherence time. Despite the absence of resistive power loss, which prevents the use of ordinary electrical circuits, the large number of conductive electrons in the Cooper-pair condensate ($\sim 10^{10}$) results in an increased decoherence rate compared to more microscopic systems [31].

As a result, the first superconducting qubits [32] were limited to a coherence time of a few nanoseconds. This was later improved by introducing new designs of Josephson junction-based qubits, notably the transmon [33] and fluxonium qubit [34], or encoding the information in bosonic modes (Fig. 1.1). Additionally, progress in fabrication techniques, noise filtering, and cryogenic methods, have led to a Moore-law-like improvement of the lifetime T_1 and coherence time T_2 (see Sec. 2.2.1 for a proper definition of these 2 quantities), with recent implementations achieving coherence times of a few milliseconds. Nevertheless, such coherence times are still insufficient in order to perform any useful quantum computation before losing the quantum information. While further improvements based on material science are still possible, notably preventing the detrimental impact of quasiparticles [35], another axis of research emerged based on the design of *logical qubits*: Quantum Error Correction.

1.2 QUANTUM ERROR CORRECTION WITH SUPERCONDUCTING CIRCUITS

The concept of quantum error correction has its roots in the historical development of classical error correction techniques in the late 1940s. This field emerged as a response to the unreliable computers of that era, which utilized vacuum tubes in their circuitry. These early computers, especially when executing lengthy algorithms that relied on numerous logical gates, were prone to bit-flip errors which could transform a 0 into a 1 or vice versa during computation. This could lead to erroneous results when such bit-flip errors went undetected, and even cause the computer to abruptly halt in the middle of a computation. Frustrated by this, Richard Hamming [36] and Marcel Golay [37] independently developed the first error-correcting codes, at the same time Claude Shannon laid the groundwork for the field of information theory [38].

The fundamental idea behind these error-correcting codes was to redundantly store the same information across multiple physical systems. This redundancy allowed for the detection and correction of bit-flip errors affecting one or more of these systems by measuring the entire ensemble of systems. Errors could then be rectified, effectively reducing the error rate and restoring the stored information.

When considering the application of these error-correcting codes to quantum computers with imperfect qubits, susceptible to decoherence, the question naturally arising is whether these codes can be adapted. While the answer is fortunately *yes* (as evidenced by the existence of this thesis), a few features of quantum mechanics must be taken into account in order to understand the challenge this represents.

One such feature is the 'no cloning' theorem, which asserts it is impossible to create an identical copy of a quantum system in an arbitrary state. The redundancy required for error correction thus cannot be provided by simply duplicating the same quantum state over multiple qubits and instead requires changing the encoding itself to define *logical qubits*.

Another challenge arises from the projective nature of measurements in quantum mechanics, which inherently destroys the information contained in a quantum system. However, while this may appear problematic at first for detecting error syndromes, this phenomenon can actually be exploited in order to design syndrome measurements that project a quantum computer into its *logical space* or some known *error spaces*. As the measured syndrome indicates in which subspace the system is projected, the error is then discretized and can then be corrected, bringing the computer back to its logical encoding. Alternatively, measurement-free techniques based on the constant removal of entropy from the system were designed which do not suffer from this measurement challenge. This work presents such a technique.

1.3 OUTLINE OF THIS THESIS

The structure of this thesis is divided into two primary sections: an initial theoretical presentation of the cat qubit, followed by its experimental realization and potential expansion of its encoding.

The initial two chapters serve as a theoretical foundation, providing the necessary background to understand the subsequent experiments. In Chapter 2, we give a more detailed presentation of the different concepts introduced in this chapter. This includes a detailed examination of the representation of a single qubit state, an analysis of the sources of errors that impact these qubits, and an exploration of how various quantum error correction schemes can be devised to combat decoherence in logical qubits. We also explore the use of biased noise qubits for simplifying existing QEC protocols when gates are available that can effectively preserve bias noise for the chosen qubit architecture. Cat qubits are highlighted as a prominent example of this approach.

Chapter 3 then focuses on cat qubits, comparing them with alternative options for bosonic qubits. We discuss different methods for stabilizing cat qubits such as measurement back action, Hamiltonian engineering, and dissipation engineering. We follow the approach of dissipation engineering and improve on existing techniques by introducing a novel circuit that allows us to stabilize cat qubits by engineering a strong 3-wave mixing interaction between the qubit and its surrounding environment.

The subsequent two chapters shift the focus toward the practical realization of this circuit, nicknamed the *autoparametric-cat* or *Auto-cat*. Chap. 4 presents the calibration procedure of this device, notably improving on existing measurement protocols by taking advantage of the strong 3-wave mixing interaction. We demonstrate the enhanced performance of this stabilized logical qubit, showcasing an exponential increase in the bit-flip time. Numerical simulations are performed which notably highlight how the measurement apparatus limits this bit-flip time to $T_{\mathrm{X}} \sim 0.3$ s.

Chapter 5 then focuses on the operations conducted on the stabilized cat qubit. We present the successful execution of a bias-preserving $\hat{Z}$ gate and a holonomic $\hat{X}$ gate, enabling universal control over a single cat qubit. Additionally, we showcase the preparation of squeezed cat states, unique states that hold potential interest in quantum error correction codes and quantum sensing.

Lastly, Chapter 6 serves as the concluding segment of this thesis, introducing a proposal for a fully protected qubit. Building upon the Auto-cat architecture, we discuss the possibility of engineering a 5-wave mixing interaction, enabling the stabilization of a 4-dimensional Hilbert space. The addition of an extra parity stabilization, performed through either measurement-based feedback or dissipation engineering, results in the stabilization of a sub-2-dimensional manifold which constitutes a fully protected logical qubit.

1.4 PUBLICATIONS

- W. C. Smith, M. Villiers, A. Marquet, J. Palomo, M. R. Delbecq, T. Kontos, P. Campagne-Ibarcq, B. Douçot, Z. Leghtas, "*Magnifying Quantum Phase Fluctuations with Cooper-Pair Pairing*", Phys. Rev. X (2022).
- U. Réglade, A. Bocquet, R. Gautier, A. Marquet, E. Albertinale, N. Pankratova, M. Hallén, F. Rautschke, L. A. Sellem, P. Rouchon, A. Sarlette, M. Mirrahimi, P. Campagne-Ibarcq, R. Lescanne, S. Jezouin, Z. Leghtas, "*Quantum control of a cat-qubit with bit-flip times exceeding ten seconds*", arXiv 2307.06617 (2023).
- A. Marquet, A. Essig, J. Cohen, N. Cottet, A. Murani, E. Abertinale, S. Dupouy, A. Bienfait, T. Peronnin, S. Jezouin, R. Lescanne, B. Huard, "*Autoparametric resonance extending the bit-flip time of a cat qubit up to 0.3 s*", arXiv 2307.06761 (2023).
- A. Marquet, S. Dupouy, U. Reglade, A. Essig, J. Cohen, E. Abertinale, A. Bienfait, T. Peronnin, S. Jezouin, R. Lescanne, B. Huard, "*Strong 2-photons dissipation for measurement and universal control of a cat qubit*", In preparation

Part I

CAT QUBITS AND THEIR USE FOR QUANTUM ERROR CORRECTION

2

QUANTUM ERROR CORRECTION 101

2.1 INTRODUCTION TO QUBITS AND THE NOTION OF DECOHERENCE

2.1.1 *Bloch sphere representation of a qubit*

A qubit represents the quantum counterpart of classical bits of information and serves as the fundamental component of a quantum computer. From an experimental perspective, any two-level system can be used as a qubit when considering its two orthogonal states, referred to as $|0\rangle$ and $|1\rangle$, as the *computational states* of the system. Examples of such qubits are the "up" and "down" states of an electron spin, the "vertical" or "horizontal" polarization of a single photon of light, the "presence" or "absence" of a photon in the mode of a transmission line, or the "ground" and "excited" states of an artificial atom constructed using superconducting circuits. Regardless of the chosen encoding method, the Hamiltonian of an isolated qubit can be expressed as

$$\hat{H}_q = -\frac{\hbar\omega_q}{2}\hat{\sigma}_z \tag{2.1}$$

where $\hbar\omega_q$ represents the energy difference between $|0\rangle$ and $|1\rangle$. The computational states are the eigenstates of the Pauli operator $\hat{\sigma}_z$ with corresponding eigenvalues of $+1$ and -1. This operator $\hat{\sigma}_z$ belongs to the SU(2) group and, along with the other Pauli operators, forms a basis for all operations performed on a qubit. Using the representation

$$|0\rangle = \begin{pmatrix} 1 \\ 0 \end{pmatrix}, \ |1\rangle = \begin{pmatrix} 0 \\ 1 \end{pmatrix}, \tag{2.2}$$

the Pauli operators can be represented as 2 × 2 matrices

$$\mathbb{1} = \begin{pmatrix} 1 & 0 \\ 0 & 1 \end{pmatrix}, \ \hat{\sigma}_x = \begin{pmatrix} 0 & 1 \\ 1 & 0 \end{pmatrix}, \ \hat{\sigma}_y = \begin{pmatrix} 0 & -i \\ i & 0 \end{pmatrix}, \ \hat{\sigma}_z = \begin{pmatrix} 1 & 0 \\ 0 & -1 \end{pmatrix}. \tag{2.3}$$

The two states $|0\rangle$ and $|1\rangle$ define the *computational space* $\operatorname{span}\{|0\rangle, |1\rangle\}$ of the qubit, which is a 2-dimensional complex Hilbert space. By virtue of the superposition principle, any state

$$|\psi\rangle = \alpha\,|0\rangle + \beta\,|1\rangle \tag{2.4}$$

with $\alpha,\ \beta \in \mathbb{C}$ and $|\alpha|^2 + |\beta|^2 = 1$ belongs to this computational space and is a valid state for the qubit. Because $|\psi\rangle$ is normalized to unity, and fixing the global phase to 0, the qubit state can be described by two variables denoted as θ and ϕ. Eq. (2.4) can then be reformulated in terms of these two variables as

$$|\psi\rangle = \cos\left(\frac{\theta}{2}\right)|0\rangle + e^{i\varphi}\sin\left(\frac{\theta}{2}\right)|1\rangle\,, \tag{2.5}$$

which defines the Bloch sphere representation of a qubit. In Figure 2.1, we illustrate this representation, depicting states such as $|0\rangle$, $|1\rangle$, $|+\rangle$, $|-\rangle$, and $|\psi\rangle$.

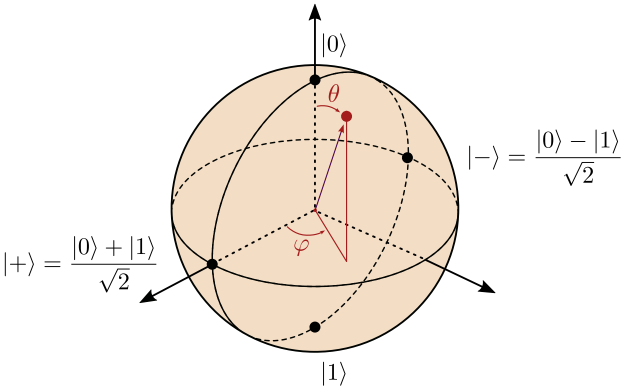

Figure 2.1: Bloch sphere representation of a qubit state, parameterized using the angles θ and φ as $|\psi\rangle = \cos\left(\frac{\theta}{2}\right)|0\rangle + e^{i\varphi}\sin\left(\frac{\theta}{2}\right)|1\rangle$

2.1.2 *Description of a qubit coupled to its environment*

While this description of a qubit using wavefunctions in a complex Hilbert space holds true for isolated quantum systems, it proves insufficient when dealing with a qubit entangled with its environment. The correct tool in this context is that of density matrices, which extends the concept of wavefunctions to consider effects such as decoherence, open quantum systems, or the preparation of statistical mixtures.

Mathematically, considering the system $\mathcal{S}$ composed of a qubit coupled with its environment as an isolated quantum system, we can fully describe it by its wavefunction $|\psi_\mathcal{S}\rangle = \sum_\lambda \gamma_\lambda |\psi_{\mathcal{E},\lambda}\rangle \otimes |\psi_{\mathcal{Q},\lambda}\rangle$[1]. For such a *pure* quantum state, its density matrix is expressed as

$$\hat{\rho}_\mathcal{S} = |\psi_\mathcal{S}\rangle \langle\psi_\mathcal{S}| \, . \tag{2.6}$$

The qubit density matrix is then obtained from $\hat{\rho}_\mathcal{S}$ by *tracing out* the environment $\mathcal{E}$

$$\hat{\rho}_\mathcal{Q} = \sum_i \langle\psi_{\mathcal{E},i}|\psi_\mathcal{S}\rangle \langle\psi_\mathcal{S}|\psi_{\mathcal{E},i}\rangle \, , \tag{2.7}$$

where $\{|\psi_{\mathcal{E},i}\rangle\}$ corresponds to any chosen basis for the environment's Hilbert space. The resulting matrix $\hat{\rho}_\mathcal{Q}$ usually describes a *mixed state* which, in contrast to a pure state, cannot be expressed in the form of $\hat{\rho}_\mathcal{Q} = |\psi_\mathcal{Q}\rangle \langle\psi_\mathcal{Q}|$.

Irrespective of whether the system is in a pure or mixed state, density matrices are Hermitian operators on a Hilbert space $\mathcal{H}$, positive semi-definite, and of trace 1. The average value of any observable $\hat{O}$ acting on the qubit is given by

$$\langle\hat{O}\rangle_{\hat{\rho}_\mathcal{Q}} = \mathrm{Tr}\left(\hat{\rho}_\mathcal{Q}\hat{O}\right) , \tag{2.8}$$

which generalizes to any density matrix and operator acting on a common Hilbert space. The unitary evolution of a density matrix $\hat{\rho}(t)$, which generalizes the Schrödinger equation [39], is given by

$$\frac{\mathrm{d}}{\mathrm{d}t}\hat{\rho}(t) = -\frac{i}{\hbar}\left[\hat{H}, \hat{\rho}(t)\right] \tag{2.9}$$

where $\hat{H}$ is the Hamiltonian of the isolated system under study. To account for errors originating from the weak coupling of a quantum system to its environment, dissipation channels are introduced and incorporated as *loss operators* into Eq.(2.9). This corresponds to the Lindblad master equation [40], which we present and illustrate in Sec. 3.2.4.

---

[1] This expression for $|\psi_\mathcal{S}\rangle$ corresponds to the canonical Schmidt decomposition, with $\{|\psi_{\mathcal{E},\lambda}\rangle\}$ (resp $\{|\psi_{\mathcal{Q},\lambda}\rangle\}$) forming a basis for the environment (resp qubit) Hilbert space.

2.1.3 *Errors affecting a qubit*

The density matrix describing a qubit can be conveniently expressed using the Pauli matrices as

$$\hat{\rho} = \frac{1}{2}\left(\mathbb{1} + \langle\hat{\sigma}_x\rangle\hat{\sigma}_x + \langle\hat{\sigma}_y\rangle\hat{\sigma}_y + \langle\hat{\sigma}_z\rangle\hat{\sigma}_z\right), \tag{2.10}$$

where $\langle\hat{\sigma}_x\rangle$, $\langle\hat{\sigma}_y\rangle$, and $\langle\hat{\sigma}_z\rangle$ represent the mean value of the operators $\hat{\sigma}_x$, $\hat{\sigma}_y$ and $\hat{\sigma}_z$. They correspond to the coordinates of the qubit *inside* of the Bloch sphere, which is described by a vector $\mathbf{u} = (\langle\hat{\sigma}_x\rangle, \langle\hat{\sigma}_y\rangle, \langle\hat{\sigma}_z\rangle)$, with $|\mathbf{u}| \leq 1$. The norm of this vector $\mathbf{u}$ serves as a measure of the information known about the state, with pure quantum states corresponding to the limit where $|\mathbf{u}| = 1$.

One crucial quantity derived from the qubit's density matrix is the Von Neumann entropy, expressed as

$$S = -\mathrm{Tr}\left(\hat{\rho}\log\left(\hat{\rho}\right)\right). \tag{2.11}$$

In the case of a qubit in a pure quantum state, its density matrix is idempotent ($\hat{\rho} = \hat{\rho}^2$) resulting in an entropy of 0. Any deviation of the entropy from this vanishing value quantifies the deviation of the qubit from such a pure state. To illustrate how *decoherence* can increase the entropy of a system, we consider the example of a qubit initially prepared in the state $|+\rangle = \left(|0\rangle + |1\rangle\right)/\sqrt{2}$. Its density matrix can be expressed as

$$\hat{\rho} = |+\rangle\langle+| = \frac{1}{2}\left(|0\rangle\langle 0| + |0\rangle\langle 1| + |1\rangle\langle 0| + |1\rangle\langle 1|\right) = \frac{1}{2}\begin{pmatrix}1 & 1\\ 1 & 1\end{pmatrix} \tag{2.12}$$

and its entropy $S = 0$. However, due to the interaction of this qubit with its environment, the off-diagonal terms of $\hat{\rho}$ (referred to as *coherences*) decay to zero. The entropy associated with the resulting density matrix

$$\hat{\rho} = \frac{1}{2}\left(|0\rangle\langle 0| + |1\rangle\langle 1|\right) = \frac{1}{2}\begin{pmatrix}1 & 0\\ 0 & 1\end{pmatrix} \tag{2.13}$$

then increases to $S = \ln(2)$, corresponding to the Shannon entropy of a maximally undetermined classical bit of information[2]. This increase in

---

[2] It is noteworthy that despite the Von Neumann entropy predating the Shannon entropy by almost 20 years (introduced in 1932 compared to Shannon's work in 1948), the Von Neumann entropy serves as an extension of the latter to the quantum realm. These two quantities only coincide after decoherence, when the density matrix describes a statistical superposition of orthogonal quantum states.

entropy corresponds to a loss of information about the qubit state, lost to the environment. The characteristic time over which these coherences disappear to the environment is called the *decoherence time*, denoted as T_2. Using the Bloch-Redfield model of decoherence [41, 42], which assumes that noise sources are only weakly coupled to the qubit with correlation times shorter than the system dynamics, this decoherence time can be decomposed as

$$\frac{1}{T_2} = \frac{1}{2T_1} + \frac{1}{T_\varphi}. \tag{2.14}$$

The time T_1 is called the energy decay time and T_φ the pure dephasing time. Note that in the context of quantum computing, T_1 and T_2 are related to the *bit-flip* and *phase-flip* time.

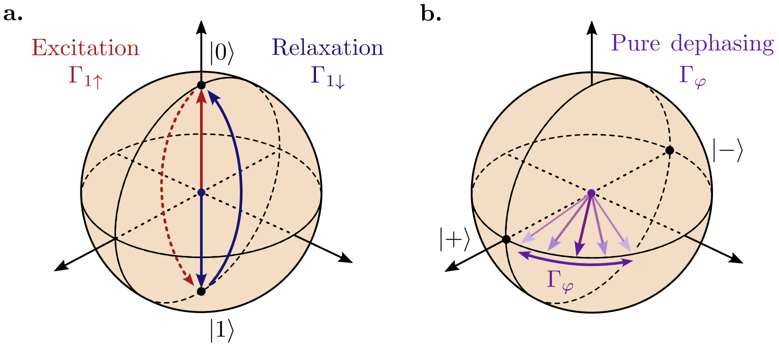

Figure 2.2: **a.** Energy decay of a qubit resulting from energy exchanges with a bath of temperature T. When the qubit is in $|0\rangle$, it can absorb energy from its environment which excites it to $|1\rangle$ at a rate $\Gamma_{1\uparrow}$. Similarly, when the qubit is in its excited state $|1\rangle$, it can emit energy at a rate $\Gamma_{1\downarrow}$. For a cold enough bath where $\hbar\omega_q \gg \mathrm{k_B}T$, the absorption process is suppressed since $\Gamma_{1\uparrow} = e^{-\hbar\omega_q/\mathrm{k_B}T}\Gamma_{1\downarrow}$, and the energy decay time is limited by the relaxation of the qubit to its ground state. **b.** Diffusion at a rate Γ_φ of the phase φ of a qubit, resulting from fluctuations in the qubit frequency.

2.1.3.1 *Energy decay time T_1*

The energy decay time characterizes the typical time it takes for a qubit to relax to equilibrium. It originates from the interaction between the qubit and its environment, considered as a bath of temperature T, leading to energy exchanges. Such energy exchanges are described by an excitation rate $\Gamma_{1\uparrow}$ (transitions from $|0\rangle$ to $|1\rangle$) and a relaxation rate $\Gamma_{1\downarrow}$ (transitions from $|1\rangle$ to $|0\rangle$), represented in Fig. 2.2**a**. Together, these two rates define the longitudinal relaxation rate

$$\Gamma_1 = \frac{1}{T_1} = \Gamma_{1\uparrow} + \Gamma_{1\downarrow}. \tag{2.15}$$

The ratio between $\Gamma_{1\uparrow}$ and $\Gamma_{1\downarrow}$ is given by the Boltzmann equilibrium statistics, which leads to the detailed balance relationship

$$\frac{\Gamma_{1\uparrow}}{\Gamma_{1\downarrow}} = e^{-\hbar\omega_q/\mathrm{k_B}T}. \tag{2.16}$$

There, $\mathrm{k_B} = 1.38.10^{-23}$ J.K^{-1} is the Boltzmann constant and $\hbar\omega_q$ the energy difference between $|0\rangle$ and $|1\rangle$. At equilibrium, when the populations in the ground and excited states stabilize, the population in the ground state is expressed as

$$p(|0\rangle) = \tanh\left(\hbar\omega_q/2\mathrm{k_B}T\right), \text{ with } p(|1\rangle) = 1 - p(|0\rangle). \tag{2.17}$$

For typical superconducting qubits with $\omega_q/2\pi \sim 5$ GHz, operated in a dilution refrigerator at 10 mK, $p(|1\rangle) \approx 0.1\%$ and the qubit is often considered in its ground state at equilibrium. Furthermore, when simulating the dynamic of a qubit using the Lindblad master equation, excitations $\Gamma_{1\uparrow}$ are often neglected and only energy decay $\Gamma_{1\downarrow}$ is considered.

2.1.3.2 *Pure dephasing time T_φ*

While the energy decay time can be understood from the point of view of statistical physics, the pure dephasing time T_φ is a purely quantum-mechanical phenomenon that describes the loss of information about the phase of a quantum superposition. It originates from any process that can be described, using the Lindblad equation, by the dissipator

$$\hat{L}_\varphi = \frac{\sqrt{\kappa_\varphi}}{2}\hat{\sigma}_z. \tag{2.18}$$

Notable example of such processes are uncontrolled fluctuations in the qubit frequency ω_q, eventually leading to a diffusion of the phase φ (Fig. 2.2**b.**), or unread measurements performed by the environment.

Considering the uncontrolled oscillations of a qubit's frequency, no information is lost to the many degrees of freedom of a bath during this process, contrary to energy relaxation. As a result, while we don't know the exact unitary operation required to compensate for the uncontrolled fluctuations of ω_q, some operations such as spin-echo [43] or dynamical decoupling pulses [44] can still be applied. The degree to which information can be retrieved depends on the noise structure, the dephasing rate Γ_φ, or the speed at which these unitary operations can be performed.

2.2 REDUCING THE DECOHERENCE RATE IN SUPERCONDUCTING QUBITS

As previously mentioned, errors affecting a qubit originate from its coupling with a noisy environment. Following the demonstration of [45], we model this coupling by an interaction Hamiltonian

$$\hat{H}_{\text{int}} = g\,\hat{O}_q\,\hat{\lambda} \tag{2.19}$$

with g the coupling strength of the interaction and $\hat{O}_q$ an operator impacting the qubit degrees of freedom. The environment, considered as a source of noise, is represented by an operator $\hat{\lambda}$ which produces fluctuations $\delta\lambda$. The coupling strength is proportional to the qubit sensitivity to variations in a parameter λ which describes the environment (such as an external flux or charge offset), resulting in the relation

$$g\,\hat{O}_q = \frac{\partial \hat{H}_q}{\partial \lambda}. \tag{2.20}$$

The Hamiltonian $\hat{H}_q$ corresponds to the qubit Hamiltonian, depending on the parameter λ. Noise originating from the environment is described by a power spectral density $S(\omega)$, which depends on its exact physical origin. It is linked with the time average of the correlation function of λ as [46, 47]

$$S(\omega) = \int_{-\infty}^{\infty} e^{i\omega t}\langle \delta\lambda(t)\delta\lambda(0)\rangle\,\mathrm{d}t. \tag{2.21}$$

2.2.1 *Limitation of the qubit lifetimes from external noise*

2.2.1.1 *Energy decay time T_1*

Noise originating from the environment at the qubit frequency ω_q can cause unwanted transitions between the qubit ground and excited state. This is a stochastic process that, when averaging multiple trajectories of the qubit over several experiments, appears as an exponential decay towards the equilibrium state given by Eq. (2.17) with a characteristic timescale corresponding to the relaxation time T_1. The relaxation rate $\Gamma_1 = 1/T_1$ is expressed as a function of the power spectral density at the qubit frequency using Fermi's Golden rule

$$\Gamma_1 = \frac{1}{\hbar^2}\left|\langle 0|\frac{\partial \hat{H}_q}{\partial \lambda}|1\rangle\right|^2 S\left(\omega_q\right) = \frac{g^2}{\hbar^2}\left|\langle 0|\hat{O}_q|1\rangle\right|^2 S\left(\omega_q\right). \tag{2.22}$$

This formula can be decomposed into two main contributions. A first term, $S\left(\omega_q\right)$, which simply characterizes the noise amplitude at ω_q. The second term $g^2\left|\langle 0|\hat{O}_q|1\rangle\right|^2$ then represents the ability of the operator $\hat{O}_q$ to induce transitions between $|0\rangle$ and $|1\rangle$. This second contribution is maximized in the case of a *transverse* coupling, corresponding to $\hat{O}_q \propto \hat{\sigma}_x$.

2.2.1.2 *Pure dephasing time T_φ*

Now considering the case of a *longitudinal* coupling with $\hat{O}_q \propto \hat{\sigma}_z$, noise from the environment results in a stochastic modulation of the qubit frequency

$$\hat{H}_q = \frac{\hbar}{2}\left(\omega_q + \delta\omega(t)\right)\hat{\sigma}_z, \text{ with } \delta\omega(t) = \frac{\partial \omega_q}{\partial \lambda}\delta\lambda(t). \tag{2.23}$$

This results in an accumulated phase

$$\delta\varphi(t) = \frac{\partial \omega_q}{\partial \lambda}\int_0^t \delta\lambda(t^{'})\,\mathrm{d}t^{'} \tag{2.24}$$

which, as was the case for energy decay, depends on the realization of the experiment. In order to describe experimentally measured evolutions, based on the averaging of multiple trajectories, we are interested in the mean value of this accumulated phase. To be more precise, we consider the quantity $\langle e^{i\delta\varphi(t)}\rangle$, which is given by

$$\langle e^{i\delta\varphi(t)}\rangle = e^{-\frac{1}{2}\langle\delta\varphi(t)^2\rangle}, \tag{2.25}$$

considering the stochastic process $\delta\lambda(t)$ follows a Gaussian distribution[3]. We then compute

---

[3] Owing to the central limit theorem.

$$
\begin{aligned}
\langle \delta\varphi(t)^2 \rangle &= \left(\frac{\partial \omega_q}{\partial \lambda}\right)^2 \left\langle \int_0^t \delta\lambda(t^{'})\,\mathrm{d}t^{'} \int_0^t \delta\lambda(t^{''})\,\mathrm{d}t^{''} \right\rangle \\
&= \left(\frac{\partial \omega_q}{\partial \lambda}\right)^2 \int_0^t \int_0^t \mathrm{d}t^{'}\,\mathrm{d}t^{''} \left\langle \delta\lambda(t^{'})\,\delta\lambda(t^{''}) \right\rangle .
\end{aligned}
\tag{2.26}
$$

We introduce the power spectral density in this equation by inverting Eq. (2.21), yielding

$$
\begin{aligned}
\langle \delta\varphi(t)^2 \rangle &= \left(\frac{\partial \omega_q}{\partial \lambda}\right)^2 \int_{-\infty}^{\infty} S(\omega) \left| \int_0^t e^{-i\omega t^{'}}\,\mathrm{d}t^{'} \right|^2 \mathrm{d}\omega \\
&= t^2 \left(\frac{\partial \omega_q}{\partial \lambda}\right)^2 \int_{-\infty}^{\infty} S(\omega)\,\mathrm{sinc}\left(\omega t/2\right)^2\,\mathrm{d}\omega.
\end{aligned}
\tag{2.27}
$$

From Eq. (2.27), we see that noise at all frequencies now contributes to the dephasing rate. The function $\mathrm{sinc}\left(\omega t/2\right)^2$ then acts as a filter function on the noise $S(\omega)$, preferably selecting low-frequency noise. This is particularly detrimental when noises such as the $1/f$ noise are the dominant source of errors, in which case the filter function can be modified by applying the previously mentioned spin-echo or dynamical decoupling sequences [45].

2.2.2 *Sources of noise*

Several sources of stochastic noise can limit the coherence time of superconducting qubits, with several reviews exploring in detail their microscopic origin [45, 48, 49]. In this section, we briefly present 3 of the major physical sources of errors and the expression of the corresponding power spectral density.

2.2.2.1 *Charge noise*

Charge noise originates from charge fluctuations at the interface of the superconductor, inside the Josephson junction oxide (see Sec. 3.1.2), or in the bulk of the superconducting material. Microscopically, it can be attributed to the fluctuations of charge carriers, often modeled as an ensemble of Two-Level Systems (TLS) interacting with the circuit's electric fields, or bulk dielectric loss. The spectral density at low frequencies takes the form

$$
S_Q(\omega) = A_Q^2 \left(\frac{2\pi \times 1\mathrm{Hz}}{\omega}\right)^{\gamma_Q}
\tag{2.28}
$$

with $A_Q^2 = (10^{-3}e)^2/\text{Hz}$ and $\gamma_Q \sim 1$. Early realizations of superconducting qubits based on the design of the Cooper Pair Box [32, 50] were particularly sensitive to such noise, which limited their coherence time to a few microseconds.

2.2.2.2 *Flux noise*

Another source of stochastic noise is fluctuations of the magnetic field that biases flux tunable qubits[4]. For superconducting loops with large areas (typically greater than 1 mm^2), such fluctuations can originate from external magnetic sources such as the microwave in the coffee room or neighbors playing with magnets. Reducing this area to $100 - 10\ \mu\text{m}^2$, the impact of these external sources becomes negligible, although flux noise is not completely suppressed. The noise spectral density actually becomes relatively independent of the loop area, given by an effective model [45]

$$S_\Phi(\omega) = A_\Phi^2 \left(\frac{2\pi \times 1\text{Hz}}{\omega} \right)^{\gamma_\Phi} \tag{2.29}$$

with $A_Q^2 = (1\ \mu\Phi_0)^2/\text{Hz}$ and $0.8 \lesssim \gamma_\Phi \lesssim 1$. This noise is attributed to the random reversing of spins located at the surface of the superconducting metal. Computation regarding the average dipole coupling strength leads to an estimation of the surface spin density $\sigma = 5 \times 10^{17}/\text{m}^2$, corresponding to a spin per 2 nm^2. The exact nature of these spins remains unclear, although absorbed molecular 0_2 appears to be a significant contributor [51], with active research investigating their properties and how to mitigate their effect [52, 53]

2.2.2.3 *Quasiparticles poisoning*

Finally, a last source of noise is quasiparticles tunneling through the Josephson junctions of the circuit (see Sec. 3.1.2), which could lead to both energy relaxation and pure dephasing errors. These quasiparticles physically correspond to unpaired electrons, originating from broken Cooper pairs. While the BCS theory indeed predicts such isolated electrons, owing to a thermal equilibrium between the spontaneous breaking of Cooper pairs and their recombination, it only predicts a density of $\sim 10^{-23}$ quasiparticles per Cooper pair at 40 mK. This drastically underestimates the observed density, which generally falls in the $10^{-8}/10^{-6}$ range [35].

---

[4] Flux tunable qubits contain in their design a superconducting loop which can contain one or several Josephson junctions. The flux threading these loops is quantified and is necessarily a multiple of the magnetic flux quantum $\Phi_0 = h/2e$.

The origin of this excess of quasiparticles is still unclear. Different sources outside the superconducting device appear as potential candidates, among which pair-breaking photons [54] or phonons generated by extrinsic sources. Such phonons are most likely generated in the substrate of superconducting devices (See Appendix. c) due to high energy particles passing through it. These high-energy phonons then quickly propagate throughout the sample, with an energy large enough to break Cooper pairs by exciting them higher than the superconducting gap. These can lead to correlated errors across multiple qubits of the same chip, which is particularly detrimental for quantum error correction using the approach of surface codes [55] (See Sec.2.4.2.2).

2.2.3 *Mitigating these errors by improving the hardware*

2.2.3.1 *Decreasing the noise power spectral density*

An effective strategy for reducing decoherence is to simply reduce the noise seen by superconducting qubits. Specifically, in cases of charge or flux noise, this entails reducing the density of two-level systems, charge-trapping sites, or spurious spins, by improving existing fabrication techniques and introducing new materials.

Surface cleaning is critical to mitigate the presence of such TLS, notably by removing organic residues that are deposited on the sample surface during fabrication [56, 57] (see Appendix. c which details the fabrication process at ENS de Lyon). Alternatively, one could improve the coherence time of charge qubits with substrate annealing [58][5], or optimize the materials used for the substrate and the superconducting ground plane [57]. Because the microscopic origin of flux noise remains unknown, experiments are still performed that seek to characterize the properties of these magnetic defects [59, 60, 53], with optical surface treatment being explored as a way to remove them [51].

Additionally, to prevent thermal noise from reaching the sample, particular attention is given to the attenuation and the filtering of the lines reaching the qubit. This includes working with well-thermalized attenuators with good anchoring to their stage within the dilution refrigerator, the use of ecosorb filters that absorb high-frequency noise ($\omega/2\pi \gtrsim 12$ GHz), and narrow-band filters centered around the frequency of the corresponding qubit or resonator.

---

[5] Substrate annealing consists of heating a material above its recrystallization temperature and maintaining this temperature for an appropriate amount of time before cooling it down. During this process, atoms are free to migrate in the crystal lattice which allows to correct defects in the crystalline structure.

An overview of these techniques can be found in [61] with the cryogenic setup used in this thesis represented in Appendix .b.

Finally, the detrimental impact of quasiparticles can be mitigated by using phonon traps, whose goal is to prevent phonons from propagating in the substrate and generate quasiparticles by breaking Cooper pairs. The role of these traps is to absorb these propagating phonons before the qubit does, before releasing this excitation as low-energy particles that is unable to break Cooper pairs. Such traps were demonstrated using normal metal, depositing metals such as Au or Cu directly in contact with the superconductor [62, 63]. However, a possible drawback of these normal metal traps is their Ohmic losses which can lead to additional relaxation for neighboring qubits. While their design can be optimized in order to limit the impact of such losses, this issue can be solved by using superconducting traps, made with a superconductor with a lower energy gap than the rest of the circuit [64].

2.2.3.2 *Improving qubit design, making them insensitive to noise*

A second approach, further reducing the noise spectral density, involves reducing the sensibility of superconducting qubits to noise. This entails the introduction of new qubit designs whose Hamiltonian is tailored to suppress relaxation errors or pure dephasing.

Such a protected qubit is the transmon, introduced in 2007 by Koch et al. [33], whose design and Hamiltonian are presented in Sec. 3.1.2. Its design makes the transition frequency between its ground and first excited state, ω_{01}, exponentially insensitive to charge noise in a parameter E_J/E_c. However, the charge operator $\hat{n}_c$ can still induce undesired transitions between the two computational states as $|\langle 0| \hat{n}_c |1\rangle| \neq 0$, leading to relaxation. Improvements in the transmon's lifetime, reaching $T_1 \sim 500$ μs as shown in Fig. 1.1, were the result of noise filtering.

Another somewhat noise-insensitive qubit is the fluxonium, introduced in 2009 by Manucharyan et al. [34], which displayed a coherence time $T_2 = 1.48$ ms in a recent experiment [65]. Mainly sensible to flux noise due to the superconducting loop present in its design, it can be protected against either dephasing or bit-flip errors depending on the external flux at which it is operated [47].

Finally, a design that aims at protecting quantum information against both dephasing and bit-flip errors, originating from both charge and phase noise, is the so-called "$0-\pi$" qubit [66]. However, while a recent realization of this qubit [67] managed to reach a bit-flip time $T_1 = 1.56$ ms, coherence time was still limited to $T_2 = 8.5$ μs, notably due to a spurious mode inherent of the design.

2.3 QUANTUM ERROR CORRECTION

While improving the design, fabrication, and shielding of superconducting circuits has led to an improvement of the coherence time by more than seven orders of magnitude (Fig. 1.1), current devices are still prone to errors and unable to run any useful quantum algorithms. Further improvements can still be made to superconducting devices in order to continue extending this lifetime, further reducing the noise amplitude and designing new protected qubits, but this strategy proves increasingly challenging.

Alternatively, instead of focusing on the superconducting hardware, software protection can be envisioned based on the design of logical qubits. These are made of several physical qubits which redundantly store the quantum information such that, if one of these physical qubits were to fail, this error can be detected and corrected to restore the logical information.

2.3.1 *The spirit of error correction*

2.3.1.1 *Introduction to the repetition code*

The field of quantum error correction finds its origins in the classical error-correcting codes invented at the beginning of the 20^{th} century. They work by introducing new physical bits to store the logical information, defining logical bits that are more robust against errors affecting each of their physical components. An example of such a code is the phonetic alphabet, used by pilots to communicate with their traffic control centers, where letters are replaced with the commonly known expressions "Alpha", "Beta", "Charlie", etc... Although one is more likely to slightly mispronounce "Alpha" than just the letter "a", the increased distance between code words in the phonetic alphabet makes it easier to distinguish and prevents miscommunications due to noise from the radio or a strong french accent from the pilot.

The first error-correcting code targeted at correcting errors in a classical computer was developed at Bell Laboratories by Richard Hamming [36] in 1950. In this protocol, four bits of information are encoded using seven physical bits in such a way that any individual bit-flip affecting a physical qubit can be detected and corrected while preserving the logical information. Subsequent development of classical error-correcting codes then improved their density, requiring fewer bits of redundancy to store the logical information, and increased the number of errors a code could correct.

This section introduces the simplest example of an error-correcting code: the repetition code. Such a code uses $d_X = 2n+1$ physical bits to encode one logical bit, protected against n physical bit-flip errors. The logical states 0_L

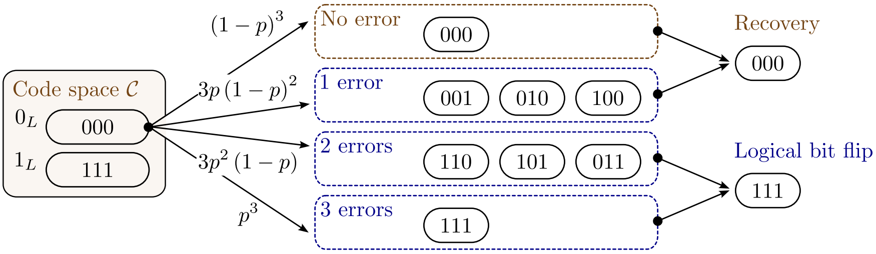

Figure 2.3: The code space $\mathcal{C}$ defining the encoding of the distance three repetition code is defined by the two logical states $0_L = 000$ and $1_L = 111$. All three physical bits have the same probability p of undergoing a bit-flip error, which would bring the system from the code space to one of the corresponding error spaces. After a majority vote, a recovery operation is applied which brings the system back onto $\mathcal{C}$. This recovery operation induces a logical bit-flip error if more than 1 error has occurred, flipping the correct bit otherwise.

and 1_L which define the *code space* $\mathcal{C}$ then physically correspond to having all of these physical bits in either 0 or 1,

$$0_L = 000...00,\ 1_L = 111...11. \tag{2.30}$$

When trying to store or transmit this logical information, we consider that each physical bit can suffer a bit-flip error with a probability p, bringing the system out of the code space and onto an *error space*. Such errors can be detected by measuring the state of each physical bit, a majority vote then indicating which bits are the most likely to have suffered from a bit-flip error. A recovery operation can then be applied whose goal is to flip the erroneous bits, recovering the initial logical state if less than n bit-flip errors occurred and inducing a logical bit-flip error otherwise. An illustration of this process for a distance three repetition code ($d_X = 3$) is represented in Fig. 2.3. The question that naturally arises is, was it worth it to complexity the system by introducing more bits? Is the bit-flip error rate of the logical qubit smaller than the physical error rate p?

The probability of a logical bit-flip error corresponds to the probability for at least $n+1$ physical bits to undergo a bit-flip error

$$
\begin{aligned}
p_{\text{Logical}} &= \sum_{k=n+1}^{2n+1} \binom{2n+1}{k} p^k \left(1-p\right)^{2n+1-k}, \\
\text{with } \binom{2n+1}{k} &= \frac{(2n+1)!}{k!\,(2n+1-k)!}.
\end{aligned}
\tag{2.31}
$$

The dependence of p_{Logical} on the physical error rate p is shown in Fig. 2.4 for different code distance d_X. These curves illustrate that for large error rates, the repetition code performs worse than an isolated physical qubit due to an increased number of physical errors that the code is unable to correct. Only when p goes below an *error threshold*, $p_{\text{Th}} = 0.5$ for the repetition code, does the logical bit outperform its physical components. Below this threshold, going to a larger size for the repetition code further decreases the logical bit flip probability, improving the performance of the error-correcting code.

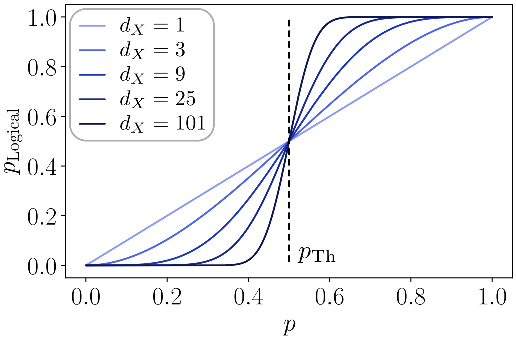

Figure 2.4: Logical error probability p_{Logical} as a function of the physical error probability for different distances of the repetition code d_X. An error threshold $p_{\text{Th}} = 0.5$ is observed, below which the performance of the repetition code improves for larger code distance, with a sharper transition at p_{Th}.

2.3.1.2 *The challenges of the quantum world*

Quantum error correction uses the same fundamental ideas to extend the coherence time of qubits, encoding the information into larger Hilbert spaces so that errors affecting physical qubits can be detected and corrected. However, some key features of quantum mechanics must be taken into account when adapting classical error-correcting codes to the quantum world [68].

First is the *no-cloning theorem* [69] which states that no quantum operation $\hat{\mathcal{O}}$ can operate the mapping

$$\hat{\mathcal{O}}\left(|\psi\rangle \otimes |\phi\rangle\right) = |\psi\rangle \otimes |\psi\rangle \tag{2.32}$$

for an arbitrary state $|\psi\rangle$. This is the result of the linearity of quantum mechanics as, considering an initial state

$$|\Psi\rangle = \left(\alpha\,|0\rangle + \beta\,|1\rangle\right) \otimes |0\rangle\,, \tag{2.33}$$

the application of such an operation $\hat{\mathcal{O}}$ would result in a state

$$\hat{\mathcal{O}}\,|\Psi\rangle = \alpha^2\,|00\rangle + \alpha\beta\left(|01\rangle + |01\rangle\right) + \beta^2\,|11\rangle\,. \tag{2.34}$$

While Eq. (2.33) is linear in α and β, Eq. (2.34) is quadratic in these same parameters which is only possible if the operator $\hat{\mathcal{O}}$ itself depends on α and β. These 2 quantities being unknown for an arbitrary initial state, such an operator cannot be constructed. While this theorem does not prevent the demonstration of quantum error correction, it limits the strategies that can be employed, notably preventing the strategy of duplicating quantum information during an algorithm.

A second key feature of quantum mechanics is the measurement back action that collapses the state of a quantum system after a measurement. This effect, if not taken into consideration when designing the encoding, leads to unrecoverable errors which corrupt the quantum information. An illustration of this effect is the "naive" quantum counterpart of the distance three-repetition code, where the logical encoding is defined as

$$|0_L\rangle = |000\rangle\,,\ |1_L\rangle = |111\rangle\,. \tag{2.35}$$

Considering the state

$$|\psi\rangle = \alpha\,|0_L\rangle + \beta\,|1_L\rangle\,, \tag{2.36}$$

the quantum information is stored in the complex coefficients α and β. When strictly following the protocol of the classical repetition code, we first measure the state of the first physical qubit. Assuming that no error occurred, this measurement would project the system in $|0_L\rangle$ with probability $|\alpha|^2$ and $|1_L\rangle$

with probability $|\beta|^2$, after which these coefficients are no longer accessible. Thankfully, this issue can be solved by designing *syndrome measurements* which make use of these projective measurements to collapse the logical qubit into a known error space without learning anything about the stored logical information.

Finally, a fundamental difference being classical and quantum error correction lies in the type of errors that we need to correct. While classical bits are only impacted by bit-flip errors, a qubit suffers from both bit-flip and phase-flip errors! This additional error, which does not have any classical counterpart, makes quantum error-correcting codes particularly challenging to implement.

2.3.2 *The fundamental theorems of Quantum Error Correction*

2.3.2.1 *Using Kraus maps to model error channels*

Errors impacting a qubit during a time interval[6] τ are modeled using a Kraus map $\mathcal{E}$, acting on the density matrix through the relation

$$\mathcal{E}\left(\hat{\rho}\right) = \sum_{\mu} \hat{M}_{\mu} \hat{\rho} \hat{M}_{\mu}^{\dagger}. \tag{2.37}$$

This operation is trace-preserving, which is ensured by the relation $\sum_{\mu} \hat{M}_{\mu}^{\dagger} \hat{M}_{\mu} = \mathbb{1}$. In the context of quantum information, the Kraus operators $\hat{M}_{\mu}$ are referred to as the *noise operators* or *error operators*, each of them representing an error channel due to the coupling with a noisy environment[7]. The goal of QEC is then to design a recovery operation $\mathcal{R}$ such that [70]

$$\forall \hat{\rho} \in \mathcal{C},\ \left(\mathcal{R} \circ \mathcal{E}\right)\left(\hat{\rho}\right) = \hat{\rho}. \tag{2.38}$$

2.3.2.2 *Knill-Laflamme condition for QEC*

Under which conditions does such a recovery operation exist? The Knill-Laflamme condition [71, 72] precisely answers this question, providing a necessary and sufficient condition for the existence of $\mathcal{R}$. Considering a code

---

[6] This time interval typically corresponds to the duration of an error-correcting cycle. In the example of the repetition code, this would be the time required to measure the syndrome measurements and perform the recovery operation.

[7] Kraus operators are not unique as any set $\left\{\hat{N}_{\mu}\right\}$, verifying $\hat{N}_{\mu} = \sum_{\nu} \gamma_{\mu\nu} \hat{M}_{\mu}$ with $\gamma_{\mu\nu}$ the coefficients of a unitary matrix, define the same Kraus map $\sum_{\mu} \hat{N}_{\mu} \hat{\rho} \hat{N}_{\mu}^{\dagger} = \sum_{\mu} \hat{M}_{\mu} \hat{\rho} \hat{M}_{\mu}^{\dagger}$.

space $\mathcal{C}$ and the associated projector $\hat{\Pi}_\mathcal{C}$, affected by an error channel $\mathcal{E}$ described by the Krauss operators $\left\{\hat{M}_\mu\right\}$, a recovery operation $\mathcal{R}$ exists if and only if

$$\hat{\Pi}_\mathcal{C}\hat{M}_\mu^\dagger\hat{M}_\nu\hat{\Pi}_\mathcal{C} = \alpha_{\mu\nu}\hat{\Pi}_\mathcal{C}, \tag{2.39}$$

with $\alpha_{\mu\nu}$ the coefficients of a Hermitian matrix α. Alternatively, considering a basis of the computational space $\{|\psi_i\rangle\}$, this condition can be expressed as

$$\langle\psi_i|\,\hat{M}_\mu^\dagger\hat{M}_\nu\,|\psi_j\rangle = \alpha_{\mu\nu}\,\delta_{ij}. \tag{2.40}$$

To gain some intuitive understanding of this condition, we start by simply considering the image of the code space under an error $\hat{M}_\mu$. From $\mathcal{C}$, a state $|\psi_i\rangle$ is projected into the error space $\mathcal{E}_\mu$, with $\hat{M}_\mu\,|\psi_i\rangle$ representing some distorted image of the input state. Eq. (2.40) then ensures two orthogonal states $|\psi_i\rangle$ and $|\psi_j\rangle$ of the code space remain orthogonal in $\mathcal{E}_\mu$

$$\langle\psi_i|\,\hat{M}_\mu^\dagger\hat{M}_\mu\,|\psi_j\rangle = \alpha_{\mu\mu}\,\delta_{ij} = 0, \tag{2.41}$$

with $||\hat{M}_\mu\,|\psi_i\rangle\,||^2 = ||\hat{M}_\mu\,|\psi_j\rangle\,||^2 = \alpha_{\mu\mu}$. All errors $\hat{M}_\mu$ then produce a faithful image of the code space, proportional to a unitary transformation, which can be corrected after determining the error that affected the system. However, how can we be sure that we will be able to know which error $\hat{M}_\mu$ impacted the system?

The easy case to consider is when the matrix α is diagonal, with $\alpha_{ij} = 0$ for $i \neq 0$. Under this condition, we see from Eq. (2.40) that two error spaces $\mathcal{E}_\mu$ and $\mathcal{E}_\nu$ corresponding to two distinct errors $\hat{M}_\mu$ and $\hat{M}_\nu$ are orthogonal

$$\forall\,|\psi\rangle \in \mathcal{C},\ \langle\psi|\,\hat{M}_\mu^\dagger\hat{M}_\nu\,|\psi\rangle = 0. \tag{2.42}$$

A syndrome measurement can then be designed in order to distinguish the different error spaces, without acquiring information about the state within the corresponding error space. The situation is slightly more complex when considering the general case where the matrix α has non-zero non-diagonal elements, corresponding to a situation where error spaces are not necessarily orthogonal. What could then happen is that after an error $\hat{M}_\mu$ projects the system onto the error space $\mathcal{E}_\mu$, we measure if the system is in $\mathcal{E}_\nu$. Because $\mathcal{E}_\mu$ and $\mathcal{E}_\nu$ are not orthogonal, our measure could indicate that the system is

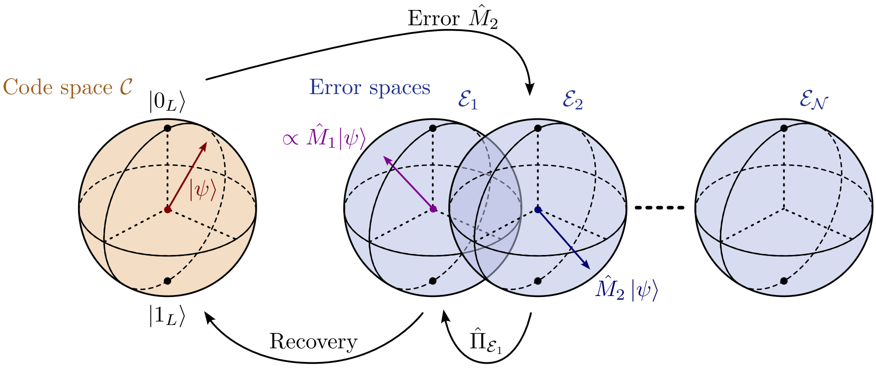

Figure 2.5: Illustration of the Knill-Laflamme theorem for non-orthogonal error spaces $\{\mathcal{E}_\mu\}$. After an error $\hat{M}_2$, a syndrome is measured which projects the system into $\hat{\Pi}_{\mathcal{E}_1}\hat{M}_2|\psi\rangle \propto \hat{M}_1|\psi\rangle$. A recovery operation that corrects for the error $\hat{M}_1$ then brings the system back into the code space and restores the quantum information.

indeed in $\mathcal{E}_\nu$, after which we correct for the error $\hat{M}_\nu$ although it was $\hat{M}_\mu$ that generated an error.

In this case, the Knill-Laflamme condition ensures that during the syndrome measurement, the state $\hat{M}_\mu|\psi\rangle$ is projected in $\mathcal{E}_\nu$ onto a state proportional to $\hat{M}_\nu|\psi\rangle$. The constant of proportionality $\alpha_{\mu\nu}$ does not depend on the initial state $|\psi\rangle \in \mathcal{C}$. Correcting for the error $\hat{M}_\nu$, although this error never physically occurred, then brings the system back to $\mathcal{C}$ while preserving the initial state (see Fig. 2.5). Being able to work with non-orthogonal error spaces is specific to quantum mechanics, illustrating how projective measurements can be exploited to design new error-correcting codes.

2.3.2.3 *Error discretization theorem*

The Knill-Laflamme condition ensures the existence of a recovery operation for a given set of error operators $\left\{\hat{M}_\mu\right\}$ affecting a quantum system. Considering the case of a qubit, what set of error operators should we consider? Naively, one could consider $\left\{\hat{M}_\mu\right\} = \mathrm{SU}(2)$ as a qubit can be affected by any operator of this group. However, considering such a continuous ensemble of errors isn't efficient, notably when designing error-correcting codes.

The error discretization theorem [72] states that, for a given set of errors $\left\{\hat{E}_\mu\right\}$ correctable by a recovery map $\mathcal{R}$, the set $\left\{\hat{F}_\mu\right\}$ where operators $\hat{F}_\mu$ are linear combinations of $\hat{E}_\nu$ is also correctable by $\mathcal{R}$. All operators in SU(2) being a linear combination of the Pauli matrices, the design of error-correcting codes then reduces to designing codes robust against Pauli errors. Furthermore, because $\hat{\sigma}_x\hat{\sigma}_z = -i\hat{\sigma}_y$, a code that can correct for any 2 Pauli errors can correct for any error in the SU(2) group.

This justifies the classification, already introduced in this chapter, where errors are referred to as either bit-flip or phase-flip errors. Bit-flips correspond to a $\hat{\sigma}_x$ error, inducing swap between $|0\rangle$ and $|1\rangle$ while phase-flips refer to $\hat{\sigma}_z$ errors which flip $|+\rangle$ and $|-\rangle$.

2.4 QUANTUM ERROR CORRECTION USING ARRAYS OF QUBITS

2.4.1 *Quantum version of the repetition code*

We demonstrate the application of this framework in the context of quantum error correction, particularly focusing on quantum error-correcting codes constructed from an array of physical qubits. The most basic illustration of such a code is the distance three repetition code which, as defined in Eq. (2.35), protects the quantum information against any single-qubit errors with $\left\{\hat{M}_\mu\right\} = \{\mathbb{1}, \hat{\sigma}_{x_1}, \hat{\sigma}_{x_2}, \hat{\sigma}_{x_3}\}$. Starting from the code space $\mathcal{C} = \text{span}\left\{|000\rangle, |111\rangle\right\}$, such an error would either leave the system in the code space or transition it into one of the error spaces $\mathcal{E}_1$, $\mathcal{E}_2$ and $\mathcal{E}_3$, respectively corresponding to the first, second and third qubit flipping. Considering the state

$$|\psi\rangle = \alpha\,|000\rangle + \beta\,|111\rangle \tag{2.43}$$

for instance, a bit-flip error impacting the first qubit would change the state into $\alpha\,|100\rangle + \beta\,|011\rangle$ that belongs to $\mathcal{E}_1$. By measuring the two commuting observables $(\hat{\sigma}_{z_1}\hat{\sigma}_{z_2}, \hat{\sigma}_{z_2}\hat{\sigma}_{z_3})$ the different error spaces can be distinguished (see Table. 2.1) without projecting the quantum information. A recovery operation can then be applied which returns the system back into the code space, reducing the probability of a logical bit-flip from the physical bit-flip probability p to $p_L \propto p^2$

Similar to the classical case, the logical bit-flip rate can be further reduced by increasing the number of qubits d_X in the repetition code, resulting in an exponential decrease of the logical error rate, with $p_L \propto (2p)^{d_X/2}$ (Fig. 2.4). However, this exponential decrease in bit-flip errors comes at the (modest) cost of a linear increase in phase-flip errors, which are not protected by the encoding. These phase-flip errors are addressed by the dual version of the repetition code, defined in its three-qubit form as

$$|+_L\rangle = |+++\rangle\,,\ |-_L\rangle = |---\rangle\,. \tag{2.44}$$

Measuring the syndromes $\hat{\sigma}_{x_1}\hat{\sigma}_{x_2}, \hat{\sigma}_{x_2}\hat{\sigma}_{x_3}$ enables the detection and correction of phase flip errors, while bit-flip errors remain unprotected.

Space	**Syndrome measurement**
$\mathcal{C}$	1, 1
$\mathcal{E}_1$	-1, 1
$\mathcal{E}_2$	-1, -1
$\mathcal{E}_3$	1, -1

Table 2.1: Syndrome measurements corresponding to the different error subspaces, with $\mathcal{C}$ being defined as the eigenspace with eigenvalue one of the syndromes $\hat{\sigma}_{z_1}\hat{\sigma}_{z_2}, \hat{\sigma}_{z_2}\hat{\sigma}_{z_3}$.

2.4.2 *Extension of the encoding, simultaneously correcting bit-flip and phase-flip errors*

2.4.2.1 *Bacon-Shor codes*

To protect a qubit against both bit-flip and phase-flip errors, it becomes necessary to increase the redundancy, notably achieved in superconducting circuits by increasing the dimensionality of the code. From the one-dimensional architecture of the repetition code, we then consider two-dimensional configurations that define a single logical qubit. The natural extension of the repetition code using this two-dimensional architecture was developed in 2005 by Bacon [73], now commonly known as the Bacon-Shor code family. These can be envisioned as two separate repetition codes pieced together, one designed to mitigate bit-flip errors and the other tailored to address phase-flip errors. The layout corresponding to a Bacon-Shor code with parameters $d_X = 5$ and $d_Z = 3$ is shown in Fig. 2.6.

This code can be intuitively comprehended by considering an *inner* and *outer* layer of error correction. Using the bit-flip repetition code as the inner layer of protection, each row of the code defines a partially protected qubit where bit-flip errors are exponentially suppressed, albeit at the cost of a linear increase in phase-flip errors. These are then corrected by the outer repetition code, defining the logical encoding as

$$\begin{aligned}|+_L\rangle &= \frac{1}{\sqrt{2}^{d_Z}}\left(|0\rangle^{\otimes d_X} + |1\rangle^{\otimes d_X}\right)^{\otimes d_Z}\\ |-_L\rangle &= \frac{1}{\sqrt{2}^{d_Z}}\left(|0\rangle^{\otimes d_X} - |1\rangle^{\otimes d_X}\right)^{\otimes d_Z}.\end{aligned} \tag{2.45}$$

The stabilization is ensured by measuring the syndromes $\hat{\sigma}_{z_i}\hat{\sigma}_{z_{i+1}}$ between pairs of neighboring qubits in the same row, and $\hat{\sigma}_{x_i}\hat{\sigma}_{x_{i+1}}$ between the partially protected qubits defined in two consecutive rows. Note that another approach for this code can be envisioned where the inner repetition code corrects for phase-flip errors while the outer one corrects for the remaining bit-flips. The logical states are then defined as

$$\begin{aligned}|0_L\rangle &= \frac{1}{\sqrt{2}^{d_X}}\left(|+\rangle^{\otimes d_Z} + |-\rangle^{\otimes d_Z}\right)^{\otimes d_X}\\ |1_L\rangle &= \frac{1}{\sqrt{2}^{d_X}}\left(|+\rangle^{\otimes d_Z} - |-\rangle^{\otimes d_Z}\right)^{\otimes d_X}.\end{aligned} \tag{2.46}$$

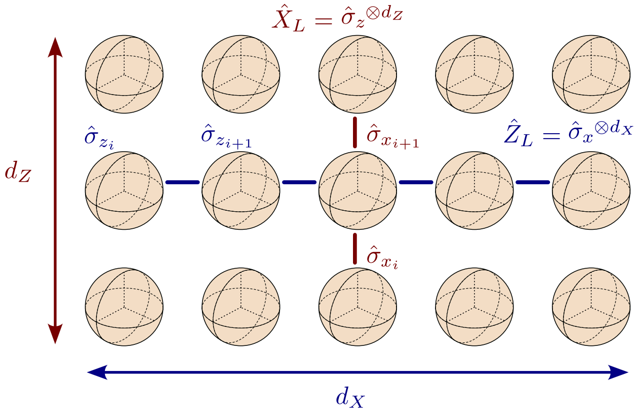

Figure 2.6: Layout of the Bacon-Shor code for $d_X = 5$ and $d_Z = 3$. The logical operators $\hat{X}_L$ and $\hat{Z}_L$ are built from products of operators $\hat{\sigma}_x$ and $\hat{\sigma}_z$ acting on the physical qubits in a column (red) or row (blue).

Irrespective of which repetition layer is the inner or outer one, the logical error rate of the corresponding logical qubit depends on d_X and d_Z as

$$\begin{aligned}p_{X_L} &\propto \left(2\, d_Z\, p_{X_{\text{physical}}}\right)^{d_X/2}\\ p_{Z_L} &\propto \left(2\, d_X\, p_{Z_{\text{physical}}}\right)^{d_Z/2}.\end{aligned} \tag{2.47}$$

Here $p_{X_{\text{physical}}}$ and $p_{Z_{\text{physical}}}$ represent the probabilities for one of the physical qubits to suffer from a bit-flip or phase-flip error. This equation might suggest that going to an arbitrarily low bit-flip and phase-flip error rate is achievable by simply increasing d_X and d_Z, the exponential suppression of p_{X_L} and p_{Z_L} compensating the small linear increase. However, it is crucial to note that this exponential suppression only occurs when each of the repetition codes is operated below its threshold (see Fig. 2.4). In the Bacon-Shor code, the probability of a given error (bit-flip or phase-flip) increases linearly with the distance of the dual repetition code, thus potentially pushing its error rate beyond threshold[8]. This would for instance correspond to the situation where $p_{Z_{\text{physical}}} d_X > 0.5$, after which the outer repetition layer becomes ineffective and actually degrades the system by introducing additional errors.

Due to the competition between reducing the logical error rate and staying below the threshold of a repetition code, Bacon-Shor codes themselves do not possess a threshold. Instead, an optimal code size (d_X, d_Z) can be determined for a given set of physical error rates $\left(p_{X_{\text{physical}}}, p_{Z_{\text{physical}}}\right)$. As a result, these codes have mainly been explored in the context of relatively small code sizes, often serving as the foundational layer within a larger concatenated coding scheme [74, 75]. However, it should be noted that large Bacon-Shor codes, used independently as a logical qubit without concatenation, can provide remarkable protection when the physical error rate is sufficiently low. For instance, if we consider a physical error rate of $p_{X_{\text{physical}}} = p_{Z_{\text{physical}}} = 0.1\%$, a Bacon-Shor code with dimensions 173×173 is projected to have a logical error rate as low as $p_{X_L} = p_{Z_L} \approx 2.10^{-28}$ [76].

2.4.2.2 *The CSS surface code*

Another promising approach using two-dimensional arrays of superconducting qubits is the CSS surface code, originally developed in 1996 by Calderbank, Shor, and Steane [78, 79]. In this encoding scheme, qubits are categorized as either *data* or *measurement* qubits, represented in Fig. 2.7**a** as open or filled circles. Measurement qubits are used in order to stabilize the quantum information stored in the data qubits, with syndromes corresponding to the local product $\hat{\sigma}_{z,a}\hat{\sigma}_{z,b}\hat{\sigma}_{z,c}\hat{\sigma}_{z,d}$ or $\hat{\sigma}_{x,a}\hat{\sigma}_{x,b}\hat{\sigma}_{x,c}\hat{\sigma}_{x,d}$ between four neighboring data qubits.

The pulse sequence used to measure these syndromes is represented in Fig. 2.7**b** and Fig. 2.7**c**. For the Z-measurement qubit, the sequence begins

---

[8] This is in contrast to a simple repetition code where the error probability is fixed by the physical qubit implementation.

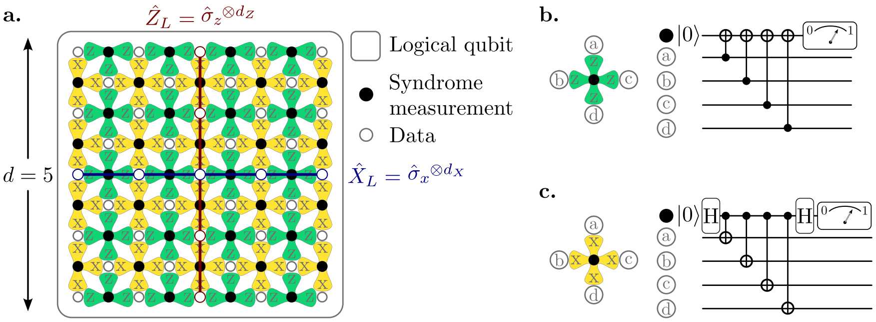

Figure 2.7: **a.** Layout of the CSS surface code and its corresponding stabilizers for a distance five surface code. Data qubits are represented by open circles and measurement qubits by filled circles. Qubits responsible for measuring the syndrome $\hat{\sigma}_{x,a}\hat{\sigma}_{x,b}\hat{\sigma}_{x,c}\hat{\sigma}_{x,d}$ are positioned at the center of the yellow regions, while those measuring $\hat{\sigma}_{z,a}\hat{\sigma}_{z,b}\hat{\sigma}_{z,c}\hat{\sigma}_{z,d}$ are located in the green regions. **b.** Pulse sequence mapping the Z-stabilizer's value onto the corresponding measuring qubit. The measurement qubit is prepared in its ground state and CNOT gates are applied with the data qubits serving as the controls. **c.** Pulse sequence mapping the X-stabilizer's value onto the corresponding measuring qubit. The measurement qubit is prepared in $|+\rangle$ using a Hadamard gate, after which CNOT gates are applied with the measurement qubit as the control. Figure adapted from Fig. 1 of [77].

by initializing it in its ground state $|0\rangle$ before applying four CNOT gates[9] which use the four nearest-neighbor data qubits as the control. A readout of the measurement qubit then projects the system into an eigenstate of $\hat{\sigma}_{z,a}\hat{\sigma}_{z,b}\hat{\sigma}_{z,c}\hat{\sigma}_{z,d}$ with eigenvalue ±1. A similar pulse sequence is employed for the X-measurement qubit, with the addition of Hadamard gates applied before and after the CNOT gates. In this case, the CNOT gates use the measurement qubit as the control. This circuit is effectively equivalent to replacing the CNOT gates in Fig. 2.7**b** with Controlled-Z gates, resulting in the projection of the system into an eigenstate of $\hat{\sigma}_{x,a}\hat{\sigma}_{x,b}\hat{\sigma}_{x,c}\hat{\sigma}_{x,d}$ after measurement.

Since all these local syndromes commute, even though data qubits are involved in multiple syndrome measurements, they can all be simultaneously measured in a single round of error correction. This leads to the determination of 40 syndromes with values ±1 for the code illustrated in Fig. 2.7**a**, corresponding to $2^{40} \approx 10^{12}$ possible subspaces within the system's total

---

[9] A CNOT or controlled-not gate applies a gate $\hat{\sigma}_x$ to a target qubit if the control qubit is in its excited state $|1\rangle$, and stays idle if it is in $|0\rangle$.

Hilbert space. The code space $\mathcal{C}$ is then defined as the subspace where all syndromes equal 1, with the logical operators $\hat{Z}_L$ and $\hat{X}_L$ corresponding to the product of local $\hat{\sigma}_z$ and $\hat{\sigma}_x$ operators acting on data qubits.

All syndromes are regularly monitored during an operation of this logical qubit to detect deviation from their desired value of 1. When an error is identified, the challenge then lies in determining which error affected the array. This task is relatively straightforward when errors are sufficiently rare, resulting in spatially and temporally isolated errors that can be matched to a specific physical qubit error. Such errors can then be immediately corrected before the next round of correction, or alternatively, they can be tracked and corrected in software at the end of the computation. However, when a significant number of errors occur within a correction cycle, especially when resulting in chained errors involving adjacent qubits, decoding the measured syndromes becomes trickier. Because of this, minimum weight perfect-matching (MWPM) algorithms [80, 81] are used which automatically estimate the best choice of recovery operation based on the measured set of syndromes.

Using these algorithms as decoders, simulations were conducted to assess the performance of the resulting logical qubit as a function of a physical error rate p [77]. This physical error rate encompasses various error sources, including errors in the preparation and measurement of single qubits, infidelities in single and two-qubit gates, as well as the natural decay of the physical qubits. In contrast to Bacon-Shor codes, a threshold $p_{Th} \approx 0.5\%$ was identified below which an exponential reduction in the logical error rate was observed, depending on the code distance d as

$$p_L \approx 0.03 \left(\frac{p}{p_{Th}} \right)^{(d+1)/2} . \tag{2.48}$$

The remaining logical errors correspond to occurrences where a large amount of errors resulted in an erroneous decoding by the MWPM algorithm, resulting in an erroneous correction that compromised the logical information.

2.4.2.3 *Physical implementations of the CSS surface code*

The CSS surface code is amongst the most popular quantum error-correcting codes, with multiple experiments coming from both academic groups and industrial players. In this section, we present three of these realizations and the achieved performances. A summary of the device's parameters for each experiment is presented in Table. 2.2.

DISTANCE 3 SURFACE CODE USING ZURICH'S SAMPLE

The first successful implementation of a distance three surface code using superconducting qubits, capable of correcting any single Pauli error that may occur during a correction cycle, was demonstrated in 2021 at ETH Zurich by Krinner et.al [82]. In this experimental setup, a logical qubit was encoded using a grid of seventeen qubits, nine of which served as data qubits while the remaining eight functioned as auxiliary qubits responsible for measuring X-type or Z-type stabilizers.

The stabilizers of the surface code were measured for up to $n = 16$ cycles, any changes in their values signaling an error affecting one of the physical qubits. By monitoring the evolution of these syndromes, a MWPM algorithm can then be used which exploits spatial and temporal correlations in the measured syndromes to infer the necessary recovery operation after the final error-correction cycle. Discarding instances where leakage was detected during the operation[10], corresponding to 8% of the data, a bit-flip error probability per cycle of $\varepsilon_{3,\,\mathrm{X}} = 3.2\%$ was measured, along with a phase-flip error probability $\varepsilon_{3,\,\mathrm{Z}} = 2.9\%$. Given the associated cycle duration $\tau_{\text{cycle}} = 1.1\ \mu$s, these error rates translates into logical bit-flip and phase-flip times

$$\begin{aligned} T_{X,L} &= \frac{\tau_{\text{cycle}}}{2\,\varepsilon_{3,\,\mathrm{X}}} = 16.4\ \mu\text{s}, \\ T_{Z,L} &= \frac{\tau_{\text{cycle}}}{2\,\varepsilon_{3,\,\mathrm{Z}}} = 18.2\ \mu\text{s}. \end{aligned} \tag{2.49}$$

These are notably shorter than the average coherence time of the physical qubits that constitute the surface code, indicating the code was not operated below its threshold.

DISTANCE 3 SURFACE CODE WITH THE ZUCHONGZHI 2.1

Just two months after the experiment conducted by Krinner et al., another experiment showcased the operation of a distance three surface code using a subset of seventeen qubits extracted from the 66 qubits of the *Zuchongzhi 2.1* chip [84, 85]. However, there were notable differences in this experiment's performance. While the fidelity of one and two-qubit gates was similar to the previous experiment, the measurement infidelity experienced a significant

---

[10] Such a leakage would correspond to a data or measurement qubit getting excited higher than its first excited state. This could be attributed to quasiparticles causing correlated errors across the chip [55] or excitations induced by the readout of measurement qubit [83].

increase, reaching approximately 4.752%, as opposed to the 0.9% measured in [82]. Additionally, the average coherence time of the physical qubits was relatively brief with $T_2 = 5.3$ μs and the duration of an error correction relatively long at $T_{\text{cycle}} = 4.153$ μs, primarily limited by the duration of the readout ≈ 3.9 μs.

These physical parameters translate to an increased logical error per cycle with $\varepsilon_{3,\,\mathrm{X}} = \varepsilon_{3,\,\mathrm{Z}} = 26\%$ when applying the recovery operation after the final error-correction cycle. Although this represented a 20% enhancement compared to the uncorrected surface code's error rate of $\varepsilon_{3,\,\mathrm{X}} = 32\%$ and $\varepsilon_{3,\,\mathrm{Z}} = 33\%$, the associated coherence time $T_{\text{cycle}}/2\varepsilon_{3,\,\mathrm{Z}} = 7.98$ μs remained significantly shorter than the average lifetime of the physical qubits.

DISTANCE 3 & 5 SURFACE CODE WITH THE SYCAMORE CHIP

Seven months later, in July 2022, Google AI introduced its own adaptation of the surface code, using subsets of the *Sycamore chip* with its interconnected ensemble of 72 qubits [86]. Selecting the desired array of qubits, a distance three surface code was operated. This encoding was then extended to a distance five surface code, whose layout is represented in Fig. 2.7**a**.

In terms of the performance of the code's physical components, Google's results were similar to [82], featuring slightly improved fidelity for one and two-qubit gates but at the expense of increased readout infidelity. This similarity in physical components naturally led to a comparable logical error rate per cycle, yielding $\varepsilon_3 = 3.028 \pm 0.023\%$. There, ε_3 corresponds to an averaged value of the error rate over the cardinal states of the Bloch sphere. Given a cycle duration of $T_{\text{cycle}} = 0.931$ μs, this resulted in a logical coherence time of ≈ 15 μs which remained shorter than the average coherence time of the physical qubits. This observation indicates that the physical error rate remained above the code threshold, despite the gate fidelities and qubit lifetimes being close to state-of-the-art standards.

However, an intriguing shift occurred when expanding the code to a distance five surface code, consisting of 25 data qubits and 24 measurement qubits. In this scenario, the logical error rate per cycle decreased to $\varepsilon_5 = 2.914 \pm 0.016\%$, despite the system remaining above threshold. This phenomenon can be attributed to the existence of a *crossover regime*, evidenced in simulations, corresponding to the physical error rate approaching the error threshold within a few percentage points. Within this regime, finite size effects lead to an initial reduction of the logical error rate for increasing code distance, only to see it rise later on.

Parameter	**ETH Zurich**	**Zuchongzhi 2.1**	**Sycamore**
Single qubit gate errors	0.09%	0.098%	0.01%
Two qubits gate errors	1.5%	1.035%	0.5%
Measurement infidelity	0.9%	4.752%	2.0%
Average physical T_1	32.5 μs	28.4 μs	20 μs
Average physical T_2	37.5 μs	5.3 μs	30 μs
Correction cycle duration τ_{cycle}	1.1 μs	4.153 μs	0.931 μs
Logical error per cycle ε_3	3 %	26 %	3.026%
Logical error per cycle ε_5			2.914%

Table 2.2: **Physical parameters of the different surface codes.**

2.4.3 *Easing the hardware requirements using biased noise qubits*

These experiments showcase the difficulty of operating a CSS surface code below its error threshold, despite the efforts dedicated to increasing the lifetime of physical qubits, the fidelity of one and tow-qubit gates, or the accuracy of qubit readout. Furthermore, even after reaching this error threshold, operating a logical qubit on which useful algorithms can be performed would require at least $10^5 - 10^6$ physical qubits per logical qubit [77], far beyond what is currently feasible with superconducting circuits. To ease the error threshold of the CSS surface code, leading to fewer qubits being necessary to define a single logical qubit, an alternative variant of the surface code was introduced in 2020: the XZZX surface code [87].

2.4.3.1 *The XZZX surface code*

The XZZX surface code [87] is similar in its structure to the conventional CSS surface code, the primary distinction between these two encodings lying in the structure of their syndromes. While the CSS surface code employs two types of measurement qubits responsible for measuring X-type or Z-type syndromes, all measurement qubits in the XZZX surface code are dedicated to measuring the same syndrome $\hat{\sigma}_{z,a}\hat{\sigma}_{x,b}\hat{\sigma}_{x,c}\hat{\sigma}_{z,d}$ between four neighboring data qubits (Fig. 2.8**a.**). These syndromes are measured similarly to the X-stabilizers of the CSS surface code, replacing the CNOT gates between the measurement qubit and the data qubits a and b with controlled-Z gates. The pulse sequence shown in Fig. 2.8**c.** is executed simultaneously on all measurement qubits, ensuring that no data qubit is simultaneously engaged in two gates during the operation

This local change of basis leads to the XZZX surface code reacting to Pauli errors differently than the CSS surface code. In particular, a key feature of this encoding is that bit-flip errors occurring on a data qubit lead to vertically aligned syndrome measurements indicating a value of -1. Similarly, phase-flip errors affecting data qubits would result in horizontal error patterns (Fig. 2.8**b.**). This property can be exploited when designing the decoder, particularly when the physical qubits exhibit a significant noise bias[11]

$$\eta = \frac{p_z}{p_x + p_y} \tag{2.50}$$

where p_x, p_y and p_z respectively correspond to the probability of a physical X, Y, and Z Pauli-error. A decoder can then be tailored to assign greater importance to vertical error patterns when determining the appropriate recovery operation. This leads to a more unambiguous identification of errors, particularly when compared to the CSS surface code or an unbiased XZZX code where all directions are equally weighted, resulting in an increased error threshold. Note that in the limit $\eta \to \infty$, bit-flip errors can be completely discarded and the XZZX surface code effectively behaves as a repetition code, protecting the logical information against phase-flip errors. This intuition is confirmed by the error threshold increasing with η, reaching $p_{\mathrm{Th}} = 0.5$.

2.4.3.2 *What biased-noise qubit to use in such architecture ?*

Several biased noise qubits can be envisioned as the building blocks of an XZZX surface code, including qubits based on technologies such as trapped ions or Rydberg atoms. However, a crucial feature lacking in these technologies is the ability to perform operations that preserve the bias in the noise characteristics of the physical qubits[12]. These operations are essential for preventing bit-flip or phase-flip errors from being converted into their respective conjugate errors. In the absence of such gates, the unique advantage of the XZZX surface code would quickly disappear as the noise bias vanishes after a few rounds of error correction.

---

[11] A large noise bias corresponds to scenarios where physical bit-flip errors are largely suppressed, leaving phase-flip as the primary source of logical errors within the surface code. Small biases $\eta \ll 1$ can also be exploited, which in the limit of $\eta \to 0$ would make the code equivalent to a repetition code correcting for bit-flip errors.

[12] A no-go theorem demonstrated in the appendix of [88] shows that no bias-preserving two-qubit gates exist for two-level systems. An extra degree of freedom is necessary in order to continuously deform the encoding, such as the complex amplitude α describing a cat qubit.

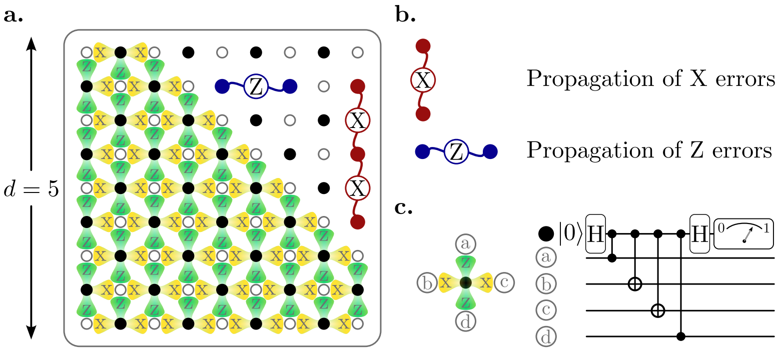

Figure 2.8: **a.** Layout of the XZZX surface code and its corresponding stabilizers for a distance five surface code. Data qubits are depicted as open circles, while measurement qubits are shown as filled circles. **b.** Graphic representation illustrating the propagation of logical errors affecting data qubits. Vertical error strings indicate bit-flip errors, while horizontal strings represent phase-flip errors **c.** Pulse sequence mapping the code stabilizer's value onto the corresponding measuring qubit. The measurement qubit is prepared in $|+\rangle$ using a Hadamard gate, after which controlled-Z and CNOT gates are applied using the data qubits as the control.

A particularly appealing design is that of *cat qubits*, with recent proposals exploring their use in an XZZX surface code [89] or in a simple repetition code [88, 90] for a sufficiently large detuning η. Similar to a repetition code, cat qubits exhibit an inherent protection against bit-flip errors which are exponentially suppressed with a parameter α, at the expense of a linear increase of the phase-flip error rate. A repetition code of cat qubits would then effectively behave as a Bacon-Shor code.

2.5 CHAPTER SUMMARY

In this chapter, we formalized the notion of what constitutes a qubit and how its state can be described using a pure state $|\psi\rangle$ when isolated, or a density matrix $\hat{\rho}$ when entangled with its surrounding environment. We presented how this interaction between a qubit and a noisy environment can lead to decoherence, which we decompose into bit-flip and phase-flip-errors. Focusing on the physical sources of decoherence, strategies can be implemented that reduce the power spectral density of these external sources of noise. Alternatively, new qubit designs can be envisioned that exhibit greater resilience to such noise sources and are less sensitive to decoherence. Over the past two decades, both of these strategies have been pursued, resulting in a remarkable improvement in the coherence time of superconducting qubits. This improvement spans seven orders of magnitude, with coherence times increasing from a few nanoseconds in the early days of the Cooper-pair box [32] to tens of milliseconds in recent experiments [28].

Despite these impressive advancements, the current coherence times still fall short of what is required to effectively demonstrate practical quantum algorithms, motivating the use of quantum error-correcting codes. The fundamental idea behind QEC is to redundantly store the logical information across many physical qubits, providing redundancy to the system. By doing so, even if a physical qubit encounters an error, the logical information can still be retrieved by monitoring the ensemble. Various encoding schemes have been developed which depend on the arrangement of physical qubits, including the repetition code, the CSS surface code, and the XZZX surface code. In this thesis, we particularly focus on the XZZX surface code, envisioned in the limit $\eta \to \infty$ where it can effectively be replaced by a repetition code. To be more precise, we only consider the physical qubits from which such a code can be built: the cat qubits. These cat qubits are introduced in Chapter 3, which broadly explores the concept of bosonic qubits stored within superconducting cavities.

3

BOSONIC CODES

Bosonic codes encoded using superconducting circuits offer a promising approach towards quantum error correction [91, 92]. Using continuous-variable systems, such as a harmonic oscillator realized in superconducting circuits, these codes compactly encode the quantum information in multi-photon states of a *memory* mode [93, 94, 95]. Unlike the previously presented strategies which rely on numerous physical two-level systems to define logical qubits, bosonic codes exploit the infinite-dimensional Hilbert space of the harmonic oscillator to store and protect the logical information. This hardware-efficient approach drastically reduces the required number of physical elements, although registers of harmonic oscillators might be needed depending on the encoding. This simplifies both the design and operation of these devices. More essentially, it mitigates the performance degradation caused by uncontrolled cross-talks or error propagation that can arise when using interconnected physical elements in traditional repetition or surface codes.

From the infinite-dimensional Hilbert space of the harmonic oscillator, bosonic qubits are defined by selecting a suitable 2-dimensional subspace. Various encoding strategies have emerged, each capitalizing on different symmetry properties of the logical state's Wigner functions [92]. Notable examples include the kitten code [96], the GKP code [97], and the cat code coming in either its 2-legged [98, 99, 100, 101, 102] or 4-legged version [103, 104].

To prevent leakage of logical information into the larger memory Hilbert space, several strategies can be employed which all aim to prevent the buildup of entropy in the superconducting cavity. One approach involves biasing the memory phase space through Hamiltonian engineering, creating local minima in its potential. By increasing the potential barrier between these minima, the system's exploration of phase space is restricted thus actively preventing the generation of entropy. Alternatively, the entropy created in the memory can be continuously removed using either measurement-based feedback or dissipation engineering. Measurement-based feedback entails measuring a syndrome to identify and correct errors that corrupted the logical information, leveraging the symmetries of the state to design the proper syndrome. Dissipation engineering on the other hand involves tailoring the coupling between the memory and its environment to induce an effective dissipation that stabilizes the desired states. This method continuously removes entropy from the system, similar to measurement-based feedback, but does not require any external intervention. The experiments presented in this thesis focus on this method.

This chapter presents various bosonic encodings, with particular emphasis on the stabilization of 2-legged cat qubits through Hamiltonian and dissipation engineering. We begin by introducing the fundamental components of a bosonic code, followed by an introduction of the Wigner function and its role in graphically representing quantum states and the impact of memory errors. We then introduce the kitten, GKP, and cat codes, before illustrating how Hamiltonian engineering, measurement-based feedback, and dissipation engineering can be employed to stabilize cat qubits. Finally, we present advancements in the stabilization of cat states through dissipation engineering, modifying the interaction between the memory and its environment to achieve higher dissipation rates.

3.1 BUILDING BLOCKS OF A BOSONIC CODE

3.1.1 *The quantum Harmonic Oscillator*

Bosonic quantum error correction relies on encoding logical information in harmonic oscillators. In circuit QED, these modes can notably be hosted by three-dimensional (3D) cavities or two-dimensional (2D) resonators, each with unique characteristics for preserving quantum information.

3D cavities are typically bulky structures, ranging from approximately 2 to 10 centimeters in size when operating in the 2 to 12 GHz frequency range. This bulkiness is imposed by the dielectric constant of the vacuum that encompasses the electromagnetic mode. While this presents certain technical challenges, it also allows to reach high-quality factors due to the spread of the mode throughout the cavity's volume, resulting in a low peak electric field at the cavity surface. Remarkably, rectangular cavities can achieve quality factors as high as $Q = 10^7$ [105], whereas niobium superconducting radio frequency (SRF) cavities employed in particle accelerators for high-energy physics can reach Q values as high as 10^{10} to 10^{11} [106].

On the other hand, 2D resonators are fabricated by patterning superconducting thin films on top of substrates with relatively large dielectric constants. This enables them to be more compact compared to their bulky 3D counterparts for a given frequency range. However, this compactness comes at the cost of an increased peak electric field amplitude, rendering the resonator more susceptible to material defects or organic residues and limiting the quality factor to approximately $Q = 10^7$ [47, 107]. Although this relatively low-quality factor introduces decoherence and limits the lifetime of logical information, the heightened peak electric field allows for stronger coupling between the harmonic mode and its environment. This characteristic becomes particularly advantageous when designing quantum error-correcting codes as it enables to drastically modify the memory's properties by interacting with its environment, preventing the accumulation of entropy. Additionally, 2D resonators provide a versatile platform that facilitates swift design modifications and can be easily fabricated using standard lithography techniques.

Harmonic oscillators encoded in superconducting circuits are effectively described by an LC circuit 3.1. Bellow the superconductor critical temperature T_c, electrons bond to form Cooper pairs in the superconducting metal [20] and the circuit opposes no resistance to DC currents. Small losses originating from AC currents are usually ignored, and no resistance is then added to the equivalent electrical circuit. Furthermore, the bath of cooper pairs acts as an effective collective mode which can be characterized by two conjugate variables: the magnetic flux ϕ winding through the inductor and the charge Q across the capacitor. Following the derivation of [108, 109], these quantities relate to the circuit voltage V and current i as

$$\begin{cases} \phi\left(t\right) = \displaystyle\int_{-\infty}^{t} V\left(\tau\right) \mathrm{d}\tau \\ Q\left(t\right) = \displaystyle\int_{-\infty}^{t} i\left(\tau\right) \mathrm{d}\tau. \end{cases} \tag{3.1}$$

Expressed as a function of ϕ, the capacitance energy writes $\frac{1}{2}CV^2 = \frac{1}{2}C\dot{\phi}^2$ and the inductance energy $\frac{1}{2L}\phi^2$. Interpreting the former as the circuit kinetic energy and the latter as its potential energy, the Lagrangian can be expressed as

$$\mathcal{L} = \frac{1}{2}C\dot{\phi}^2 - \frac{1}{2L}\phi^2 \tag{3.2}$$

with C the circuit capacitance and L its inductance. Replacing $\dot{\phi}$ by $Q = C\dot{\phi}$, the Lagrangian becomes

$$\mathcal{L} = \frac{1}{2C}Q^2 - \frac{1}{2L}\phi^2 \tag{3.3}$$

and takes the same form as that of a mechanical oscillator, describing an object of mass C connected to a spring with a constant $1/L$. The frequency of the LC circuit describing the memory mode is given by $\omega_m = 1/\sqrt{LC}$, and its characteristic impedance by $Z = \sqrt{L/C}$. The Hamiltonian is then obtained from the Legendre transform of the Lagrangian

$$H = \frac{\delta \mathcal{L}}{\delta \dot{\phi}} \dot{\phi} - \mathcal{L} = \frac{1}{2C} Q^2 + \frac{1}{2L} \phi^2, \tag{3.4}$$

The quantum version of this Hamiltonian is derived by promoting the two classical variables ϕ and Q to quantum operators $\hat{\phi}$ and $\hat{Q}$, which verify the commutation relation

$$\left[\hat{\phi}, \hat{Q}\right] = i\hbar\,\mathbb{1}. \tag{3.5}$$

This expression can be made more intuitive by introducing the creation and annihilation operator $\hat{a}^\dagger$ and $\hat{a}$, defined by the relation

$$\begin{cases} \hat{Q} = iQ_{\text{ZPF}} \left(\hat{a}^\dagger - \hat{a}\right) \\ \hat{\phi} = \phi_{\text{ZPF}} \left(\hat{a}^\dagger + \hat{a}\right). \end{cases} \tag{3.6}$$

There, $Q_{\text{ZPF}} = \sqrt{\frac{\hbar}{2Z}}$ and $\phi_{\text{ZPF}} = \sqrt{\frac{\hbar Z}{2}}$. The Hamiltonian then takes the form

$$\hat{H} = \hbar\omega_m \left(\hat{a}^\dagger \hat{a} + \frac{1}{2}\right) \tag{3.7}$$

with $\left[\hat{a}, \hat{a}^\dagger\right] = \mathbb{1}$. From this expression, we can recognize the form of a quantum harmonic oscillator with $\hat{a}$ and $\hat{a}^\dagger$ the corresponding ladder operators. The eigenstates of this circuit are the Fock states $\{|n\rangle, n \in \mathbb{N}\}$, defined by the relation

$$\hat{a}^\dagger \hat{a} |n\rangle = n |n\rangle. \tag{3.8}$$

These states physically correspond to having n quanta of energy $\hbar\omega_m$, called *photons*, in the electromagnetic field. The operators $\hat{a}$ and $\hat{a}^\dagger$ respectively destroy or create an excitation in the harmonic oscillator. By employing Eq. (3.8), the energy of the system can be expressed as $E_n = n\hbar\omega_m + 1/2$ with n the number of mode excitations.

While these resonators serve as fundamental components for quantum error correction and are ideal for storing quantum information, they cannot

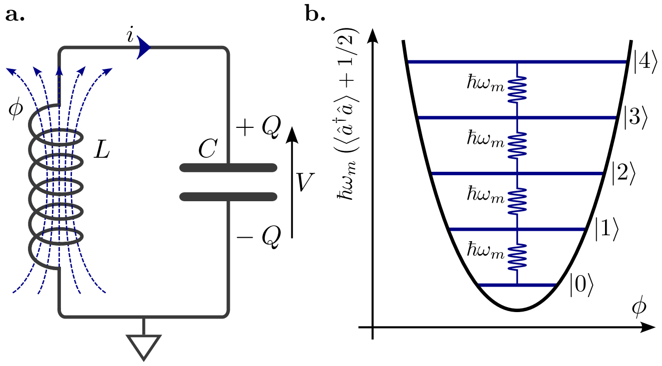

Figure 3.1: **a.** Representation of a superconducting resonator or cavity as an equivalent LC circuit. The electromagnetic mode is described by the conjugates variables ϕ and Q, their link with the circuit current and voltage is given by Eq. (3.1). **b.** Potential of the Harmonic oscillator as a function of ϕ, and energy spacing of the resonator eigenstates. Each Fock states $|n\rangle$ has an energy $E_n = n\hbar\omega_m + 1/2$.

be used alone in a bosonic code. This limitation stems from the regular energy spacing, $E_{n+1} - E_n = \hbar\omega_m$ remaining constant regardless of the photon number n. Consequently, it becomes impossible to target a specific transition between two Fock states starting from the vacuum state. The only states that can be encoded by driving the memory at its frequency $\omega_m/2\pi$ are coherent states $|\alpha\rangle$, $\alpha \in \mathbb{C}$, defined as

$$|\alpha\rangle = \hat{D}(\alpha)\,|0\rangle = e^{-|\alpha|^2/2} \sum_n \frac{\alpha^n}{\sqrt{n!}}\,|n\rangle\,. \tag{3.9}$$

Here, $\hat{D}(\alpha) = e^{\alpha\hat{a}^\dagger - \alpha^*\hat{a}}$ represents the displacement operator, and $|0\rangle$ denotes the vacuum state of the memory. Coherent states are Gaussian states, and their Wigner function follows a Gaussian distribution in the memory's phase space. However, as discussed in Sec. 3.2, these states alone are insufficient for quantum computing, as any algorithm based solely on Gaussian states can be efficiently simulated by a classical computer [110, 111]. Therefore, in order to encode and stabilize quantum states that exhibit greater inherent quantum characteristics and offer a real quantum advantage, we need to introduce a non-linear element to the system: the Josephson junction.

3.1.2 *A source of nonlinearity: the Josephson junction*

The Josephson junction, originally introduced by Brian Josephson in 1962 [23], plays a pivotal role in circuit quantum electrodynamics (QED) by providing nonlinearity to the system. It consists of two superconducting islands separated by an insulating barrier that enables coherent tunneling of Cooper pairs. This phenomenon is mathematically described by the two Josephson equations:

$$\begin{cases} V(t) = \dfrac{\Phi_0}{2\pi}\dfrac{\mathrm{d}\varphi(t)}{\mathrm{d}t} \\ I(t) = I_c \sin\left(\varphi(t)\right). \end{cases} \tag{3.10}$$

These equations establish a connection between the voltage across the junction, denoted by $V(t)$, and the current flowing through it, denoted by $I(t)$, with the phase difference $\varphi(t)$ between the two superconducting islands. Here, $\Phi_0 = h/2e$ represents the superconducting flux quantum and I_c the critical current that can flow through the junction. Using Eq. (3.1), the variable $\varphi(t)$ can be related to the generalized magnetic flux as $\dot{\varphi}(t) = \frac{2\pi}{\phi_0}\dot{\phi}(t)$. The energy associated with the junction can then be determined by integrating the dissipated power over time

$$E = \int V(t)I(t)\mathrm{d}t = \frac{I_c\Phi_0}{2\pi}\int \sin\left(\varphi(t)\right)\frac{\mathrm{d}\varphi(t)}{\mathrm{d}t}\mathrm{d}t = -E_J\cos(\varphi(t)), \tag{3.11}$$

with $E_J = \frac{I_c\Phi_0}{2\pi}$ the energy associated with the Josephson junction. To establish a quantum description of the Josephson junction, the variable φ is promoted to a quantum operator $\hat{\varphi}$. The potential energy of the Josephson junction can then be expressed as $-E_J\cos\left(\hat{\varphi}\right)$. Alternatively, this potential energy can be written in terms of $\hat{n}_c$, the conjugate operator to $\hat{\varphi}$, and its eigenstates $|N\rangle$ representing the number N of Cooper pairs on one side of the junction. Using the commutation relation $\left[\hat{\varphi}, \hat{N}\right] = \mathbb{1}$, it can be shown [108] that $e^{i\hat{\varphi}} = \sum_{N\in\mathbb{Z}} |N-1\rangle\langle N|$. This leads to a potential energy of the form

$$\hat{U}_J = -\frac{1}{2}E_J\sum_{N\in\mathbb{Z}} |N+1\rangle\langle N| + |N\rangle\langle N+1|, \tag{3.12}$$

clearly highlighting the origin of this potential energy to be the tunneling of Cooper pairs across the insulating barrier of the Josephson junction. This non-linear potential of the Josephson junction can be used to tailor the coupling between a resonator and its environment. This is of particular interest for bosonic codes in order to have universal control of the memory and encode non-Gaussian states [112, 113, 114], reach large squeezing of coherent and cat states using parametric pumping [115, 116], and tailor the coupling between 2 resonators [117, 102]. Furthermore, replacing the inductance of an LC circuit with a Josephson junction defines a resonant mode whose two lowest energy levels can be used as a qubit.

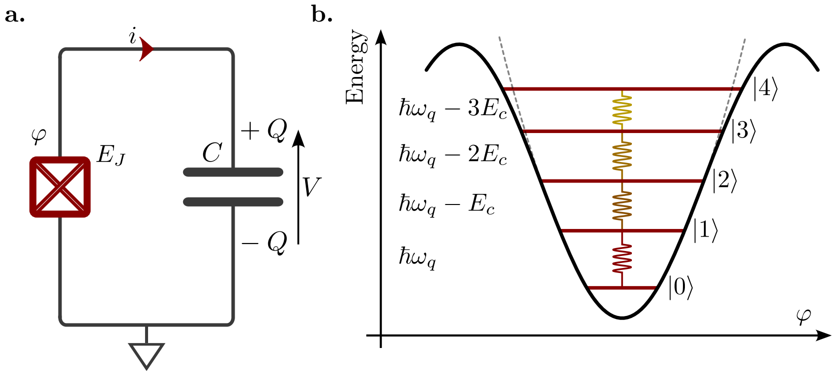

Figure 3.2: **a.** Representation of a Transmon qubit. The inductance of Fig. 3.1 is replaced by a Josephson junction acting as a non-linear inductance. **b.** Potential of the transmon qubit as a function of φ, and energy spacing of the transmon eigenstates. To first order, the energy difference between 2 successive energy levels decreases as $E_{n+1} - E_n = \hbar\omega_q - nE_c$.

The Hamiltonian of this circuit (Fig. 3.2**a.**) can be expressed as

$$\hat{H} = 4E_c\left(\hat{n}_c - n_g\right)^2 - E_J\cos\left(\varphi\right) \tag{3.13}$$

with $E_c = \frac{e^2}{2(C+C_J)}$ the capacitive energy of the system and n_g a charge offset due to a voltage source or parasitic charges on the superconducting islands. $C_J \sim 1$ fF is the junction parasitic capacitance while $C \sim 1$ pF is the added parallel capacitance. As introduced in [33], operating this device in the regime $E_J \gg E_c$ defines the *transmon* regime where the qubit is insensitive to charge noise, ie. noise in the value of n_g. This historically allowed to increase the qubit coherence time while keeping a simple design, making the transmon the most widely used qubit in superconducting circuits. In particular, surface codes at IBM and Google all use transmons as their physical two-level systems. In the transmon regime $E_J \gg E_c$, the phase of the transmon is localized at $\varphi \approx 0$ and the cosine function appearing from the Josephson junction potential can be truncated to its 4^{th} order expansion. The Hamiltonian in Eq. (3.13) can then be expressed as a function of the transmon's creation and annihilation operators $\hat{q}^\dagger$ and $\hat{q}$ as [118]

$$\hat{H} = \left(\sqrt{8E_J E_c} - E_c\right)\hat{q}^\dagger\hat{q} - \frac{E_c}{2}\hat{q}^{\dagger 2}\hat{q}^2, \tag{3.14}$$

giving a transmon frequency $\omega_q = \sqrt{8E_J E_c} - E_c$ and an anharmonicity E_c. This allows the transmon transitions to each have a different frequency (Fig. 3.2**b.**), but sets a limit on the minimal value of E_c which allows us to address them separately. In practice, E_c is chosen to be in the $100-300$ MHz range while keeping the condition $E_J/E_c \gtrsim 50$. This gives a transmon anharmonicity larger than the qubit decoherence rate $\Gamma_2/2\pi$, typically in the $1-100$ kHz range, hence a good spectral resolution of the transmon two lowest energy states. The transmon can then be approximated as a two-level system with a Hamiltonian $\hat{H} = \frac{\hbar\omega_q}{2}\sigma_z$.

Our experiments make use of a transmon qubit for tomography purposes, using it to directly measure the memory Wigner function (see measures in Chap. 4 and Chap. 5), and to stabilize the memory parity using a parametric pumping scheme (see Chap. 6).

3.1.3 *Coupling a transmon with a Harmonic Oscillator*

3.1.3.1 *Capacitive coupling under the Rotating Wave Approximation*

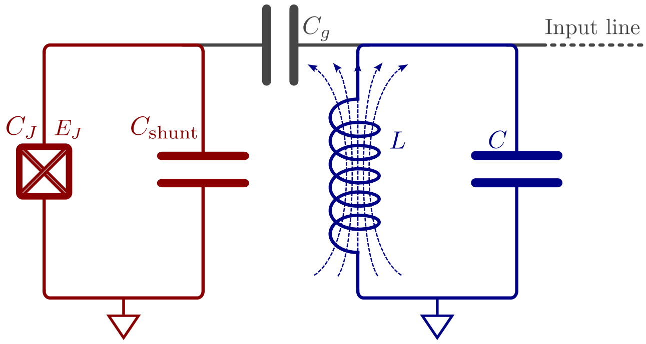

Figure 3.3: Representation of a transmon qubit capacitively coupled to a resonator through a capacitor C_g. An input line is used to drive the harmonic mode.

The transmon can be coupled to a resonator through a capacitive coupling, using a capacitance C_g which couples the charge of both modes. This coupling can be understood as an additional charge offset on the transmon's superconducting islands. Using a similar form as in Eq. (3.13), the Hamiltonian describing the circuit of Fig. 3.3 can be written as [30]

$$\hat{H} = 4E_c \left(\hat{n}_c - \frac{C_g}{2eC} \hat{Q} \right)^2 - E_J \cos\left(\hat{\varphi}\right) + \hbar\omega_m \hat{a}^\dagger \hat{a}. \tag{3.15}$$

The operator $\hat{Q}$ is the charge operator of the resonator, and $E_c = \frac{e^2}{2(C_{\text{shunt}}+C_J)}$ with the notations introduced in Fig. 3.3. Note that this Hamiltonian is only valid if the coupling can be treated as a perturbation, which amounts to the condition $C_g \ll C$, $C_J + C_{\text{shunt}}$. Truncating once again the cosine potential of the Josephson junction to its 4^{th} order, which is valid in the transmon regime $E_J \gg E_c$, this Hamiltonian becomes

$$\hat{H} = \hbar\omega_m^{'} \hat{a}^\dagger \hat{a} + \hbar\omega_q \hat{q}^\dagger \hat{q} - \frac{E_c}{2} \hat{q}^{\dagger 2} \hat{q}^2 - \hbar g \left(\hat{a}^\dagger - \hat{a}\right)\left(\hat{q}^\dagger - \hat{q}\right). \tag{3.16}$$

There, $\omega_m^{'}$ is the normalized frequency of the resonator and g the coupling rate between the two modes, expressed as [119]

$$g = \frac{\omega_m C_g}{C_J + C_{\text{shunt}}} \left(\frac{E_J}{2E_c} \right)^{1/4} \sqrt{\frac{\pi Z}{R}}, \tag{3.17}$$

with, Z the characteristic impedance of the resonator and $R = h/e^2$ the quantum of resistance. This Hamiltonian can be further simplified when the coupling rate is small compared to the two modes resonant frequencies $g \ll \omega_q$, $\omega_m^{'}$. Under this condition, the Rotation Wave Approximation can be applied (see Appendix. a) and Eq. (3.16) becomes

$$\hat{H} = \hbar\omega_m^{'} \hat{a}^\dagger \hat{a} + \hbar\omega_q \hat{q}^\dagger \hat{q} - \frac{E_c}{2} \hat{q}^{\dagger 2} \hat{q}^2 + \hbar g \left(\hat{a}^\dagger \hat{q} + \hat{a} \hat{q}^\dagger\right). \tag{3.18}$$

This form highlights the role of the capacitive coupling as an interaction where quanta of energy are exchanged between the transmon and resonator. Restricting the transmon to its first 2 energy levels, it can be treated as a qubit and Eq. (3.18) takes the form of the well-known Jaynes-Cummings Hamiltonian [120]:

$$\hat{H}_{\text{JC}} = \hbar\omega_m^{'} \hat{a}^\dagger \hat{a} + \hbar\frac{\omega_q}{2}\sigma_z + \hbar g \left(\hat{a}\sigma_+ + \hat{a}^\dagger \sigma_-\right). \tag{3.19}$$

3.1.3.2 *The dispersive regime and readout of the transmon qubit*

Superconducting circuits are most often operated in the *dispersive regime*, defined by the condition $g \ll \omega_q - \omega_m = \Delta$. Under this condition, the transmon's non-linearity $-\frac{E_c}{2}\hat{q}^{\dagger 2}\hat{q}^2$ in Eq. (3.18) can be treated as a perturbation while the linear part of the Hamiltonian

$$\hat{H}_{\text{lin}} = \hbar\omega_m \hat{a}^\dagger \hat{a} + \hbar\omega_q \hat{q}^\dagger \hat{q} + \hbar g \left(\hat{a}^\dagger \hat{q} + \hat{a}\hat{q}^\dagger\right) \tag{3.20}$$

is diagonalized using a Bogoliubov transformation

$$\hat{U}_{\text{Disp}} = e^{\frac{g}{\Delta}\left(\hat{a}^\dagger \hat{q} - \hat{q}^\dagger \hat{a}\right)}. \tag{3.21}$$

The resonator and transmon modes hybridize as

$$\begin{aligned} \hat{\hat{a}} &= \hat{U}^\dagger_{\text{Disp}} \hat{a} \hat{U}_{\text{Disp}} = \cos\left(\frac{g}{\Delta}\right)\hat{a} + \sin\left(\frac{g}{\Delta}\right)\hat{q} \\ \hat{\hat{q}} &= \hat{U}^\dagger_{\text{Disp}} \hat{q} \hat{U}_{\text{Disp}} = \cos\left(\frac{g}{\Delta}\right)\hat{q} - \sin\left(\frac{g}{\Delta}\right)\hat{a}, \end{aligned} \tag{3.22}$$

with the operators $\hat{\hat{a}}$ and $\hat{\hat{q}}$ describing the hybridized resonator and transmon modes after the Bogoliubov transformation. Note that these hybridized modes are the ones we probe experimentally, the bare modes being usually inaccessible. The dispersive Hamiltonian is then expressed as

$$\hat{H}_{\text{Disp}}/\hbar = \tilde{\omega}_m \hat{\hat{a}}^\dagger \hat{\hat{a}} + \tilde{\omega}_q \hat{\hat{q}}^\dagger \hat{\hat{q}} - \chi_{\text{q,q}} \hat{\hat{q}}^{\dagger 2} \hat{\hat{q}}^2 - \chi_{\text{m,m}} \hat{\hat{a}}^{\dagger 2} \hat{\hat{a}}^2 - \chi_{\text{q,m}} \hat{\hat{q}}^\dagger \hat{\hat{q}} \hat{\hat{a}}^\dagger \hat{\hat{a}}. \tag{3.23}$$

The normalized frequencies and non-linearities are given (in first order in the perturbation development) by

$$\begin{aligned} &\tilde{\omega}_m = \frac{1}{2}\left(\omega_m + \omega_q - \sqrt{\Delta^2 + 4g^2}\right),\ \tilde{\omega}_q = \frac{1}{2}\left(\omega_m + \omega_q + \sqrt{\Delta^2 + 4g^2}\right) \\ &\chi_{\text{q,q}} = \frac{E_c}{2},\ \chi_{\text{m,m}} = \frac{E_c}{2}\left(\frac{g}{\Delta}\right)^4,\ \chi_{\text{q,m}} = 2E_c \frac{g^2}{\Delta\left(\Delta - E_c/\hbar\right)}. \end{aligned}$$

The non-linearities $\chi_{\text{q,q}}$, $\chi_{\text{m,m}}$ are respectively called the transmon and memory *self-Kerr* rates, with $\chi_{\text{q,m}}$ being the *cross-Kerr* coupling rate between the two modes. While the qubit anharmonicity $\frac{E_c}{2}$ remains unchanged after this transformation, it is interesting to notice that the hybridized "resonator" mode inherits some non-linearity. This nonlinearity is small however, being of 4^{th} order in the parameter $g/\Delta \ll 1$, and the resonator mode remains only weakly non-harmonic. The cross-Kerr term of this Hamiltonian can be thought of as a resonator frequency shift that depends on the number of excitations in the transmon mode. This is evident by rewriting Eq. (3.23) as

$$\hat{H}_{\mathrm{Disp}}/\hbar = \left(\tilde{\omega}_m - \chi_{\mathrm{q,m}}\hat{\tilde{q}}^\dagger\hat{\tilde{q}}\right)\hat{\tilde{a}}^\dagger\hat{\tilde{a}} + \tilde{\omega}_q\hat{\tilde{q}}^\dagger\hat{\tilde{q}} - \chi_{\mathrm{q,q}}\hat{\tilde{q}}^{\dagger 2}\hat{\tilde{q}}^2 - \chi_{\mathrm{m,m}}\hat{\tilde{a}}^{\dagger 2}\hat{\tilde{a}}^2, \quad (3.24)$$

with the resonator frequency shifting by $-\chi_{\mathrm{q,m}}$ for every quanta of energy in the transmon. The dispersive regime is particularly interesting when $\chi_{\mathrm{q,m}}$ is larger than both the relaxation and decoherence rates of the resonator and qubit modes. Under this condition, it becomes possible to control the memory state conditionally on the transmon state. This enables the preparation of Fock states (see Sec. 3.2.3.2), memory displacements conditioned on the transmon's state, or more generally the preparation of any arbitrary state using gradient ascent pulse engineering (GRAPE) [121]. Alternatively, one could control the transmon conditionally on the memory state, which is crucial in order to measure Wigner functions (see Sec. 3.2)

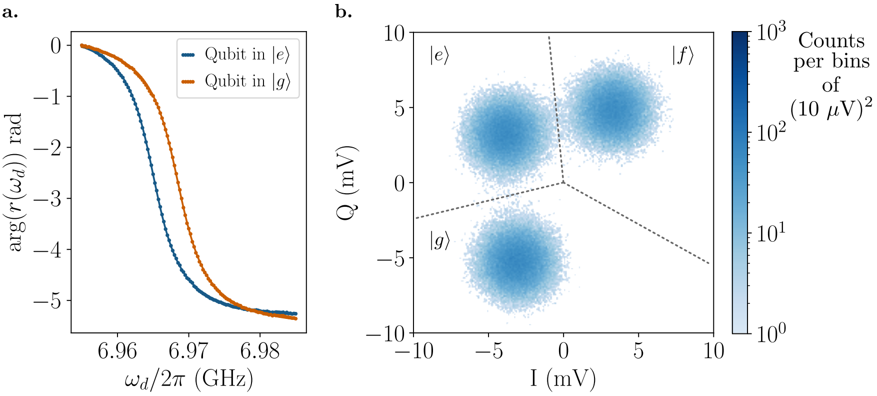

Figure 3.4: **a.** Spectroscopy of a resonator in reflection. A drive is sent to the resonator with the transmon initialized in its ground $|g\rangle$ or excited state $|e\rangle$. The reflected signal is measured, and its phase is shown as a function of the drive frequency **b.** Histogram of 10^7 measurements of the resonator quadrature for a transmon initialized in $|g\rangle$, $|e\rangle$ or $|f\rangle$ with equal probability.

We measure this frequency shift experimentally using the device introduced in Chap. 4. A drive at varying frequency ω_d is sent to the resonator (the readout resonator in the device) using the input line represented in Fig. 3.3. The reflected signal $r(\omega_d)$ is then measured, which evolves with the drive frequency as (see Appendix. d)

$$r(\omega_d) = \left\langle \frac{\kappa_{m,c} - \kappa_{m,i} + 2i\left(\omega_d - \left(\tilde{\omega}_m - \chi_{\mathrm{q,m}}\,\hat{\tilde{q}}^\dagger\hat{\tilde{q}}\right)\right)}{\kappa_{m,c} + \kappa_{m,i} - 2i\left(\omega_d - \left(\tilde{\omega}_m - \chi_{\mathrm{q,m}}\,\hat{\tilde{q}}^\dagger\hat{\tilde{q}}\right)\right)} \right\rangle . \tag{3.25}$$

There, $\kappa_{m,i}$ corresponds to the resonator intrinsic loss due to surface or radiative losses, while $\kappa_{m,c}$ is the rate at which the resonator decays through the input line. The resonator frequency $\tilde{\omega}_m - \chi_{\mathrm{q,m}}\hat{\tilde{q}}^\dagger\hat{\tilde{q}}$ is probed by fitting the phase of the reflected signal using Eq. (3.25). A frequency shift of $\chi_{\mathrm{q,m}}/2\pi = 3.5$ MHz can indeed be measured when the transmon gets excited (Fig. 3.4**a.**).

A common use of this frequency shift is to readout the state of the transmon by probing the resonator mode. Driving the resonator with a signal of amplitude α_{in} at a frequency ω_d, and neglecting here $\chi_{\mathrm{m,m}}$, the resonator state can be described by a classical field of complex amplitude

$$\alpha(\omega_d) = \frac{2\sqrt{\kappa_{m,c}}}{(\kappa_{m,c} + \kappa_{m,i}) - 2i\left(\omega_d - \left(\tilde{\omega}_m - \chi_{\mathrm{q,m}}\hat{\tilde{q}}^\dagger\hat{\tilde{q}}\right)\right)}\,\alpha_{in}(\omega_d). \tag{3.26}$$

We measure the outgoings field amplitudes at a fixed drive frequency $\omega_d = \tilde{\omega}_m - \chi_{\mathrm{q,m}}$. Owing to the resonator frequency shift, the field amplitudes corresponding to a transmon in its ground, first or second excited states can then be distinguished, which allows to readout the transmon state using the resonator (Fig. 3.4**b.**). Note that from Eq. (3.26), we see that the separation between the different Gaussian distributions can be increased by increasing the amplitude of the propagating field α_{in}. However, even for relatively low numbers of photons in the resonator, this can lead to spurious effects such as unwanted excitations of the transmon which limit the readout fidelity [122]. Techniques such as cavity cloaking [123] are currently developed to circumvent this issue.

3.2 REPRESENTING THE CAVITY STATE: THE WIGNER FUNCTION

3.2.1 *Mathematical definition*

To graphically represent the quantum state encoded in the memory and gain intuition on the inner workings of various bosonic codes, we use the Wigner-Weyl transformation [124, 125]. This transformation directly gives a bijection between the density matrix $\hat{\rho}$ describing the memory mode and a real function on the memory phase space $W(\beta)$. The position $\hat{x}$ and momentum $\hat{p}$ quadratures are respectively defined as

$$\begin{cases} \hat{x} = \dfrac{\hat{a}+\hat{a}^\dagger}{2} \\ \hat{p} = \dfrac{\hat{a}-\hat{a}^\dagger}{2i}. \end{cases} \tag{3.27}$$

The corresponding basis in position and momentum are denoted $\{|x\rangle, x \in \mathbb{R}\}$ and $\{|p\rangle, p \in \mathbb{R}\}$. The Wigner function can then be expressed by projecting the memory density matrix $\hat{\rho}$ into either one of these bases [40]

$$\begin{aligned} W(\beta = x+ip) &= \frac{1}{\pi}\int_{\mathbb{R}} e^{-2ipy} \langle x+y/2|\,\hat{\rho}\,|x-y/2\rangle \,\mathrm{d}y \\ &= \frac{1}{\pi}\int_{\mathbb{R}} e^{2ixu} \langle p+u/2|\,\hat{\rho}\,|p-u/2\rangle \,\mathrm{d}u. \end{aligned} \tag{3.28}$$

This function is commonly interpreted as a quasi-probability distribution as it is normalized to unity

$$\int_{\mathbb{C}} W(\beta)\mathrm{d}\beta = \mathrm{Tr}\left(\hat{\rho}\right) = 1, \tag{3.29}$$

but can still present negative values. Only when integrating the Wigner function along any axis do we obtain a proper probability distribution for the corresponding variable. For instance, defining the function

$$f(x) = \int_{\mathbb{R}} W(x,p)\mathrm{d}p \tag{3.30}$$

gives the probability distribution of the position quadrature. This function is immediately normalized to 1 according to Eq. (3.29), and it can be shown that $f(x) \geq 0$ irrespective of the value of x. $f(x)$ is the distribution of outcomes one would obtain using a homodyne measurement to measure $\hat{x}$ when the system is in $\hat{\rho}$. A similar probability distribution $g(p)$ can be defined in momentum by integrating the Wigner function along the position quadrature. The Wigner function providing a complete description of $\hat{\rho}$, it can be used to compute the mean value of any operator $\hat{O}$ acting on the memory Hilbert space

$$\begin{aligned} &\left\langle \hat{O} \right\rangle = \int_{\mathbb{C}} W(\beta)O(\beta)\mathrm{d}\beta, \\ &\text{with } O(\beta = x+ip) = \frac{1}{\pi}\int_{\mathbb{R}} e^{-2ipy} \langle x+y/2|\,\hat{O}\,|x-y/2\rangle \,\mathrm{d}y. \end{aligned} \tag{3.31}$$

This expression can be understood as an averaging of the physical quantity $O(\beta = x{+}ip)$ over the memory phase space, weighted by the quasi-probability distribution $W(\beta)$. Experimentally, Eq. (3.31) can be used to reconstruct the memory density matrix $\hat{\rho}$ using the measured Wigner function to estimate the mean value of $|n\rangle\langle m|$. Here $|n\rangle$ refers to Fock state n, and the mean value $\langle |n\rangle\langle m| \rangle_\rho$ directly gives the value of $\rho_{n,m} = \langle n|\,\hat{\rho}\,|m\rangle$.

3.2.2 *The importance of negativities in the Wigner function*

Gaussian states are states whose Wigner function is a Gaussian function in the memory phase space. These states are commonly encountered with coherent states $|\alpha\rangle$, $\alpha \in \mathbb{C}$, being a prominent example. The Wigner function of such a coherent state, obtained by driving a harmonic oscillator at its resonant frequency, is a Gaussian function centered around α with a width of 1/2 (Fig. 3.5**a.**). An important theorem [110, 111] gives some insight into the use of Gaussian states for quantum computing. It states that any process whose initialization, evolution, and measurement, can be fully described using only Gaussian states, can be efficiently simulated by a classical algorithm. This makes non-Gaussian states an important tool for quantum computing in order to obtain any sort of quantum advantage.

Another theorem worth mentioning is Hudson's theorem [126] which proves that a single-mode pure quantum state is non-Gaussian if and only if its Wigner function presents negative values. This theorem has later been extended to multimode states by Soto and Claverie [127]. This makes Wigner negativities a key property to determine the usefulness of a state for quantum computing, with the Wigner negativity volume becoming an indicator of a state's non-classical nature [128]. In particular, the different encodings presented in Sec. 3.3 all present negativities in the Wigner function of most of their states.

3.2.3 *A few commonly encountered Wigner functions*

To illustrate the concept of the Wigner function, we introduce that of some commonly encountered states. More specifically we focus on the representation of coherent states, squeezed states, and Fock states, all of which are encountered in the measurements later presented.

3.2.3.1 *Coherent and squeezed states*

Already introduced in Sec. 3.1.1, coherent states are encoded by driving a harmonic oscillator with a classical drive at its resonant frequency. This dynamic is captured by the following Hamiltonian

$$\hat{H} = i\hbar\left(\epsilon_d \hat{a}^\dagger - \epsilon_d^* \hat{a}\right), \tag{3.32}$$

with ϵ_d a dimentionless drive amplitude. After a time t, the memory initially in its vacuum state $|0\rangle$ evolves towards

$$|\alpha\rangle = e^{-\frac{i}{\hbar}\hat{H}t}|0\rangle = e^{\epsilon_d t\hat{a}^\dagger - \epsilon_d^* t\hat{a}}|0\rangle, \tag{3.33}$$

which indeed correspond to the coherent states as defined in Eq. (3.9). For a constant drive amplitude ϵ_d, we find $\alpha = \epsilon_d t$, and in the more general scenario of a time-varying drive, $\alpha = \int_0^t \epsilon_d(u)\mathrm{d}t$. The Wigner function of a coherent state $|\alpha\rangle$ is a Gaussian function on $\mathbb{C}$ of standard deviation $\sigma = 1/2$ centered at α (Fig. 3.5**a.**) The drive amplitude ϵ_d can then be understood as the speed at which this Gaussian pattern moves across the phase space. Interestingly, these states [1] saturate the Heisenberg uncertainty relation. Consequently, their Wigner function has the smallest possible spread in the memory phase space.

Squeezed coherent states can then be defined from these coherent states by introducing the squeezing operator $\hat{S}(r) = e^{\frac{1}{2}\left(r^*\hat{a}^2 - r\hat{a}^{\dagger\,2}\right)}$, with $r = |r|\,e^{i\theta}$ the squeezing parameter. Mathematically, these states can be expressed in one of two 2 ways depending on the order of the displacement and squeezing operations

$$\begin{aligned}|\alpha, r\rangle &= \hat{D}(\alpha)\hat{S}(r)|0\rangle \\ &= \hat{S}(r)\hat{D}(\gamma)|0\rangle,\end{aligned} \tag{3.34}$$

with $\gamma = \alpha\cosh(|r|) + \alpha^* e^{i\theta}\sinh|r|$. From now on we will use the first convention, squeezing the vacuum before the displacement. The resulting Wigner function of these states resembles that of a coherent state compressed into an ellipse of the same area, still saturating the Heisenberg bound. The compressed quadrature exhibits reduced fluctuations, visible in the Wigner function by a reduced standard deviation $e^{-|r|}/2$. In the opposite direction, fluctuations are amplified and the standard deviation increases to $e^{|r|}/2$. An example is shown in Fig. 3.5**b.**, for a squeezing of $r = 0.75$ and $\alpha = 2$.

---

[1] The Heisenberg uncertainty relation is saturated if and only if the state is a pure Gaussian state $|\alpha, r\rangle$

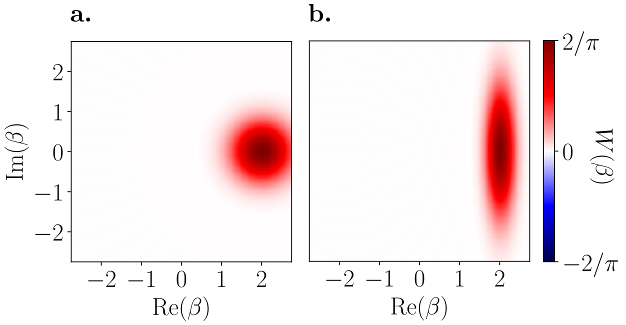

Figure 3.5: **a.** Wigner function $W(\beta)$ of a coherent state $|\alpha\rangle$ with $\alpha = 2$. **b.** Wigner function of a squeezed coherent state $|2, 0.75\rangle$, obtained by applying the squeezing operator $\hat{S}(r)$ with $r = 0.75$ on the vacuum $|0\rangle$, before applying a displacement $\hat{D}(\alpha)$ with $\alpha = 2$.

These squeezed states are particularly useful in metrology due to their ability to enhance the sensitivity of measurements beyond the standard quantum limit (SQL). In gravitational wave detection for instance, squeezed states were used to increase the sensitivity of interferometric measurements, enabling the detection of faint gravitational wave signals that would otherwise remain undetectable with traditional techniques [129]. Squeezed states are now routinely implemented in circuit QED [130, 131, 115], and recent proposals highlight their benefit for improving on existing bosonic codes [132, 133, 134]

However, these states by themselves -without considering the superposition of coherent or squeezed states- do not present any negativities. Some of the more naturally encountered states that do present non-Gaussian Wigner functions are Fock states.

3.2.3.2 *Fock states*

As discussed in Sec. 3.1.1, Fock states are eigenvectors of the Hamiltonian governing a harmonic oscillator:

$$\hat{H} = \hbar\omega_m \left(\hat{a}^\dagger \hat{a} + \frac{1}{2}\right). \tag{3.35}$$

To give them a physical interpretation, the Fock state $|n\rangle$ corresponds to having n excitations in the oscillator's electromagnetic field, resulting in an associated energy $E_n = \hbar\omega_m n + 1/2$. With the exception of the vacuum state $|0\rangle$, these states are non-classical in the sense that they can not be prepared by simply applying a coherent drive to the memory hosting the harmonic mode.

Interestingly, being eigenstates of the memory Hamiltonian allows their preparation through the back-action of an energy measurement. Alternatively, one can leverage the dispersive coupling between the memory and an auxiliary qubit. When the coupling rate g is smaller than both the memory and qubit frequencies, i.e., $g \ll \omega_m, \omega_q$, the Rotating Wave Approximation (see Appendix.a) can be applied and the system is accurately described by the Jaynes-Cummings model [120]

$$\hat{H}_{\mathrm{JC}}/\hbar = \omega_m \hat{a}^\dagger \hat{a} + \frac{\omega_q}{2}\sigma_z + g\left(\hat{a}\sigma_+ + \hat{a}^\dagger\sigma_-\right). \tag{3.36}$$

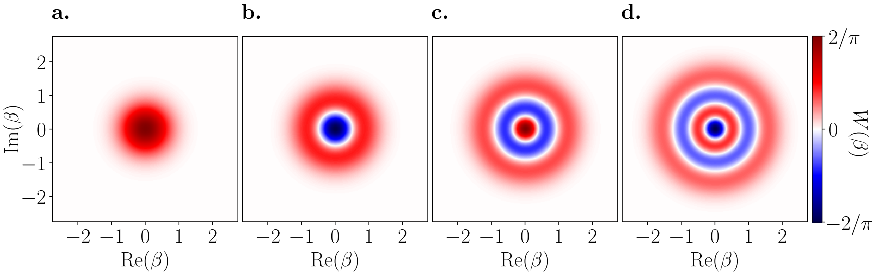

Figure 3.6: Wigner function $W(\beta)$ of **a.** Fock state $|0\rangle$, **b.** Fock state $|1\rangle$, **c.** Fock state $|2\rangle$ **d.** Fock state $|3\rangle$.

The non-linear coupling can then be used to inject or remove photons from the memory, using the auxiliary qubit. The Wigner function of Fock state $|n\rangle$ is given by:

$$W_n(\beta) = (-1)^n \frac{2}{\pi} e^{-2|\beta|^2} L_n\left(4|\beta|^2\right), \tag{3.37}$$

where $L_n(x)$ represents the Laguerre polynomial of order n. Notably, for $n > 1$, the Wigner functions of Fock states exhibit negativities (Fig. 3.6), revealing their non-classical nature and making them interesting candidates for quantum computing applications.

One particularly relevant code based on Fock states is the 0/1 code, employing $|0\rangle$ and $|1\rangle$ as the two logical states of a qubit. This encoding, despite being vulnerable to photon loss which induces a bit-flip type of error (see Sec 3.2.4), is often used as a benchmark for other bosonic qubits.

3.2.4 *Impact of common errors affecting the resonator*

The Wigner function serves not only as an intuitive representation of a quantum state[2] and a mean to gauge its "quantum usefulness" but also as a tool to illustrate the effects of errors affecting the memory. For a weak enough coupling to a large environment, such errors are described using the formalism of the Lindblad master equation [40]. This equation describes the expected evolution of the memory density matrix $\hat{\rho}(t)$, taking into account both the Hamiltonian evolution and the impact of errors, modeled as an ensemble of jump operators $\left\{\hat{L}_\mu\right\}$. This equation reads

$$\begin{aligned}&\frac{\mathrm{d}}{\mathrm{d}t}\hat{\rho} = -\frac{i}{\hbar}\left[\hat{H},\hat{\rho}\right] + \sum_\mu \mathcal{D}\left(\hat{L}_\mu\right)\hat{\rho},\\ &\text{with } \mathcal{D}\left(\hat{L}_\mu\right)\hat{\rho} = \hat{L}_\mu\hat{\rho}\hat{L}_\mu^\dagger - \frac{1}{2}\left(\hat{L}_\mu^\dagger\hat{L}_\mu\hat{\rho} + \hat{\rho}\hat{L}_\mu^\dagger\hat{L}_\mu\right).\end{aligned} \tag{3.38}$$

$\mathcal{D}\left(\hat{L}_\mu\right)$ is the Lindblad super-operator describing the impact of errors on the memory, while the commutator $\left[\hat{H},\hat{\rho}\right]$ captures the Hamiltonian evolution of the system. Note that in the case of a pure quantum state and in the absence of jump operators, Eq. (3.38) reduces to the usual Schrödinger equation [39]. In this section, we focus on two processes that can impact the memory state: single-photon loss described by the jump operator $\hat{L}_1 = \sqrt{\kappa_1}\hat{a}$ and memory self-Kerr characterized by an additional term in the Hamiltonian $-\hbar\chi_{\mathrm{m,m}}\hat{a}^{\dagger 2}\hat{a}^2$. Crucially, we show that in both cases the impact on the Wigner function is only a local deformation in the memory phase space. This feature holds true for all physical errors commonly affecting the memory. Keeping that in mind gives a better understanding of bosonic codes' inner workings.

3.2.4.1 *Single-photon loss*

The most common error impacting a Harmonic oscillator is the loss of a single photon, described by the jump operator

$$\hat{L}_1 = \sqrt{\kappa_1}\hat{a} \tag{3.39}$$

---

[2] Quantum mechanics can be completely described using the phase-space formalism, independently introduced in 1946 by Hilbrand Groenewold [135] and in 1947 by Joe Moyal [136]. Wave functions or density matrices are replaced by quasiprobability distributions, and the product between two operators by a star product.

with κ_1 the single photon loss rate and $\hat{a}$ the memory annihilation operator. The single photon loss rate relates to the memory lifetime T_1 through the relation $\kappa_1 = 1/T_1$. Going to the interaction picture rotating at the memory frequency ω_m, the Lindblad master equation takes the form

$$\frac{\mathrm{d}}{\mathrm{d}t}\hat{\rho} = \mathcal{D}\left(\hat{L}_1\right)\hat{\rho}. \tag{3.40}$$

From this equation, one can derive the evolution of the memory starting from an initial state $|\Psi_0\rangle$. In particular, starting from a coherent state $|\alpha\rangle$, the state remains a coherent state with an exponentially decaying amplitude $\left|\alpha e^{-\frac{\kappa_1}{2}t}\right\rangle$ (Fig. 3.7). As mentioned, this evolution simply corresponds to a local deformation of the Wigner function in phase space, decaying to the memory vacuum at a rate $\kappa_1/2$.

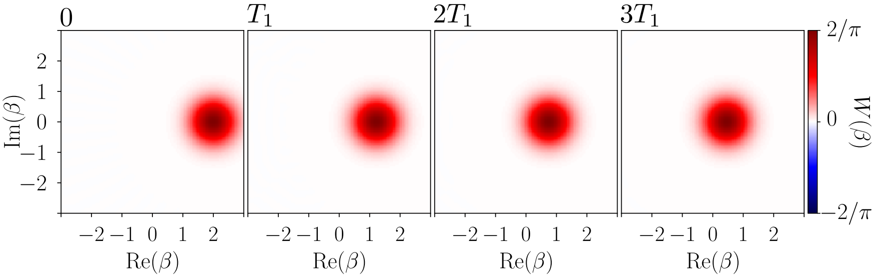

Figure 3.7: Simulated evolution of the memory Wigner function over time. The system starts in the coherent state $|\alpha\rangle$ with $\alpha = 2$ and is submitted to single-photon loss at a rate κ_1.

This evolution can initially seem counter-intuitive as coherent states have the unique property of being eigenstates of the annihilation operator $\hat{a}|\alpha\rangle = \alpha|\alpha\rangle$. It can however be understood via the thought experiment of placing a photon detector in the memory environment, which registers whenever a photon is lost [40]. If a photon is detected, the coherent state is indeed unchanged and remains in the same state. Conversely, when no photon loss is detected, the measurement back action updates the memory state to a coherent state of lower amplitude. This updating logic stems from the notion that, if no photon loss is detected during a time interval t, the memory likely contained fewer photons than initially believed.

3.2.4.2 *Memory self-Kerr term*

A second effect that impacts the memory state can be modeled as an extra contribution to the Hamiltonian of a harmonic oscillator: the memory self-Kerr term. It originates from the coupling of the memory to a non-linear element - typically a transmon - in order to encode, readout and stabilize non-trivial states. The harmonic mode then inherits some nonlinearity through this coupling, captured at first order by an additional term $-\hbar\chi_{\mathrm{m,m}}\hat{a}^{\dagger 2}\hat{a}^2$ in the Hamiltonian. It induces a frequency difference between the transitions $|n\rangle \to |n+1\rangle$ depending on the initial photon number n, which can be seen as a memory frequency dependence on its average photon number.

The simulated impact of this term on the memory, starting from an initial state $|\alpha\rangle$, is shown in Fig. 3.8**a.**. We compare this simulation with an experiment performed on the device later presented. This measurement was performed at ϕ_{tomo} in order to cancel the two-photon dissipation (see Chap. 4 for more details). Using the value $\kappa_1/2\pi = 14$ kHz, independently calibrated, the memory self Kerr was fitted to $\chi_{\mathrm{m,m}}/2\pi = 220$kHz. Note that a detuning of $\Delta/2\pi = 1$MHz was added in simulation to match with the experimental data (Fig. 3.8**b.**). The Lindblad equation describing the memory in the interacting frame finally reads

$$\frac{\mathrm{d}}{\mathrm{d}t}\hat{\rho} = -i\left[\Delta\hat{a}^\dagger\hat{a} - \chi_{\mathrm{m,m}}\hat{a}^{\dagger 2}\hat{a}^2, \hat{\rho}\right] + \mathcal{D}\left(\sqrt{\kappa_1}\hat{a}\right)\hat{\rho}. \tag{3.41}$$

The impact of this self-Kerr effect is to induce a rotation in the memory phase space, faster for larger amplitudes $|\beta|$. Once again, this corresponds to a local deformation in phase space, with no population "teleporting" from one side of the phase space to another.

Interestingly, if well-controlled, this effect can be used as a means to control quantum information. Indeed, as can be seen in Fig. 3.8**b.**, negativities appear in the system even when starting from a coherent state, which highlights the quantum nature of the prepared state. Furthermore, it can be noted that superpositions of 4, 3, or 2 coherent states can be prepared by stopping the evolution at times $\pi/2\chi_{\mathrm{m,m}}$, $3\pi/4\chi_{\mathrm{m,m}}$, or $\pi/\chi_{\mathrm{m,m}}$. This was first demonstrated by Kirchmair et al. in 2013 [137]. As introduced in [138] it can notably be exploited to perform bias-preserving gates on cat qubits (see Sec. 3.3.3)).

We observe that the re-focused states obtained at 1120ns, 1520ns, and 2380ns in Fig. 3.8**a.** differ significantly from the ideal superposition of coherent states. Particularly visible in the fringes at 2380ns, this is due to a relatively small value of $\chi_{\mathrm{m,m}}$ compared to κ_1. The memory then loses photons during

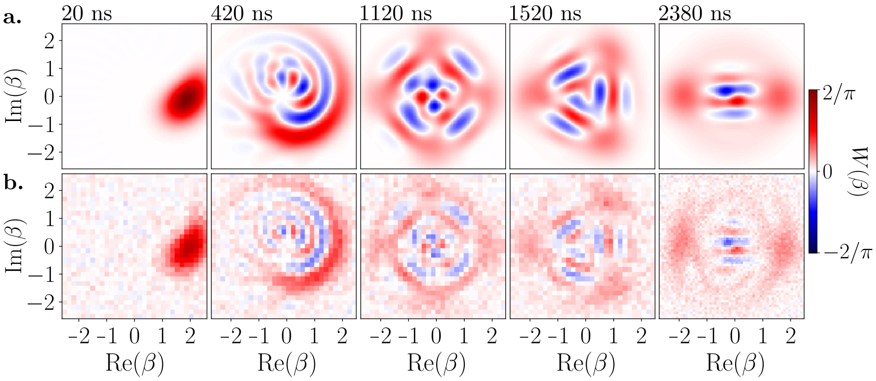

Figure 3.8: **a.** Simulated Wigner function of the memory over time. The system is initialized in the coherent state $|\alpha\rangle$ with $\alpha = 1.9$, and its evolution is simulated using Eq. (3.41). The parameter $\chi_{\mathrm{m,m}}$ is fitted to best reproduce the measured evolution. **b.** Measured Wigner function over time.

the time $\pi/\chi_{\mathrm{m,m}}$, distorting the final state. This can easily be corrected by increasing $\chi_{\mathrm{m,m}}$, but would result in a larger memory nonlinearity causing other issues for bosonic codes. Finally, it can be noted that the measurements slightly differ from simulations, which can be attributed to other error channels not taken into account in the model of Eq. (3.41).

3.3 SMALL ZOOLOGY OF BOSONIC CODES

In this section, we present a short zoology of the bosonic codes most widely used in superconducting circuits. For each code, we introduce the logical states defining the logical qubit. Using the symmetry properties of their Wigner functions, we highlight the types of errors against which each code is protected. Sec. 3.4 then introduces 3 different methods used to stabilize these bosonic qubits, with Sec. 3.5 focusing on using dissipation to stabilize cat qubits. This section takes inspiration from [92].

3.3.1 *Kitten code*

The Kitten code, or Binomial code, is arguably the simplest bosonic code protecting the logical information from the loss of a single photon. Introduced in [96], it was notably implemented in [139] nearly reaching the break-even point, meaning that the code almost decreased one error below that of any of its physical components. A recent experiment [140] then managed to go beyond break-even, beating the cavity lifetime by 16%. The logical states defining this encoding are

$$|0_{\text{Kitten}}\rangle = \frac{|0\rangle + |4\rangle}{\sqrt{2}}, \ |1_{\text{Kitten}}\rangle = |2\rangle \,, \tag{3.42}$$

with $|0\rangle$, $|2\rangle$ and $|4\rangle$ being the Fock states 0, 2 and 4. With this encoding, the loss of a single photon maps a logical state with an even parity $|\Psi_{\text{Kitten}}\rangle = \alpha\,|0_{\text{Kitten}}\rangle + \beta\,|1_{\text{Kitten}}\rangle$ to an error state with an odd parity $|\Psi_{\text{Error}}\rangle = (\alpha\,|3\rangle + \beta\,|1\rangle)$. The error space is then orthogonal to the code space, a prerequisite to fulfill the Knill-Laflamme conditions (see Sec. 2.3.2.2). Error can be detected by measuring the memory parity $\hat{\Pi} = (-1)^{\hat{a}^\dagger\hat{a}}$. The recovery operation then consists in mapping $|3\rangle$ and $|1\rangle$ back to the logical states $|0_{\text{Kitten}}\rangle$ and $|1_{\text{Kitten}}\rangle$, restoring the logical information. Note that for this scheme to work, it is necessary for the two logical states to have the same mean number of photons

$$\langle 0_{\text{Kitten}}|\, \hat{a}^\dagger\hat{a}\, |0_{\text{Kitten}}\rangle = \langle 1_{\text{Kitten}}|\, \hat{a}^\dagger\hat{a}\, |1_{\text{Kitten}}\rangle = 2. \tag{3.43}$$

An intuitive explanation for this condition comes from the environment, which should be incapable of distinguishing these two states. Otherwise, after the loss of a single photon, the state with the larger photon number is favored as it was the most likely to lose one. This introduces a bias before the recovery operation, which can not be corrected and corrupts the logical information.

The ability of the Kitten code to correct for single photon loss can also be understood through the symmetry properties of the logical states' Wigner function (Fig. 3.9**a.**). Indeed, this code belongs to the broader family of Rotation-Symmetric bosonic codes [141], where the discrete rotation operator $\hat{Z}_N = e^{i\pi\hat{a}^\dagger\hat{a}/N}$ corresponds to the logical $\hat{Z}_L$, here with $N = 2$. Consequently, $\hat{Z}_N^2 = e^{2i\pi\hat{a}^\dagger\hat{a}/N}$ acts as the identity on the code space, or equivalently, the Wigner function of any state within the code space remains invariant under a rotation of $2\pi/N$. A code satisfying this condition ensures that the support of a state $|\Psi_L\rangle$ belonging to the code space is the space generated by all the Fock states multiple of N, i.e

$$|\Psi_L\rangle = \sum_{k=0}^{\infty} c_k\,|kN\rangle \,. \tag{3.44}$$

It follows that the code can be protected against the loss of up to $N-1$ photons. In the case of the Kitten code, although the Wigner function of $|0_{\text{Kitten}}\rangle$ and $|0_{\text{Kitten}}\rangle$ is invariant under rotations of $\pi/2$, their superposition is only invariant under rotations of π. This corresponds to the situation where $N=2$, and it can be verified that $\hat{Z}_N = e^{i\pi\hat{a}^\dagger\hat{a}/2}$ indeed acts as the logical $\hat{Z}_L$ operator. The code is then protected against $N-1=1$ photon loss.

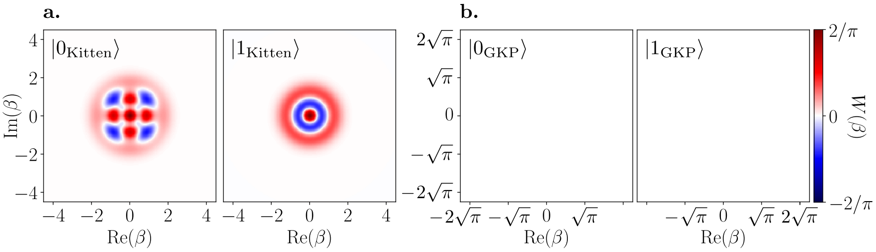

Figure 3.9: **a.** Wigner functions of the Kitten code logical states $|0_{\text{Kitten}}\rangle$ and $|0_{\text{Kitten}}\rangle$. **b.** Wigner functions of the GKP code logical states $|0_{\text{GKP}}\rangle$ and $|0_{\text{GKP}}\rangle$

3.3.2 *GKP code*

The GKP code, named after Gottesman, Kitaev, and Preskill [97], exploits translation symmetries to protect quantum information. In its simplest version, known as the square lattice GKP code (Fig. 3.9**b.**), the logical states $|0_{\text{GKP}}\rangle$ and $|1_{\text{GKP}}\rangle$ are eigenstates of the two commuting operators

$$\begin{aligned} \hat{S}_x &= e^{2i\sqrt{\pi}\hat{x}} = \hat{D}\left(i\sqrt{2\pi}\right) \\ \hat{S}_p &= e^{-2i\sqrt{\pi}\hat{p}} = \hat{D}\left(\sqrt{2\pi}\right), \end{aligned} \tag{3.45}$$

with eigenvalue 1. The 2 quadratures $\hat{x}$ and $\hat{p}$ are defined in Eq. (3.27). A more general definition of the GKP code can be provided as being the eigenstates of $\hat{D}(i\gamma)$ and $\hat{D}(\delta)$, with the condition $\gamma\delta = 2k\pi$, $k \in \mathbb{N}^*$. This condition ensures these two operators commute. Since the two stabilizers $\hat{S}_x$ and $\hat{S}_q$ commute they can be simultaneously measured, which amounts to measuring their phase $2\sqrt{\pi}\hat{x}$ and $-2\sqrt{\pi}\hat{p}$ modulo 2π. In turn, this is equivalent to measuring the two quadratures $\hat{x}$ and $\hat{p}$ modulo $\sqrt{\pi}$. Any translation in phase space smaller than $\sqrt{\pi}$ can thus be detected by simultaneously measuring

$\hat{S}_x$ and $\hat{S}_q$. A counter-displacement can then be applied, bringing the system back to the code space. Because errors affecting the memory only generate local deformation of the Wigner function, this method is efficient if the correcting procedure is fast enough so that no displacement larger than $\sqrt{\pi}$ has time to occur, and if no additional errors are generated by the correction protocol.

This code has been implemented using post-selection in a trapped-ion mechanical oscillator [142], and using superconducting circuits [143]. More recently, an experiment using reinforcement learning to optimize the operation of a GKP code managed to go beyond the break-even point [144], extending the coherence of the logical information by a factor 2.27 ± 0.07.

3.3.3 *Cat code, superposition of* $2N$ *coherent states.*

The cat code is another Rotation-Symmetric bosonic code, based on the superposition of $2N$ coherent states distributed equidistantly around a circle of radius α. By tracking the memory parity, these states can be protected against the loss of $N-1$ photons. This is the encoding investigated in this thesis.

3.3.3.1 $N=1$, *the 2-component cat code.*

The first case to consider simply corresponds to a qubit whose code space is generated by the two coherent states $|\alpha\rangle$ and $|-\alpha\rangle$ (Fig. 3.10**a.**). This encoding does not protect against any photon loss event, which becomes evident when developing the states $|C_\alpha^\pm\rangle$ (Fig. 3.10**b.**) in the Fock basis

$$\begin{aligned} \left|C_\alpha^+\right\rangle &= \mathcal{N}_+\left(|\alpha\rangle + |-\alpha\rangle\right) \propto \sum_k \frac{\alpha^{2k}}{\sqrt{2k!}}\,|2k\rangle \\ \left|C_\alpha^-\right\rangle &= \mathcal{N}_-\left(|\alpha\rangle - |-\alpha\rangle\right) \propto \sum_k \frac{\alpha^{2k+1}}{\sqrt{2k+1!}}\,|2k+1\rangle\,. \end{aligned} \tag{3.46}$$

The coefficients $\mathcal{N}_+$ and $\mathcal{N}_-$ are normalisation factors, exponentially close to $1/\sqrt{2}$ as $|\alpha|^2$ increases. From Eq. (3.46), we see that losing a single photon induces a phase-flip error which can not be corrected as the system remains in the code space. Furthermore, the rate at which phase-flip errors occur increases linearly with $\bar{n} = |\alpha|^2$ due to the effective memory lifetime decreasing as $T_{1,\text{eff}} = T_1/\bar{n}$ when the number of photons increases.

Despite this flaw, the 2-component cat code remains a strong candidate for quantum error correction due to bit-flip errors being exponentially suppressed

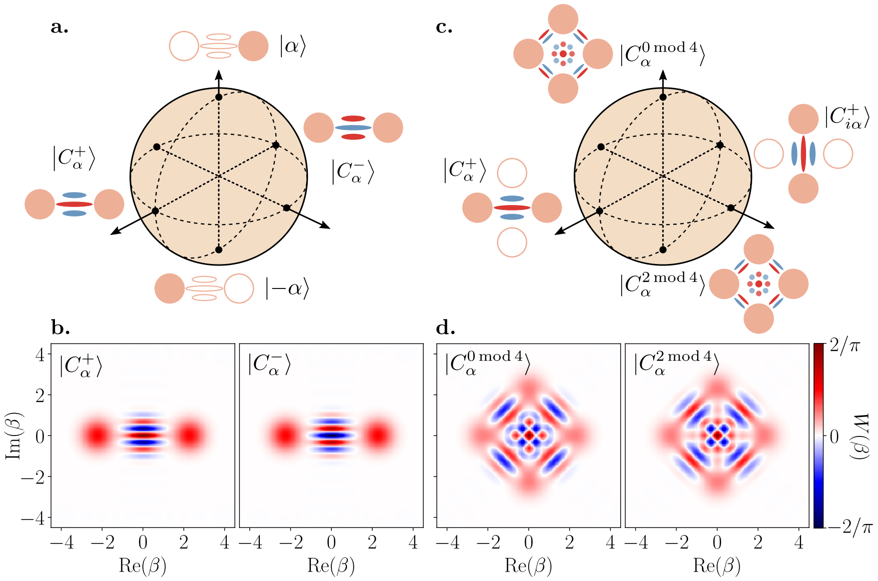

Figure 3.10: **a.** Bloch sphere defining the 2-component cat code, the logical states are the coherent states $|\pm\alpha\rangle$. Bit-flip errors are exponentially suppressed with $|\alpha|^2$ at the cost of a linear increase of the phase-flip error rate. **b.** Wigner function of $\left|C_\alpha^+\right\rangle$ and $\left|C_\alpha^-\right\rangle$, $\alpha = 2.25$, having respectively an even and odd parity. **c.** Bloch sphere defining the 4-component cat code. Logical states are $\left|C_\alpha^{0 \bmod 4}\right\rangle$ and $\left|C_\alpha^{2 \bmod 4}\right\rangle$, each of them having a given parity modulo 4. Phase-flip errors are exponentially suppressed with $|\alpha|^2$, and bit-flips can be corrected as in the Kitten code. **d.** Wigner function of $\left|C_\alpha^{0 \bmod 4}\right\rangle$ and $\left|C_\alpha^{2 \bmod 4}\right\rangle$ for $\alpha = 2.25$.

with $|\alpha|^2$. This property can be intuitively understood thanks to the local nature of errors impacting the memory. As the two coherent states separate for increasing values of $|\alpha|$, the probability of a physical error to induce a bit-flip exponentially decreases as the overlap $\langle\alpha|{-\alpha}\rangle \propto e^{-4|\alpha|^2}$. Note that in an actual experiment, the bit-flip error rate decreases as $\Gamma_\mathrm{X} \propto e^{-\lambda|\alpha|^2}$, the factor $\lambda \leq 4$ depending on the experimental implementation.

The 2-component cat, in the regime of large $|\alpha|$, exhibits a large noise bias. As explained in Sec. 2.4.3, this can be exploited to simplify existing quantum error correction protocols. In particular, assuming bit-flip errors can be completely ignored, a simple repetition code can be used to correct the remaining phase-flip errors [88, 145, 146, 70]. Crucially, bias-preserving gates have been designed for the 2-component cat qubit [138, 147], without which no repetition code could be implemented.

3.3.3.2 $N = 2$, *the 4-component cat code.*

The previous encoding can be extended by considering the Hilbert space generated by the four coherent states $\{|\alpha\rangle, |-\alpha\rangle, |i\alpha\rangle, |-i\alpha\rangle\}$. From this 4-dimensional Hilbert space, one can define a qubit whose logical states (see Fig. 3.10**d.**) are defined as

$$\begin{aligned} |0_L\rangle &= \left|C_\alpha^{0 \bmod 4}\right\rangle = \mathcal{N}_0 \left(|\alpha\rangle + |-\alpha\rangle + |i\alpha\rangle + |-i\alpha\rangle\right) \propto \sum_k \frac{\alpha^{4k}}{\sqrt{4k!}} |4k\rangle \\ |1_L\rangle &= \left|C_\alpha^{2 \bmod 4}\right\rangle = \mathcal{N}_2 \left(|\alpha\rangle + |-\alpha\rangle - |i\alpha\rangle - |-i\alpha\rangle\right) \propto \sum_k \frac{\alpha^{4k+2}}{\sqrt{4k+2!}} |4k+2\rangle , \end{aligned} \tag{3.47}$$

with $\mathcal{N}_0$ and $\mathcal{N}_2$ being normalisation factors. Due to the overlap between the corresponding $|+_L\rangle = |C_\alpha^+\rangle$ and $|-_L\rangle = \left|C_{i\alpha}^+\right\rangle$ (Fig. 3.10**c.**) decreasing exponentially with $|\alpha|^2$, we can immediately deduce that phase-flips are exponentially suppressed in this encoding. The reasoning explaining this exponential decrease is the exact same as with bit-flips in the case of the 2-component cat code. Additionally, because $\left|C_\alpha^{0 \bmod 4}\right\rangle$ and $\left|C_\alpha^{2 \bmod 4}\right\rangle$ respectively have a parity of 0 and 2 photons modulo 4, this code can be protected against the loss of a single photon, similarly to the Kitten code. Assuming the parity protection performs well enough, this could protect the 4-component cat against both phase-flip and bit-flip errors.

This qubit was stabilized in 2016 by Ofek et al. [104] using measurement-based feedback. It is the first experiment to reach the break-even point with bosonic qubits. However, the exponential decrease in phase-flip rate is yet to be seen. Using dissipation to stabilize the 4-component cat code could allow one to do so, as was the case for the exponential increase of bit-flip in the 2-component cat qubit. Adding a parity stabilization protocol such as in [148] could then lead to a fully protected qubit.

It is worth mentioning that the 4-component cat qubit is expected to have similar performance as the pair-cat code [149, 150], which encodes the logical information in the difference between the photon number of 2 harmonic modes.

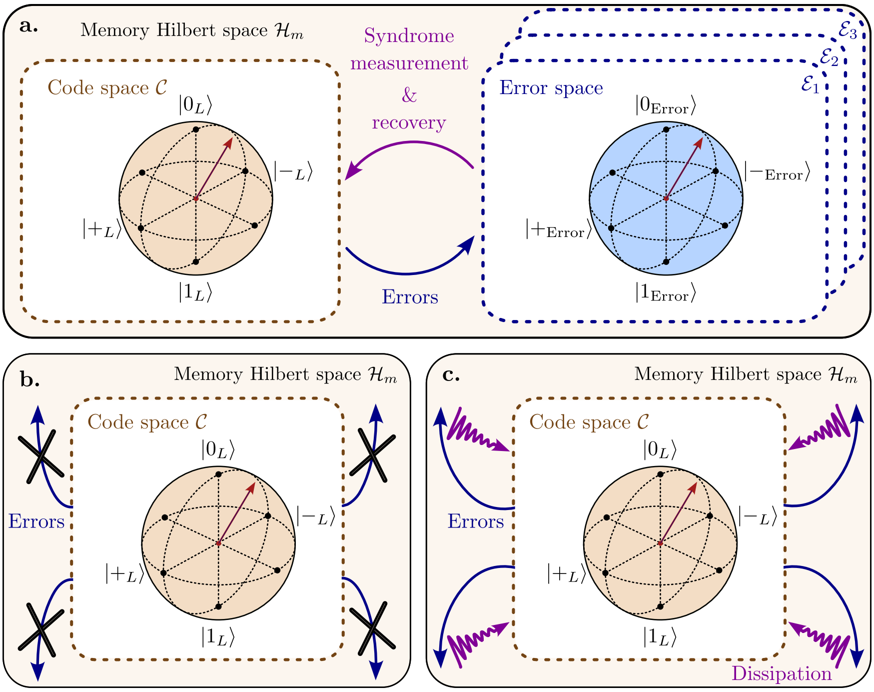

Figure 3.11: **a.** Protection of a bosonic code using measurement-based feedback. After an error, the memory state is in an error subspace which a syndrome measurement can distinguish from the code space $\mathcal{C}$. A recovery operation is then applied to bring the memory back to the code space. **b.** Schematic representation of the Hamiltonian engineering protection method. By engineering the memory Hamiltonian, leakage from the code space is prevented. **c.** Schematic representation of the dissipation engineering method. By tailoring a dissipation channel, entropy is constantly being removed from the system to stabilize the code space.

3.4 STABILISATION OF LOGICAL BOSONIC QUBITS

Different methods can be used in order to stabilize these states and protect the logical information. Irrespective of the specific approach chosen, the fundamental idea revolves around preventing the accumulation of entropy in the memory. This objective can be achieved using active measurement-based feedback, or through passive techniques involving Hamiltonian or dissipation engineering. Moreover, a combination of different stabilization methods can be envisioned, such as in the case of a repetition code of 2-

component cat qubits or the joint application of Hamiltonian and dissipation engineering to stabilize a single cat [151]. In this section, we briefly review the measurement-based feedback method before focusing on the 2 passive approaches. Additionally, we illustrate how both passive approaches can be used to stabilize a 2-component cat qubit.

3.4.1 *Measurement based feedback*

Measurement-based feedback involves the active intervention of an experimenter to extract entropy from the system. The fundamental idea is to encode logical information within a memory code space $\mathcal{C}$, with various error operators $\left\{\hat{E}_i\right\}$ mapping the code space to distinct orthogonal error spaces $\{\mathcal{E}_i\}$. These different sub-spaces being orthogonal, a syndrome can be designed that effectively differentiates $\mathcal{C}$ from the error spaces $\mathcal{E}_i$, while preserving the quantum information. Note that this is only possible for error channels verifying the Knill-Laflamme criteria (see Sec. 2.3.2.2). Consequently, a recovery operation can be implemented to bring the memory back into the code space. The entropy is expelled into the environment during the syndrome measurement. A schematic of this process is represented in Fig. 3.11**a.**.

Measurement-based feedback stands as the most widely employed approach, with several prominent examples being the repetition code, surface code, Kitten code, or GKP code. Note that, up to this point, all experiments achieving the break-even point of QEC have relied on measurement-based feedback [104, 140, 144].

3.4.2 *Hamiltonian engineering*

A second approach involves tailoring the memory Hamiltonian to ensure that states within the code space $\mathcal{C}$ are ground states of this modified Hamiltonian. The Hamiltonian can be engineered using parametric pumping, which allows for the selection of desired terms in the Hamiltonian expansion while neglecting other terms through the Rotation Wave Approximation (see Appendix.a). By creating a significant energy gap between the ground and excited states, unwanted excitations out of the code space become unlikely, thereby protecting the stored logical information (Fig. 3.11**b.**). The maximal speed of logical gates is set by this energy gap. In essence, this approach can be seen as biasing the memory phase space, creating local minima that restrict the memory's ability to explore its phase space and prevent the generation of entropy.

A prominent application of this Hamiltonian engineering method is the so-called *Kerr-cat* code [98, 99, 152], which combines the effects of self-Kerr and squeezing Hamiltonian terms to stabilize cat qubits. In the implementation of [153], the memory hosting the logical information is physically realized using an array of charge-driven SNAIL transmons, driven by a pump at frequency $\omega_p/2\pi$. This non-linear system is described by the Hamiltonian

$$\hat{H}/\hbar = \omega_m \hat{a}^\dagger \hat{a} + \sum_{k=3}^{\infty} g_k \left(\hat{a} + \epsilon_p e^{-i\omega_p t} + \text{h.c}\right)^k, \tag{3.48}$$

with g_k the non-linear coupling term of order k and ϵ_p the pump amplitude. In the rotating frame generated by the operator $\hat{U} = e^{-i\frac{\omega_p}{2}\hat{a}^\dagger\hat{a}}$, this Hamiltonian becomes

$$\hat{H}/\hbar = \delta \hat{a}^\dagger \hat{a} + \sum_{k=3}^{\infty} g_k \left(\hat{a} e^{-i\frac{\omega_p t}{2}} + \epsilon_p e^{-i\omega_p t} + \text{h.c}\right)^k, \tag{3.49}$$

with $\delta = \frac{\omega_p}{2} - \omega_m$. This detuning is set to 0 by enforcing the condition $\omega_p = 2\omega_m$. Considering the limit of small nonlinearity, terms of order $k \geq 5$ can be neglected due to the non-linear coupling decreasing as $g_k \propto O(\varphi^k_{\text{ZPF,m}})$, with $\varphi_{\text{ZPF,m}} < 1$ the zero point fluctuation of the memory mode. Keeping only non-oscillating terms according to the 1^{st} order RWA, the Hamiltonian becomes

$$\hat{H}/\hbar = -\chi_{\text{m,m}} \hat{a}^{\dagger 2} \hat{a}^2 + \left(\epsilon_2 \hat{a}^{\dagger 2} + \epsilon_2^* \hat{a}^2\right), \tag{3.50}$$

with $\chi_{\text{m,m}}$ the memory self-Kerr and $\epsilon_2 = g_3 \epsilon_p$ the amplitude of the effective squeezing drive. Eq. (3.50) can then be factorized as

$$\hat{H}/\hbar = -\chi_{\text{m,m}} \left(\hat{a}^{\dagger 2} - \frac{\epsilon_2}{\chi_{\text{m,m}}}\right)\left(\hat{a}^2 - \frac{\epsilon_2^*}{\chi_{\text{m,m}}}\right) + \frac{|\epsilon_2|^2}{\chi_{\text{m,m}}}. \tag{3.51}$$

This form makes evident that the two coherent states $|\pm\alpha\rangle$, $\alpha = \sqrt{\epsilon_2^*/\chi_{\text{m,m}}}$, are eigenstates of $\hat{H}$ with the corresponding energy $\hbar|\epsilon_2|^2/\chi_{\text{m,m}}$. More precisely, they are the two degenerate ground states[3] of the Hamiltonian, separated from the rest of the spectrum by an energy gap

---

[3] The negative sign in the Hamiltonian of Eq. (3.50) seems to indicate that these coherent states correspond to a maximum of energy of the system. This Hamiltonian is actually written in the rotating frame where it is described by quasienergy eigenstates with negative energies [154].

$$E_{\mathrm{gap}}/\hbar = 4\chi_{\mathrm{m,m}}|\alpha|^2 = 4|\epsilon_2|^2. \tag{3.52}$$

Increasing the pump amplitude then widens the gap between the ground and excited states, preventing the leakage of the memory out of the code space $\mathcal{C}$. However, experiments using this Kerr-cat architecture did not demonstrate the expected exponential increase in bit-flip time. Instead, a staircase pattern is observed where the bit-flip time increases in steps as a function of $|\alpha|^2$, resulting from spectral kissing in the excited-states spectrum [99]. Note that this approach can be extended for the stabilization of $2N$ coherent states using the Hamiltonian

$$\hat{H}/\hbar = -\chi_{\mathrm{m,m}}\hat{a}^{\dagger 2N}\hat{a}^{2N} + \left(\epsilon_2\hat{a}^{\dagger 2N} + \epsilon_2^*\hat{a}^{2N}\right). \tag{3.53}$$

3.4.3 *Dissipation engineering*

Another approach, explored in detail in this thesis, is to tailor an effective loss operator that stabilizes the desired states. To engineer this dissipation, an additional lossy mode called *buffer* is introduced in the system which couples to the memory through a designed non-linear coupling (Fig. 3.12). The memory and buffer dynamics is governed by

$$\begin{aligned} \hat{H}/\hbar &= g\hat{A}\hat{b}^\dagger + g^*\hat{A}^\dagger\hat{b} \\ \hat{L}_b &= \sqrt{\kappa_b}\hat{b}, \end{aligned} \tag{3.54}$$

with κ_b the buffer single-photon loss rate, g the non-linear coupling rate and $\hat{A}$ an operator acting on the memory. In the limit $\kappa_b \gg |g|$ the buffer can be adiabatically eliminated, resulting in an effective dynamics of the memory described by

$$\hat{L}_{\mathrm{eff}} = \sqrt{\kappa_{\mathrm{eff}}}\hat{A}, \text{ with } \kappa_{\mathrm{eff}} = \frac{4|g|^2}{\kappa_b}. \tag{3.55}$$

Choosing the appropriate operator $\hat{A}$, this effective dissipation can stabilize the code space by passively and continuously dumping entropy from the memory into the environment, using the buffer mode as an intermediate (Fig. 3.11**c.**).

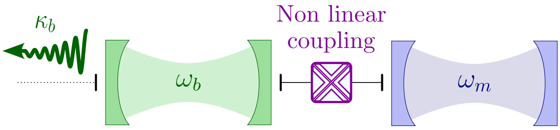

Figure 3.12: Schematic of the memory - blue - coupled to a buffer - green - mode through a non-linear coupling. The buffer is strongly coupled to the environment, resulting in a photon loss rate much stronger than the non-linear coupling $\kappa_b \gg |g|$.

3.4.3.1 *Adiabatic elimination of the buffer mode*

Eq. (3.55) is obtained using a technique called adiabatic elimination [117, 155, 156], which makes use of the condition $\kappa_b \gg |g|$ to obtain the effective dynamics of the memory. The bipartite memory & buffer system is described by the density matrix $\hat{\rho}$, evolving according to the Lindblad equation

$$\frac{\mathrm{d}}{\mathrm{d}t}\hat{\rho} = -i\left[g\hat{A}\hat{b}^\dagger + g^*\hat{A}^\dagger\hat{b}, \hat{\rho}\right] + \mathcal{D}(\sqrt{\kappa_b}\hat{b})\hat{\rho}. \tag{3.56}$$

To separate the buffer and memory dynamics, the density matrix $\hat{\rho}$ is written as

$$\begin{aligned}\hat{\rho} = {} & \hat{\rho}_{00} \otimes |0\rangle\langle 0| \\ & + \delta\left(\hat{\rho}_{10} \otimes |1\rangle\langle 0| + \hat{\rho}_{10} \otimes |1\rangle\langle 0|\right) \\ & + \delta^2\left(\hat{\rho}_{11} \otimes |1\rangle\langle 1| + \hat{\rho}_{20} \otimes |2\rangle\langle 0| + \hat{\rho}_{02} \otimes |0\rangle\langle 2|\right) + O\left(\delta^3\right).\end{aligned} \tag{3.57}$$

δ is a small parameter of order $|g|/\kappa_b$, and $\hat{\rho}_{ij} = \langle i|\,\hat{\rho}\,|j\rangle$ is an operator acting on the memory with $|i\rangle$ and $|j\rangle$ being Fock states of the buffer mode $\hat{b}$. This form is justified by the condition $|g| \ll \kappa_b$ which ensures that photons are removed from the buffer faster than the non-linear coupling rate, guaranteeing only a low number of photons are present in the buffer. The adiabatic elimination then aims at finding the dynamic of

$$\hat{\rho}_m = \mathrm{Tr}_b\left(\hat{\rho}\right) = \sum_{i\in\mathbb{N}} \langle i|\,\hat{\rho}\,|i\rangle \approx \hat{\rho}_{00} \tag{3.58}$$

at first order in δ. To do so, we project Eq. (3.56) in the buffer Fock state $|0\rangle$ which yields

$$\frac{1}{\kappa_b}\frac{\mathrm{d}}{\mathrm{d}t}\hat{\rho}_{00} = -i\frac{\delta}{\kappa_b}\left(g^*\hat{A}^\dagger\hat{\rho}_{10} - g\hat{\rho}_{01}\hat{A}\right) + \delta^2\hat{\rho}_{11} + O(\delta^3). \tag{3.59}$$

We then compute the evolution of $\hat{\rho}_{10}$, $\hat{\rho}_{01}$, and $\hat{\rho}_{11}$ which all appear in the dynamic of $\hat{\rho}_{00}$

$$\frac{1}{\kappa_b}\frac{\mathrm{d}}{\mathrm{d}t}\hat{\rho}_{01} = i\frac{g^*}{\delta\kappa_b}\hat{\rho}_{00}\hat{A}^\dagger - \frac{1}{2}\hat{\rho}_{01} + O(\delta) \tag{3.60a}$$

$$\frac{1}{\kappa_b}\frac{\mathrm{d}}{\mathrm{d}t}\hat{\rho}_{10} = -i\frac{g}{\delta\kappa_b}\hat{A}\hat{\rho}_{00} - \frac{1}{2}\hat{\rho}_{10} + O(\delta) \tag{3.60b}$$

$$\frac{1}{\kappa_b}\frac{\mathrm{d}}{\mathrm{d}t}\hat{\rho}_{11} = \frac{i}{\delta\kappa_b}\left(g^*\hat{\rho}_{10}\hat{A}^\dagger - g\hat{A}\hat{\rho}_{01}\right) - \hat{\rho}_{11} + O(\delta) \tag{3.60c}$$

We see that Eq. (3.60a) and Eq. (3.60b) share the same structure, with a term proportional to $\hat{\rho}_{00}$ that can be viewed as an external drive and a second damping term. The variation of $\hat{\rho}_{00}$ being of order $O(\delta^2)$ - see Eq. (3.59) - compared to the damping term of order $O(\delta)$, we can make the adiabatic approximation and consider $\hat{\rho}_{01}$ and $\hat{\rho}_{10}$ to continuously be in their steady state. This gives the system of equations

$$\hat{\rho}_{01} = 2i\frac{g^*}{\delta\kappa_b}\hat{\rho}_{00}\hat{A}^\dagger \tag{3.61a}$$

$$\hat{\rho}_{10} = -2i\frac{g}{\delta\kappa_b}\hat{A}\hat{\rho}_{00}. \tag{3.61b}$$

Both $\hat{\rho}_{01}$ and $\hat{\rho}_{10}$ being proportional to $\hat{\rho}_{00}$, the same reasoning can then be applied to Eq. (3.60c), giving the approximate expression

$$\hat{\rho}_{11} = 4\frac{|g|^2}{\delta\kappa_b}\hat{A}\hat{\rho}_{00}\hat{A}^\dagger. \tag{3.62}$$

Injecting these relations in Eq. (3.59) finally yields

$$\begin{aligned}\frac{\mathrm{d}}{\mathrm{d}t}\hat{\rho}_{00} &= \frac{4|g|^2}{\kappa_b}\left(\hat{A}\hat{\rho}_{00}\hat{A}^\dagger - \frac{1}{2}\left\{\hat{A}^\dagger\hat{A}, \hat{\rho}_{00}\right\}\right)\\ &= \mathcal{D}\left(\sqrt{\frac{4|g|^2}{\kappa_b}}\hat{A}\right)\hat{\rho}_{00}.\end{aligned} \tag{3.63}$$

As previously stated in Eq. (3.55), the dynamics of the memory is then indeed approximated by an effective dissipation $\hat{L}_{\mathrm{eff}} = \sqrt{\kappa_{\mathrm{eff}}}\hat{A}$ after adiabatically eliminating the buffer.

3.4.3.2 *Stabilization of 2-component cat qubits*

This result is very general and works irrespective of the operator $\hat{A}$ appearing in the non-linear coupling. A notable application, studied in this thesis, is the stabilization of 2-component cat qubits using the dissipation operator

$$\hat{L}_2 = \sqrt{\kappa_2}\left(\hat{a}^2 - \alpha^2\right). \tag{3.64}$$

It is experimentally realized by engineering a 2-to-1 photon exchange Hamiltonian between the memory and buffer modes. A classical drive of amplitude ϵ_d is then applied to the buffer, with the injected photons being converted into pairs of photons in the memory mode. This system is described by the Hamiltonian

$$\begin{aligned} \hat{H}/\hbar &= g_2 \hat{a}^{\dagger 2}\hat{b} + g_2^* \hat{a}^2 \hat{b}^\dagger + \epsilon_d \hat{b}^\dagger + \epsilon_d^* \hat{b} \\ &= g_2 \left(\hat{a}^{\dagger 2} + \frac{\epsilon_d^*}{g_2}\right)\hat{b} + g_2^* \left(\hat{a}^2 + \frac{\epsilon_d}{g_2^*}\right)\hat{b}^\dagger . \end{aligned} \tag{3.65}$$

After adiabatically eliminating the buffer mode, the memory dynamics is governed by the dissipator of Eq. (3.64) with $\alpha^2 = -\epsilon_d/g_2^*$ and $\kappa_2 = 4|g_2|^2/\kappa_b$. The coherent states $|\pm\alpha\rangle$ are unaffected by this dissipation, with all other states in the memory Hilbert space being projected to the manifold $\mathrm{span}\left(|\alpha\rangle, |-\alpha\rangle\right)$. Reaching large values for the two-photon rate κ_2 - and thus for the 2-to-1 exchange rate g_2 - is critical in this strategy. First, in order to observe the exponential improvement of bit-flip time, it should overcome any parasitic processes affecting the memory such as dephasing, thermal excitation, Kerr effect, frequency shifts due to a thermally populated auxiliary qubit [102, 157] or gate drives. Second, its value sets a higher bound on cat qubit gate speed, to avoid non-adiabatic errors, and needs to be large compared to the residual single-photon loss rate κ_1, the main cause of phase-flip errors [145]. Besides, a repetition code made of a chain of cat qubits can protect against phase-flip errors under the condition $\kappa_2/\kappa_1 \gtrsim 10^2$ [146, 88, 145].

3.5 ENGINEERING THE COUPLING BETWEEN MEMORY AND BUFFER MODE

3.5.1 *4-wave mixing nonlinearity*

The first experiments which stabilized cat qubits through dissipation relied on a 4-wave mixing element to mediate the 2-to-1 photon interaction. To

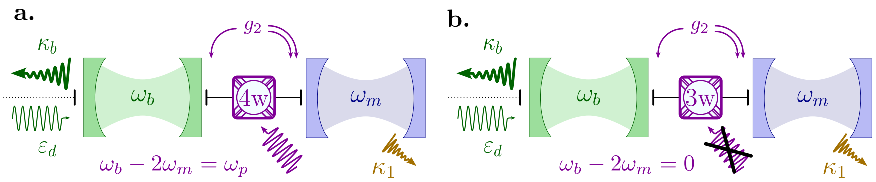

Figure 3.13: **a.** A 4-wave mixing coupler such as a transmon or ATS swaps pairs of photons of a memory mode at ω_m for single photons of a buffer mode at ω_b at a rate g_2 owing to a pump at $|\omega_b - 2\omega_m|$. The buffer loss rate κ_b thus leads to an effective two-photon dissipation rate κ_2 that scales with pump amplitude. Driving the buffer mode on resonance at a displacement rate ϵ_d stabilizes a cat code $\{|\pm\alpha\rangle\}$. **b.** A three-wave mixing coupler passively performs the same photon exchange when $\omega_b = 2\omega_m$.

activate the desired Hamiltonian, this non-linear element is driven by a pump at frequency $\omega_p = \omega_b - 2\omega_m$, with ω_b and ω_m the frequency of the buffer and memory modes respectively (Fig. 3.13**a.**). This frequency-matching condition ensures that energy is conserved during the process. Applying a classical drive of amplitude ϵ_d to the buffer, the bipartite system memory & buffer is then described to first order by the Hamiltonian of Eq. (3.65), neglecting for now spurious terms in the Hamiltonian.

The first realizations at Yale University [117, 101] relied on a transmon qubit to generate the nonlinearity. In this scheme, the coupling rate g_2 is given by

$$g_2 = \chi_{\mathrm{m,b}} \frac{\epsilon_p^*}{2}, \tag{3.66}$$

with ϵ_p the dimensionless pump amplitude (see Sec. 3.2.3.1 which introduced the concept of a dimensionless pump driving a harmonic mode) and $\chi_{\mathrm{m,b}}$ the cross-Kerr coupling between the memory and buffer. This coupling corresponds to an additional term $-\chi_{\mathrm{m,b}}\hat{a}^\dagger\hat{a}\hat{b}^\dagger\hat{b}$ in the system's Hamiltonian. Maximizing g_2 then amounts to working at large pump amplitudes ϵ_p. However, pushing ϵ_p to excessively high values leads to higher states of the transmon being excited, effectively killing the stabilization. This sets a limit to the maximal attainable value of g_2. In the first paper of 2015 [117] demonstrating such a stabilization, a pump amplitude of $\epsilon_p = 1.1$ was achieved, leading to a 2-to-1 coupling rate $g_2/2\pi = 111$ kHz. Stabilization of a cat qubit was observed, but not the exponential increase in bit-flip time T_{X}. This was primarily due to parasitic terms such as the cross-Kerr coupling

$\chi_{\mathrm{m,b}}/2\pi = 206$ kHz being comparable to the two-photon dissipation rate $\kappa_2/2\pi = 50$ kHz. A later experiment improved on this design [101], reaching a two-photon dissipation rate $\kappa_2/2\pi = 176$ kHz, which was remarkably 100 times larger than the single photon-loss rate $\kappa_1/2\pi = 1.7$ kHz. However, parasitic terms still prevented observing the exponential increase of T_{X}.

This issue was later solved using an ATS as the coupling element [102]. This circuit exhibits a flux sweet spot where parasitic terms can be inhibited. There, the 2-to-1 coupling rate reads

$$g_2 = \frac{E_j}{2\hbar}\epsilon_p \varphi_{\mathrm{ZPF,m}}^2 \varphi_{\mathrm{ZPF,b}}, \tag{3.67}$$

with $\varphi_{\mathrm{ZPF,m}}$ and $\varphi_{\mathrm{ZPF,b}}$ the zero point fluctuation of the memory and buffer mode. Despite a coupling rate $g_2/2\pi = 0.36$ MHz similar to previous experiments, the purer Hamiltonian allowed to see an exponential increase in bit-flip time, reaching $T_{\mathrm{X}} \approx 1$ ms for $|\alpha|^2 \approx 5$. The limiting element was no longer the coupling element itself but an auxiliary transmon used to perform the Wigner tomography of the memory. Removing this transmon, bit-flip times of 100 s were observed [157], with a recent experiment I participated in showing both bit-flip times exceeding 10 s and the coherent manipulation of a cat qubit [158].

3.5.2 *Switching to a passive 3-wave interaction*

In order to increase the 2-to-1 coupling rater, we introduce a new design relying on 3-wave mixing instead. This additionally alleviates the need for an additional pump to mediate the 2 photon interaction, thus simplifying the design. The frequency-matching condition becomes

$$2\omega_m = \omega_b, \tag{3.68}$$

so that energy is preserved during the conversion (Fig. 3.13**b.**). This condition is characteristic of autoparametric systems so that the buffer field passively performs a parametric driving of the memory [159]. We nicknamed this circuit as the *autoparametric cat*, or alternatively the *Auto-cat* to highlight its ease of use.

3.5.3 *Introduction of the circuit*

The Auto-cat can be understood as a limit case of a degenerate parametric amplifier [160, 161, 162]. These are usually made of a resonator m connected to a pump mode c via a nonlinear element such that their interaction Hamiltonian reads $\hbar g_2 \hat{m}^2 \hat{c}^\dagger + h.c.$.

Driving the pump mode c at $2\omega_m$ with a large enough power, parametric oscillations spontaneously occur when the number of photons in the pump mode exceeds the threshold $n_{\text{thr}} = \kappa_m^2/(4g_2)^2$. This threshold corresponds to the number of photons at which the gain process compensates the losses of mode m. Above threshold, two possible mechanisms prevent the number of photons from indefinitely increasing: the Kerr effect or pump depletion. The mode m then emits radiation with two possible phases [163, 164, 165], corresponding to two coherent states $|\alpha\rangle$ and $|-\alpha\rangle$ of the resonator m.

The first limiting mechanism is the self-Kerr effect in the resonator m, induced by the nonlinearity used to generate the interaction. As the number of photons in the resonator increases, the mode resonance frequency shifts until the pump at $2\omega_m$ is so far detuned that the gain and loss processes balance each other. This Kerr limitation is the most standard one in Josephson junction amplifiers and is crucial for the stabilization of Kerr cats [152, 98, 99, 166]. The second limiting mechanism is pump depletion, which is more common at optical wavelength. The stiff pump approximation breaks down if the number of photons in the pump mode is affected by how fast pump photons are consumed to generate photons in mode m. The rate at which pump photons are regenerated by the drive is then not fast enough to produce pairs of photons in mode m.

The autoparametric design is not impacted by the Kerr limitation and instead operates in the pump depletion limit. The resonator m is used as the memory and the far-detuned pump mode is replaced by a buffer mode b that resonates at the memory frequency $2\omega_m$, satisfying Eq. (3.68). The high Q limit of the memory mode lowers the parametric oscillation threshold to $n_{\text{thr}} \ll 1$, while a resonant driving on mode b ensures the regeneration rate of pump photons in the buffer mode is minimal. In the steady state, the buffer is subject to two opposing driving forces: the buffer drive and the action of the memory mode on the buffer via the 2-to-1 photon exchange Hamiltonian. These 2 compensate exactly and the buffer reaches a steady state close to the vacuum, while the memory state converges to a superposition of $|\alpha\rangle$ and $|-\alpha\rangle$.

This realization is at the origin of the Auto-cat design. We started from a superconducting circuit widely used for degenerate parametric amplification: a resonator comprising a DC flux biased SQUID that is flux pumped at twice its frequency and acts as our memory mode [161]. Other non-linear elements could be chosen from the variety of Josephson amplifiers that have been designed over the past two decades. In this particular circuit, there exists another mode associated with the flux degree of freedom which has a differential symmetry with respect to the SQUID junctions but is often ignored for its very high frequency [167]. In this experiment, this mode is used as our buffer mode and is brought down in frequency while preserving its symmetry. This is done by adding a weak junction E_W in the SQUID loop (Fig. 3.14) and splitting the capacitance on either side of the SQUID. The symmetry is preserved and used advantageously to be able to couple preferentially to the buffer mode without needing frequency selective filtering to protect the memory lifetime. This basis structure is then diluted with open and shorted stubs as shown in Fig. 4.1 to tune the modes φ_{ZPF}.

3.5.4 *Hamiltonian derivation*

The simplified circuit of the autoparametric cat, neglecting the added stubs used to tune the zero point fluctuations of the phase φ_{ZPF} of the modes, is represented in (Fig. 3.14). The mixing element consists of two main Josephson junctions with energy E_J symmetrically arranged within a superconducting loop that is threaded with an external magnetic flux ϕ_{ext}. These two junctions in parallel configuration have a common mode serving as a memory mode and a differential mode, associated with the flux degree of freedom of the loop, and serving as a buffer mode. A third Josephson junction with energy E_W is added in the loop in order to lower the relatively high frequency of the buffer mode and increase its flux tunability. This configuration is similar to previously realized circuits [167, 168, 169, 170, 171]

We derive this system's Hamiltonian by first computing the effective inductance of each junction with the flux bias. We then find the eigenmodes of the linear part of the Hamiltonian and compute the circuit's nonlinearities.

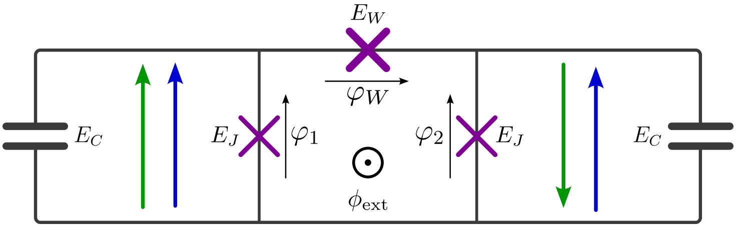

Figure 3.14: Simplified circuit diagram of the device. Only the modes of the ring of junctions are considered for simplicity. For each junction, the phase drop φ_x is decomposed as the sum of an oscillating part and an equilibrium part $\varphi_x = \tilde{\varphi}_x + \bar{\varphi}_x$.

3.5.4.1 *Equilibrium phase configuration*

First, we compute the effective inductance of the central mixing element. This element comprises 2 identical main junctions with Josephson energy E_J and one weaker junction with energy $E_W = \beta_J E_J$ with $\beta_J < 1$. Following the procedure detailed in [172], we compute the equilibrium phase drop across each junction $\bar{\varphi}_1$, $\bar{\varphi}_2$ and $\bar{\varphi}_W$. Note that each phase drop φ_x is decomposed as a sum of a constant part $\bar{\varphi}_x$ and a dynamical part $\tilde{\varphi}_x$. Using the second Josephson relation Eq. (3.10) and current conservation inside the loop imposes that $\bar{\varphi}_1 = -\bar{\varphi}_2$. This justifies the notation $\bar{\varphi}_J = \bar{\varphi}_1$ as the main junction phase drop. Current conservation further dictates that

$$\bar{\varphi}_J = \arcsin(\beta_J \sin \bar{\varphi}_W). \tag{3.69}$$

The phase drop around the whole loop $\bar{\varphi} = \bar{\varphi}_W + \bar{\varphi}_1 - \bar{\varphi}_2$ then reads

$$\bar{\varphi} = \bar{\varphi}_W + 2\arcsin(\beta_J \sin \bar{\varphi}_W). \tag{3.70}$$

Besides, the superconducting loop is threaded by an external flux $\phi_{\text{ext}} = \varphi_{\text{ext}}\varphi_0$, which leads to the constraint $\varphi_1 + \varphi_W - \varphi_2 = \varphi_{\text{ext}}$. This translates into

$$\bar{\varphi} = \varphi_{\text{ext}} \text{ and } \tilde{\varphi}_1 + \tilde{\varphi}_W - \tilde{\varphi}_2 = 0\,. \tag{3.71}$$

Finding the configuration of phase drops at equilibrium thus consists in first determining $\bar{\varphi}_W(\varphi_{\text{ext}})$ by solving the equation $\varphi_{\text{ext}} = \bar{\varphi}(\bar{\varphi}_W)$, of which a graphical representation is shown in Fig. 3.15**a**. The value of $\bar{\varphi}_J$ is then deduced from Eq. (3.69), and the effective inductive energies of each junction $\bar{E}_J = E_J \cos(\bar{\varphi}_J)$, $\bar{E}_W = E_W \cos(\bar{\varphi}_W)$ can then be calculated. The effective inductances follow as $\bar{L}_J = \varphi_0^2/\bar{E}_J$ and $\bar{L}_W = \varphi_0^2/\bar{E}_W$. In the case $\beta_J > 1/2$, the function $\bar{\varphi}_W(\varphi_{\text{ext}})$ is multi-valued [172] as shown in Fig. 3.15**b**. In order to avoid hysteresis effects or instabilities, we chose $\beta_J < 1/2$ which is equivalent to $E_W < E_J/2$.

This mixing element can be further studied to determine the presence of a flux sweet spot where memory flux noise is canceled. It is defined as the flux $\varphi_0\varphi_{\text{ext}}^{(\text{sweet})}$ such that

$$\left.\frac{d\omega_m}{d\varphi_{\text{ext}}}\right|_{\varphi_{\text{ext}}^{(\text{sweet})}} = 0. \tag{3.72}$$

We focus on the case where $\varphi_{\text{ext}}^{(\text{sweet})} \in [0, \pi]$ because of the 2π periodicity of the solutions and by symmetry around $\varphi_{\text{ext}} = 0$. The symmetry of the circuit of Fig. 3.14 implies that the memory mode, the common mode of this circuit, does not participate in the weak junction. The memory frequency ω_m is then proportional to $\bar{E}_J(\varphi_{\text{ext}}) = E_J \cos(\bar{\varphi}_J)$, which gives an immediate solution for Eq. (3.72) at $\varphi_{\text{ext}} = 0$. This solution is discarded however since we require $\bar{\varphi}_J \neq 0$ at the sweet spot in order to preserve a non-zero 3-wave mixing interaction rate. The flux sweet spot is, therefore, a local extremum of $\bar{\varphi}_J(\varphi_{\text{ext}})$. From Eq. (3.69), we deduce that $\varphi_{\text{ext}}^{(\text{sweet})}$ is close to $\bar{\varphi}_W = \pi/2$ since this is where $\sin(\varphi_W)$ is maximal. Finally, the condition $\varphi_{\text{ext}} < \pi$ imposes an upper bound on β_J since, for $\bar{\varphi}_W = \pi/2$, Eq. (3.70) comes down to $\pi/2 + 2\arcsin\beta_J < \pi$ and thus $\beta_J < 1/\sqrt{2}$.

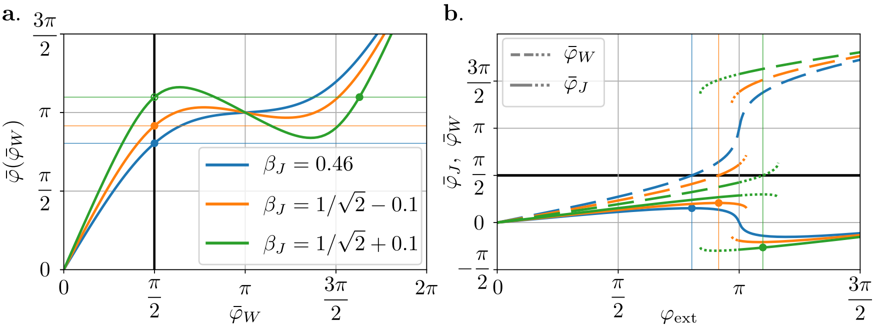

Figure 3.15: Flux sweet spots of the mixing element. **a.** Sum $\bar{\varphi}$ of the phase differences across the three junctions as a function of the phase difference $\bar{\varphi}_W$ across the weak junction, calculated using Eq. (3.70) for $\beta_J = E_W/E_J = 0.46$ as in the experiment (blue), $\beta_J < 1/\sqrt{2}$ (orange) and $\beta_J > 1/\sqrt{2}$ (green). A flux bias imposes $\varphi_{\text{ext}} = \bar{\varphi}$ so that these curves show which values of $\bar{\varphi}_W$ are possible. **b.** Phase differences $\bar{\varphi}_J$ (solid-dotted) and $\bar{\varphi}_W$ (dashed-dotted) as a function of φ_{ext}. Same color code for the values of β_J as in **a.**. Dotted lines correspond to extensions of the solutions that are stable but not the lowest energy configuration. **a.**/**b.** The black vertical/horizontal line corresponds to $\bar{\varphi}_W = \pi/2$. In **a.** it crosses $\bar{\varphi}$ at $\varphi_{\text{ext}}^{(\text{sweet})}$ (thin horizontal colored lines). In **b.** it crosses $\bar{\varphi}_W$ where $\bar{\varphi}_J$ has a sweet spot at the same values of $\varphi_{\text{ext}}^{(\text{sweet})}$ (thin vertical colored lines). The blue and orange closed circles correspond to sweet spots in the lowest energy configuration. The open green circle emphasizes that while the sweet spot exists, it is not the lowest energy configuration. At this value of φ_{ext} (vertical green line) another configuration is favored (green closed circle) which is not a flux sweet spot.

The condition $E_W < E_J/\sqrt{2}$ then ensures a sweet spot is visible at $\varphi_{\text{ext}}^{(\text{sweet})} = \pi/2 + 2\arcsin\beta_J$ (blue and orange closed circle in Fig. 3.15**b.**). Close to the sweet spot, at first order, $\bar{\varphi}_J$ is constant and $\bar{\varphi}_W = \pi/2 + \delta\varphi_{\text{ext}}$

where $\delta\varphi_{\text{ext}} = \varphi_{\text{ext}} - \varphi_{\text{ext}}^{(\text{sweet})}$ is the flux offset from the sweet spot. At second order, $\bar{\varphi}_J$ is then given by

$$\begin{aligned}\bar{\varphi}_J &= \arcsin(\beta_J \sin(\pi/2 + \delta\varphi_{\text{ext}})) \\ &= \arcsin\left(\frac{E_W}{E_J}(1 - \frac{\delta\varphi_{\text{ext}}^2}{2})\right).\end{aligned} \tag{3.73}$$

Note that the single minimum condition $\beta_J < 1/2$ verified in the experiment - see Table. 4.1- is well within this limit. On the opposite, the regime $1/2 < \beta_J < 1/\sqrt{2}$ comprises a sweet spot in the lowest energy flux configuration (orange closed circle in Fig. 3.15**b.**) but the existence of another higher energy minimum might be detrimental. Finally, for $\beta_J > 1/\sqrt{2}$, there exists a sweet spot which is however not the lowest energy phase configuration (green open circle in Fig. 3.15**b.**).

3.5.4.2 *Eigenmodes*

After finding the equilibrium phase differences and the effective inductive energies $\bar{E}_J$ and $\bar{E}_W$, we determine the eigenmodes of the system and compute the zero point fluctuation of the phase across each dipole of the linear equivalent circuit. The potential energy of the linear system modeling the circuit reads $U_{\text{lin}} = \bar{E}_J\tilde{\varphi}_1^2/2 + \bar{E}_J\tilde{\varphi}_2^2/2 + \bar{E}_W\tilde{\varphi}_W^2/2$. Hence, incorporating the constraints of Eq. (3.71), we find

$$\begin{aligned}U_{\text{lin}}\left(\tilde{\varphi}_1, \tilde{\varphi}_2\right) &= \frac{\bar{E}_J}{2}\tilde{\varphi}_1^2 + \frac{\bar{E}_J}{2}\tilde{\varphi}_2^2 + \frac{\bar{E}_W}{2}(\tilde{\varphi}_1 - \tilde{\varphi}_2)^2 \\ T\left(\dot{\tilde{\varphi}}_1, \dot{\tilde{\varphi}}_2\right) &= \frac{\hbar^2}{16E_C}\dot{\tilde{\varphi}}_1^2 + \frac{\hbar^2}{16E_C}\dot{\tilde{\varphi}}_2^2\end{aligned} \tag{3.74}$$

where T is the kinetic energy of the system and E_C is the charging energy of each capacitor. We diagonalize the system by performing the change of variable

$$\begin{cases}\varphi_m = \dfrac{\tilde{\varphi}_1 + \tilde{\varphi}_2}{2} \\ \varphi_b = \dfrac{\tilde{\varphi}_1 - \tilde{\varphi}_2}{2},\end{cases}$$

where φ_m and φ_b correspond to the common and differential modes of the circuit, respectively corresponding to the memory and buffer modes. The potential and kinetic energies of the circuit then read

$$\begin{aligned} U_{\text{lin}}\left(\varphi_m,\varphi_b\right) &= \frac{E_{L,m}}{2}\varphi_m^2 + \frac{E_{L,b}}{2}\varphi_b^2 \\ T\left(\dot{\varphi}_m,\dot{\varphi}_b\right) &= \frac{\hbar^2}{8E_C}\dot{\varphi}_m^2 + \frac{\hbar^2}{8E_C}\dot{\varphi}_b^2. \end{aligned}$$

with $E_{L,m} = 2\bar{E}_J$ and $E_{L,b} = 2\bar{E}_J + 4\bar{E}_W$. The mode frequencies and zero-point fluctuations of the buffer and memory mode are given by

$$\begin{aligned} \omega_b \quad &= \sqrt{4E_C E_{L,b}}\varphi_{\text{ZPF},b} = \left(E_C/E_{L,b}\right)^{1/4} \\ \omega_m \quad &= \sqrt{4E_C E_{L,m}}\varphi_{\text{ZPF},m} = \left(E_C/E_{L,m}\right)^{1/4} \end{aligned} \tag{3.75}$$

so that, in second quantization, the linear part of the Hamiltonian is

$$\hat{H}_{\text{lin}}/\hbar = \omega_m \hat{a}^\dagger\hat{a} + \omega_b\hat{b}^\dagger\hat{b}. \tag{3.76}$$

The annihilation operators are defined by their relation to the phase differences

$$\begin{aligned} \hat{\varphi}_m &= \varphi_{\text{ZPF},m}\left(\hat{a}+\hat{a}^\dagger\right) \\ \hat{\varphi}_b &= \varphi_{\text{ZPF},b}\left(\hat{b}+\hat{b}^\dagger\right). \end{aligned} \tag{3.77}$$

The frequencies of both the memory and buffer modes depend on ϕ_{ext} through the dependency of $\bar{\varphi}_J$ and $\bar{\varphi}_W$.

Note that, as the equilibrium phase $\bar{\varphi}_W$ associated to the weak junction E_W is more sensitive to the external flux, we see from Eq. (3.75) that ω_b has an increased susceptibility to the external flux compared to the memory frequency. Since the memory mode does not participate in the central inductive element of the SQUID, adding this weak junction then increases the buffer susceptibility to flux without increasing the memory self-Kerr rate. This makes the buffer responsible for meeting the frequency matching condition $2\omega_m = \omega_b$ while the memory can afford a much weaker dependence on flux, hence limiting the impact of flux noise.

In the actual circuit, stub resonators are connected to the ring of junctions so that the mode frequencies and zero point fluctuations are modified. The external flux ϕ_{ext} is then chosen to verify the condition $\omega_b = 2\omega_m$, defining the *Quantum Error Correction flux* ϕ_{QEC}. Simulations were performed to match ϕ_{QEC} with $\phi_{\text{ext}}^{(\text{sweet})}$, although a deviation can experimentally be observed. Numerically fitting the frequency dispersion versus flux (see Fig. 4.4**d.**) with the full model gives $\varphi_{\text{ZPF},m} = 0.0305$ and $\varphi_{\text{ZPF},b} = 0.0648$ at ϕ_{QEC}.

3.5.4.3 *Nonlinearities*

Around the DC solution of the system, the full potential

$$U(\tilde{\varphi}_1,\tilde{\varphi}_2) = -E_J\cos(\tilde{\varphi}_1+\bar{\varphi}_J) - E_J\cos(\tilde{\varphi}_2-\bar{\varphi}_J) - E_W\cos(\tilde{\varphi}_2-\tilde{\varphi}_1+\bar{\varphi}_W) \tag{3.78}$$

can be used to compute the nonlinearities. Using the former change of variable we get

$$U\left(\varphi_m,\varphi_b\right) = -2E_J\cos\left(\varphi_m\right)\cos\left(\varphi_b+\bar{\varphi}_J\right) - E_W\cos\left(2\varphi_b-\bar{\varphi}_W\right). \tag{3.79}$$

The potential energy is represented in Fig. 3.16 for the experimental circuit parameters $E_W/h \approx 115$ GHz and $E_J/h \approx 250$ GHz (see Table. 4.1) for several values of the external flux bias ϕ_{ext}. As expected from the change of variable, the global minimum is located at $(\varphi_m,\varphi_b)=(0,0)$ for any flux bias φ_{ext}. Other minima exist owing to the periodicity of the Josephson potential but there is a potential barrier of $2E_J \approx k_B \times 22$ K to overcome in order to transit from one solution to the other as can be seen in Fig. 3.16. Expanding the sin and cos function up to 4^{th} order in the phases then gives the Hamiltonian parameters.

3^{rd} ORDER TERMS We now consider working at ϕ_{QEC} yielding the condition $\omega_b = 2\omega_m$ and restrict our analysis to terms surviving the Rotating Wave Approximation (see Appendix. a). The only 3^{rd} order terms to consider is then

$$\hat{H}_{3^{\text{rd}}}/\hbar = E_J\sin\left(\bar{\varphi}_J\right)\varphi_{\text{ZPF},b}\,\varphi^2_{\text{ZPF},m}\left(\hat{b}\,\hat{a}^{\dagger\,2}+\hat{b}^{\dagger}\hat{a}^2\right).$$

This Hamiltonian corresponds to the 2-photon exchange Hamiltonian, responsible for converting single photons in the buffer into pairs of photons in the memory mode and back. Plugging in the value of $\bar{\varphi}_J$ around the sweet spot Eq. (3.73), we obtain $\hbar g_2 \approx E_W\left(1-\delta\varphi^2_{\text{ext}}/2\right)\varphi^2_{\text{ZPF},m}\varphi_{\text{ZPF},b}$. Comparing this expression to the 2-to-1 coupling rate of the ATS, Eq. (3.67), the dimensionless pump ϵ_p is then replaced by the term $\left(1-\delta\varphi^2_{\text{ext}}/2\right)$. Operating at $\delta\varphi_{\text{ext}}=0$, i.e at $\phi_{\text{QEC}}=\phi^{(\text{sweet})}_{\text{ext}}$, we expect to increase the value of g_2 which was previously limited by relatively low pump amplitudes ϵ_d. From the frequency dispersion versus flux (Fig. 4.4**d**) we expect $g_2/2\pi = 6.2$ MHz, very close to what is experimentally extracted from Fig. 5.4**b.**.

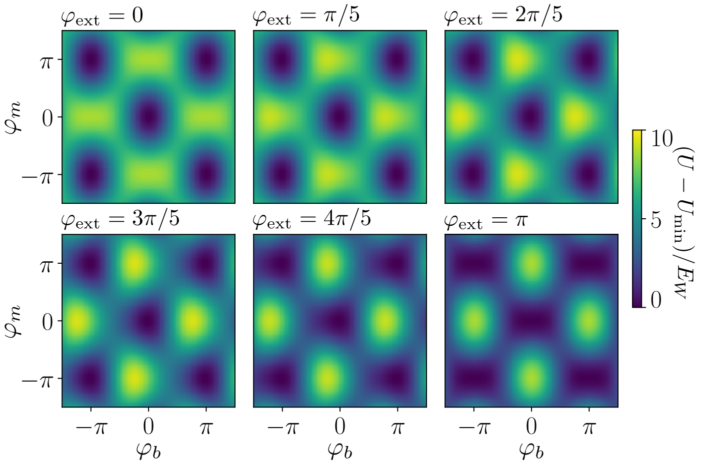

Figure 3.16: Potential energy $U(\varphi_m, \varphi_b)/E_W$ for $E_W/h = 115$ GHz and $E_J/h = 250$ GHz at six different flux biases. For each flux bias, an offset $U_{\rm min}(\varphi_{\rm ext})$ is subtracted to Eq. (3.79) in order to set the potential global minimum to 0 and better highlight the height of the potential barrier.

$4^{\rm th}$ ORDER TERMS Expanding even further the Hamiltonian to $4^{\rm th}$ order terms leads to the expression of the memory and buffer self-Kerr rates, as well as the cross-Kerr coupling rate between these 2 modes

$$\begin{aligned} \hbar\chi_{\rm m,m} &= \bar{E}_J \varphi_{{\rm ZPF},m}^4 \\ \hbar\chi_{\rm b,b} &= \bar{E}_J \varphi_{{\rm ZPF},b}^4 + 8\bar{E}_W \varphi_{{\rm ZPF},b}^4 \\ \hbar\chi_{\rm m,b} &= 2\bar{E}_J \varphi_{{\rm ZPF},m}^2 \varphi_{{\rm ZPF},b}^2. \end{aligned} \tag{3.80}$$

Note that it is the equivalent Josephson energies $(\bar{E}_J, \bar{E}_W)$ that appear and not the bare ones (E_J, E_W). The corresponding Hamiltonian reads

$$\hat{H}_{4^{\rm th}}/\hbar = -\frac{\chi_{\rm m,m}}{2}\hat{a}^{\dagger 2}\hat{a}^2 - \frac{\chi_{\rm b,b}}{2}\hat{b}^{\dagger 2}\hat{b}^2 - \chi_{\rm m,b}(\hat{a}^\dagger\hat{a})(\hat{b}^\dagger\hat{b}).$$

3.6 CHAPTER SUMMARY

This chapter introduced the notion of bosonic codes, taking advantage of the infinite-dimensional Hilbert space of a harmonic oscillator to store and protect the logical information. We presented the notion of the Wigner function as both a tool to graphically represent the memory state, and gain intuition on the impact of errors as being local deformations of the memory phase space. Taking advantage of the states' Wigner function symmetries, different quantum error-correcting codes can be envisioned, each protecting against different types of errors. Amongst these codes, the cat code emerges as particularly appealing due to its ability to exponentially suppress an error channel. Several experiments already demonstrated the stabilization of a cat qubit, using measurement-based feedback [104], Hamiltonian engineering [141, 99, 166], or dissipation engineering [117, 101, 102, 157, 158]. In this thesis, we introduce a new design to stabilize cat qubits through dissipation engineering, using a 3-wave interaction to mediate the interaction between memory and buffer. This design should yield increased 2-to-1 photon coupling compared to previous experimental implementations, allowing for improved gate fidelities and making the cat qubit robust to larger error channels. Chap. 4 presents the experiential realization of the *Auto-cat* and the obtained evolution of bit-flip time and phase-flip rate, with Chap.5 focusing on the coherent manipulation of this qubit.

Part II

STABILIZATION AND CONTROL OF A CAT QUBIT USING THE AUTO-CAT DESIGN

4

STABILIZATION AND MEASUREMENT OF CAT STATES

The coupling element introduced in Sec. 3.5.3 was realized using superconducting circuits, with added stubs used to tune the modes zero point fluctuations φ_{ZPF} and lower the buffer mode frequency. A single input line couples to the circuit in order to provide both fast flux bias and drive the buffer mode. Additionally, a transmon qubit is inductively coupled to the memory with $\chi_{\mathrm{q,m}}/2\pi = 170$ kHz to perform the Wigner tomography of the memory mode [173, 174, 175].

This chapter details the experimental implementation of this device, with a particular focus on the design of the input line that leverages circuit symmetries to achieve a strong coupling with the buffer mode while preserving the quality factor of the memory. The corresponding microwave simulations were realized by Antoine Essig from the company Alice & Bob. We then characterize the circuit parameters and find the quantum error correction flux ϕ_{QEC} by studying the evolution of ω_b and ω_m with the external flux. After detailing the method used to measure Wigner functions using a second *tomography flux* denoted as ϕ_{tomo}, we estimate the obtained two-photon dissipation rate κ_2 using the relaxation of cat qubits towards the manifold $\mathrm{span}\left(|0\rangle, |1\rangle\right)$ at ϕ_{QEC}. The obtained ratio $\kappa_2/\kappa_1 \approx 150$ is the highest value obtained so far and proves useful in order to improve on the existing Wigner measurement method. Finally, we present the evolution of bit-flip time T_{X} and phase-flip rate Γ_{Z} with the memory photon number $|\alpha|^2$. The phase-flip rate exhibits the expected linear increase at a rate of $2\kappa_1$, whereas T_{X} increases exponentially until reaching 0.3 s. We explain this saturation by the transmon higher excited states getting populated, which was observed experimentally.

Remark: The main results presented in this chapter can be found in [176].

4.1 EXPERIMENTAL IMPLEMENTATION OF THE AUTO-CAT

4.1.1 *Design of the input line*

From the simplified circuit presented in Fig. 3.14, open and shorted stubs are added to lower the buffer mode frequency (Fig. 4.1**a.**), while preserving the symmetry (respectively anti-symmetry) of the memory mode (respectively buffer mode) with respect to the circuit symmetry axis (blue in Fig. 4.1**b.**). A transmon with its dedicated readout resonator is then added to perform the tomography of the memory mode. Additionally, a single input line (red in Fig. 4.1**b.**) is used to both set the flux ϕ_{ext} threading the coupling element and apply the classical drive

$$\hat{H}_d = \epsilon_d \hat{b}^\dagger + \epsilon_d^* \hat{b} \tag{4.1}$$

of Eq. (3.65). However, designing this input line to preferably couple to the buffer mode while preserving the memory quality factor proves challenging. This is notably due to the frequency tunability of the circuit which makes it difficult to engineer a filter that protects the memory lifetime. Instead, we leverage the symmetries of the circuit (Fig. 4.1**a.**) so that two propagating modes of the input line have opposite coupling to the memory mode, effectively canceling the leakage of the memory through this line.

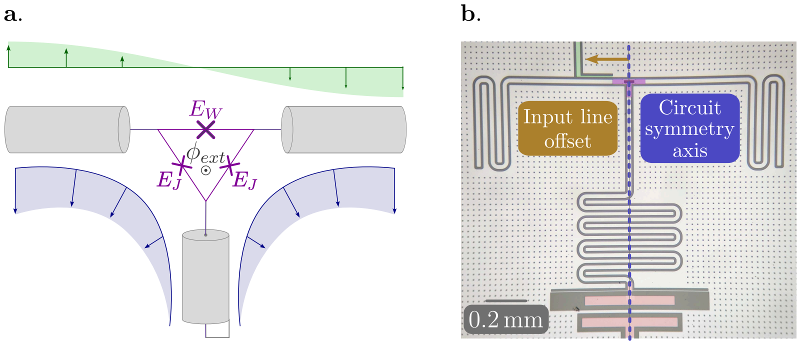

Figure 4.1: **a.** Scheme of the autoparametric cat. The three-wave mixing coupler is a ring of three Josephson junctions threaded by a flux $\phi_{\text{ext}} = \varphi_{\text{ext}}\varphi_0$, with $\varphi_0 = \hbar/2e$, Josephson energies $E_W/h \approx 115$ GHz and $E_J/h \approx 250$ GHz. The buffer (green) and memory (blue) mode geometries are represented as field vectors. **b.** Optical image of the device. False colors highlight the input buffer/flux line (green), the tomography transmon and coupling capacitor to its readout resonator (red) as well as the three-wave mixing coupler (purple) (see Appendix. b). The device symmetry axis is highlighted in blue and the offset of the input line with respect to the symmetry axis in orange.

A first design for the input line design that can benefit from these symmetries is a slot-line made of a gap separating two ground planes [177]. This transmission line has a single propagating mode, which is anti-symmetric since opposed currents flow in the two ground planes. When the slot line is aligned with the circuit symmetry axis, only the buffer mode is coupled to the transmission line while the memory mode is protected by symmetry. However, if this input line design is optimal from a point of view of memory filtering, it is not compatible with fast flux bias as it cannot bring a DC current close to the Josephson junction loop.

In contrast, a co-planar waveguide (CPW) transmission line contains a center track so that it can be used for fast flux biasing the loop. A CPW transmission line contains two quasi-transverse electromagnetic propagating modes [178]. One is symmetric with respect to the transmission line axis with identical currents in the ground planes but an opposite one in the central line. We call it the co-planar waveguide mode. The other is anti-symmetric with respect to the transmission line axis with opposing currents in the two ground planes and no current in the central line. We call it the slot line mode. Importantly, the slot line mode is suppressed by increasing the density of wirebonds that connect the two ground planes.

When the CPW transmission line is aligned on the circuit symmetry axis, the buffer (respectively memory) mode is only coupled to the slot-line mode (respectively co-planar waveguide mode) by symmetry. To reduce the memory coupling rate, an offset is introduced between the CPW transmission line and the circuit symmetry axis (orange arrow in Fig. 4.1**b.**). The buffer mode stays dominantly coupled to the slot-line mode whereas the memory mode now couples to both slot-line and co-planar waveguide modes. This can be seen in the electromagnetic simulations of Fig. 4.2 by looking at the currents of the memory mode around the input line. The memory mode coupling to the co-planar waveguide (respectively slot-line) mode decreases (respectively increases) with the shift length, which is observed in the dominant geometry of the memory currents around the input line (see Fig. 4.2).

The memory coupling rate to the transmission line is then given by the sum of the coupling rates to the co-planar waveguide and slot-line modes and can be simulated. Fig. 4.3**a.** shows the variation of the simulated memory coupling quality factor Q as a function of the input line offset for different positions of the first wirebond. While the wirebond position has only a minimal impact, two optimal offsets can be observed (a positive one $l_+ = 425\ \mu$m and a negative one $l_- = -175\ \mu$m for the chosen wirebond distance of 600 μm) for which the total coupling rate to the slot-line and co-planar waveguide modes is minimized leading to an enhanced Q factor of the memory. If the l_+ offset leads to a slightly higher memory Q factor, it is however not compatible with fast flux bias as the mutual inductance is too small. On the contrary, the l_- offset has a large enough mutual inductance (about 2 pH) for fast

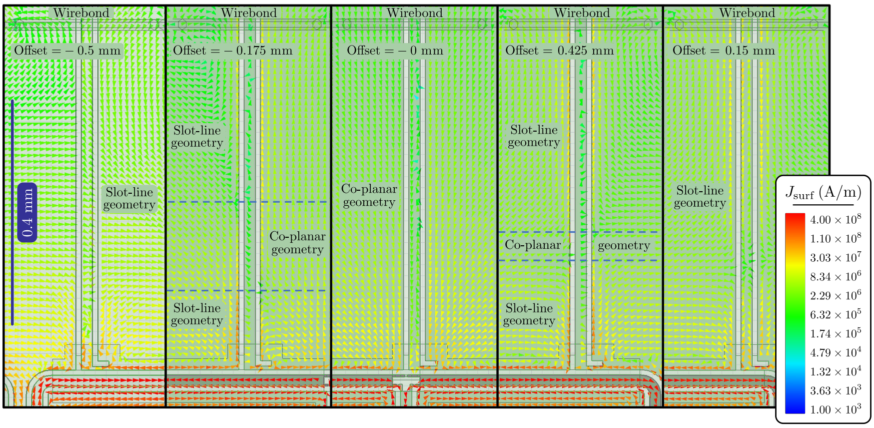

Figure 4.2: Electromagnetic simulations (using Ansys HFSS) of the current field of the memory mode around the input line for various offsets of the input line with respect to the circuit symmetry axis. Colors indicate surface currents according to the legend. For large offsets (-500 μm and 500 μm), the current field is characteristic of a slot-line geometry (opposite current in the two ground planes) indicating that the memory is mostly coupled to the slot-line propagating mode. For zero offset, the current field is characteristic of a co-planar geometry (identical current on the two ground planes and opposite current in the central track) indicating that the memory is mostly coupled to the co-planar waveguide propagating mode. For the two optimal offsets (-175 μm and 425 μm) leading to the highest memory coupling quality factor, the current field is a mix of slot-line and co-planar geometries.

flux bias. Besides, when choosing the buffer quality factor by tuning the distance d_w between the circuit and the first wirebond (Fig. 4.3**b.**), the l_+ offset increases with d_w whereas l_- is almost constant. Thus, using the offset l_-, one can improve the memory quality factor while preserving the buffer quality factor tunability with wirebond position and a mutual inductance compatible with fast flux bias.

4.1.2 *Flux dependence of ω_m and ω_b*

In order to calibrate the value of ϕ_{QEC} at which the frequency matching condition $\omega_b = 2\omega_m$ is verified, we perform a spectroscopy of the buffer and memory mode for various values of the external flux ϕ_{ext}. Besides, fitting the dependencies $\omega_b\left(\phi_{\text{ext}}\right)$ and $2\omega_m\left(\phi_{\text{ext}}\right)$ gives access to the device parameters using the model of Sec. 3.5.4.

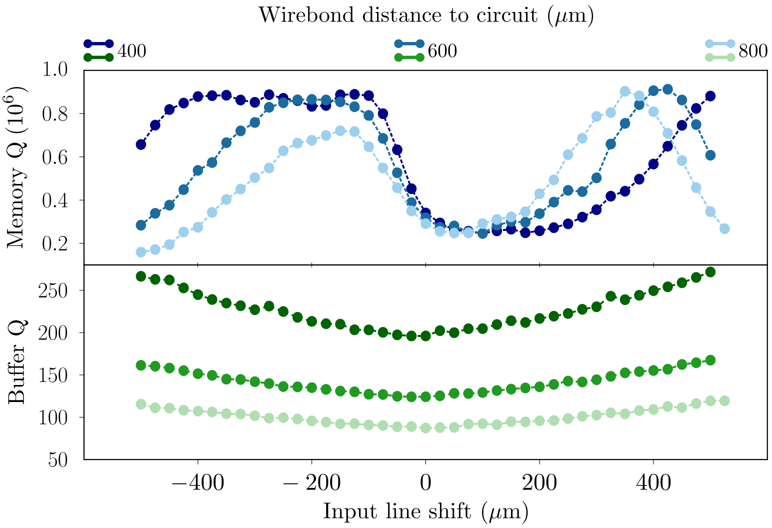

Figure 4.3: Simulated memory (**a.**) and buffer (**b.**) quality factors (Q) as a function of the input line offset with respect to circuit symmetry axis for various distances d_w between the circuit and the first wirebond. Choosing the distance at which the first wirebond is bonded enables tuning the buffer quality factor. If the positive optimal input line offset depends strongly on the first wirebond position, it is not the case for the negative optimal input line offset.

To measure the buffer frequency at a specific flux ϕ_{ext}, we applied a simultaneous DC and RF pulse through the input line of the device, as illustrated in Fig.4.4**a**. Both signals are square pulses, with the DC drive setting the external flux, while the RF pulse frequency ω_d was varied in the range of 7 to 8.3GHz. By measuring the reflection coefficient of the RF pulse $r(\omega_d)$ and fitting its dependence on ω_d for each value of ϕ_{ext} (Fig.4.4**b.**), we were able to reconstruct $\omega_b(\phi_{\text{ext}})$. Note that the function used for fitting $r(\omega_d)$ strongly depends on the detuning between the memory and buffer, $|\omega_b - 2\omega_m|$, as explained in Appendix. d.

The memory spectroscopy is performed using the readout transmon, galvanically coupled to the memory with a cross-Kerr rate of $\chi_{\text{q,m}}/2\pi =$ 170 kHz. While a DC drive sets the desired external flux ϕ_{ext}, a pulse at varying frequency ω_d is applied to the memory. This leads to a displacement $\hat{D}(\beta)$ of the memory if the drive is resonant with the memory frequency, $\omega_d = \omega_m(\phi_{\text{ext}})$, otherwise leaving it in its vacuum state. A selective π pulse is then applied to the transmon, which excites the qubit to its 1^{st} excited state $|e\rangle$ if the memory remained in its vacuum state, leaving it in $|g\rangle$ if the memory displacement was ineffective (Fig. 4.4**c.**). The transmon is then measured using the readout resonator with the dispersive readout scheme discussed in Sec. 3.1.3.2. This pulse sequence effectively amounts to asking the circuit " Is the drive frequency ω_d resonant with the memory frequency ω_m? ", encoding the answer into the transmon population. By finding the drive frequency that leaves the transmon in its ground state $|g\rangle$ for each external flux, we could ω_m as a function of ϕ_{ext}.

The measured $\omega_b\left(\phi_{\text{ext}}\right)$ and $2\omega_m\left(\phi_{\text{ext}}\right)$ are represented in Fig. 4.4**d.**, with the frequency matching being verified at $\phi_{\text{QEC}} = 0.312\phi_0$ at which $\omega_b\left(\phi_{\text{QEC}}\right) = 2\omega_m\left(\phi_{\text{QEC}}\right) \approx 2\pi \times 7.896$ GHz. The sample parameters slightly deviate from what was simulated, notably evident from the difference between ϕ_{QEC} and $\phi_{\text{ext}}^{(\text{sweet})}$ which were designed to coincide. These deviations can in particular be attributed to fabrication issues. Additionally, we introduce a third flux $\phi_{\text{tomo}} = 0.168\phi_0$, which was used for the Wigner tomography of the cat qubit (see Sec. 4.2.2 for further details)

4.1.3 *Summary of the device parameters*

Using the dependence of the buffer and memory frequencies with the external flux, several parameters of the device can be estimated by employing the theoretical model introduced in Sec. 3.5.4. Note that the added stubs used to tune the modes φ_{ZPF} were added to the theory in order to best reproduce the experimental results in Fig. 4.4**d**. A summary of the device parameters is provided in Table. 4.1, along with the corresponding measurement or estimation method employed for each parameter.

4.2 MEASURING THE WIGNER FUNCTION OF A CAT QUBIT

Having characterized the device parameters and identified the flux ϕ_{QEC} where the frequency matching condition is verified, the preparation of a cat state is quite straightforward. Starting from the vacuum state in the memory at ϕ_{QEC}, we simply turn on a drive with an amplitude $|\epsilon_d| = |\alpha|^2 g_2$ (Fig. 3.13**b.**) at twice the memory frequency $\omega_d = 2\omega_m$ for a time of ≈ 300 ns. The effective dissipation acting on the memory during that time

$$\hat{L}_2 = \sqrt{\kappa_2}\left(\hat{a}^2 - \alpha^2\right) \tag{4.2}$$

stabilizes the cat qubit manifold $\text{span}\left(|\alpha\rangle, |-\alpha\rangle\right)$, and the memory evolves towards $|C_+^\alpha\rangle \propto |\alpha\rangle + |-\alpha\rangle$, the state in the cat manifold with the same parity as the initial vacuum state. Indeed, the memory parity is preserved

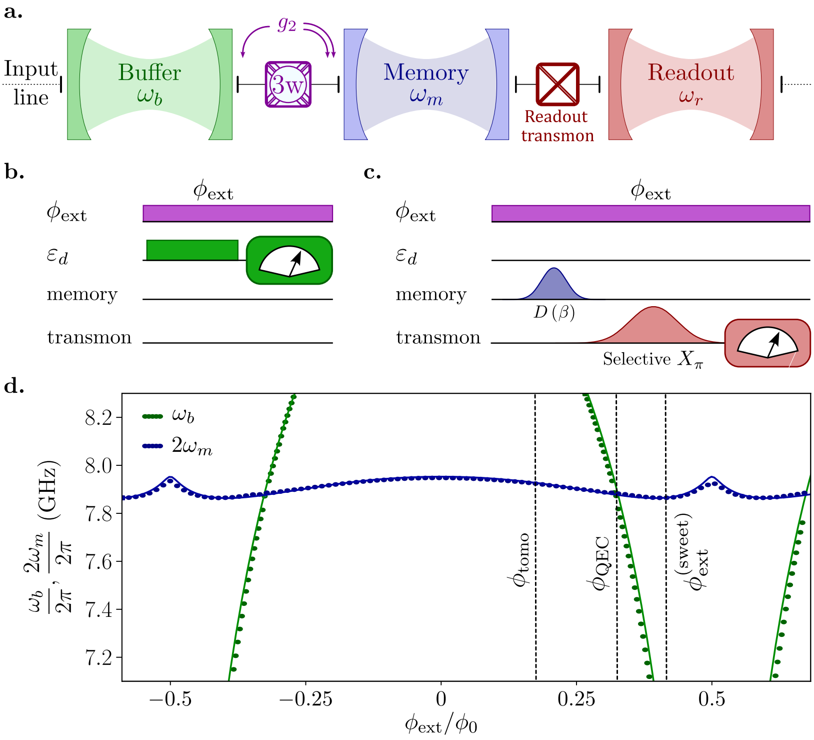

Figure 4.4: **a.** Schematic of the complete device. The autoparametric coupler mediates the 2-to-1 photon interaction between the memory and buffer at a rate g_2. On the buffer side, the input line is used to set ϕ_{ext} and drive the buffer mode with drive amplitude ϵ_d. Finally, a tomography transmon is galvanically coupled to the memory and can be read out using a readout resonator at ω_r **b.** Pulse sequence used to perform the spectroscopy of the buffer at a flux ϕ_{ext} **c.** Pulse sequence used to perform the spectroscopy of the memory at a flux ϕ_{ext} **d.** Dots: measured resonance frequency of the buffer ω_b (green) and twice the measured resonance frequency of the memory $2\omega_m$ (blue) as a function of the flux threading the ring. Dashed lines indicate the flux biases where the circuit is operated. Solid lines: Best fit of the circuit parameters (see Sec. 3.5.4).

during this process as it only exchanges pairs of photons with its environment. The time of ≈ 300 ns is chosen to be shorter than the characteristic time $1/|\alpha|^2\kappa_1$ of a photon loss, yet long enough for the two-photon dissipation and drive to stabilize the memory into the cat qubit manifold.

Table 4.1: **Estimated parameters of the device.**

Parameter	**Value**	**Method of determination**
Quantum Error Correction flux ϕ_{QEC}	$0.312\ \phi_0$	Memory and buffer spectroscopy
Tomography flux ϕ_{tomo}	$0.168\ \phi_0$	Optimization of the memory displacements $\hat{\mathcal{D}}\left(\beta\right)$
Sweet spot $\phi_{\mathrm{ext}}^{(\mathrm{sweet})}$	$0.4\ \phi_0$	Memory and buffer spectroscopy
Memory frequency $\omega_m\left(\phi_{\mathrm{QEC}}\right)/2\pi$	3.948 GHz	Memory and buffer spectroscopy
Buffer frequency $\omega_b\left(\phi_{\mathrm{QEC}}\right)/2\pi$	7.896 GHz	Memory and buffer spectroscopy
Transmon frequency $\omega_{\mathrm{q}}/2\pi$	5.387 GHz	Ramsey interferometry at ϕ_{tomo}
Readout resonator frequency $\omega_{\mathrm{r}}/2\pi$	6.967 GHz	Reflection measurement, Fig. 3.4**a.**
Effective inductive energy $\bar{E}_J\left(\phi_{\mathrm{QEC}}\right)/\hbar$	228 GHz	Memory and buffer spectroscopy
Effective inductive energy $\bar{E}_W\left(\phi_{\mathrm{QEC}}\right)/\hbar$	51 GHz	Memory and buffer spectroscopy
Effective inductive energy $\bar{E}_J\left(\phi_{\mathrm{tomo}}\right)/\hbar$	242 GHz	Memory and buffer spectroscopy
Effective inductive energy $\bar{E}_W\left(\phi_{\mathrm{tomo}}\right)/\hbar$	97 GHz	Memory and buffer spectroscopy
Memory participation ratio $\varphi_{\mathrm{ZPF},m}$	0.0305	Memory and buffer spectroscopy
Buffer participation ratio $\varphi_{\mathrm{ZPF},b}$	0.0648	Memory and buffer spectroscopy
Predicted two-to-one coupling rate $g_2/2\pi$	6.2 MHz	Memory and buffer spectroscopy
Memory self-Kerr $\chi_{\mathrm{m,m}}$	0.220 MHz	Coherent state deformation, Fig. 3.8
Buffer self-Kerr $\chi_{\mathrm{b,b}}$	10 MHz	Estimated using Eq. (3.80)
Transmon to memory cross-Kerr $\chi_{\mathrm{q,m}}$	0.170 MHz	Ramsey interferometry with a displaced cavity, Fig. 4.8**a.**
Buffer to memory cross-Kerr $\chi_{\mathrm{b,m}}$	1.6 MHz	Estimated using Eq. (3.80)
Transmon to readout cross-Kerr $\chi_{\mathrm{q,r}}$	3.5 MHz	Reflection measurement, Fig. 3.4**a.**
Two-to-one coupling rate $g_2/2\pi$	6 ± 0.5 MHz	Fidelity of logical $\hat{Z}$ rotations, Fig. 5.4
Memory single photon loss $\kappa_1/2\pi$	14 kHz	Decay $\vert 1\rangle \rightarrow \vert 0\rangle$, Fig. 4.11**b.**
Memory effective 2 photons loss $\kappa_2/2\pi$	2.16 MHz	Decay $\left\vert \mathcal{C}_\alpha^+\right\rangle \rightarrow \vert 0\rangle$ or $\left\vert \mathcal{C}_\alpha^-\right\rangle \rightarrow \vert 1\rangle$, Fig. 4.9**b.**
Memory dephasing rate $\kappa_\varphi^m/2\pi$	0.08 MHz	Ramsey interferometry Zeno blocked on the manifold $\mathrm{span}\left(\vert 0\rangle, \vert 1\rangle\right)$
Buffer single photon loss $\kappa_b/2\pi$	40 MHz	Reflection measurement, Fig.d.2
Readout resonator linewidth $\kappa_r/2\pi$	1.8MHz	Reflection measurement, Fig. 3.4**a.**
Transmon T_1	18 μs	Standard decay measurement
Transmon T_2	15 μs	Ramsey interferometry
Memory thermal population $n_{\mathrm{th,m}}$	0.011 photon	Ramsey interferometry
Transmon thermal population $n_{\mathrm{th,q}}$	0.015 photon	Standard transmon readout

While this preparation is extremely simple, using a single tone to stabilize a cat qubit, measuring the Wigner function of this state cannot be performed at ϕ_{QEC} due to the strong two-photon dissipation. To circumvent this issue, we define an alternative flux ϕ_{tomo} at which the two-photon dissipation is no longer active. The fast flux line is then used to quickly switch from ϕ_{QEC}, where the cat states are prepared, to ϕ_{tomo} where they are measured. This is detailed in Sec. 4.2.2.

This section introduces the standard protocol used to measure the Wigner function of the memory, using the dissipatively coupled transmon, and how it can be improved using the fast flux line to measure cat qubits at ϕ_{tomo}. After presenting how the phase of a cat state can be stabilized over time using our measurement protocol, we present 3 methods used to calibrate the memory displacement amplitudes.

4.2.1 *Standard measurement of the Wigner function*

To have an intuition on how to measure the memory Wigner function, we use an alternative definition from that provided in Sec. 3.2

$$W(\beta) = \frac{2}{\pi} \left\langle \hat{\mathcal{D}}(\beta)^{\dagger} \hat{\rho} \hat{\mathcal{D}}(\beta) e^{i\pi \hat{a}^{\dagger}\hat{a}} \right\rangle, \tag{4.3}$$

with $\hat{\rho}$ the memory density matrix and $\hat{\mathcal{P}} = e^{i\pi\hat{a}^{\dagger}\hat{a}}$ the parity operator. The equivalence between this expression and Eq. (3.28) is demonstrated in the Appendix of [40]. This expression gives a direct interpretation of the Wigner function as the expectation value of the memory photon number parity, after a displacement by an amplitude $-\beta$. To measure the value of the Wigner function at a point β, we use the technique first introduced in 1997 by Lutterbach and Davidovich [179], first implemented in the context of cavity QED in 2002 [174] and in circuit QED in 2013 [175]. This method exactly follows the physical intuition given by Eq. 4.3 by first displacing the memory before using a dispersively coupled qubit to measure its parity. We present alternative parity measurements protocol in Sec. 4.3.3.

The displacement $\hat{D}(-\beta)$ is realized by driving the memory at the frequency ω_m for 20 ns. The relatively short pulse duration ensures that the memory self-Kerr effect does not have time to deform the memory state, and that the pulse is effective irrespective of the memory photon number. The transmon is then prepared in an equal superposition of ground and excited states by applying an unconditional $\pi/2$ pulse, after which the system is left idle for a duration $T_{\mathrm{parity}} = \pi/\chi_{\mathrm{q,m}} \approx 2.8\ \mu$s. During this idle time, the superposition accumulates a relative phase dependent on the number of photons

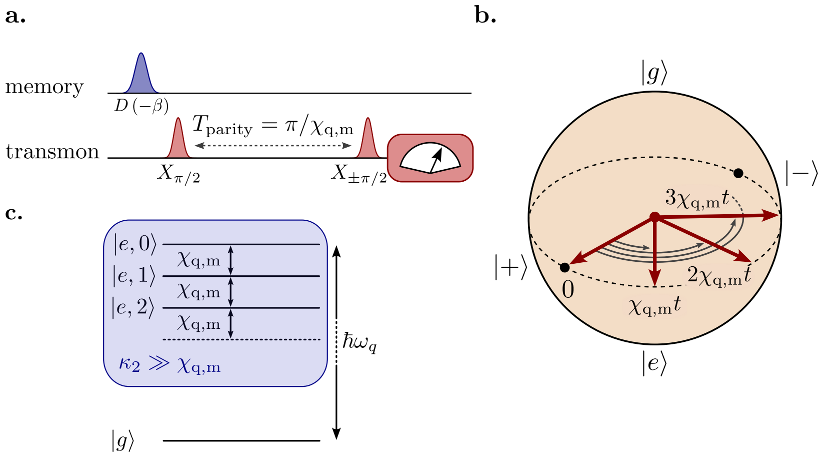

Figure 4.5: **a.** Pulse sequence used to measure the Wigner function of the memory through a dispersively coupled qubit. **b.** Illustration of the qubit evolution during the idle time between the two $\pi/2$ pulses. Starting from the superposition $|+\rangle = (|g\rangle + |e\rangle)\sqrt{2}$, a relative phase $n\chi_{\text{q,m}}t$ is accumulated after a time t, with n the memory photon number **c.** Energy levels of the transmon qubit, dispersively coupled to the memory. The energy of the transmon first excited state $|e\rangle$ depends on the memory photon number, with a separation of $\chi_{\text{q,m}}$. When the two-photon dissipation $\hat{L}_2 = \sqrt{\kappa_2}\hat{a}^2$ is activated, the energy levels are broaden by κ_2 and overlap in the regime $\kappa_2 \gg \chi_{\text{q,m}}$.

n inside the memory (Fig. 4.5**b.**). This phase accumulation stems from the qubit frequency which depends on the memory photon number as $\omega_q - n\chi_{\text{q,m}}$, with ω_q the bare qubit frequency. After a time $T_{\text{parity}} = \pi/\chi_{\text{q,m}} \approx 2.8\ \mu\text{s}$, even and odd numbers of photons are respectively mapped onto the $|+\rangle$ and $|-\rangle$ states of the transmon. An unconditional $\pm\pi/2$ pulse is then applied to the transmon, mapping the memory parity into the population of its ground and excited states, and the transmon is finally readout using the readout cavity [174, 40]. The signals corresponding to a positive and negative final $\pi/2$ pulses are subtracted to obtain $W\,(\beta)$. Note that this subtraction is theoretically unnecessary as this measurement could be performed using successive $\pi/2$ pulses only. However, doing so allows to remove unwanted offsets that could originate from the experimental setup.

4.2.2 *Using the fast flux line*

This measurement protocol would be ineffective at ϕ_{QEC} due to the strong two-photon dissipation. Indeed, the engineered dissipation mechanism that stabilizes the manifold span $(|\alpha\rangle, |-\alpha\rangle)$ impedes proper displacements $\hat{D}(-\beta)$, the very first step of the pulse sequence shown in Fig. 4.5**a**. Furthermore, it would also render impossible the parity measurement using the transmon qubit by inhibiting the dissipative coupling. As this dissipation broadens the memory energy levels by κ_2, the qubit energy levels all overlap in the regime $\kappa_2 \gg \chi_{\mathrm{q,m}}$ (Fig. 4.5**c.**) reached in this experiment. Ultimately, this prevents the qubit from having the desired dynamics during the idle step of the protocol.

To overcome these challenges, the Wigner tomography is performed at ϕ_{tomo} where $|\omega_{b,\mathrm{tomo}} - 2\omega_{m,\mathrm{tomo}}| > 1$ GHz. At this flux, two-photon dissipation is inactive due to the 2-photon exchange Hamiltonian not being preserved in the rotating wave approximation, enabling the usual Wigner tomography. To rapidly switch between ϕ_{QEC} and ϕ_{tomo}, we make use of the fast flux line that sets the desired magnetic flux in approximately 20 ns.

While the memory dynamics at $\phi_{\mathrm{tomo}}$is primarily dominated by the self-Kerr rate $\chi_{m,m}/2\pi \approx 220$ kHz, which only marginally affects the state during the 20 ns it takes to switch the flux, it is crucial to keep the drive $\epsilon_d(\alpha)$ on before shifting from ϕ_{QEC} to ϕ_{tomo}. The memory dynamics at ϕ_{QEC} is indeed dominated by the 2-photon dissipation with a rate κ_2, which significantly impacts the system in 20 ns. To prevent state distortion prior to the Wigner tomography, the drive $\epsilon_d(\alpha)$ is thus maintained during the flux change. This drive at $\omega_{b,\mathrm{QEC}}$ does not affect the memory at ϕ_{tomo}, where the frequency matching condition is no longer satisfied.

4.2.3 *Phase correction of the stabilized cat*

Owing to the change in memory frequency when the flux is switched between ϕ_{QEC} and ϕ_{tomo}, a carefully designed driving sequence must be followed in order to track the reference frame of the cat qubit. We set a local oscillator at $\omega_{\mathrm{LO},m} = 2\pi \times 3.988481$ GHz and another one at twice this frequency $\omega_{\mathrm{LO},b} = 2\omega_{\mathrm{LO},m}$ (see Fig. 4.6). They are generated using 2 channels of an Anapico APUASYN20 so that their phases are locked (see Appendix. b).

The memory displacement pulse applied for Wigner tomography at the flux ϕ_{tomo} is generated by mixing the local oscillator at $\omega_{\mathrm{LO},m}$ with a pulse generated by the AWG at exactly $\omega_{\mathrm{IF},m,\mathrm{tomo}}/2\pi = 40$ MHz. In contrast, at the flux ϕ_{QEC}, the cat qubit is stabilized with a buffer drive at a frequency

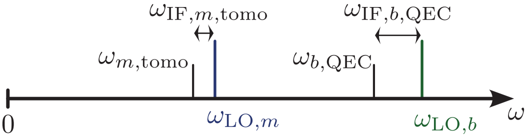

Figure 4.6: Repartition of the frequencies of local oscillators generated by the APUASYN20 synthesizer, intermediate frequencies generated by the OPX DACs, and resonance frequencies of the device.

$\omega_{b,\mathrm{QEC}} = 2\omega_{m,\mathrm{QEC}}$ that is not given by $2(\omega_{\mathrm{LO},m} - \omega_{\mathrm{IF},m,\mathrm{tomo}})$ owing to the frequency change of the memory between the two flux working points. The drive at $\omega_{m,\mathrm{QEC}}$ is in fact generated by mixing the local oscillator at $2\omega_{\mathrm{LO},m}$ with a pulse generated by the AWG at $\omega_{\mathrm{IF},b,\mathrm{QEC}} = 2(\omega_{\mathrm{LO},m} - \omega_{m,\mathrm{QEC}}) \approx 2\pi \times 120$ MHz.

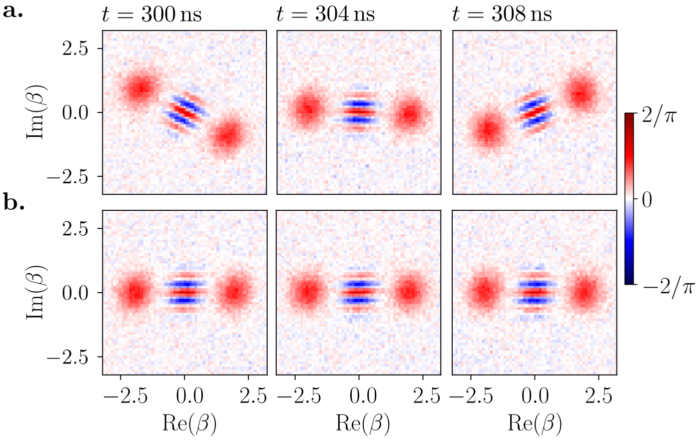

Figure 4.7: Wigner Tomography of the cat state $|C_\alpha^+\rangle$ with $\alpha = 2$ for 3 stabilization times: 300, 304 and 308 ns. **a.** Evolution of the cat state when no phase compensation is applied. **b.** Evolution of the cat when the accumulated phase between the 2 local oscillators is taken into account before memory displacement.

Owing to the detuning of about 20 MHz between $\omega_{\mathrm{IF},b,\mathrm{QEC}}/2$ and $\omega_{\mathrm{IF},m,\mathrm{tomo}}$, the stabilized coherent states $|\pm\alpha\rangle$ of the cat qubit are offset by a time increasing phase in the frame of the displacement pulses used for Wigner tomography. When trying to perform the desired displacement $\hat{D}(-\beta) = \hat{D}(-|\beta|e^{i\theta})$ for the Wigner tomography, this accumulated phase induces a displacement with an angle

$$\theta_{\text{offset}}(t) = \theta + (\omega_{\text{IF},b,\text{QEC}}/2 - \omega_{\text{IF},m,\text{tomo}})\,t,$$

where t is the time spent at ϕ_{QEC}. This can be seen as cat states whose orientation in phase-space changes over time (Fig. 4.7**a.**). Taking this phase offset into account, we compensate the accumulated phase directly on the AWG to keep the orientation of the cat qubit states constant in phase space when reconstructing their Wigner Tomography (Fig. 4.7**a.**). This is of particular interest for the measurement of T_{X} where we need to measure the evolution of $W(\pm\alpha)$, which can then be done by measuring only 2 points of the Wigner function, greatly speeding up this already time-consuming measurement.

4.2.4 *Calibration of the memory displacements*

The displacements $\hat{D}(-\beta)$ applied on the memory during Wigner tomography are performed by applying a drive at frequency $\omega_{\text{m, tomo}}$. We calibrate how the displacement amplitudes β depend on the voltage amplitude V_d at the level of the DAC by 3 methods (Fig. 4.8). We then verify how good is the match between the proportionality factor $\mu = \mathrm{d}\beta/\mathrm{d}V_d$ they provide.

4.2.4.1 *Ramsey interferometry*

The first calibration method relies on a Ramsey sequence [180, 181]. Starting from the memory in its vacuum state, a drive of amplitude V_d is applied to displace the memory to a coherent state $|\beta\rangle$. Accounting for the residual thermal occupation of the memory mode, the mean number of photons is $\bar{n} = \beta^2 + n_{\text{th}}$. The dispersively coupled qubit is then prepared in an equal superposition of ground and excited states by applying an unconditional $\pi/2$ pulse. After a varying time t, the superposition accumulates a phase $\chi_{\text{q,m}} \langle \hat{a}^\dagger \hat{a} \rangle t$ that depends on the memory photon number $\langle \hat{a}^\dagger \hat{a} \rangle$. A second unconditional $\pm\pi/2$ pulse is applied on the qubit, which is then measured to give 2 average signals $S_\pm$. The signal $s(t)$ is defined as the difference between these two 2 signals

$$s(t) = S_+ - S_-. \tag{4.4}$$

We first estimate the thermal population in the memory n_{th} from the evolution of the signal when no displacement is applied, i.e. $V_d = 0$ mV. The memory density matrix can then be written as a Boltzmann distribution

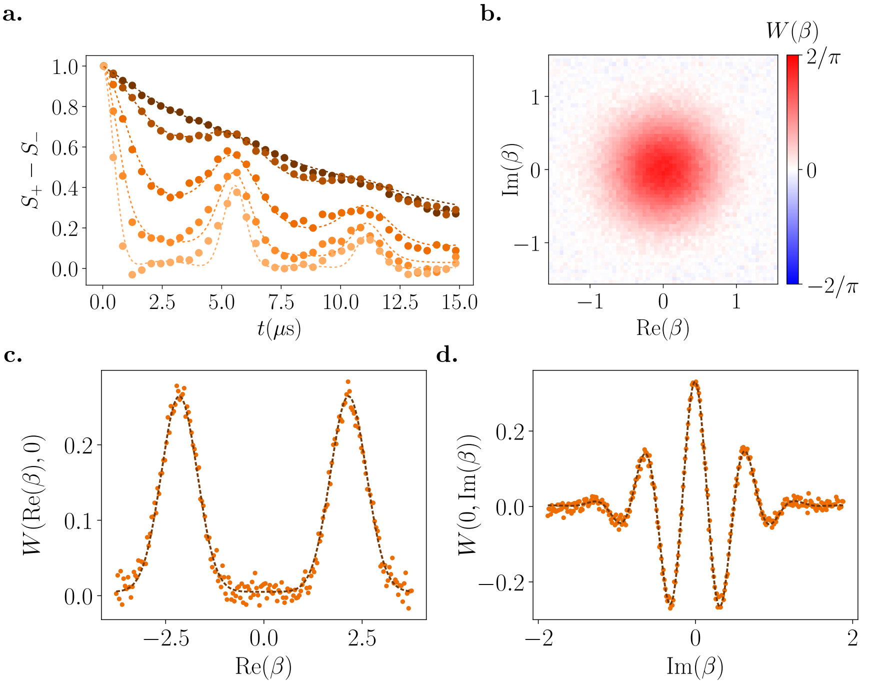

Figure 4.8: **a.** Ramsey interferometry. Dots: measured signal $S_+ - S_-$ between 2 Ramsey-like experiments for various voltages $V_d = 0, 10, 20, 30, 40,$ mV from top to bottom. Lines: Fit of the measurements to Eq. (4.8) leading to a photon number $\bar{n} = 0.011, 0.10, 0.35, 0.81, 1.45$. The residual thermal population is thus $n_{\text{th}} = 0.01$. **b.** Measured Wigner function of the memory in thermal equilibrium with its environment. The conversion used between V_d and $|\beta|$ to plot it is made by a Gaussian fit of the measurement with the Wigner function of a thermal state with $n_{\text{th}} = 0.011 \pm 0.002$ photons on average. **c.** Dots: Cuts of the Wigner tomography of a stabilized cat qubit along $\beta \in \mathbb{R}$ after 100 μs of dephasing. Line: Theoretical prediction. **d.** Same plot along $\beta \in i\mathbb{R}$, 500 ns after the buffer drive is turned on.

$$\hat{\rho}_{\text{th}} = \sum_n \frac{n_{\text{th}}^n}{(1+n_{\text{th}})^{n+1}} |n\rangle \langle n| \tag{4.5}$$

and $s(t)$ evolves as [180]

$$s(t) = e^{-t/T_2} \sum_n \frac{n_{\text{th}}^n}{(1+n_{\text{th}})^{n+1}} \cos(n\chi_{\text{q,m}} t) \tag{4.6}$$

Under the condition $n_{\text{th}} \ll 1$, Eq. (4.7) reduces to

$$s(t) = e^{-t/T_2} \left(1 + n_{\text{th}} \left(\cos(\chi_{\text{q,m}} t) - 1\right)\right). \tag{4.7}$$

We use this form to extract[1] the thermal population from Fig. 4.8**a**, yielding $n_{\text{th}} = 0.017 \pm 0.002$.

When applying a displacement $\hat{\mathcal{D}}(\beta)$ to the memory, with $|\beta|^2 \gg n_{\text{th}}$, the thermal population can be ignored and the memory state approximated to a coherent state $|\beta\rangle$. The signal then evolves as [181]

$$s(t) = \cos\left(|\beta|^2 \sin\left(\chi_{\text{q,m}} t\right)\right) e^{|\beta|^2 (\cos(\chi_{\text{q,m}} t) - 1) - t/T_2}. \tag{4.8}$$

From the measurements shown in Fig. 4.8**a**, for $V_d > 0$ mV, we can extract the cross-Kerr coupling rate $\chi_{\text{q,m}}/2\pi = 170$ kHz between memory and transmon qubit. We also obtain the dependence of $|\beta|^2$ on V_d, from which we deduce $\mu = 31.33 \pm 0.85\ \text{V}^{-1}$. Note that this calibration method is similar to the parity measurement sequence for varying idle time.

4.2.4.2 *Thermal state tomography*

Another calibration method is to perform a Wigner tomography of the memory thermal state, using the independently measured average occupation $n_{\text{th}} = 0.017$. From the expression of the memory density matrix as a Boltzmann distribution, the associated Wigner function writes

$$W_{\text{th}}(\beta) = \sum_n \frac{n_{\text{th}}^n}{(1 + n_{\text{th}})^{n+1}} W_n(\beta), \tag{4.9}$$

where $W_n(\beta) = (-1)^n \frac{2}{\pi} e^{-2|\beta|^2} L_n\left(4|\beta|^2\right)$ is the Wigner function of Fock state $|n\rangle$. Laguerre polynomials obey the following rule

$$\sum_n t^n L_n\left(4|\beta|^2\right) = \frac{1}{1-t} e^{4t|\beta|^2/(1-t)}.$$

Therefore, we obtain

---

[1] The cross-Kerr coupling rate appearing in the equation is obtained using coherent states instead of thermal states as discussed below.

$$\begin{aligned} W_{\mathrm{th}}\left(\beta\right) &= \frac{2}{\pi\left(1+n_{\mathrm{th}}\right)} e^{-2|\beta|^2} \sum_n \left(\frac{-n_{\mathrm{th}}}{1+n_{\mathrm{th}}}\right)^n L_n\left(4\left|\beta\right|^2\right) \\ &= \frac{2}{\pi\left(1+2n_{\mathrm{th}}\right)} e^{-2|\beta|^2/(1+2n_{\mathrm{th}})}. \end{aligned} \tag{4.10}$$

Using a conversion factor $\mu = 31.49 \pm 0.14$ V^{-1} rescales the displacement amplitudes from voltages V_d into complex amplitudes β for the measured Wigner function in (Fig. 4.8**b.**), in such a way that the standard deviation σ, of this Gaussian distribution is $\sigma = \sqrt{1+2n_{\mathrm{th}}}/2$, with $n_{\mathrm{th}} = 0.01$.

4.2.4.3 *Measurement of cat states fringes*

Our last method to calibrate the conversion factor is based on the Wigner tomography of a cat state [28]. The particular features of the cat Wigner function allow us to directly estimate μ, assuming the distortion due to memory self-Kerr or thermal population is negligible. The Wigner function of an even cat state of size α, $|C_\alpha^+\rangle$, can be written as

$$W_\alpha^+\left(\beta\right) = \frac{1}{\pi}\left(e^{-2|\alpha-\beta|^2} + e^{-2|\alpha+\beta|^2} + 2\cos\left(4\mathrm{Im}\left(\alpha^*\beta\right)\right)e^{-2|\beta|^2}\right). \tag{4.11}$$

Introducing δV_α and δV_{I} the drive voltages corresponding to respectively a displacement of 2α (distance between the two Gaussian distributions in Fig. 4.8**c.**) and the periodicity of the fringes $\pi/2\alpha$ (seen in Fig. 4.8**d.**), this yields

$$\begin{cases} 2\alpha = \mu\,\delta V_\alpha \\ \dfrac{\pi}{2\alpha} = \mu\,\delta V_{\mathrm{I}} \end{cases}$$

Therefore $\mu = \sqrt{\pi/\left(\delta V_\alpha \delta V_{\mathrm{I}}\right)}$. The values of δV_α and δV_{I} are measured via cuts of the Wigner function in the direction and orthogonal to the cat state (Fig. 4.8**c.**,**d.**). The conversion factor obtained via this method is $\mu = 31.41 \pm 0.04$ V^{-1}, once again compatible with the previous calibrations. With the conversion factor being calibrated, this method can actually be used in order to estimate the cat size by simply looking at the fringes periodicity, as has been done in [28].

4.2.4.4 *Calibration*

To conclude this section, the three methods are compatible with $\mu = 31.4 \pm 0.1\ \mathrm{V}^{-1}$. We use this value of $\mu = 31.4\ \mathrm{V}^{-1}$ for all measurements in the Auto-cat.

4.3 ESTIMATION OF κ_2 AND κ_1, USING THE LARGE RATIO $\kappa_2/\kappa_1 \approx 150$

Before studying the performance of the stabilized cat qubit, i.e the evolution of the bit-flip time and phase-flip rate with $|\alpha|^2$, a key figure of merit to look at is the effective two-photon dissipation rate acting on the memory. We measure this two-photon loss rate κ_2 in Sec. 4.3.1 by monitoring the memory decay once the drive $\epsilon_d(\alpha)$ has been turned off. Comparing the obtained value of $\kappa_2/2\pi \approx 2.16 \pm 0.1$ MHz at ϕ_{QEC} with κ_1, measured in Sec. 4.3.2 using the relaxation of Fock state $|1\rangle$ to vacuum, yields a ratio $\kappa_2/\kappa_1 \approx 1.5 \times 10^2$ much larger than in previous implementations of two-photon dissipation using four-wave mixing [117, 101, 102, 157]. We present in Sec. 4.3.3 how to take advantage of this large ratio to improve on the previously presented Wigner measurement protocol, and in particular better reconstruct the cat fringes.

4.3.1 *Determination of κ_2 using engineered relaxation of cat qubits*

In order to measure the rate κ_2, we first prepare $|C_\alpha^+\rangle$ or $|C_\alpha^-\rangle$ by driving the buffer with a drive $\epsilon_d(\alpha)$ at ϕ_{QEC}. Turning off $\epsilon_d(\alpha)$ while remaining at ϕ_{QEC} then ensures the memory loses pairs of photons to the environment at the rate κ_2. $|C_\alpha^\pm\rangle$ then converges to a state in the manifold $\mathrm{span}(|\alpha\rangle, |-\alpha\rangle)$ with the same parity as the initial state. An example of such an evolution starting from $|C_\alpha^+\rangle$, $\alpha = 2.5$, is shown at a few decay times in Fig. 4.9**b**. The complete list of measured decay times for this evolution is $t = 0$, 4, 8, 12, 20, 28, 40, 60, 100, 160, 240 and 320 ns.

In order to extract the rate κ_2 from these dynamics, the initial density matrix describing the memory is approximated by

$$\rho = p\,|C_\alpha^+\rangle\langle C_\alpha^+| + (1-p)\,|C_\alpha^-\rangle\langle C_\alpha^-|\,. \tag{4.12}$$

α is extracted by fitting the initial measured Wigner tomography, while p is deduced from the value of $W(0)$ which fully characterizes the parity of the state. The obtained description of the initial density matrix is however

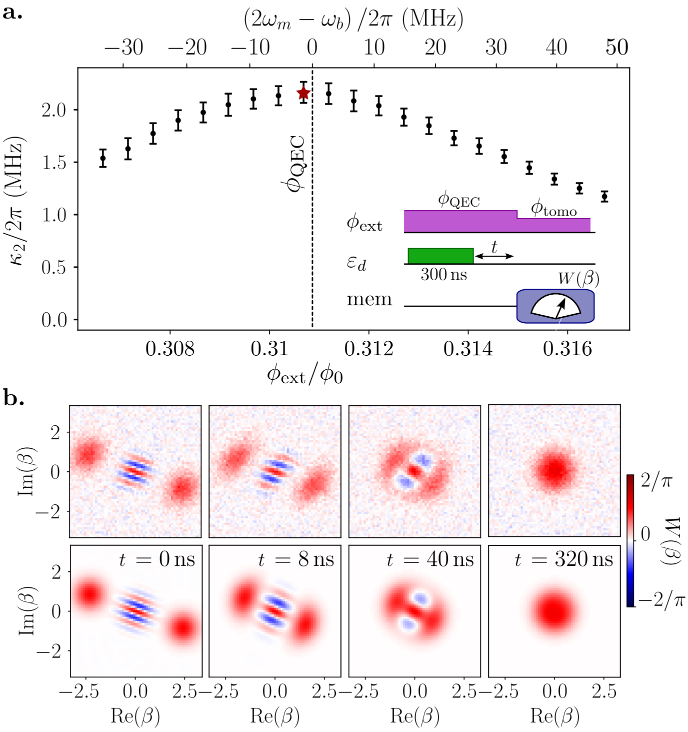

Figure 4.9: **a.** Dots: Measured two-photon relaxation rate κ_2 as a function of flux bias close to $\phi_{\rm QEC}$. Error bars represent statistical uncertainties. Inset: pulse sequence used for the measurement. The detuning between buffer frequency and twice the memory frequency is indicated on the top axis. **b.** Top: Measured Wigner functions of the memory after the decay times indicated on the figure for $|\alpha| = 2.5$ and at the flux indicated by the star in **a.**. Bottom: results of the simulation using $\kappa_2/2\pi = 2.16$ MHz.

only an approximation as it does not take into account possible leakage out of the code space due to the memory self Kerr effect, dispersive coupling to transmon and buffer modes, or potential heating effect. From this initial state, Eq. (4.12), the evolution of the memory state is then simulated using the Hamiltonian and loss operators

$$\begin{aligned} \hat{H}/\hbar &= -\frac{\chi_{\rm m,m}}{2}\hat{a}^{\dagger 2}\hat{a}^2 \\ \hat{L}_1 &= \sqrt{\kappa_1}\hat{a},\ \hat{L}_2 = \sqrt{\kappa_2}\hat{a}^2. \end{aligned} \tag{4.13}$$

The single photon loss rate $\kappa_1/2\pi \sim 14$ kHz is extracted from the decay of the single photon state $|1\rangle \to |0\rangle$ (see Sec. 4.3.2). Using the memory self-Kerr rate $\chi_{\mathrm{m,m}} = 2\pi \times 220$ kHz measured at ϕ_{tomo} (see Fig. 3.8) and its predicted flux dependence Eq. (3.80), we estimate the self-Kerr rate at ϕ_{QEC}, $\chi_{\mathrm{m,m}}/2\pi \sim 206$ kHz. Minimizing the difference between experimental and simulated Wigner functions at all times t

$$\sum_{\mathrm{t}} \int_{\mathbb{C}} \left|W_{\mathrm{exp}}\left(\beta,t\right) - W_{\mathrm{sim}}\left(\beta,t\right)\right| \mathrm{d}\beta \tag{4.14}$$

then allows us to fit the value of κ_2 that best reproduces the memory dynamics. This procedure is repeated for various flux biases around ϕ_{QEC} in Fig. 4.9**a.**, which shows the range of detuning $\omega_b - 2\omega_m$ over which the two-photon loss rate decreases.

The uncertainty shown in Fig. 4.9**a.** is then calculated using the result of the minimization method $\Delta\kappa_2 \leq \sqrt{\mathrm{tol} \times H^{-1}}$, with tol being the tolerance given for the convergence of the algorithm and H^{-1} the inverse of the Hessian matrix. It should be noted that, due to the large two-to-one photon coupling $g_2/2\pi = 6$ MHz, the condition for the adiabatic elimination of the buffer

$$8g_2\alpha < \kappa_b \tag{4.15}$$

is not verified as soon as $\alpha \gtrsim 1$. This results in a deviation between the measured Wigner functions in Fig. 4.9**b.** and the evolution predicted by the simple model of Eq. (4.13). The impact of this non-adiabacity on the cat qubit stabilization is described in Sec. 4.4.1.2. Actually, due to the breakdown of Eq. (4.15), the buffer mode gets populated during the two-photon dissipation. In turn, the memory sees an effective drive originating from this buffer population, inducing small deformations of the Wigner function. Particularly visible at 8 ns where the buffer is close to being maximally populated, this effect vanishes at 40 ns after the memory loses enough photons for the system to re-enter the adiabatic regime. This effect can be taken into account in the simulation by including the buffer dynamics without adiabatic elimination (Fig. 4.10). However this bipartite evolution does not provide an effective value of κ_2 acting on the memory mode, hence the benefit of sticking with the simpler model.

Note that we have tried other methods to estimate κ_2, in particular by extracting $\bar{n} = \langle \hat{a}^\dagger \hat{a} \rangle$ from the measured Wigner function

$$\bar{n} = \int_{\mathbb{C}} W_{\mathrm{exp}}\left(\beta\right) \beta^2 \mathrm{d}\beta - 0.5 \tag{4.16}$$

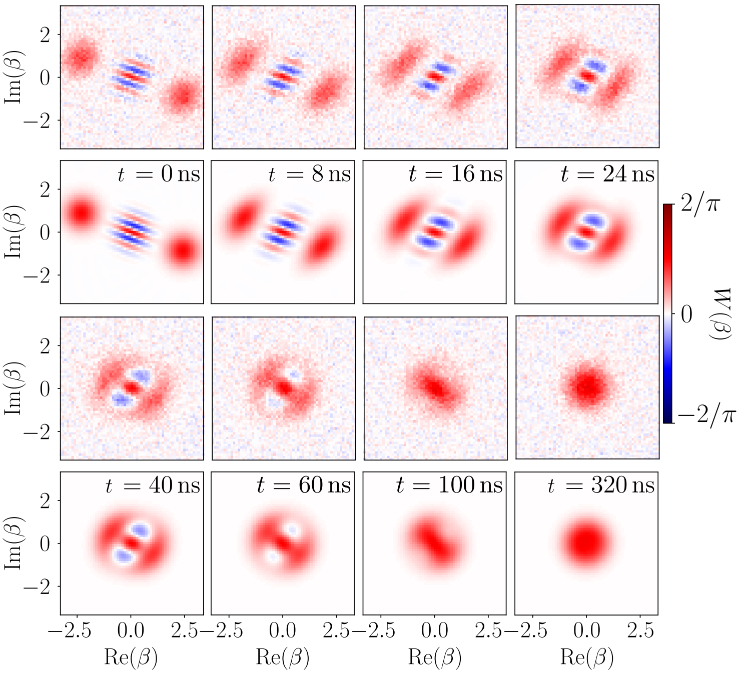

Figure 4.10: Evolution of the Wigner functions of the memory starting close to a cat state $\left|C_\alpha^+\right\rangle$ and under the effect of two-photon dissipation at ϕ_{QEC} without driving the buffer. First and third lines: measured Wigner functions at various times indicated on the figure. Second and fourth lines: simulated Wigner functions of the memory without the adiabatic elimination of the buffer, and assuming a two-photon coupling rate $g_2/2\pi = 6$ MHz (Fig. 5.4**b**).

and compare it with the theoretical expression given in [182]. However, reconstructing $\bar{n}$ with this method has proven quite challenging due to the measurement noise of the Wigner tomography, which would have made it necessary to use Maximum Likelihood Estimation (MLE) [183] in order to circumvent this issue.

4.3.2 *Determination of κ_1 using the relaxation of a single photon*

The single-photon dissipation rate κ_1 is measured by observing the decay from Fock state $|1\rangle$ to the memory vacuum. The Fock state $|1\rangle$ is prepared in the memory by first preparing the state $|C_\alpha^-\rangle$, which we then let evolve under the action of the two-photon dissipation at a rate $\kappa_2 \gg \kappa_1$ (Fig. 4.11**a.**). The parity of the memory is preserved during this process so that the memory state ends up in the subspace generated by $\{|0\rangle, |1\rangle\}$ with the same parity as $|C_\alpha^-\rangle$: that is the Fock state $|1\rangle$. In practice, we start in $0.7\,|1\rangle\langle 1| + 0.3\,|0\rangle\langle 0|$. All that is necessary to measure κ_1 is then to monitor the memory parity $\pi W(0)/2$ as it evolves towards 1, here corresponding to the vacuum state.

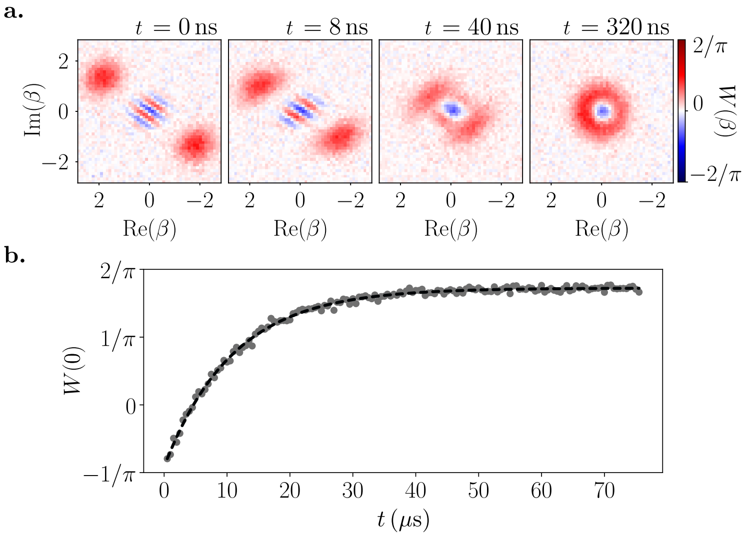

Figure 4.11: **a.** Measured Wigner functions of the memory starting close to $|C_\alpha^-\rangle$ after the decay times indicated on the figure. **b.** Dots: Measured evolution of $W(0)$ as a function of the time t spent after the memory has been prepared close to $|C_\alpha^-\rangle$. Note the much longer timescale for this single photon decay compared to the sub μs time needed to prepare Fock state $|1\rangle$ in **a**. Dashed line: Fit of the exponential relaxation to vacuum.

In order to prepare $|C_\alpha^-\rangle$, we prepare $|C_\alpha^+\rangle$ as in Fig. 4.9 and then apply a Z gate (see Sec 5.1.2). Even if the preparation and gate are not optimized, as in this measurement, the decay rate can still be extracted with excellent accuracy as it only affects the initial value of $W(0)$ during the decay from $|1\rangle$ to $|0\rangle$ (Fig. 4.11**b.**).

The evolution of $W(0)$ in Fig. 4.11**b.** is fitted by an exponential relaxation at a rate $\kappa_1/2\pi = 14$ kHz. Repeating this measurement over the course of months, we found that the rate $\kappa_1/2\pi$ typically varies by ±2 kHz around this average value. Note that $|1\rangle$ could have been prepared using the dissipatively coupled qubit, but the relatively low value of the cross-Kerr coupling $\chi_{\mathrm{q,m}}$ compared to κ_1 prevented preparing it with good fidelity.

4.3.3 *Improving on the usual parity measurement protocols*

This large ratio $\kappa_2/\kappa_1 \approx 150$ can be leveraged to improve the Wigner measurement by removing pairs of photons from the memory after the initial displacement $\hat{\mathcal{D}}(-\beta)$. This prevents several problems in the parity measurements arising from a large number of photons in the memory. In this section, we introduce 2 alternative methods to the parity measurement protocol introduced in Sec. 4.2.1, based on estimating the probability P_n for the memory to contain n photons. We then present how both these parity measurement protocols and the interferometric approach can benefit from the evacuation of pairs of photons from the memory, and how we implement it in the Auto-cat. Additionally, we discuss prospective methods (yet to be realized) that could take full benefit of this alternative approach.

4.3.3.1 *Coherent oscillations with an auxiliary qubit*

The Fock states being eigenstates of the parity operator $\hat{\Pi} = e^{i\pi \hat{a}^\dagger \hat{a}}$, with eigenvalue 1 for even Fock states and -1 for odd ones, an alternative definition of the Wigner function is given by

$$W\left(\beta\right) = \frac{2}{\pi} \sum_n \left(-1\right)^n P_n\left(\beta\right). \tag{4.17}$$

There, $P_n\left(\beta\right)$ is the probability for the memory to contain n photons after the displacement $\hat{\mathcal{D}}(-\beta)$. Physically, this formula simply says that the parity measurement can be performed by measuring the population in each Fock state.

This method of measuring the parity was first demonstrated in 2009 by Hofheinz et al. [184], using a method they introduced in 2008 [185]. The probabilities $P_n\left(\beta\right)$ are measured by coupling an auxiliary qubit to the memory, this system being described by the Jaynes-Cummings Hamiltonian

$$\hat{H}_{\mathrm{JC}}/\hbar = \omega_m \hat{a}^\dagger \hat{a} + \frac{\omega_q}{2}\sigma_z + \frac{g}{2}\left(\hat{a}\sigma_+ + \hat{a}^\dagger \sigma_-\right). \tag{4.18}$$

Bringing the qubit at resonance with the memory after the initial displacement, i.e. setting $\omega_q = \omega_m$, coherent oscillations take place between the states $|g, n\rangle$ (describing a qubit in its ground state and n photons in the memory) and $|e, n-1\rangle$ with an angular frequency $\Omega_n = \sqrt{n}g$. In the absence of decoherence and dissipation impacting the system, the probability of finding the qubit in its excited state after an interaction time τ then reads

$$P_e(\tau) = \sum_{n=1}^{\infty} P_n(\beta) \frac{1-\cos(\Omega_n \tau)}{2}. \tag{4.19}$$

P_e oscillates at a frequency $\Omega_n/2\pi$ when the memory is in a pure Fock state $|n\rangle$, with a more complex evolution when different Fock states are occupied due to the irrational ratio between the different oscillation frequencies. The probabilities $P_n(\beta)$ can be obtained from the evolution of $P_e(\tau)$ using a Fourier transform, owing to the functions $\{\cos(\Omega_n\tau)\}_{n\in\mathbb{N}}$ being orthogonal.

From the measurement of $P_n(\beta)$, the Wigner function can be directly estimated using Eq. (4.17). Alternatively, denoting as $\{\beta_m\}$ the ensemble of displacements experimentally measured, one could solve the set of linear equations

$$P_n(\beta_m) = \langle n| \hat{\mathcal{D}}(-\beta_m)\, \hat{\rho}\, \hat{\mathcal{D}}(\beta_m) |n\rangle = \sum_{i,j} M_{n,m,i,j}\rho_{i,j} \tag{4.20}$$

with $\rho_{i,j} = \langle i| \hat{\rho} |j\rangle$ and $M_{n,m,i,j} = \langle n| \hat{\mathcal{D}}(-\beta_m) |i\rangle \langle j| \hat{\mathcal{D}}(\beta_m) |n\rangle$. Measuring $P_n(\beta_m)$ for an appropriate set of displacement $\{\beta_m\}$ (which can be optimized in order to better reconstruct the quantum information, see the Appendix of [186]), the density matrix of the memory can be estimated from Eq. (4.20) using a least square regression. This regression is performed by imposing that the memory density matrix is Hermitian, positive semi-definite and of trace one.

To effectively reconstruct the probabilities $P_n(\beta_m)$ up to a cutoff n_c, the time step τ_{step} between two successive points in the trajectory $P_e(\tau)$ has to be smaller than $\pi/\sqrt{n_c}g$ in order to verify Shannon criteria. Assuming the total timescale of the measurement correspond to at least 1 period of the oscillation at Ω_1, which corresponds to a minimal number of measurement $2\sqrt{n_c}$. Note that this parity measurement is not QND.

4.3.3.2 *Estimation of P_n using a selective $\hat{X}_\pi^n$ pulse*

Another method used for the parity measurement, still based on the measurement of the probabilities $P_n(\beta_m)$, uses selective $\hat{X}_\pi^n$ pulses instead of the continuous trajectory $P_e(\tau)$ of the qubit. First implemented in 2013 [137], the auxiliary qubit is here coupled to the memory in the dispersive regime (see Sec. 3.1.3.2). The Hamiltonian of this system reads

$$\hat{H}_{\text{Disp}}/\hbar = \omega_m \hat{a}^\dagger \hat{a} - \chi_{\text{m,m}} \hat{a}^{\dagger 2}\hat{a}^2 + \frac{1}{2}\left(\omega_q - \chi_{\text{q,m}}\hat{a}^\dagger\hat{a}\right)\sigma_z, \tag{4.21}$$

where the cross-Kerr term is included in the Hamiltonian as a frequency shift of the qubit frequency depending on the number of photons in the memory. In the regime where $\chi_{\mathrm{q,m}}$ is larger than both the relaxation and decoherence rates of the memory and qubit modes, a pulse of duration $\tau > 1/\chi_{\mathrm{q,m}}$ can be applied to the qubit during which no errors have time to occur (for small photon number). Setting the frequency of this drive to $\omega_d = \omega_q - N\chi_{\mathrm{q,m}}$, $N \in \mathbb{N}$, it induces coherent oscillations between the states $|g, N\rangle$ and $|e, N\rangle$. The condition $\tau > 1/\chi_{\mathrm{q,m}}$ ensures the drive has no impact on the states $|g, k\rangle$ for $k \neq N$. The drive is calibrated to act as a selective $\hat{X}^n_\pi$ pulse on the qubit, bringing it to its excited state $|e\rangle$ only if resonant with the qubit frequency. Measuring P_e after applying this pulse directly gives the value of P_n. The parity can then be estimated by applying these selective $\hat{X}^n_\pi$ to the qubit at frequencies $\omega_q - n\chi_{\mathrm{q,m}}$, $n \in \mathbb{N}$, until a cutoff n_c, and measure the qubit population.

Because it probes each frequency one after another, this protocol requires n_c measurements to estimate the probabilities $\{P_n\}_{n<n_c}$. Note that the interferometric method used in this thesis further improves on this figure, only requiring a single measurement to estimate the parity.

4.3.3.3 *Issues arising at large photon number*

Both these methods, as well as the interferometric approach to the parity measurement, are prone to errors when the memory contains a large number of photons. This is mainly due to single-photon loss errors occurring during the parity measurement protocol, the effective dissipation rate scaling linearly with the number of photons in the memory $\kappa_{1,\mathrm{eff}} = n\kappa_1$.

Regarding the first method used for the measurement of P_n (Sec. 4.3.3.1), this linear scaling of the single photon loss rate is to be compared with the oscillation rate Ω_n of each transition, scaling as $\Omega_n \propto \sqrt{n}$. In order for Eq. (4.19) to be valid and see the oscillations from which the probabilities P_n are deduced, Ω_n needs to be larger than $n\kappa_1$. The difference of scaling however indicates that, even in the regime where $g > \kappa_1$, the oscillations predicted by Eq. (4.19) will be damped at large photon number which will prevent the reconstruction of P_n.

A similar effect can be seen with the selective $\hat{X}^n_\pi$ pulses approach or the interferometric method used in this thesis. In the first case, the selective pulses have a fixed duration $T_{\text{selective}} > 1/\chi_{\mathrm{q,m}}$ in order to induce the desired selective $\hat{X}^n_\pi$ pulse. Because losing a photon during this time leads to a measurement error, it imposes that $T_{\text{selective}} < 1/n\kappa_1$. These 2 conditions cannot be simultaneously verified when $n > \chi_{\mathrm{q,m}}/\kappa_1$, preventing the measure of P_n for large photon number. The same logic can be applied to the interferometric approach where the idle time $T_{\mathrm{parity}} = \pi/\chi_{\mathrm{q,m}}$ of the parity measurement needs to be shorter than $1/n\kappa_1$.

These issues can be mitigated by working in the regime $g, \chi_{\mathrm{q,m}} \gg \kappa_1$, pushing the maximum photon number at which single-photon loss prevents the parity measurement. In our system however, $\chi_{\mathrm{q,m}}$ was specifically chosen to be small relative to the two-photon dissipation so that the thermal population of the transmon first excited state does not affect the stabilization of cat states [102, 157, 158, 176]. The measured value $\chi_{\mathrm{q,m}}/2\pi = 170$ kHz is then only about 11 times that of κ_1, inducing a noticeable loss of contrast in the reconstruction of the coherences of $|C_\alpha^+\rangle$ for large photon numbers (Fig. 4.12**b.**).

Furthermore, working with a large cross-Kerr $\chi_{\mathrm{q,m}}$ poses another challenge in our parity measurement protocol. In this regime of parameter, the desired unconditional $\hat{X}_{\pi/2}$ pulses applied on the qubit can become selective if $\bar{n}\chi_{\mathrm{q,m}}$ is greater than the $\hat{X}_{\pi/2}$ pulse bandwidth. This limitation is not observed in our system due to the low cross-Kerr coupling.

4.3.3.4 *Solving these issues using 2-photon dissipation*

These issues can be effectively addressed through minor adjustments to the pulse sequence used for the parity measurement. Following the initial displacement operation $\hat{D}(-\beta)$ at the phase ϕ_{tomo}, the flux is quickly turned back to $\phi_{\mathrm{QEC}}$where the memory loses pairs of photons to the buffer (Fig. 4.12**a.**). Leveraging the substantial ratio $\kappa_2/\kappa_1 \approx 150$, we introduce a time delay $1/\kappa_1 \gg t > \bar{n}/\kappa_2$ during which the memory decays to the manifold $\mathrm{span}(|0\rangle, |1\rangle)$ while preserving its parity. Given that the memory contains, at most, a single photon, occurrences of single photon losses are now significantly suppressed by a factor of $\bar{n}$ compared to the pre-*deflation* scenario. A better reconstruction of the cat coherences can then be achieved, increasing the contrast of the cat fringes by $e^{\kappa_1(\bar{n}-1)\pi/\chi_{\mathrm{q,m}}} \approx 14$ for $|\alpha| = 3.35$ (Fig. 4.12**c.**).

In this experiment, we leverage the robust two-photon dissipation effect offered by the Auto-cat system to eliminate photon pairs. Alternatively, one could use a transmon qubit, as discussed in Section 3.5, to achieve the same outcome. Specifically, the engineered dissipation operator $\hat{L}_2 = \sqrt{\kappa_2}\hat{a}^2$ can be generated by driving a four-wave mixing term within the transmon Hamiltonian [117, 101]. Although the resulting two-photon dissipation rate κ_2 is considerably lower than what is demonstrated in this thesis, a ratio of $\kappa_2/\kappa_1 \approx 100$ was obtained in [101] through the use of 3D cavities, which provide a lower dissipation rate κ_1. Such a ratio should allow to remove pairs of photons without suffering from single photon loss. Moreover, the

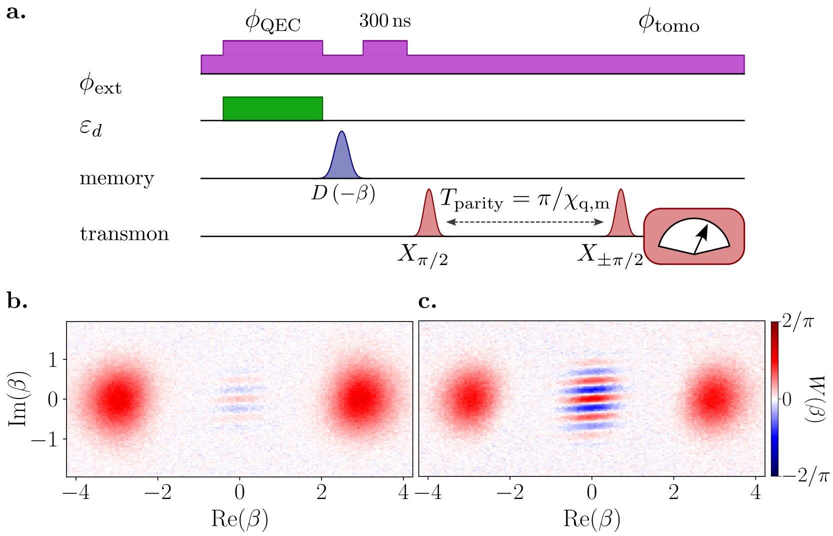

Figure 4.12: **a.** Modified pulse sequence used to perform the Wigner tomography of $|C_\alpha^+\rangle$. After applying a drive $\epsilon_d(\alpha)$ at $\phi_{\rm QEC}$ to stabilise $|C_\alpha^+\rangle$, the flux is quickly switched to $\phi_{\rm tomo}$ where the memory is displaced by $\hat{D}(-\beta)$. The flux is then quickly switched back to $\phi_{\rm QEC}$ for a time $t = 300$ ns. The standard parity measurement is then applied at $\phi_{\rm tomo}$ during which the transmon acquires information on the memory parity before being finally measured. **b.** Wigner tomography of $|C_\alpha^+\rangle$, $\alpha = 3.35$, without the 300ns of two-photons removal. **c.** Wigner tomography of $|C_\alpha^+\rangle$ using the modified pulse sequence.

same transmon qubit could be exploited for both photon pair removal and parity measurements, initially applying a pump tone to activate the 2-to-1 photon coupling and subsequently performing the desired parity measurement protocol.

4.3.3.5 *Alternative parity measurements taking advantage of the deflation*

Following the deflation process, once the memory decayed to the manifold span $(|0\rangle, |1\rangle)$, the task of measuring the parity simplifies considerably. It simply amounts to differentiate the states $|0\rangle$ and $|1\rangle$, or equivalently the measurement of P_0 or P_1. This procedure is far simpler than measuring the parity of an arbitrary memory state, and new protocols can be envisioned that simplify previous measurements.

One approach is to adapt the two protocols introduced in Section 4.3.3 and only measure P_0, thereby significantly reducing the measurement overhead.

The condition $g, \chi_{\mathrm{q,m}} \gg \kappa_1$ would remain essential, which could be an issue in future iterations of the Auto-cat as a large cross-Kerr rate is shown to limit the bit-flip time (see Sec. 4.4.4).

An alternative approach is to use a gate recently introduced in [114], the Conditional not displacement or CNOD gate. This gate was first envisioned in order to displace a resonator conditioned on an auxiliary qubit *not* being in a given state, $|e\rangle$ for instance, without relying on narrow-band pulses at selected frequencies. This is achieved by shaping the pulse drive used for the displacement such that its Fourier transform is antisymmetric around the frequency $\omega_m^{|e\rangle} = \omega_m - \chi_{\mathrm{q,m}}$. Crucially, the selectivity being provided by the pulse's symmetry properties, large-frequency bandwidths are no longer an issue and the pulse duration is not limited by the cross-Kerr coupling rate.

Within the context of parity measurement, the CNOD gate can be used by treating the deflated memory as an effective qubit and applying a drive to an auxiliary qubit or a resonator for a duration shorter than $1/\chi_{\mathrm{q,m}}$. While applying a selective $\hat{X}_\pi$ on an auxiliary qubit proves challenging in simulations, large buffer displacements $|\lambda\rangle$ conditioned on the memory state, with $\lambda \gg 1$, should be feasible. Measuring the state of this resonator and distinguishing between $|\lambda\rangle$ and its vacuum state $|0\rangle$ then gives access to the parity. Notably, the buffer mode of the Auto-cat could serve as this auxiliary resonator, elevating the need for the auxiliary transmon and a separate readout cavity.

4.4 BIT-FLIP TIME AND PHASE-FLIP RATE, EXPERIMENTS VS SIMULATIONS

4.4.1 *Experimental data*

4.4.1.1 *Measurement of T_{X} and Γ_{Z} at a given cat size*

The phase-flip rate corresponds to the loss of coherence of the cat qubit, through which any superposition of $|\pm\alpha\rangle$ decays to a mixture of these 2 coherent states [2]. In order to probe it, a cat state $|C_\alpha^+\rangle$ is first prepared in the memory by applying a drive $\epsilon_d(\alpha)$ at ϕ_{QEC}, starting from an empty cavity. The cat qubit decoherence towards $(|\alpha\rangle\langle\alpha| + |-\alpha\rangle\langle-\alpha|)/2$ is then monitored by simply measuring $W(0)$. Fitting this evolution with an exponential decay at a rate Γ_{Z} gives the value of the phase-flip rate (Fig. 4.13**a.**). Note that this measurement could have been performed starting from $|C_\alpha^-\rangle$, theoretically yielding the same phase-flip rate as

---

[2] This is valid in the case where $\Gamma_{\mathrm{Z}} \gg 1/T_{\mathrm{X}}$

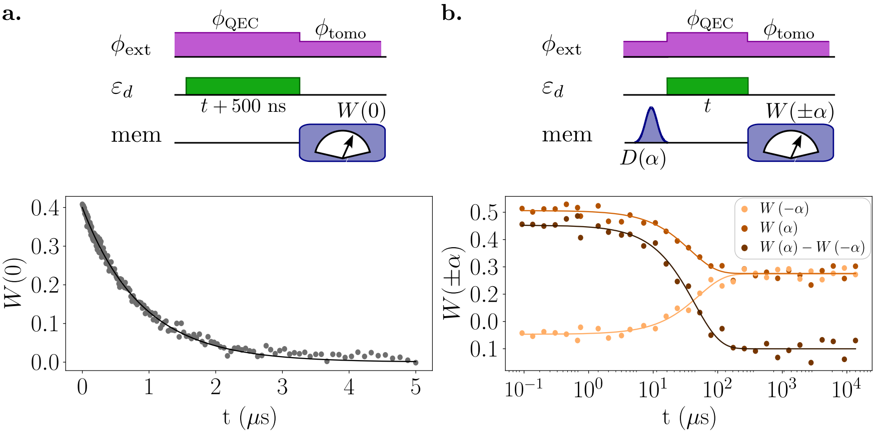

Figure 4.13: Determination of T_{x} and Γ_{Z} for $\alpha^2 \approx 6.5$. For each measurement the associated pulse sequence is shown above the experimental results, the Wigner tomography protocol used is presented in Fig. 4.12. **a.** Dots: measured $W(0)$ as a function of cat stabilization time t. Solid line: fit with an exponential decay $e^{-\Gamma_z t}$ where $\Gamma_z/2\pi = 0.16$ MHz. **b.** Dots: measured $W(-\alpha)$, $W(\alpha)$ and $W(\alpha) - W(-\alpha)$ as a function of cat stabilization time t. Solid line: fit with an exponential decay, the bit-flip time $T_{\mathrm{X}} = 60\ \mu$s is deduced from the fit of $W(\alpha) - W(-\alpha)$. Insert: associated pulse sequence.

$$\left\langle C_\alpha^+ \right| \hat{a}^\dagger \hat{a} \left| C_\alpha^+ \right\rangle = \left\langle C_\alpha^- \right| \hat{a}^\dagger \hat{a} \left| C_\alpha^- \right\rangle + O\left(e^{-|\alpha|^2}\right). \tag{4.22}$$

The bit-flip time T_{X} characterizes how fast the coherent state $|\alpha\rangle$ decays to an equal mixture of $|-\alpha\rangle$ and $|\alpha\rangle$. In order to measure it, the flux is first set to ϕ_{tomo} so that a memory drive can prepare the state $|\alpha\rangle$. The flux is then turned back to ϕ_{QEC} and the buffer drive is immediately turned on with an amplitude $\epsilon_d(\alpha)$ (Fig. 4.13**b.**). The state $|\alpha\rangle$ is then protected by the two-photon dissipation which should prevent leakage to $|-\alpha\rangle$. We measure the Wigner functions $W(\pm\alpha)$ for various waiting times and fit their difference by an exponential decay $W(\alpha) - W(-\alpha) \propto e^{-t/T_{\mathrm{X}}}$, giving the value of T_{X}.

4.4.1.2 *Dependency of* T_{X} *and* Γ_{Z} *with* $|\alpha|^2$

Measuring the bit-flip time and phase-flip error rates for varying values of $|\alpha|^2$, we observe the dependence of T_{X} and Γ_{Z} with $|\alpha|^2$ shown in Fig. 4.14.

As expected the phase-flip rate increases linearly as $\Gamma_Z = 2|\alpha|^2\kappa_1$, with κ_1 being independently measured (Fig.4.11**b.**), until it goes above 20 photons.

The bit-flip time is shown in Fig. 4.14**b.** and rises exponentially with the photon number $|\alpha|^2$ until up to 12 photons. There, T_X grows by a scaling factor of about 3.5 per added photon, smaller than the limit of 7.4 predicted in case of pure dephasing alone (solid line) [145].

We explain this discrepancy by the breakdown of the approximation of adiabatic elimination of the buffer, Eq. (4.15). Indeed simulation of the evolution of the buffer-memory bipartite system predicts smaller scaling factors (dashed blue line in Fig. 4.14**b.**). Using the experimentally measured pure dephasing rate of the memory $\kappa_\varphi^m/2\pi = 0.08$ MHz (see Sec.4.4.3.1) is key to obtaining a good match between simulations and experiment before saturation. Besides the simulated bit-flip times strongly depend on the flux ϕ_ext and we set a detuning $2\omega_m - \omega_b = 2\pi \times 3.5$ MHz in order to better reproduce the measured bit-flip times. This corresponds to a flux offset of $3 \times 10^{-4}\phi_0$, which could be attributed to flux drifts during the month that separates the measurements of Fig. 4.9**a.**, used to calibrate ϕ_QEC by maximizing κ_2, and Fig. 4.14. This notably highlights the stability of our system, whose flux was not re-tuned for a month resulting only in a small detuning, still allowing to stabilize a cat qubit.

The bit-flip time saturates at 0.36 ± 0.15 s, reached for $|\alpha|^2 \approx 20$. Simulations reveal that while the transmon first excited state no longer limits T_X [102], residual excitation of the transmon higher states sets a higher bound to the bit-flip time. Despite a relatively small dispersive shift $\chi_\mathrm{q,m}/2\pi = 170$ kHz, these higher excited states of the transmon exit the dispersive regime yielding a large frequency shift on the memory comparable to $\kappa_2|\alpha|^2$, effectively turning off the cat qubit stabilization and inducing a bit-flip error. We measure the higher excited states of the transmon while stabilizing cat qubits of various mean photon numbers $|\alpha|^2$ (see Sec. 4.4.3.2), and infer the rate at which they get populated (red dots in Fig. 4.9**b.**). The measured saturation in bit-flip time seems to reach this upper bound, indicating that the excitation of transmon higher states is the dominant limiting mechanism. The intermediate regime $10 < |\alpha|^2 < 15$ shows a sub-exponential increase of T_X that could be attributed to self-Kerr effect and pure dephasing of the buffer mode. In this region, we observe that the variance of the two peaks at $\beta = \pm\alpha$ in $W(\beta)$ is larger than for a coherent state. This is consistent with a thermalization of the memory by a thermal occupation of the buffer mode, owing to self-Kerr effect combined with pure dephasing.

We detail the simulations used to obtain the blue and red curves of Fig. 4.9**b.** in Sec. 4.4.4. As mentioned, key ingredients of these simulations are the bare memory phase flip rate and the transmon excited states population, independently measured in Sec.4.4.3.

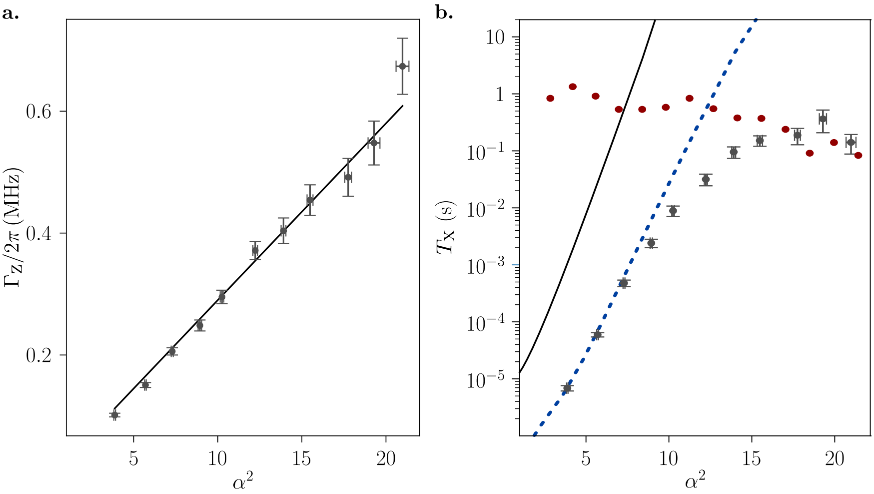

Figure 4.14: **a.** Dots: measured phase flip rate Γ_Z (linear scale) of the cat code as a function of photon number $|\alpha|^2$. All values are obtained by fitting $W(0)$ to an exponential decay in time. Error bars represent statistical uncertainties. Line: expected rate $2|\alpha|^2\kappa_1$. **b.** Dots: measured bit flip time (log scale) of the cat code as a function of photon number $|\alpha|^2$. All values are obtained by fitting the difference $W(\alpha) - W(-\alpha)$ to an exponential decay in time. Error bars represent statistical uncertainties. Solid black line: expected bit-flip time with $\kappa_\varphi^m/2\pi = 0.08$ MHz under the adiabatic elimination of the buffer: $e^{2|\alpha|^2}/(|\alpha|^2\kappa_\varphi^m)$. Dashed blue line: simulated bit-flip time with the same κ_φ^m, assuming a detuning $2\omega_m - \omega_b = 2\pi \times 3.5$ MHz. Red dots: predicted limitation of T_X imposed by the measured excitation of higher states of the transmon (see Sec. 4.4.3.2).

4.4.2 *Dependence of T_X and Γ_Z on the drive frequency ω_d*

The cat stabilization works by driving the buffer on resonance at ϕ_{QEC}. Now, what would happen if we drive it off-resonantly?

Figure 4.15 shows the measured $W(0)$ as a function of flux and drive frequency ω_d after 5 μs of stabilization. The red regions where $W(0) \approx 2/\pi$ correspond to a memory unaffected by the drive so that it remains in its vacuum state. In contrast, a white region where $W(0) \ll 1$ corresponds to regions where a mixture of coherent states has formed in the memory.

Note that the stabilization time of 5 μs was chosen so that the formed cat states have time to decohere to a mixture of $|\pm\alpha\rangle$. Otherwise, due to the 2-to-1 coupling preserving the memory parity, the white region would not be observed. The figure, reminding of an avoided level crossing, actually corresponds to the autoparametric version of that between $\omega_b(\phi_{\text{ext}})$ and $2\omega_m(\phi_{\text{ext}})$.

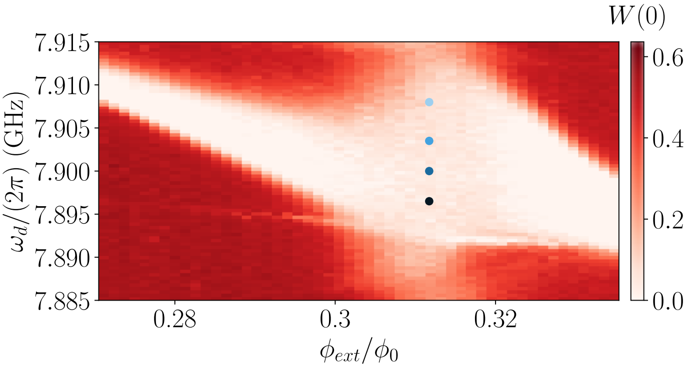

Figure 4.15: Anticrossing of the autoparametric memory-buffer system. Measured $W(0)$ after applying a buffer drive at ω_d for 5 μs while at ϕ_{ext}. Dots: frequencies and flux corresponding to the data presented in Fig.4.16.

The dependence of T_{x} and Γ_{Z} on mean photon number α^2 is measured for 4 buffer drive frequencies at ϕ_{QEC} (dots in Fig. 4.15). The same initial behavior for $\Gamma_{\text{Z}}\left(\alpha^2\right)$ can be seen for all 4 curves, with an initial linear increase of the phase-flip rate (Fig. 4.16**a.**). The slope of the linear increase is given by $\Gamma_{\text{Z}} = 2\left|\alpha\right|^2/T_{1,\text{eff}}$, with $T_{1,\text{eff}}$ the effective memory lifetime. This effective lifetime matches the memory lifetime measured by looking at the decay from $|1\rangle$ to $|0\rangle$ at the optimal drive frequency, with a drastic deterioration as the detuning of the drive frequency increases.

The dependence of $T_{\text{x}}\left(\alpha^2\right)$ is measured for the same four drive frequencies (Fig. 4.16**b.**). A similar behavior for $T_{\text{x}}\left(\alpha^2\right)$ can be seen for the 4 different drive frequencies, with an initial exponential increase before reaching a maximum for some optimal cat size (Fig. 4.16**b.**). This optimal bit-flip time strongly depends on the chosen drive frequency, with the curves shown in Fig. 4.14 corresponding to the frequency that gives us the largest measured bit-flip time T_{X}.

Note that the 1D-cuts of the Wigner functions $W(\beta)$ from which are extracted the bit-flip times (Fig. 4.19**d.**), exhibit a broadening of the Gaussian distribution around $\pm\alpha$ with increasing α and with increasing drive detuning. This can result from a distortion of the cat qubit manifold and/or a thermalization of the memory. As discussed in Sec. 4.4.4.3, based on reasonable assumptions, we show numerical evidence that both the shorter bit-flip times at other detuning and the broadening of the Wigner distribution can originate from the dephasing and the self-Kerr effect of the buffer mode.

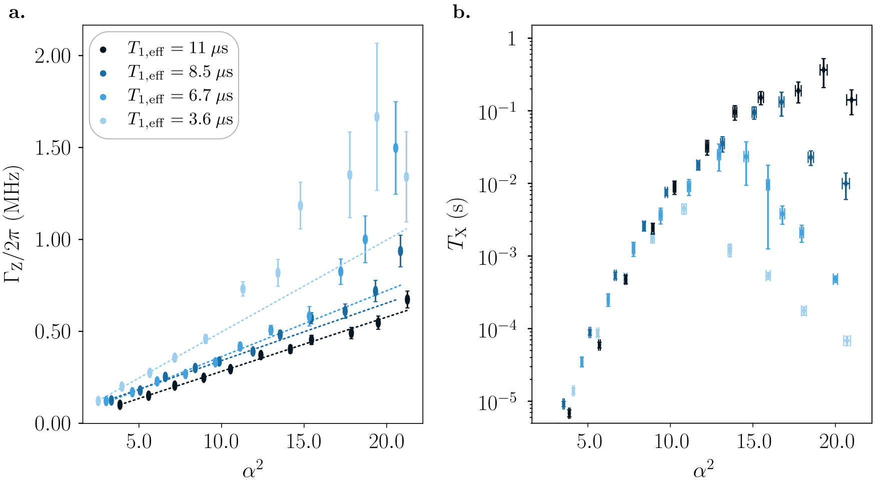

Figure 4.16: **a.** Dots: measured Γ_Z as a function of α^2 for 4 different drive frequencies. Dashed line: Linear fit of the measured data with $\Gamma_Z = 2\left|\alpha\right|^2/T_{1,\mathrm{eff}}$. where the fit parameter $T_{1,\mathrm{eff}}$ is shown as an inset **b.** Dots: measured T_x as a function of α^2 for 4 different drive frequencies.

4.4.3 *Complementary measurements*

4.4.3.1 *Memory dephasing rate*

The memory pure dephasing rate κ_φ^m, used for numerical simulations of the bit-flip time evolution, is measured with a Ramsey-like experiment. A state close to $\left(|0\rangle + |1\rangle\right)/2$ is prepared in the memory by first displacing the memory to the coherent state $|\alpha\rangle$, with $\alpha = 2.1$, and letting it decay under the loss operator $\hat{L}_2 = \sqrt{\kappa_2}\hat{m}^2$. By Zeno effect, the 2-photon loss constraints the memory dynamics to the $\{|0\rangle, |1\rangle\}$ manifold, hence acting as a qubit whose basis states are 0 and 1 photon in the memory. This state is then left idle for a time t, during which it rotates around the Z axis of the Bloch sphere at the detuning Δ between the memory drive frequency and $\omega_{\mathrm{m,QEC}}$, in the frame of the drive frequency. The memory state evolves under the Hamiltonian and loss operator

$$\begin{aligned}\hat{H}/\hbar &= -\frac{\Delta}{2}\left(\left|1\right\rangle\left\langle 1\right| - \left|0\right\rangle\left\langle 0\right|\right)\\ \hat{L}_1 &= \sqrt{\kappa_1}\left|0\right\rangle\left\langle 1\right|,\ \hat{L}_\varphi = \sqrt{\frac{\kappa_\varphi^m}{2}}\left(\left|1\right\rangle\left\langle 1\right| - \left|0\right\rangle\left\langle 0\right|\right).\end{aligned} \tag{4.23}$$

The readout is performed by mapping the obtained state onto the manifold span $(|\alpha\rangle, |-\alpha\rangle)$ by driving the buffer mode with a drive $\epsilon_d(\alpha)$. This maps the eigenvectors of $(|1\rangle\langle 0| + |0\rangle\langle 1|)$ onto the two coherent states. The Wigner function $W(\pm\alpha)$ (Fig. 4.17) is then measured, and the data fitted to extract the detuning Δ, and the dephasing rate $\kappa_\varphi^m/2\pi \approx 0.08$ MHz.

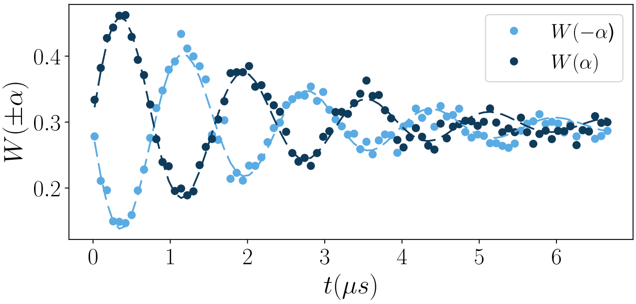

Figure 4.17: Ramsey-like experiment on the memory manifold span $(|0\rangle, |1\rangle)$. Dots: measured Wigner tomography $W(\pm\alpha)$. Dashed line: Fit used to extract the dephasing rate $\kappa_\varphi^m/2\pi = 0.08$ MHz and detuning $\Delta_b = \omega_b - \omega_d = -3$ MHz.

4.4.3.2 *Population of the higher excited states of the transmon*

The transmon used for Wigner tomography, dispersively coupled to the memory mode, has been shown to be one of the main factors limiting the bit-flip time T_X at large photon numbers. In this experiment, the 2 photon dissipation rate κ_2 is much greater than the dispersive shift $\kappa_2 \gg \chi_{q,m}$. This ensures that the population in the qubit first excited state only has a negligible detrimental impact on the cat qubit stabilization, and does not introduce additional bit-flip errors [102, 157].

However, simulations show that populations of higher excited states of the transmon have an impact on the bit-flip time. The transmon populations are probed by measuring the transmon state, while a cat qubit is stabilized in the memory mode. The drive frequency of the readout resonator is chosen in order to resolve the transmon states up to its 5^{th} excited state. In contrast, the readout frequency used everywhere else in this work was optimized to distinguish between the transmon ground and first excited states. A cutoff is then calibrated to separate the states $|0\rangle, |1\rangle, |2\rangle, |3\rangle$, and $|4\rangle$ from the others, allowing to measure the transmon population for each amplitude α of the cat qubit (Fig. 4.18**b.**).

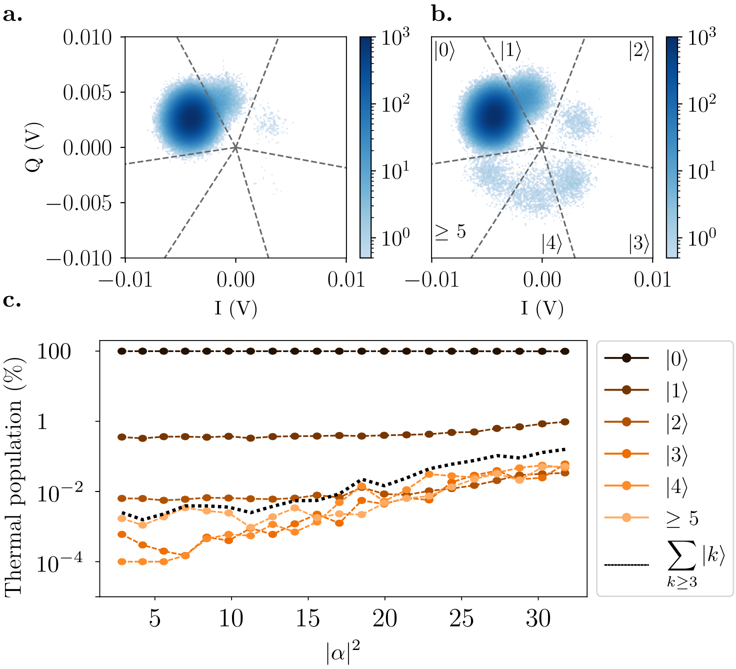

Figure 4.18: **a.** Histogram of 10^7 measurements of the readout quadratures when the transmon and memory are in thermal equilibrium with the cold environment. Each bin is $(10\ \mu\mathrm{V})^2$ **b.** Same histogram when a cat qubit space is stabilized for 100 μs with a mean photon number $|\alpha|^2 \approx 30$. **c.** Dots: measured occupation of the transmon states as a function of the stabilized mean number of photons in the memory. Excitation numbers are indicated by colors of increasing brightness. Black dotted line: sum of the populations in states higher than $|3\rangle$.

As can be seen in Fig. 4.18**c.**, the transmon populations in states of higher energy than $|3\rangle$ get excited for $|\alpha|^2 > 10$. This increase in transmon higher excitations is clearly correlated with the occupation of the memory mode. Besides it does not follow a Boltzmann distribution.

We attribute the increase of the occupation of transmon states above $|3\rangle$ to a resonance between the memory and the higher levels of the transmon. The negative anharmonicity $\omega_{12} - \omega_{01} = -2\pi \times 181$ MHz of the transmon results in a transition frequency between the 6^{th} and 7^{th} excited states being close to that of the memory. Note that such a resonance usually occurs when the resonator frequency is placed below that of the transmon. This phenomenon, which also happens with a simple Duffing oscillator, was recently investigated theoretically in Ref. [187] and experimentally in Ref. [188]. As the number of photons in the resonator increases, the states below and above the 6^{th} and 7^{th} states of the transmon also hybridize.

In the steady state, we expect these hybridized states to be equally populated [189, 187], and this population to increase with the number of photons in the resonator. This qualitative signature of a growing number of hybridized states is observed in Fig. 4.18**c**. Note that this is in contrast with an overall increase in the temperature, where one would expect the hierarchy of populations to roughly follow the Boltzmann distribution.

We simulate the coupling between the memory and the transmon higher excited states to study how a finite population of these hybridized states sets an upper bound on the bit-flip time T_{X}.

4.4.4 *Simulations*

The theoretical blue and red curves shown in Fig. 4.9**b.**, which predict the evolution of the bit-flip time, were obtained using numerical simulations reproducing our system. These simulations were performed by Joachim Cohen from Alice & Bob. In this section, we introduce the theoretical model used to predict the initial dependency of T_{X} on $|\alpha|^2$ for $|\alpha|^2 \lesssim 10$. We briefly summarize how the Hamiltonian and the dissipation parameters were experimentally obtained, and highlight the impact of the memory dephasing $\mathcal{D}[\sqrt{\kappa_\varphi^m}\hat{a}^\dagger\hat{a}]\,(\hat{\rho})$ and buffer photons on the bit-flip time.

Finally, using the measured population of the transmon's higher excited states, we present how they limit the bit-flip of the stabilized cat to about time to $T_{\mathrm{X}} \approx 0.3$ s.

4.4.4.1 *Model used for the simulations*

The master equation used to simulate the density matrix $\hat{\rho}$ of the memory and buffer modes in the Auto-cat can be written as

$$\begin{aligned}\frac{d\hat{\rho}}{dt} =& -\frac{i}{\hbar}[\hat{H},\hat{\rho}]\\ &+\mathcal{D}[\sqrt{\kappa_1}\hat{a}](\hat{\rho})+\mathcal{D}[\sqrt{\kappa_\varphi^m}\hat{a}^\dagger\hat{a}](\hat{\rho})\\ &+\mathcal{D}[\sqrt{\kappa_b}\hat{b}](\hat{\rho})+\mathcal{D}[\sqrt{\kappa_\varphi^b}\hat{b}^\dagger\hat{b}](\hat{\rho})\end{aligned} \tag{4.24}$$

where $\mathcal{D}[\hat{L}]\rho = \hat{L}\rho\hat{L}^\dagger - \hat{L}^\dagger\hat{L}\rho/2 - \rho\hat{L}^\dagger\hat{L}/2$ is the Lindblad superoperator. The four last terms respectively model the single photon dissipation of the memory, the pure dephasing of the memory, the single photon dissipation of the buffer, and the pure dephasing of the buffer. The effective Hamiltonian of the system takes the form

$$\begin{aligned}\frac{\hat{H}}{\hbar} =& \Delta_m \hat{a}^\dagger\hat{a} + \Delta_b \hat{b}^\dagger\hat{b} \\ &- \frac{\chi_{\mathrm{m,m}}}{2}\hat{a}^{\dagger 2}\hat{a}^2 - \frac{\chi_{\mathrm{b,b}}}{2}\hat{b}^{\dagger 2}\hat{b}^2 - \chi_{\mathrm{m,b}}\hat{a}^\dagger\hat{a}\ \hat{b}^\dagger\hat{b} \\ &+ g_2(\hat{a}^2 - \alpha^2)\hat{b}^\dagger + g_2^*(\hat{a}^{\dagger 2} - \alpha^{*2})\hat{b}.\end{aligned} \tag{4.25}$$

There, $\Delta_b = \omega_b - \omega_d$ is the detuning of the drive $\epsilon_d\,(\alpha)$ with respect to the buffer frequency, and $\Delta_m = \omega_m - \omega_b/2 + \Delta_b/2$. This detuning is taken into account in order to consider a small miscalibration or drift of the external flux ϕ_{ext}, resulting in a deviation from the frequency matching condition $\omega_b = 2\omega_m$.

We estimate $\chi_{\mathrm{m,m}}/2\pi = 0.206$ MHz at ϕ_{QEC}, deduced from the memory self-Kerr rate $\chi_{\mathrm{m,m}}/2\pi = 0.220$ MHz at ϕ_{tomo} (Fig. 3.8) using Eq. (3.80). The single photon decay rates $\kappa_1/2\pi = 14$ kHz, and $\kappa_b/2\pi = 40$ MHz were respectively deduced from the decay of a single photon in the memory (Fig. 4.11**b.**) and a reflection measurement of the buffer (see Appendix.d). The memory pure dephasing $T_\varphi^m = 1/\kappa_\varphi^m = 2\ \mu$s was estimated using a Ramsey-like experiment on the memory (see Sec. 4.4.3.1), which also gave an estimation of $\Delta_b/2\pi = -3$ MHz from the oscillations of Fig. 4.17. From this memory dephasing rate, the buffer dephasing can be estimated assuming that the dephasing rate on the memory is mostly due to flux noise

$$\frac{\kappa_\varphi^b}{\kappa_\varphi^m} = \frac{\left|\frac{\partial\omega_b}{\partial\phi_{\mathrm{ext}}}(\phi_{\mathrm{QEC}})\right|}{\left|\frac{\partial\omega_m}{\partial\phi_{\mathrm{ext}}}(\phi_{\mathrm{QEC}})\right|} = 60. \tag{4.26}$$

Finally, the self-Kerr of the buffer $\chi_{\mathrm{b,b}}/2\pi \approx 10$ MHz and the cross-Kerr between the memory and buffer $\chi_{\mathrm{m,b}}/2\pi \approx 1.6$ MHz were estimated using Eq. (3.80).

This leaves us with two fit parameters, g_2 and Δ_m. Let us first estimate the uncertainty on Δ_m. Using the measured value of Δ_b leads to $\Delta_m/2\pi = \omega_m - \omega_b/2 - 1.5$ MHz. The resonance condition $2\omega_m = \omega_b$ being sensitive to the external flux threading the loop, we estimate that $|2\omega_m - \omega_b|/2\pi < 5$ MHz from the width of the peak $\kappa_2(\varphi_{\mathrm{ext}})$ in Fig. 4.9**a.**, leading to $\Delta_m/2\pi = -1.5 \pm 2.5$ MHz. This parameter was optimized, within this range of uncertainties, to better reproduce the measured bit-flip times in Fig. 4.14**b**. This yields a detuning from the frequency matching condition

$$(2\omega_m - \omega_b)/2\pi = 3.5 \text{ MHz}, \tag{4.27}$$

and a corresponding detuning $\Delta_m/2\pi = 0.25$ MHz. The experimental value of the 2-to-1 coupling rate $g_2/2\pi = 6 \pm 0.5$ MHz was obtained by measuring the fidelity of Z gates on this cat qubit. Note that it matches the value predicted by the theoretical model (see Sec. 3.5.4).

4.4.4.2 *Impact of memory dephasing on bit-flip time* T_X

We expect pure dephasing of the memory to impact the bit-flip time T_X. In the adiabatic regime $8|\alpha|g_2 \ll \kappa_b$, the bit-flip time scales as $T_\varphi^m|\alpha|^{-2}\exp\big(2|\alpha|^2\big)$ [103, 145]. However, in our case, the adiabaticity condition is not respected for $|\alpha| \gtrsim 1$. While the memory dephasing noise limits the scaling of T_X with the photon number, we observe numerically that it is not strong enough to lead to the observed saturation.

4.4.4.3 *Impact of buffer photons on bit-flip time* T_X

During the stabilization, although the driven buffer ideally stays in the vacuum state, a finite buffer amplitude $\beta = \langle\hat{b}\rangle_\text{ss} \neq 0$ in the steady state can result in unwanted sources of bit-flip errors. The first mechanism that can limit the bit-flip time originates from the dephasing noise on the buffer. Via the drive photons, this noise can be upconverted into thermal photons in the buffer, which in turn are converted into thermal photons in the memory by the two-photon exchange term, thus creating a heating term of the form $\hat{\mathcal{D}}(\hat{a}^{\dagger 2})$. The expected thermal population is given by $n_\text{th}^b = \kappa_\varphi^b|\beta|^2/\kappa_b$.

Second, the large expected self-Kerr rate of the buffer $\chi_\text{b,b}/2\pi \approx 10$ MHz can result in a squeezing on the buffer when the latter is displaced. The single photon loss channel on a squeezed buffer then yields an effective non-zero thermal occupation given by $n_\text{th}^b = \sinh^2(r)$, where r is the effective squeezing parameter. Besides, the squeezing on the buffer results in an anti-squeezing term on the memory, which is likely to decrease the bit-flip time.

Let us estimate the displacement on the buffer. In the interaction picture, the master equation on the memory mode Eq. (4.24) reads

$$\frac{d}{dt}\hat{a} = -i\Delta_m\hat{a} - i2\chi_\text{mm}\hat{a}^\dagger\hat{a}^2 - i\chi_\text{m,b}\hat{a}\hat{b}^\dagger\hat{b} - \frac{\kappa_\varphi^m + \kappa_1}{2}\hat{a} - i2g_2\hat{a}^\dagger\hat{b}. \tag{4.28}$$

Assuming a steady-state solution of the form $\rho = |\alpha\rangle\langle\alpha| \otimes |\lambda\rangle\langle\lambda|$, with $\alpha \neq 0$, and taking the trace of the above equation, we obtain

$$\lambda = e^{i2\theta_m}\frac{-\Delta_m - 2\chi_{\mathrm{m,m}}|\alpha|^2 - \chi_{\mathrm{m,b}}|\lambda|^2 + i(\kappa_\varphi^m + \kappa_1)/2}{2g_2},$$

where $\theta_m = \arg(\alpha)$.

In the limit $\kappa_\varphi^m, \kappa_1 \ll \left|\Delta_m + 2\chi_{\mathrm{m,m}}|\alpha|^2 + \chi_{\mathrm{m,b}}|\lambda|^2\right|$, the amplitude λ becomes

$$\lambda = -e^{i2\theta_m}\frac{\Delta_m + 2\chi_{\mathrm{m,m}}|\alpha|^2 + \chi_{\mathrm{m,b}}|\lambda|^2}{2g_2}.$$

The displacement amplitude on the buffer depends on the effective memory detuning, which in turn depends on the cat size due to the self-Kerr effect. The amplitude of the buffer field in the steady state thus depends on the effective detuning of the memory, and consequently the detuning of the buffer drive $\Delta_b = \omega_b - \omega_d$ and the photon number in the memory.

Before addressing the impact of a populated buffer on the bit-flip time, let us first outline the experimental observations that cannot be explained solely by the heated transmon. As presented in Sec. 4.4.4.4, the transmon excited state population sets an upper bound around 1 s for the bit-flip time. However, measurements taken at various drive detunings reveal earlier saturation of the bit-flip time, almost two orders of magnitude below 0.3 s (see Fig. 4.16**b.**). This cannot be explained by the 1 s bound imposed by the transmon. Besides, the measured 1D-cut of the Wigner functions along the cat axis displays a broadening of the coherent states along this axis (Fig. 4.19**b.**). This distortion of the coherent states cannot be explained by the weak occupancy of the excited transmon states (below 1 % for the first excited state and below 0.1 % for the states above). It rather results from a local distortion of the code space and/or a thermalization of the memory.

Interestingly, we find that both of these experimental observations can be corroborated by the large expected self-Kerr rate of the buffer and its pure dephasing. Fig. 4.19**a.** shows the bit-flip times extracted from the simulation of Eq. (4.24), at the values of the drive detunings Δ_d corresponding to the experimental values of Fig. 4.16**b**. We observe a qualitatively similar behavior of the bit-flip times, in particular for the curves corresponding to larger detunings. In order to see a notable similar effect, the dephasing rate is here set to $\kappa_\varphi^b = 180\kappa_\varphi^m$ which is three times larger than what can be inferred from the flux dependence of the transition frequencies. We note that this parameter is not directly measured in the experiment so a larger buffer dephasing rate than predicted is conceivable.

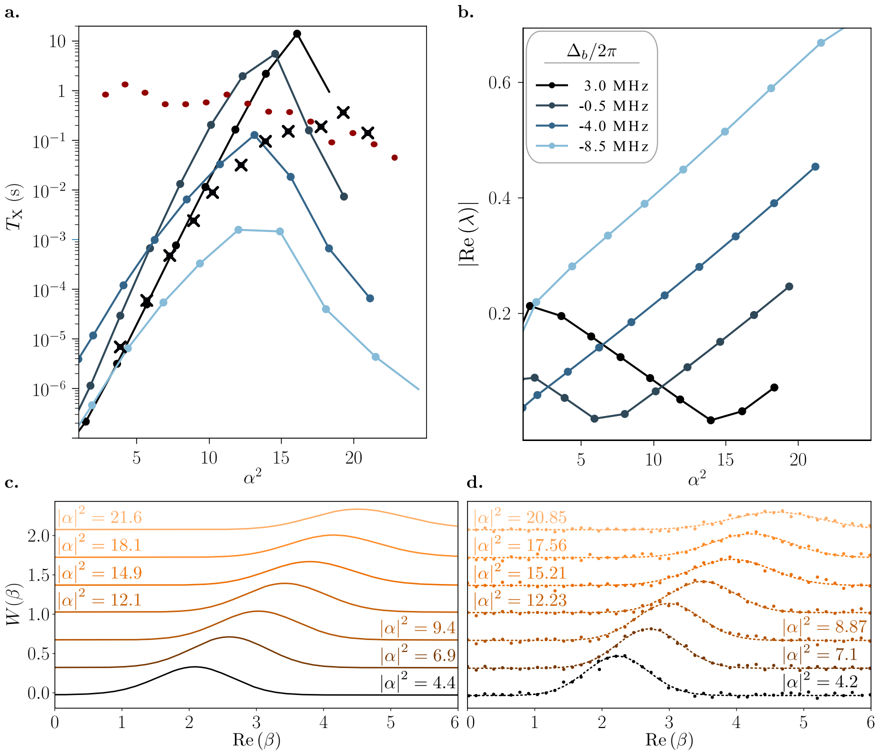

Figure 4.19: **a.** Simulated bit-flip times for various values of the drive detuning $\Delta_b = \omega_b - \omega_d$, corresponding to the values of Fig. 4.16**b**. The dephasing rate is set to $\kappa_\varphi^b = 180\kappa_\varphi^m$, and the memory detuning from the buffer is $2\omega_m - \omega_b = 2\pi \times 3.5$ MHz. As a reference, we indicate the measured optimal bit-flip times (black crosses) and the bound independently set by the transmon (red dots). **b.** Corresponding amplitudes of the buffer mode in the steady state as a function of average photon number $|\alpha|^2$ in the memory for the same detunings. The imaginary part is zero. **c.** Simulated probability distributions of the quadrature defined by the direction of α in the memory phase space $\mathrm{P}(\mathrm{Re}(\beta)) = |\langle \mathrm{Re}(\beta)|\psi\rangle|^2$, plotted for several values of $|\alpha|^2$. A shift is applied between each distribution for readability. The detuning is set to $\Delta_b/2\pi = -8.5$ MHz. As the photon number increases, the distribution broadens. **d.** Corresponding measurements at $\Delta_b/2\pi = -8.5$ MHz. Dots: measured Wigner function $W(\beta)$. Dashed lines: Gaussian fit of the experimental data from which the mean photon number $|\alpha|^2$ is deduced. The same broadening can be observed for increasing photon numbers.

In Fig. 4.19**b.** are shown the corresponding amplitudes of the buffer mode. As expected, the amplitude correlates with the detuning and the maximal bit-flip time of each curve. The linear increase or decrease with $|\alpha|^2$ is due to the self-Kerr effect on the memory and to the cross-Kerr effect between buffer and memory, which modify the effective detuning on the memory as $|\alpha|^2$ and $|\beta|^2$ grow. The increasing amplitude combined with the self-Kerr effect and dephasing rate of the buffer mode leads to the thermalization of the memory and eventually limits the bit-flip time.

Finally, Fig. 4.19**c.** and Fig. 4.19**d.** shows a comparison between the simulated and measured probability distribution of the memory state along the cat axis for $\Delta_b/2\pi = -8.5$ MHz. The distribution broadens as $|\alpha|^2$ increases due to buffer thermal photons, leading to a saturation of the bit-flip time for this detuning.

4.4.4.4 *Impact of high excited states of the transmon on bit-flip time* T_X

Populating the higher excited states of the transmon is another mechanism that can limit the bit-flip time of the stabilized cat qubit. Indeed, this population results in a shift of the memory frequency which, if exceeding the tolerance of the stabilization scheme, could limit a bit-flip time as high as hundreds of milliseconds even for a small population. In this section, we evaluate the magnitude of the frequency shifts that can be reached when the memory field drives the transmon.

In our system, the transmon is inductively coupled to the memory and capacitively coupled to a readout resonator. For simplicity, we do not consider the Purcell filter of the readout resonator. The Hamiltonian of this system reads

$$\begin{aligned}\hat{H} =& 4E_C(\hat{n}_q - n_g)^2 - E_J \cos\hat{\theta}_q + \hbar\omega_m \hat{a}^\dagger\hat{a} + \hbar\omega_r \hat{r}^\dagger\hat{r} \\ &+ \hbar g_{\mathrm{q,m}} \sin\hat{\theta}_q(\hat{a} + \hat{a}^\dagger) - i\hbar g_{\mathrm{q,r}}\hat{n}_q(\hat{r} - \hat{r}^\dagger),\end{aligned} \tag{4.29}$$

where $\hat{n}_q$ and $\hat{\theta}_q$ are the transmon charge and phase operators, n_g is a charge offset, $\hat{r}$ is the annihilation operator of the readout resonator, ω_r the frequency of the readout resonator. The coupling rates $g_{\mathrm{q,m}}/2\pi$ and $g_{\mathrm{q,r}}/2\pi$ are respectively the coupling rates between the transmon and the memory/readout resonator. We find the values of the charging energy $E_C/h = 169.4$ MHz and the Josephson energy $E_J/h = 22.85$ GHz, as well as that of the coupling rates $g_{\mathrm{q,r}}/2\pi = 67$ MHz and $g_{\mathrm{q,m}}/2\pi = 225$ MHz, by fitting the measured low energy spectrum of the system which includes frequencies, anharmonicity and dispersive shifts of the system. Note that, although we are only concerned about the interaction between the memory and transmon, the readout resonator is included in the simulated dynamics to correctly fit the spectrum of the system.

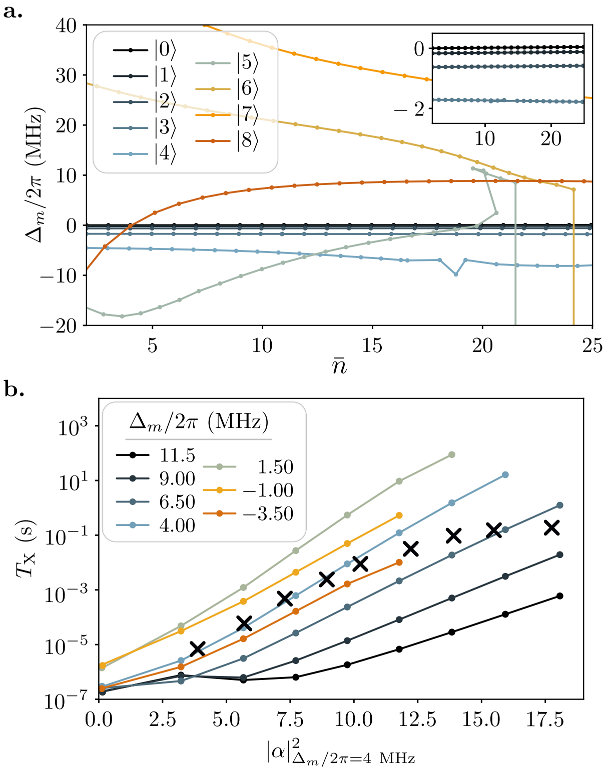

Figure 4.20: **a.** Dots: simulated memory frequency shift as a function of mean photon number $\bar{n}$ in the memory for various transmon states. The vertical lines are due to state mistracking. Inset: zoom on the small dispersive shifts for low transmon excitation. **b.** Effect of memory detuning Δ_m on the bit-flip time T_X. The bit-flip time is plotted as a function of the drive amplitude for several values of Δ_m. The drive amplitude is converted to the corresponding photon number at $\Delta_m = 4$ MHz, which approximately corresponds to the detunings set for Fig. 4.14**b**. The black crosses indicate the experimentally measured bit-flip times shown in Fig. 4.14**b**.

From Eq. (4.29), we compute the frequency shifts of the cavity as a function of the transmon state and the number of photons in the resonator (see Fig. 4.20**a.**) by diagonalizing the Hamiltonian. In the inset, one recognizes the dispersive shift $\chi_{\mathrm{q,m}}/2\pi = 0.170$ MHz when the transmon is in its first excited state $|1\rangle$. This is notably the regime where the parity measurement is performed during the Wigner tomography, after having removed pairs of photons from the memory using the 2-photon dissipation. While populating one of the first 3 excited states of the transmon causes small enough frequency shifts of the memory (inset) which can be handled by the stabilization scheme, populating higher excited states can result in frequency shifts as large as 30 MHz. Such large frequency shifts are due to the non-perturbative hybridization of the transmon states, thus exiting the dispersive regime of the coupling between transmon and memory (see Sec.3.1.3.2).

For small frequency shifts, the state remains confined to a manifold spanned by two coherent states, although the cat size might slightly vary. Indeed, using a semi-classical analysis (Eq. (S22) of [157]), in the limit where $\kappa_1 \ll |\Delta_m|$ and $\kappa_b \gg |\Delta_b|$, the photon number reads $|\alpha_\Delta|^2 = |\alpha_0|^2 - \frac{|\Delta_m|\kappa_b}{4|g_2|^2}$, where $|\alpha_0|^2$ is the photon number at zero detuning at the same drive amplitude. This equation has a solution if $|\Delta_m| < 4|g_2|^2|\alpha_0|^2/\kappa_b$. Using the measured and extracted values $\kappa_b/2\pi = 40$ MHz and $g_2/2\pi = 6$ MHz leads to $|\Delta_m| < 3.6|\alpha_0|^2$ MHz, that is the minimal condition for a 2D-manifold to be stabilized. The impact of the detuning Δ_m on the bit-flip time is illustrated in Fig. 4.20**b**, where the bit-flip time is plotted for various detunings as a function of the drive amplitude. The drive amplitude is converted to the photon number corresponding to the detuning $\Delta_m/2\pi = 4$ MHz.

The detuning associated with the first and second excited states (below 20 photons) is below 1 MHz, making the condition $|\Delta_m| < 3.6|\alpha_0|^2$ MHz largely satisfied. This is numerically verified in Fig. 4.20**b.**. In this case, the bit flip rate takes the form $T_\mathrm{X}^{-1} = \sum_{i,|\Delta_i|<\Delta_\mathrm{max}} p_i T_\mathrm{X}^{-1}(\Delta_i)$. The small detunings associated with the first and second excited states make the weighted contribution $p_i T_\mathrm{X}^{-1}(\Delta_i),\ i = 1, 2$ negligible compared to $p_0 T_\mathrm{X}^{-1}(\Delta_0)$.

However, detunings as large as 30 MHz become difficult for the dissipation scheme to compensate. For $|\Delta_m| = 30$ MHz, the minimal condition to generate a cat state in the cavity is $|\alpha_0|^2 > 8.5$ photons. Moreover, even if the memory becomes populated, this large detuning comes with a large displacement on the buffer mode, $\beta \sim \Delta_m/2g_2 = 2.5$ (see previous section) which can also limit the bit-flip time. Combined with its dephasing noise and large Kerr nonlinearity, the resulting bit-flip time of such a cat qubit is low. This is illustrated in Fig. 4.20**b.**, where the bit-flip time corresponding to a detuning of 9 MHz does not improve over the bare memory lifetime until $|\alpha_0|^2 = 12.5$. For simplicity, we assume that a bit-flip occurs every time the system is subject to such a large detuning for the range of photons considered here, which leads to a lower bound on the bit-flip time.

From the analysis of the transmon, it is likely that populating the layer of hybridized states will result in a large detuning and therefore a bit-flip. This allows us to derive a simple upper bound on the induced bit-flip time T_X from the measured values of the state population: it is given by the inverse rate at which this layer of states is populated γ_hyb. Let us call p_hyb the population of the hybridized states, represented as a black dotted line in Fig. 4.18**c.**, and p_1 the population of the first excited state. Note that the state $|2\rangle$ merges with the rising plateau of states around $|\alpha|^2 = 20$ photons. The rate at which the hybridized layer gets populated thus reads $\gamma_\mathrm{hyb} = \gamma_{\mathrm{hyb}\to 1} p_\mathrm{hyb}$. Using the measured $\gamma_{1\to 0}^{-1} = 18\ \mu$s and assuming $\gamma_{\mathrm{hyb}\to 1} \approx \gamma_{2\to 1} = 2\gamma_{1\to 0}$, we obtain the red dotted line in Fig. 4.14**b**.

4.5 CHAPTER SUMMARY

This chapter introduced the experimental realization of the Auto-cat design, implementing the two-to-one photon coupling using a 3-wave mixing element. We presented how this device can be controlled using a single input line, which makes use of the circuit symmetries to preferably couple to the buffer mode while preserving the memory quality factor. We show that this approach to engineering the two-photon exchange can significantly enhance the two-photon dissipation rate κ_2, exceeding the values previously obtained with parametric pumping strategies. This can notably be leveraged to improve the Wigner measurement protocol for states containing a large number of photons. Remarkably, the autoparametric scheme does not seem to activate extra relaxation processes as indicated by the linear increase of phase-flip rate up to 20 average photons.

While we achieved a notable bit flip time T_X of up to 0.3 s, we show that the pure dephasing induced by flux noise currently limits the scaling rate with respect to the photon number. This issue could be mitigated by operating closer to the flux sweet spot through improved design choices so that $\phi_\mathrm{QEC} = \phi_\mathrm{ext}^{(\mathrm{sweet})}$. Additionally, measurements and simulations single out the transmon as the main limitation of the bit-flip time for large values of $|\alpha|^2$. Removing it from the device should then alleviate the limitation on the photon number at which T_X reaches a saturation point. Consequently, the readout of the memory could be conducted via the buffer mode, leveraging the sizable two-to-one photon exchange rate [158].

5

OPERATION OF CAT QUBITS

The benchmark commonly used to characterize the performance of a stabilized cat qubit is the ratio between the engineered two-photons dissipation rate and the natural single-photon loss rate κ_2/κ_1. Notably, it is estimated that a ratio of a few hundred would be necessary in order to operate a repetition code of cat qubits below threshold, thus correcting the remaining phase-flip errors [146, 90]. Reaching a regime where useful quantum computation can be performed would be more challenging, requiring a ratio as large as $\kappa_2/\kappa_1 \sim 10^5$ [190].

From a physical standpoint, reaching a large ratio of κ_2/κ_1 is not only necessary to reach a large noise bias for the cat qubit, as showcased in the previous chapter, it is also required to manipulate and perform gates on the cat qubit with good fidelities. Indeed, when using dissipation engineering for stabilization, the gate is necessarily slower than κ_2^{-1} so that the operation remains adiabatic. During this operation, errors that mostly originate from single photon loss accumulate and corrupt the logical information at a rate κ_1. Consequently, making the gate faster by increasing κ_2 or reducing the error rate by decreasing κ_1 both result in improved gate fidelities. Note that, to increase the gate speed without necessarily increasing κ_2, a Hamiltonian confinement can be applied during the gate [151].

This chapter introduces two gates that we experimentally perform using the Auto-cat design (see Chap. 4). First, we demonstrate a Zeno gate $\hat{Z}(\theta)$ of an arbitrary angle θ by applying a displacement to the memory while the dissipation

$$\hat{L}_2 = \sqrt{\kappa_2}\left(\hat{a}^2 - \alpha^2\right)$$

stabilizes the cat manifold $\mathrm{span}\left(|\alpha\rangle, |-\alpha\rangle\right)$. This results in visible oscillations of the cat's fringes, reaching a fidelity of 96.5% for a $\hat{Z}(\pi)$ gate lasting 28 ns. We then demonstrate a gate $\hat{Y}(\theta)$ and $\hat{X}(\theta)$ using two distinct methods. Similarly to the $\hat{Z}(\theta)$ gate, the $\hat{Y}(\theta)$ gate can be realized by applying a displacement to the memory while the dissipation $\sqrt{\kappa_2}\hat{a}^2$ stabilizes the manifold $\mathrm{span}\left(|0\rangle, |1\rangle\right)$. Another possibility introduced by Albert et al. in 2016 [191] is the holonomic approach, which we use to demonstrate the gate $\hat{X}(\theta)$. This method relies on a *collision* of the 2 coherent states to induce a coherent population transfer.

Additionally, we show how working in the non-adiabatic regime (see Sec. 4.4.1.2) allows the preparation of squeezed cat states which have recently been investigated in the context of quantum error correction or quantum sensing [116, 133, 134].

Remark: The main results presented in this chapter are the core of an article in preparation.

5.1 DEMONSTRATION OF A BIAS-PRESERVING $\hat{Z}(\theta)$ GATE

5.1.1 *Calibration of the gate*

5.1.1.1 *Zeno $\hat{Z}(\theta)$ gate using two-photon dissipation*

We perform a $\hat{Z}(\theta)$ gate on the stabilized cat qubit, consisting of a rotation around the **z** axis of the cat qubit Bloch sphere (Fig. 5.1**a.**). This gate is realized by using quantum Zeno dynamics [192, 193, 194, 195, 196], leveraging the large ratio κ_2/κ_1 of the Auto-cat. Starting for instance from $|C_+^\alpha\rangle$, with the buffer drive $\epsilon_d(\alpha)$ turned on, we continuously drive the memory on resonance [101], effectively implementing a displacement whose Hamiltonian reads

$$\hat{H}_z(t)/\hbar = -i\epsilon_Z(t)e^{i\theta_z}\hat{a} + h.c.,$$

where θ_z and $\epsilon_Z(t)$ are the drive phase and amplitude. The drive phase is chosen so that, without two-photon loss, the memory drive would induce a displacement (arrow in Fig. 5.1**c.**) perpendicular to α in the memory phase space. Depending on the measurements, we alternatively used a square or a Gaussian waveform. The constant amplitude in the case of the square pulse is simply written as ϵ_Z, and the mean amplitude in the Gaussian case is denoted as $\bar{\epsilon}_Z$.

Applying this drive while simultaneously driving the buffer at ϕ_{QEC} (Fig. 5.1**b.**) implements a quantum Zeno dynamics of the cavity, the two-photon dissipation preventing leakage from the cat manifold span $(|\alpha\rangle, |-\alpha\rangle)$. The effect of the memory drive ϵ_Z is then to rotates the phase θ of the quantum superposition $(|\alpha\rangle + e^{i\theta}|-\alpha\rangle)/\sqrt{\mathcal{N}}$, which can be seen as translated fringes in the Wigner function (Fig. 5.1**c**). Note that for the Zeno dynamic to be effective, the drive amplitude needs to be small compared to the confinement rate [102] which stabilizes the cat qubit manifold

$$\epsilon_Z \ll \kappa_{\mathrm{conf}} = 2|\alpha|^2\kappa_2. \tag{5.1}$$

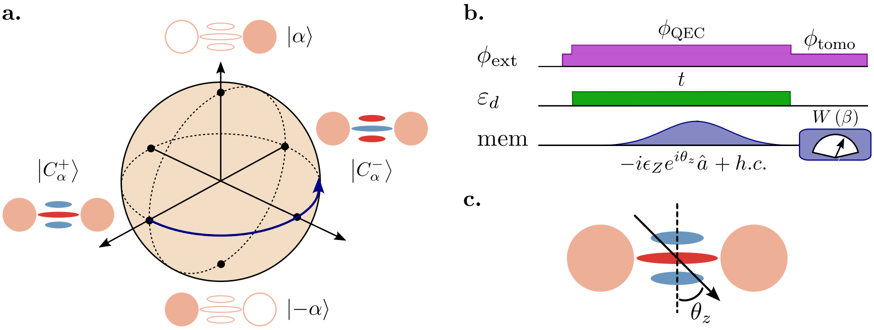

Figure 5.1: **a.** Bloch sphere of the cat qubit, whose computational basis is $|\alpha\rangle, |-\alpha\rangle$. The effect of a Z rotation is illustrated by the blue arrow. **b.** Pulse sequence for Z rotation characterization. **c.** Effect of a drive $-i\epsilon_Z e^{i\theta_z}\hat{m}+h.c.$ acting on the state $\left|C_\alpha^+\right\rangle$ of the memory.

This condition ensures the displacement does not overcome the dissipation rate, and does not induce unwanted population transfer between the two coherent states. This notably sets a maximum speed at which the gate can be performed, which increases with $|\alpha|^2$ and κ_2.

5.1.1.2 *Calibration of the drive phase*

We calibrate the phase θ_z of this gate in order to set $\theta_z=\pi$. This maximizes the gate speed for a given drive amplitude ϵ_Z, improving the gate fidelity by decreasing the time during which single-photon dissipation affects the memory.

This optimization is done by sweeping the phase of the memory drive and doing a vertical cut of the memory Wigner tomography. Looking at how fast the Wigner function fringes shift over time allows us to extract the oscillation rate Ω_z. Note that measuring $W(0)$ alone would leave the sign of Ω_z undetermined, which is why we measure a vertical cut of the Wigner function (Fig. 5.2**a.**).

Doing this measurement for different value of θ_z, (Fig. 5.2**b.**) shows an evolution $\Omega_z(\theta_z)\propto\cos(\theta_z)$. This is expected as only the vertical component of the drive $\mathrm{Re}\left(\epsilon_Z e^{i\theta_z}\right)$ effectively displaces the fringes of the cat Wigner function. The horizontal component $\mathrm{Im}\left(\epsilon_Z e^{i\theta_z}\right)$ is disabled by the 2 photon dissipation and does not affect the system, which can be seen as a cancellation of Ω_z for $\theta_z=\pm\pi/2$.

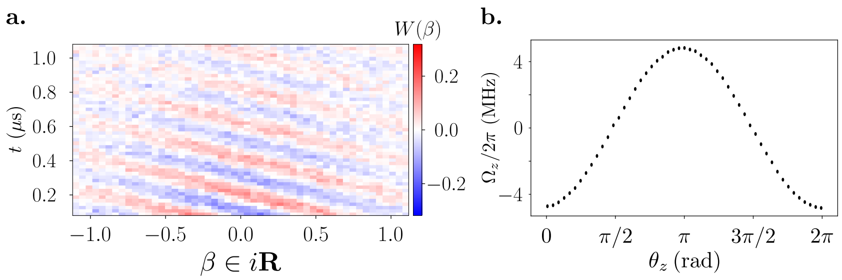

Figure 5.2: **a.** Measured Wigner function $W(\beta)$ of the memory as a function of $\beta \in i\mathbb{R}$ and time t. The displacement is a square pulse which drive parameters are $\epsilon_Z/2\pi = 1.25\,\mathrm{MHz}$ and $\theta_z = \pi/2$ **b.** Measured oscillation frequency Ω_z around the z axis of the Bloch sphere as a function of θ_z.

5.1.2 *Demonstration of the* $\hat{Z}(\theta)$ *gate*

5.1.2.1 *Experimental realization*

The measured Wigner functions of the memory are shown in Fig. 5.3**a.** after three different waiting times, while the memory is driven with a mean amplitude $\bar{\epsilon}_z/2\pi = 1.625$ MHz. Oscillations of the cat fringes are clearly visible, with a transition from $|C_\alpha^-\rangle$ to $|C_\alpha^+\rangle$. The associated measured value of $W(0)$ as a function of time is shown in Fig. 5.3**a**, which exhibits decaying oscillations around the **Z** axis of the cat qubit at a frequency Ω_Z and decay rate κ_Z.

The rotation frequency is expected to be given by

$$\Omega_Z = 4\mathrm{Re}(\epsilon_Z \alpha) \tag{5.2}$$

which is precisely what is observed in Fig. 5.4**a**. The real part appearing in Eq. (5.2) mathematically corresponds to the sole action of the drive component that is orthogonal to the cat fringes. The proportionality of Ω_Z with ϵ_Z and α can be intuitively understood, as the memory displacement is proportional to the drive amplitude and the distance between two consecutive fringes is inversely proportional to $|\alpha|$.

The decay rate κ_Z has a more subtle dependence on photon number $|\alpha|^2$ and memory drive ϵ_Z as seen in Fig. 5.4**b.**. In the ideal case and for constant ϵ_Z, the rate is expected to decay as [146, 158]

$$\kappa_Z = 2\kappa_1|\alpha|^2 + \kappa_b\epsilon_Z^2/(2|\alpha|^2 g_2^2). \tag{5.3}$$

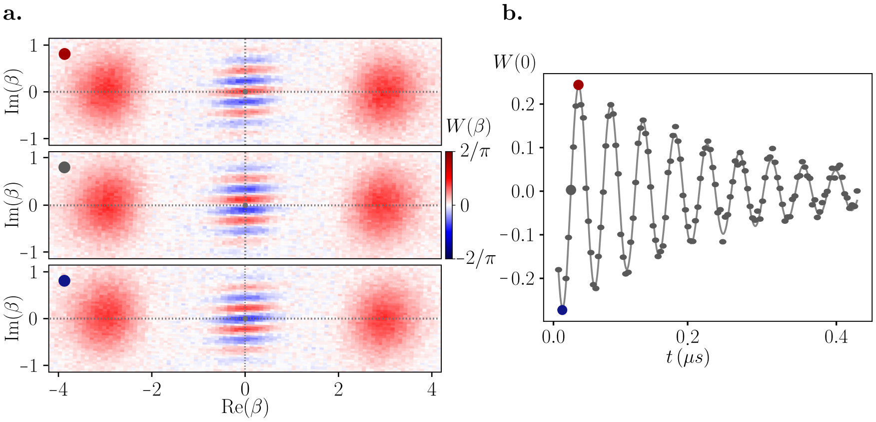

Figure 5.3: **a.** Measured Wigner functions $W(\beta)$ after a Z rotation of angle $\theta = 2\pi$, $3\pi/2$, and π from top to bottom. **b** Dots: Measured oscillations of $W(0)$ as a function of time t using the pulse sequence of Fig. 5.1**b.** where the cat code is stabilized with a photon number $|\alpha|^2 = 9.3$. An additional displacement drive at ω_m starts 240 ns after the buffer drive is turned on. Here, its amplitude $\epsilon_Z(t)$ is Gaussian shaped with a mean amplitude $\bar{\epsilon}_Z/2\pi = 1.625$ MHz. Line: fit to decaying oscillations at a frequency $\Omega_Z/2\pi = 19.8$ MHz, and decay rate $\kappa_Z/2\pi = 0.62$ MHz.

The first term of this sum corresponds to phase-flip errors occurring at a rate Γ_Z, and the second to an induced leakage out of the confined cat qubit Hilbert space when the drive amplitude ϵ_Z is too strong to be Zeno blocked. Notably, this expression remains valid even outside of the adiabatic elimination regime [147].

In practice, the experiment deviates from this simple picture owing to the self-Kerr effect on the memory, slight detuning of the drive frequency, and resonance frequency detuning induced by drifts in the flux bias. Furthermore, as simulations of $\kappa_Z(\alpha)$ are sensitive to the two-to-one photon coupling rate g_2, we use these measurements to determine the two-to-one coupling rate. Adjusting this parameter to $g_2/2\pi \approx 6 \pm 0.5$ MHz leads to a good match between measurement and simulations (see Fig. 5.4**b**). With such a coupling, the adiabatic elimination of the buffer predicts a larger two-photon dissipation rate $4g_2^2/\kappa_b \approx 3.6 \times 2\pi$ MHz than what is measured in Fig. 4.9**b.**, which is expected since the condition $8g_2|\alpha| < \kappa_b$ is not met for $|\alpha|^2 \gtrsim 1$ [158]. Interestingly, despite the observed limitation on T_X in the non-adiabatic regime, it is still possible to improve gate speed and fidelity by going to large values of $g_2|\alpha|$.

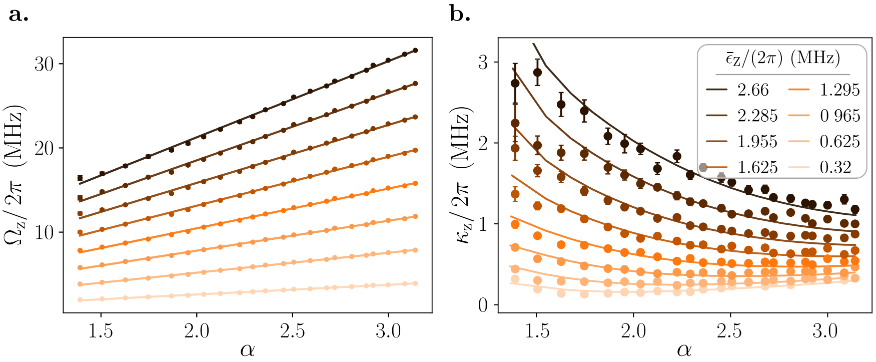

Figure 5.4: **a.** Dots: Inferred rotation frequency Ω_Z as a function of cat code amplitude α, and for various mean drive amplitudes $\bar{\epsilon}_Z/2\pi = 0.32, 0.625, 0.965, 1.295, 1.625, 1.955, 2.285,$ and 2.66 MHz from bright to dark orange. Lines: expected rotation frequency $\Omega_Z = 4\text{Re}(\bar{\epsilon}_Z\alpha)$ around Z. **b.** Dots: Inferred decay rate κ_Z as a function of $|\alpha|$ for the same drive amplitudes. Lines: simulated decay rate with $g_2/2\pi = 6$ MHz as a fit parameter and the same detuning Δ_b as in Fig. 4.14**b.**

5.1.2.2 *Comparison of κ_Z with the theoretical model*

In this section, we detail the simulations of the decay rate $\kappa_Z(|\alpha|))$ shown in Fig. 5.4**b**, performed by Joachim Cohen from Alice & Bob. We use the master equation already introduced in Sec. 4.4.4.1

$$\begin{aligned}\frac{d\hat{\rho}}{dt} =& -\frac{i}{\hbar}[\hat{H},\hat{\rho}] + \mathcal{D}[\sqrt{\kappa_1}\hat{a}](\hat{\rho}) + \mathcal{D}[\sqrt{\kappa_\varphi^m}\hat{a}^\dagger\hat{a}](\hat{\rho}) \\ &+ \mathcal{D}[\sqrt{\kappa_b}\hat{b}](\hat{\rho}) + \mathcal{D}[\sqrt{\kappa_\varphi^b}\hat{b}^\dagger\hat{b}](\hat{\rho}),\end{aligned} \tag{5.4}$$

with $\mathcal{D}[\hat{L}]\rho$ the Lindblad superoperator. The dissipation channels considered in this model are the single photon loss and pure dephasing of both the memory and buffer modes. The effective Hamiltonian of the system can be written as

$$\begin{aligned}\frac{\hat{H}}{\hbar} =& \Delta_m\hat{a}^\dagger\hat{a} + \Delta_b\hat{b}^\dagger\hat{b} - \frac{\chi_{\text{m,m}}}{2}\hat{a}^{\dagger 2}\hat{a}^2 - \frac{\chi_{\text{b,b}}}{2}\hat{b}^{\dagger 2}\hat{b}^2 - \chi_{\text{m,b}}\hat{a}^\dagger\hat{a}\ \hat{b}^\dagger\hat{b} \\ &+ g_2(\hat{a}^2 - \alpha^2)\hat{b}^\dagger + g_2^*(\hat{a}^{\dagger 2} - \alpha^{*2})\hat{b} + i\epsilon_Z e^{-i\theta_z}\hat{a}^\dagger - i\epsilon_Z e^{i\theta_z}\hat{a}\end{aligned} \tag{5.5}$$

The value of the different parameters is summarized in Sec. 4.4.4.1 and Table.4.1. Compared to the model used to simulate the bit-flip time dependence on $|\alpha|^2$, the last drive term is added to the Hamiltonian to take into account the memory displacement. The Gaussian drive envelope used for the simulations reads

$$\epsilon_Z(t) = \bar{\epsilon}_Z \frac{6}{\sqrt{2\pi}} \exp\left\{ -\frac{(t - T/2)^2}{2w^2} \right\},$$

where the time window T is the total duration of the pulse, $\bar{\epsilon}_Z$ corresponds to the average drive amplitude, and $w = T/6$ is the variance of the Gaussian pulse. The case of a square pulse is easily extended by choosing $\epsilon_Z(t) = \bar{\epsilon}_Z$ over the same time window. As for the experiment, we fit the decaying oscillations of the photon number parity to extract the rotation frequency Ω_Z and decay rate κ_Z corresponding to each drive amplitude ϵ_Z.

The decay rate κ_Z strongly depends on g_2 justifying its use to extract this parameter experimentally. For perfect frequency matching $2\omega_m = \omega_b$, the best fit to the simulation is obtained for $g_2/2\pi = 6$ MHz (solid line in Fig. 5.5**a.**). To illustrate the sensitivity of the simulations to the value of g_2, we also compute $\kappa_Z(\alpha)$ for $g_2/2\pi = 5.5$ MHz and $g_2/2\pi = 6.5$ MHz. The clear deviations in Fig. 5.5**a.** show that under the assumption that $2\omega_m = \omega_b$, g_2 can be determined with much better precision than $2\pi \times 0.5$ MHz from the measured decay rates κ_Z.

The uncertainty on g_2 is actually dominated by the values it can take over the range of conceivable detunings $\Delta_m/2\pi = -1.5 \pm 2.5$ MHz. In order to get a higher bound on this uncertainty, we choose three values for the resonance condition, $(2\omega_m - \omega_b)/2\pi = -5, 0, 5$ MHz, and search the rate g_2 that best reproduce the experiment. The fitted g_2 rates are between $2\pi \times 6.0$ MHz, and $2\pi \times 6.5$ MHz (Fig. 5.5**b.**). We therefore claim that $g_2/2\pi = 6 \pm 0.5$ MHz.

Note that in the simulations of the bit-flip time (Fig. 4.14**b.**) and in the simulations of the Z gate (Fig. 5.4**b.**), we have used the value $g_2/2\pi = 6$ MHz which best fits the gate oscillations and decay rate for the detuning $(2\omega_m - \omega_b)/2\pi = 3.5$ MHz.

5.1.2.3 *Bias preserving nature of the gate*

In order to preserve the benefit offered by bit-flip protection in cat qubits, it is crucial for logical gates to be bias-preserving [138], meaning that they do not convert phase-flip errors into bit-flip errors.

To verify the bias-preserving nature of the $\hat{Z}(\theta)$ gate, we measure the dependence of T_X when continuously driving the memory with a varying drive amplitude ϵ_Z. Similarly to the measurement presented in Fig. 4.14**b.**, the flux is first set to ϕ_tomo and the memory displaced by $\hat{D}(\alpha)$ in order to prepare the desired state $|\alpha\rangle$. The flux is then changed to ϕ_QEC and

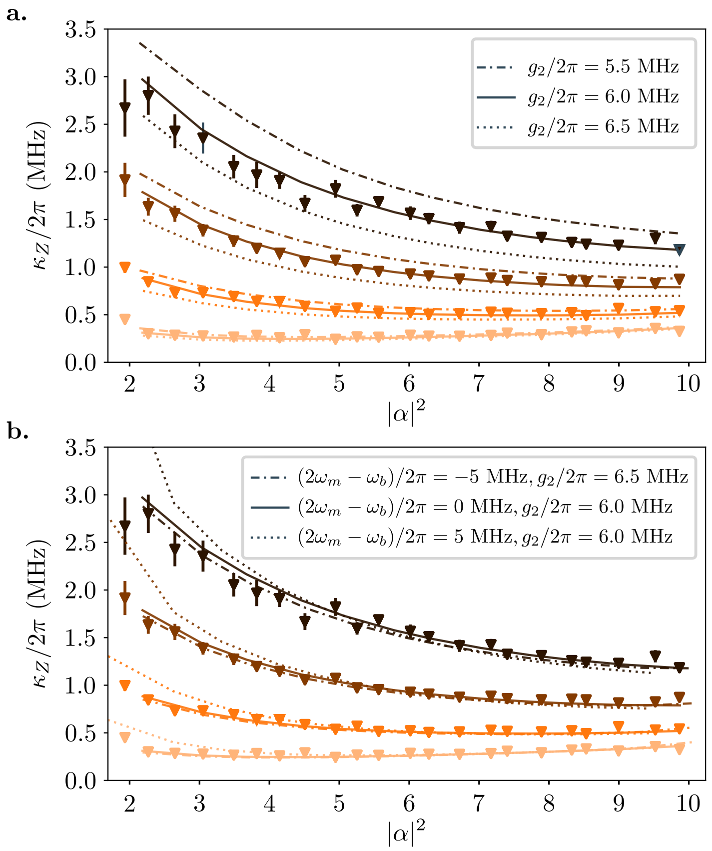

Figure 5.5: **a.** Triangles: measured decay rate κ_Z of the oscillations around Z as a function of $|\alpha|^2$ for four drive amplitudes ϵ_Z corresponding to distinct colors as in Fig. 5.4**b**. Lines: simulated decay rates κ_Z using Eq. (5.4) with three values of the rate $g_2/2\pi$ indicated as an inset. **b.** Triangles: same measurement as above. Lines: simulated κ_Z for three values of the detuning between buffer and memory $(2\omega_m - \omega_b)/2\pi = -5,\ 0,\ 5$ MHz covering its uncertainty range, and the corresponding optimal values of $g_2/2\pi = 6.5,\ 6.0,\ 6.0$ MHz.

2 drives are sent to the buffer and memory modes, with an amplitude of $\epsilon_d(\alpha)$ and ϵ_Z. The role of the drive acting on the buffer is to stabilize the cat qubit, preventing bit-flip errors from happening, while the drive acting on the memory performs the desired $\hat{Z}(\theta)$ gate. The Wigner function $W(\pm\alpha)$ is finally measured for various waiting times, and their difference $W(\alpha) - W(-\alpha) \propto e^{-t/T_\mathrm{X}}$ is fitted to extract T_X (Fig. 5.6**b**).

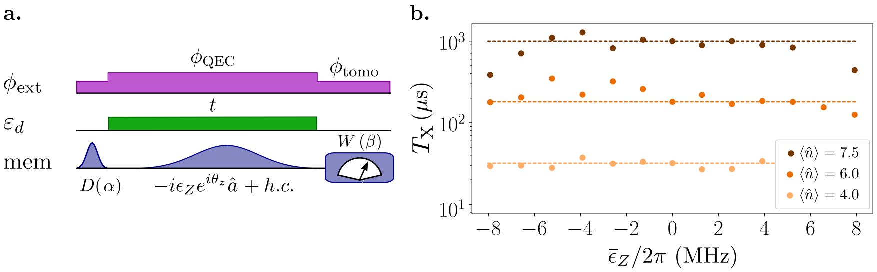

Figure 5.6: **a.** Pulse sequence for the T_{X} measurement, while continuously applying the Z gate on the memory with an average drive amplitude $\bar{\epsilon}_Z$. **b.** Dots: Measured T_{X} as a function of the average memory drive amplitude $\bar{\epsilon}_Z$ for different cat qubit sizes $\alpha = 2$, 2.4, and 2.7 (yellow to brown). Lines: measured T_{X} at $\bar{\epsilon}_Z = 0$.

The measured dependence of T_{X} on $\bar{\epsilon}_Z$ is shown in Fig. 5.6**b.** for different amplitudes α. Despite a rather large measurement uncertainty, no visible decrease of T_{X} can be observed for $|\bar{\epsilon}_Z/2\pi| < 6$ MHz, after which the displacement becomes strong enough to overcome the stabilization provided by the 2 photon dissipation. This induces an increased number of bit-flip errors, leading to a decrease of T_{X}.

The Z rotation presented in Fig. 5.3 is measured with $\bar{\epsilon}_Z/2\pi = 1.625\,\text{MHz}$. It can thus be assumed that the drive did not induce additional bit-flip errors. Comparing the measured $T_{\text{X}} \sim 10$ ms for $\alpha^2 = 9.3$ with the $Z(\pi)$ gate duration, we can estimate that bit-flip errors alone contribute to a probability $3.10{-}6$ of the gate error. The obtained gate fidelity, limited by the phase-flip error rate, is computed in the next section.

5.1.3 *Fidelity of the gate*

In a classical computer, the gate fidelity of a gate G applied on a single bit of information is characterized by the confusion matrix

$$C(G) = \begin{pmatrix} P(0|0) & P(0|1) \\ P(1|0) & P(1|1) \end{pmatrix} \tag{5.6}$$

with $P(\text{output } j|\text{input } i)$ the probability of measuring the output j knowing the system was initially in i. For instance, the ideal confusion matrix for the identity is $P(i|j) = \delta_{i,j}$ and $P(i|j) = 1 - \delta_{i,j}$ for the NOT gate. However, due to the additional complexity of a quantum bit of information and the additional degree of freedom, this formalism is insufficient to fully characterize a quantum gate. To do so we introduce the quantum counterpart of the confusion matrix, the standard process matrix χ [72, 197], and use it to characterize the gate fidelity.

5.1.3.1 *Formalism of the standard process matrix χ*

A quantum operation is fully characterized by a set of Kraus operators $\{\hat{E}_i\}$ and their effect on an arbitrary density matrix $\hat{\rho}$

$$\mathcal{E}\left(\hat{\rho}\right) = \sum_i \hat{E}_i \hat{\rho} \hat{E}_i^\dagger . \tag{5.7}$$

There, $\mathcal{E}\left(\hat{\rho}\right)$ is the density matrix of the system after application of the gate, starting from $\hat{\rho}$. Expressing it as

$$\mathcal{E}\left(\hat{\rho}\right) = \frac{1}{2}\left(\mathbb{1} + \left\langle \hat{X} \right\rangle \hat{X} + \left\langle \hat{Y} \right\rangle \hat{Y} + \left\langle \hat{Z} \right\rangle \hat{Z}\right) \tag{5.8}$$

provides a direct experimental state tomography protocol where $\left\langle \hat{X} \right\rangle$, $\left\langle \hat{Y} \right\rangle$ and $\left\langle \hat{Z} \right\rangle$ are estimated from the Wigner functions, which contain all the information about the state of the memory. These Kraus operators are decomposed into a fixed set of operators $\{\hat{F}_i\}$, typically corresponding to the Pauli operators in the case of a qubit. These constitute a basis for the ensemble of operators acting on the cat qubit. The Kraus operators can be expressed in this basis as

$$\hat{E}_i = \sum_j e_{i,j} \hat{F}_j , \tag{5.9}$$

and Eq. (5.7) is rewritten as

$$\mathcal{E}\left(\hat{\rho}\right) = \sum_{i,j} \chi_{i,j}\, \hat{F}_i \hat{\rho} \hat{F}_j^\dagger . \tag{5.10}$$

This defines the standard process matrix χ, with $\chi_{i,j} = \sum_k e_{i,k} e_{k,j}^*$. From the completeness relation of the Kraus operators $\sum_i \hat{E}_i^\dagger \hat{E}_i = \mathbb{1}$, it can be shown that this matrix is Hermitian with trace 1 and contains $d^4 - d^2$ independent real parameters for a system of dimension d (with $d = 2$ in the case of a qubit). Determining the Kraus map then amounts to finding the expression of χ which completely describes the quantum operation.

To estimate χ we introduce a basis for the space of $d \times d$ density matrices, $\{\hat{\rho}_j\}_{0\leq j\leq d^2}$, and experimentally measure the impact of our operation on this basis

$$\mathcal{E}(\hat{\rho}_j) = \sum_k \lambda_{j,k}\hat{\rho}_k. \tag{5.11}$$

The parameters $\lambda_{j,k}$ are experimentally determined by applying the quantum operation on $\hat{\rho}_j$ and measuring the resulting memory Wigner function. Furthermore, because $\{\hat{\rho}_j\}_{0\leq j\leq d^2}$ is a basis for the space of the memory density matrices, we may write

$$\hat{F}_m\hat{\rho}_j\hat{F}_n^\dagger = \sum_k \beta_{j,k}^{m,n}\hat{\rho}_k. \tag{5.12}$$

There, $\beta_{j,k}^{m,n}$ are complex coefficients that can be determined using standard linear algebra, $\{\hat{F}_i\}$ and $\{\hat{\rho}_j\}$ being both fixed by the experimentalist. The two previous equations can be combined with Eq. (5.10), yielding

$$\sum_k\sum_{m,n}\chi_{m,n}\beta_{j,k}^{m,n}\hat{\rho}_k = \sum_k \lambda_{j,k}\hat{\rho}_k. \tag{5.13}$$

This simplifies to

$$\sum_{m,n}\chi_{m,n}\beta_{j,k}^{m,n} = \lambda_{j,k} \tag{5.14}$$

using the independence of the matrices $\{\hat{\rho}_j\}$. This equation can be viewed in a matrix form, considering the action of a matrix β of size $d^4 \times d^4$ on a vector of size d^4

$$\beta\chi = \lambda. \tag{5.15}$$

This relation can then be inverted, giving the expression for the standard process matrix

$$\chi = \beta^{-1}\lambda. \tag{5.16}$$

We quickly summarize how χ is experimentally estimated. First, a set of operators $\{\hat{F}_i\}$ and a basis $\{\hat{\rho}_j\}$ are arbitrarily chosen, usually in order to ease following calculations, from which the matrix β is computed. The quantum operation under study is then applied to the memory, starting from all density matrices in the basis $\{\hat{\rho}_j\}$. Finally, the matrix λ is experimentally estimated by measuring the resulting memory Wigner function and χ is computed using Eq. (5.16).

5.1.3.2 *Expression of χ for a qubit*

Considering the case of a qubit [72], a convenient choice for $\{\hat{F}_i\}$ and $\{\hat{\rho}_j\}$ allows to find an expression for χ as a simple matrix multiplication. The operators $\{\hat{F}_i\}$ considered are

$$\hat{F}_0 = \mathbb{1},\ \hat{F}_1 = \hat{X},\ \hat{F}_2 = -i\hat{Y},\ \hat{F}_3 = \hat{Z} \tag{5.17}$$

and the density matrices $\{\hat{\rho}_j\}$

$$\hat{\rho}_0 = |g\rangle\langle g|\,,\ \hat{\rho}_1 = |g\rangle\langle e|\,,\ \hat{\rho}_2 = |e\rangle\langle g|\,,\ \hat{\rho}_3 = |e\rangle\langle e|\,. \tag{5.18}$$

The state $|g\rangle$ corresponds to the qubit ground state and $|e\rangle$ to its excited state. While $\mathcal{E}(\hat{\rho}_0)$ and $\mathcal{E}(\hat{\rho}_3)$ can directly be measured, preparing the qubit in its ground or excited state and applying the desired operation, we introduce the states $|+\rangle = (|g\rangle + |e\rangle)/\sqrt{2}$ and $|+i\rangle = (|g\rangle + i\,|e\rangle)/\sqrt{2}$ to estimate $\mathcal{E}(\hat{\rho}_1)$ and $\mathcal{E}(\hat{\rho}_2)$. These quantities can then be expressed as[1]

$$\begin{aligned}
\mathcal{E}(\hat{\rho}_1) &= \mathcal{E}(|+\rangle\langle +|) + i\mathcal{E}(|+i\rangle\langle +i|) - \frac{1+i}{2}\left(\mathcal{E}(|g\rangle\langle g|) + \mathcal{E}(|e\rangle\langle e|)\right) \\
\mathcal{E}(\hat{\rho}_2) &= \mathcal{E}(|+\rangle\langle +|) - i\mathcal{E}(|+i\rangle\langle +i|) - \frac{1-i}{2}\left(\mathcal{E}(|g\rangle\langle g|) + \mathcal{E}(|e\rangle\langle e|)\right),
\end{aligned} \tag{5.19}$$

and the χ matrix reads in terms of block matrices as

$$\chi = \frac{1}{4}\begin{pmatrix} \mathbb{1} & \sigma_x \\ \sigma_x & -\mathbb{1} \end{pmatrix}\begin{pmatrix} \rho_0^{'} & \rho_1^{'} \\ \rho_2^{'} & \rho_3^{'} \end{pmatrix}\begin{pmatrix} \mathbb{1} & \sigma_x \\ \sigma_x & -\mathbb{1} \end{pmatrix}. \tag{5.20}$$

In this last equation, the expressions $\hat{\rho}_i^{'}$ are to be understood as 2×2 matrices representing the density matrices $\mathcal{E}(\hat{\rho}_i)$.

---

[1] Note that we correct here an error of [72]

5.1.3.3 *Fidelity of the $\hat{Z}(\pi)$ gate*

The fidelity of a quantum gate is defined from the χ matrix as $F = \mathrm{Tr}\left(\chi\, \chi^{\mathrm{opt}}\right)$, with χ^{opt} being the χ matrix describing an ideal gate. In the case of a $\hat{Z}(\pi)$ gate, this ideal χ matrix reads

$$\chi^{\mathrm{opt}} = \begin{pmatrix} 0 & 0 & 0 & 0 \\ 0 & 0 & 0 & 0 \\ 0 & 0 & 0 & 0 \\ 0 & 0 & 0 & 1 \end{pmatrix}, \tag{5.21}$$

which corresponds to a matrix with all its terms null except for $\chi^{\mathrm{opt}}_{3,3} = 1$ (we use the same convention as in the previous section, with $\hat{F}_3 = \hat{Z}$). The fidelity is then directly given by $\chi_{3,3}$, estimated using Eq.(5.20) as the element $(1,1)$ of the 2×2 matrix

$$M = \frac{1}{4}\left(\sigma_x \rho_0^{'} \sigma_x - \sigma_x \rho_1^{'} - \rho_2^{'} \sigma_x + \rho_3^{'}\right). \tag{5.22}$$

We experimentally determine this 2×2 matrix using the evolution of $W(\beta)$ shown in Fig. 5.3**a**, from which we estimate the evolution of the logical Bloch coordinates $\langle \hat{\sigma}_{x,L} \rangle$, $\langle \hat{\sigma}_{y,L} \rangle$ and $\langle \hat{\sigma}_{z,L} \rangle$. These operators are defined in the cat encoding as

$$\hat{\sigma}_{x,L} = \left|C_\alpha^+\right\rangle \left\langle C_\alpha^+\right| - \left|C_\alpha^-\right\rangle \left\langle C_\alpha^-\right| \tag{5.23}$$

$$\hat{\sigma}_{y,L} = \left|C_\alpha^{+i}\right\rangle \left\langle C_\alpha^{+i}\right| - \left|C_\alpha^{-i}\right\rangle \left\langle C_\alpha^{-i}\right| \tag{5.24}$$

$$\hat{\sigma}_{z,L} = \left|\alpha\right\rangle \left\langle \alpha\right| - \left|-\alpha\right\rangle \left\langle -\alpha\right|, \tag{5.25}$$

with $\left|C_\alpha^\pm\right\rangle = \left(\left|\alpha\right\rangle \pm \left|-\alpha\right\rangle\right)/\sqrt{2}$ and $\left|C_\alpha^{\pm i}\right\rangle = \left(\left|\alpha\right\rangle \pm i \left|-\alpha\right\rangle\right)/\sqrt{2}$. The measured evolution of the three logical Bloch vector coordinates is shown in Fig. 5.7**a**. First, the gate being bias preserving as evidenced in Fig. 5.6**b**, we know it has no significant impact on the cat qubit ground and excited states $\left|\pm\alpha\right\rangle$ in the few tens of ns it takes to perform a $\hat{Z}(\pi)$ gate. We can then estimate

$$\mathcal{E}\left(\left|\alpha\right\rangle \left\langle \alpha\right|\right) = \left|\alpha\right\rangle \left\langle \alpha\right| \quad \mathcal{E}\left(\left|-\alpha\right\rangle \left\langle -\alpha\right|\right) = \left|-\alpha\right\rangle \left\langle -\alpha\right|, \tag{5.26}$$

which directly gives

$$\rho_0^{'} = \begin{pmatrix} 1 & 0 \\ 0 & 0 \end{pmatrix}, \; \rho_3^{'} = \begin{pmatrix} 0 & 0 \\ 0 & 1 \end{pmatrix}. \tag{5.27}$$

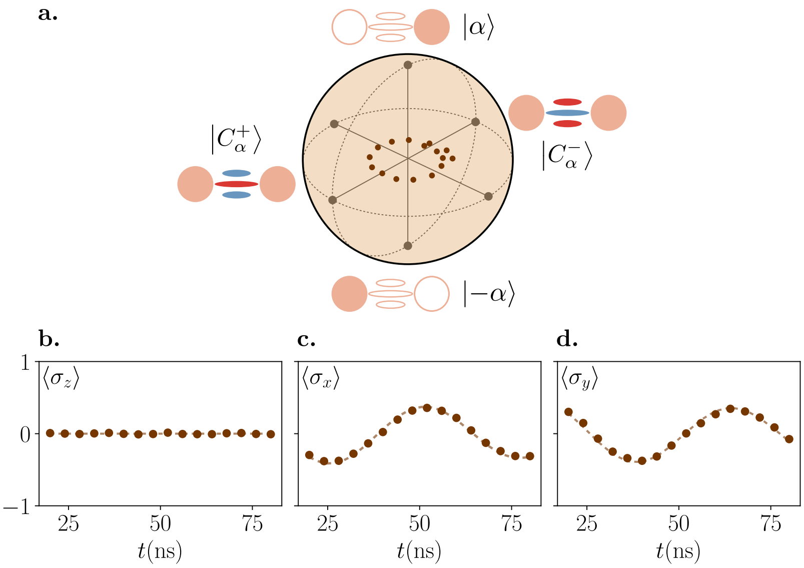

Figure 5.7: **a.** Trajectory of the cat qubit during the Z gate estimated from the Wigner functions of Fig. 5.3**a.** **b.** Dots: Mean value of $\hat{\sigma}_{z,L}$ as a function of the gate time. Line: Linear fit of $\langle\hat{\sigma}_{z,L}\rangle(t)$. **c.** Dots: Mean value of $\hat{\sigma}_{x,L}$ as a function of the gate time. Line: fit used in Fig. 5.3**b.** to oscillations at a frequency $\Omega_Z/2\pi = 19.8$ MHz, decaying at a rate $\kappa_Z/2\pi = 0.62$ MHz. A scaling factor of $\pi/2$ is applied since $W(0) = 2\langle\hat{\sigma}_{x,L}\rangle/\pi$. **d.** Dots: Mean value of $\hat{\sigma}_{y,L}$ as a function of gate time. Line: fit used in **c.** dephased by $\pi/2$.

Interestingly, the evolution of $\langle\hat{\sigma}_{z,L}\rangle(t)$ during the gate shows no visible evolution (Fig. 5.7**b.**), which is expected from its bias preserving property.

We then estimate $\rho_1^{'}$ and $\rho_2^{'}$ using Eq. (5.19). The density matrices $\mathcal{E}\left(|C_\alpha^+\rangle\langle C_\alpha^+|\right)$ and $\mathcal{E}\left(|C_\alpha^{+i}\rangle\langle C_\alpha^{+i}|\right)$ are deduced from the dynamics shown in Fig. 5.7**c.** and Fig. 5.7**d**. The evolutions of $\langle\hat{\sigma}_{x,L}\rangle$ and $\langle\hat{\sigma}_{y,L}\rangle$ are fitted to a damped oscillation at a frequency $\Omega_Z/2\pi = 19.8$ MHz, decaying at a rate $\kappa_Z/2\pi = 0.62$ MHz. From this, we can deduce

$$\begin{aligned}\mathcal{E}\left(|C_\alpha^+\rangle\langle C_\alpha^+|\right) &= \frac{1}{2}\left(\mathbb{1} - e^{-\pi\kappa_Z/\Omega_Z}\hat{\sigma}_{x,L}\right)\\ \mathcal{E}\left(|C_\alpha^{+i}\rangle\langle C_\alpha^{+i}|\right) &= \frac{1}{2}\left(\mathbb{1} - e^{-\pi\kappa_Z/\Omega_Z}\hat{\sigma}_{y,L}\right),\end{aligned} \tag{5.28}$$

which yields

$$\begin{aligned}\mathcal{E}\left(\left|\alpha\right\rangle\left\langle-\alpha\right|\right) &= -\frac{e^{-\pi\kappa_Z/\Omega_Z}}{2}\left(\hat{\sigma}_{x,L}+i\hat{\sigma}_{y,L}\right)\\ \mathcal{E}\left(\left|-\alpha\right\rangle\left\langle\alpha\right|\right) &= -\frac{e^{-\pi\kappa_Z/\Omega_Z}}{2}\left(\hat{\sigma}_{x,L}-i\hat{\sigma}_{y,L}\right);\end{aligned} \tag{5.29}$$

The matrix M defined in Eq. (5.22) then finally reads

$$M=\frac{1}{2}\begin{pmatrix}0 & 0\\ 0 & 1+e^{-\pi\kappa_Z/\Omega_Z}\end{pmatrix}. \tag{5.30}$$

From this expression we obtain the gate fidelity as $F=\left(1+\exp(-\pi\kappa_z/\Omega_z)\right)/2$. Using Gaussian pulses for the memory drive leads to $\hat{Z}(\pi)$ gate fidelities $F=95\pm2\%$ in 26 ns for $|\alpha|^2=9.3$ and for a drive amplitude $\bar{\epsilon}_Z/2\pi=1.625$ MHz. Note that the ±2% uncertainty is much larger than the error incurred from our assumption in Eq. (5.27). We further improve the gate fidelity by using square pulses. Indeed, for a fixed average drive amplitude $\bar{\epsilon}_Z$, the square pulse has the smallest maximum amplitude, hence induces the least non-adiabatic errors. We then reach $F=96.5\pm2\%$ in 28 ns for the Z gate.

5.1.3.4 *Evolution of the fidelity depending on the drive parameters*

The gate $\hat{Z}(\theta)$ is implemented for varying values of $\bar{\epsilon}_\mathrm{Z}$ and α. For each parameter set, an oscillation similar to Fig. 5.3**b.** is observed, from which the corresponding decay rate κ_Z and oscillation frequency Ω_Z are extracted. Fig. 5.8**a.** displays the fidelity $F=\left(1+\exp(-\pi\kappa_z/\Omega_z)\right)/2$ as a function of $\bar{\epsilon}_\mathrm{Z}$ and α, computed from the fitted values of κ_Z and Ω_Z. Two distinct regions can be observed, corresponding to a regime of high drive, small cat or low drive, large cat.

In the first regime where $\bar{\epsilon}_\mathrm{Z}\gg\kappa_2$ and $\alpha\sim1$, the drive amplitude is so large that the Zeno dynamics is not strong enough to prevent leakage from the cat qubit manifold. The memory state is then free to evolve after escaping from the dissipative confinement, and the parity of the refocused state (the drive is turned off so that the memory decays back to the cat manifold under the dissipation $\hat{L}_2=\sqrt{\kappa_2}\left(\hat{a}^2-\alpha^2\right)$) is not preserved. This limits the fidelity as evidenced by the blue region in Fig. 5.8**a**.

This issue can be mitigated by increasing the size $|\alpha|$ of the cat, which in turn increases the confinement rate $\kappa_\mathrm{conf}=2|\alpha|^2\kappa_2$ [102]. This makes the system resilient against larger drive amplitudes so that increasing Ω_Z produces fewer non-adiabatic errors. This is the regime of interest in order to reach the largest fidelities, as evidenced by the dark red region in Fig. 5.8**a.** and the star indicating the parameters yielding the best fidelity $F = 96.5 \pm 2\%$ in 28 ns.

We show in Fig. 5.8**b.** a simulation of the fidelity, where κ_{Z} and Ω_{Z} are computed using their theoretical expressions in Eq. (5.2) and Eq. (5.3). It closely matches the experimental data, indicating that even this simple model (which does not take into account effects such as the memory self-Kerr or possible detunings), provides an accurate description of the gate imperfections. Larger values of $|\alpha|$ could have been explored to improve the fidelity even further. However, simulations indicate this would only result in marginal improvements.

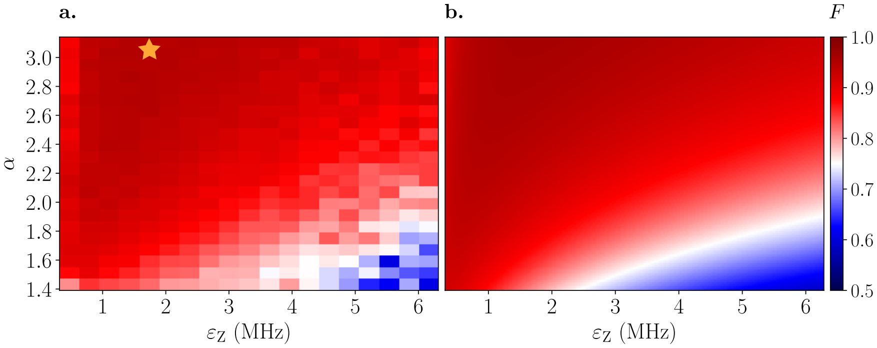

Figure 5.8: **a.** Measured fidelity $F = (1 + \exp(-\pi\kappa_z/\Omega_z))/2$ depending on drive amplitude $\bar{\epsilon}_{\text{Z}}$ and size of the cat α. The star indicates the parameters of the gate with the largest fidelity, shown in Fig. 5.3. **b** Predicted fidelity using Eq. (5.2) and Eq. (5.3) to predict κ_{Z} and Ω_{Z} from $\bar{\epsilon}_{\text{Z}}$ and α.

5.2 DEMONSTRATIONS OF THE GATES $\hat{Y}(\theta)$ AND $\hat{X}(\theta)$

Following the implementation of the $\hat{Z}(\theta)$ gate, we now focus on the experimental realization of the gates $\hat{X}(\theta)$ and $\hat{Y}(\theta)$ with the Auto-cat, thus demonstrating the universal control of a cat qubit.

The gate $\hat{X}(\theta)$ has already been realized experimentally for the special case $\theta = \pi$, which simply amounts to inverting $|\alpha\rangle$ and $|-\alpha\rangle$. To do so in a bias-preserving way [138], the encoding is continuously deformed by sweeping the phase λ of the buffer drive ϵ_d from 0 to 2π. As $\alpha = \pm\sqrt{-\epsilon_d/g_2^*}$, this induces a phase shift in the stabilized cat state, increasing from 0 to π. Consequently, the coherent states undergo the desired inversion, as shown in Fig. 5.9. Note that for this scheme to be effective, the timescale of this sweep needs to be slower than $\kappa_{\text{conf}}^{-1} = 1/(2\kappa_2|\alpha|^2)$, which ensures the memory remains in the state $\left|\pm|\alpha|e^{i\lambda/2}\right\rangle$ of the deformed cat encoding[2]. Implementing this gate in a bias-preserving way is crucial, notably in order to implement CNOT gates between two neighboring cat qubits in a repetition code [88].

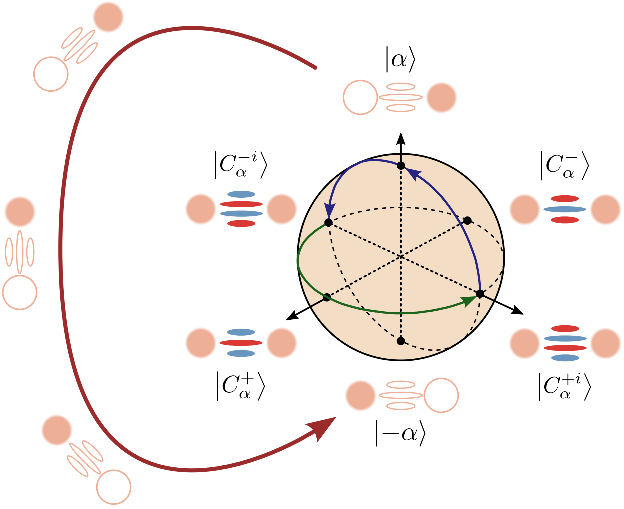

Figure 5.9: Representation of the bias preserving $\hat{X}(\pi)$ gate. If implementing this gate while remaining in the Bloch sphere of the cat, phase flip errors (green arrow) are free to occur during the operation of the gate (blue arrows), which are then converted into bit-flip errors. This is prevented by going out of the code space, continuously deforming the encoding (red arrow) such that the memory remains in the state $\left|+|\alpha|e^{i\lambda/2}\right\rangle$, with λ increasing from 0 to 2π in a time $t \gtrsim \kappa_{\text{conf}}^{-1}$.

The same approach cannot be extrapolated to implement a gate $\hat{X}$ or $\hat{Y}$ of an arbitrary angle θ, which requires a coherent population transfer between $|\alpha\rangle$ and $|-\alpha\rangle$. For instance, applying the gate $\hat{X}(\pi/2)$ on the coherent state $|\alpha\rangle$ should lead to an equal superposition of $|\alpha\rangle$ and $|-\alpha\rangle$, which cannot be realized by simply deforming the cat encoding. Intrinsically, this population transfer is incompatible with the engineered dissipation $\hat{L}_2 = \sqrt{\kappa_2}\left(\hat{a}^2 - \alpha^2\right)$, with $\alpha > 0$, which was specifically designed to prevent transitions from one coherent state to another. To circumvent this issue, we use the mapping shown in Fig. 5.10 between the cat manifold $\text{span}(|\alpha\rangle, |-\alpha\rangle)$ and the *deflated* manifold $\text{span}(|0\rangle, |1\rangle)$.

---

[2] Considering a single cat qubit, this gate can actually be simply performed with a virtual rotation. The described physical rotation only becomes necessary when considering two entangled cat qubits

Slowly turning off the buffer pump ϵ_d over a timespan $t \gtrsim \kappa_2^{-1}$, the memory adiabatically decays to $\text{span}\left(|0\rangle, |1\rangle\right)$ while preserving its parity due to the large ratio $\kappa_2/\kappa_1 = 150$. In this manifold, population transfer can be performed by either applying a coherent drive Zeno blocked by the two-photon dissipation (Sec. 5.2.1) or via a Holonomic approach based on the *collision* of the two coherent states (Sec. 5.2.2). After performing the desired operation, ϵ_d is turned back on and the memory state is mapped back to the cat qubit manifold.

Because the memory transitions through $\text{span}\left(|0\rangle, |1\rangle\right)$ during the operation of this gate, it can suffer from bit-flip errors which are not suppressed in this manifold. As a consequence, the designed gate $\hat{X}(\theta)$ is not bias-preserving. This cannot be avoided however as, in order to have a population transfer between $|\alpha\rangle$ and $|-\alpha\rangle$, a channel has to be created which allows for bit-flip errors.

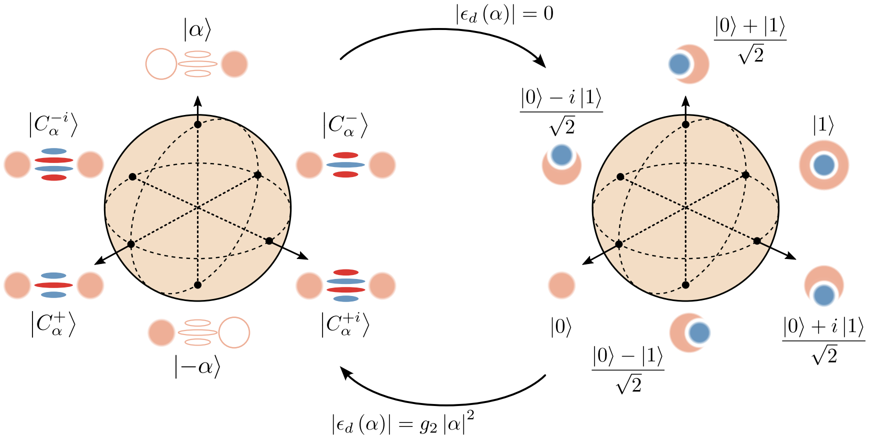

Figure 5.10: Mapping between the manifolds $\text{span}\left(|\alpha\rangle, |-\alpha\rangle\right)$ and $\text{span}\left(|0\rangle, |1\rangle\right)$. Turning on and off the buffer drive ϵ_d, the memory transitions between these two manifolds while preserving its parity.

5.2.1 *Zeno blocked oscillations in the manifold* $\text{span}\left(|0\rangle, |1\rangle\right)$

We first implement the gate $\hat{Y}(\theta)$ on the cat qubit by driving the memory on resonance at ϕ_{QEC} (Fig. 5.11**a**), after turning off the buffer drive to adiabatically map the cat qubit to $\text{span}\left(|0\rangle, |1\rangle\right)$. The memory evolution is described in this deflated manifold by the master equation

$$\frac{d\hat{\rho}}{dt} = -\frac{i}{\hbar}[\hat{H}, \hat{\rho}] + \mathcal{D}[\sqrt{\kappa_1}\hat{a}](\hat{\rho}) + \mathcal{D}[\sqrt{\kappa_\varphi^m}\hat{a}^\dagger\hat{a}](\hat{\rho}) + \mathcal{D}[\sqrt{\kappa_2}\hat{a}^2](\hat{\rho}), \tag{5.31}$$

with

$$\frac{\hat{H}}{\hbar} = -\frac{\chi_{\mathrm{m,m}}}{2}\hat{a}^{\dagger 2}\hat{a}^2 + \left(\epsilon_{\mathrm{Y}} e^{i\theta_{\mathrm{Y}}}\hat{a}^\dagger + h.c\right). \tag{5.32}$$

The dephasing rate $\kappa_\varphi^m/2\pi = 80$ kHz is estimated using a Ramsey like experiment (see Sec. 4.4.3.1), while the memory self-Kerr $\chi_{\mathrm{m,m}}/2\pi = 0.206$ MHz and single photon decay rate $\kappa_1/2\pi = 14$ kHz were respectively deduced from Fig. 3.8 and the decay of a single photon in the memory (Fig. 4.11**b**). As the memory contains at most 1 photon when applying the displacement drive, the condition $8g_2|\alpha| < \kappa_b$ is verified. This justifies the adiabatic elimination of the buffer mode and the effective two-photon dissipation $\sqrt{\kappa_2}\hat{a}^2$, with $\kappa_2 \approx 2$ MHz, appearing in the master equation.

Applying the memory displacement while at ϕ_{QEC} implements the desired quantum Zeno dynamic, with the two-photon dissipation preventing the memory from leaking out of the deflated manifold. Furthermore, ensuring the drive is parallel to the direction of the stabilized cat ($\epsilon_{\mathrm{Y}} \in \mathbb{R}$ and $\theta_{\mathrm{Y}} = 0$) results in coherent oscillations between $|0\rangle$ and $|1\rangle$ as the memory state rotates around the $\mathbf{y}$ axis of the Bloch sphere. The buffer drive is then turned back on, which maps the memory back onto the cat manifold. The experimental realization of this gate is shown in Fig. 5.11**b-d.** for a fixed displacement amplitude ϵ_{Y} and varying duration t. When no displacement is applied for $t = 0$, the memory remains in $|0\rangle$ which is then mapped to $|C_\alpha^+\rangle$ after turning the buffer drive back on. When applying the displacement drive for 1.6 μs and 2.6 μs, the desired Zeno dynamic is observed with the memory evolving towards $(|0\rangle + |1\rangle)/\sqrt{2}$ and $|1\rangle$ respectively. These states are then mapped onto the cat manifold to states resembling $|\alpha\rangle$ and $|C_\alpha^-\rangle$. However, a noticeable deviation from these ideal states can be seen after the gate, which is particularly visible in the poorly contrasted fringes of what should be $|C_\alpha^-\rangle$.

These errors can be explained by the relatively long duration of the displacement pulse during which memory dephasing makes the state superposition decohere. Indeed, for the Zeno dynamic to be effective and prevent leakage from the deflated manifold span$(|0\rangle, |1\rangle)$, the displacement amplitude ϵ_{Y} needs to be smaller than the two-photon dissipation rate κ_2. This constraint is notably much stricter than for the $\hat{Z}(\theta)$ gate previously presented, as in this case, the Zeno dynamic is effective even for $\kappa_2 < \epsilon_{\mathrm{Z}} < \kappa_{\mathrm{conf}}$. A gate

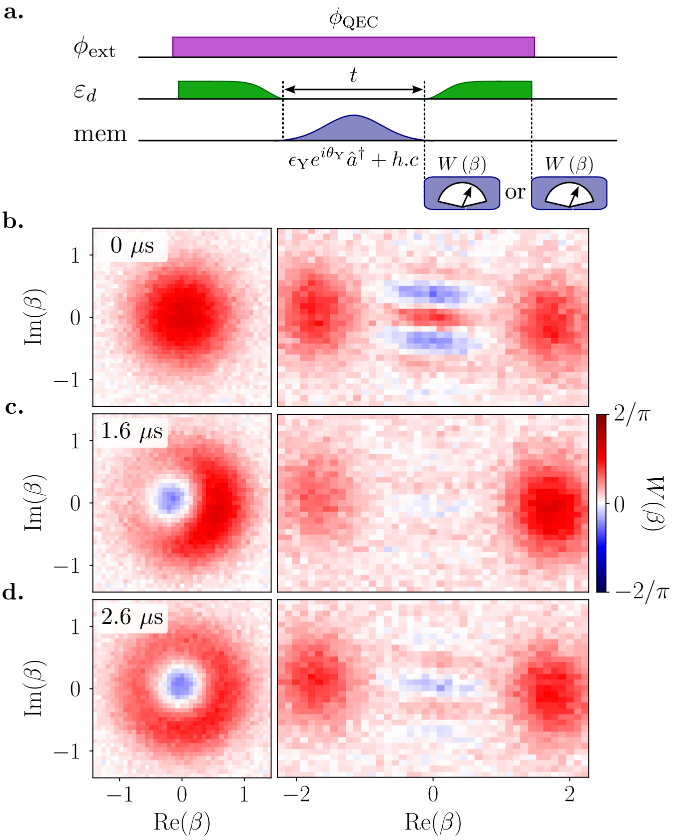

Figure 5.11: **a.** Pulse sequence for the gate $\hat{Y}(\theta)$. After turning off the buffer drive, and mapping the memory state onto the deflated manifold, a displacement of amplitude ϵ_{Y} is applied to the memory that induces the desired Zeno dynamic. The memory is then mapped back onto the cat encoding by turning the buffer drive back on. Wigner tomography is performed after the displacement or at the end of the pulse sequence **b.** Memory vacuum state $|0\rangle$ when no memory displacement is applied (left) and the corresponding mapping to $\left|C_\alpha^+\right\rangle$. **c.** Memory state $\approx (|0\rangle + |1\rangle)/\sqrt{2}$ after displacing the memory for $t = 1.6$ μs while at ϕ_{QEC} (left). The memory should then be mapped to $|\alpha\rangle$ (right) **d.** Memory state $\approx |1\rangle$ after applying the drive ϵ_{Y} for $t = 2.6$ μs (left), ideally mapped to $\left|C_\alpha^-\right\rangle$ in the cat encoding (right).

$\hat{Y}(\pi)$ would then take at least around 1 μs. In contrast, working at large values of $|\alpha|$ for the $\hat{Z}(\theta)$ gate allows us to increase ϵ_{Z} and perform $\hat{Z}(\pi)$ gate in tens of ns. The main source of errors during this 1 μs spent in the deflated manifold is not single-photon loss, as is the case for the $\hat{Z}(\theta)$ gate, but memory dephasing. While dephasing does not impact the fidelity of the $\hat{Z}(\theta)$ gate thanks to the phase space separation between $|\alpha\rangle$ and $|-\alpha\rangle$, the manifold $\mathrm{span}(|0\rangle, |1\rangle)$ does not benefit from this protection. As a consequence, memory dephasing induces decoherence during the displacement at a rate κ_φ^m, resulting in decohere cat states after re-inflation. We see in particular in Fig. 4.17 that quantum information is almost completely lost after 5 μs. Note that, as $\kappa_\varphi^m \sim 6\kappa_1$, the memory dephasing is indeed the main source of decoherence and not single-photon loss.

This issue could be mitigated by reducing the memory dephasing rate, in particular by making sure that $\phi_{\mathrm{QEC}} = \phi_{\mathrm{ext}}^{(\mathrm{sweet})}$ (see Sec. 3.5.4) in future iterations of this device. Alternatively, one could use an alternative approach for the gate which does not rely on Zeno dynamic and does not require spending significant time in $\mathrm{span}(|0\rangle, |1\rangle)$. We use such an approach in the following section and implement a *Holonomic* $\hat{X}(\theta)$ gate.

5.2.2 *Holonomic approach*

5.2.2.1 *Optimisation of the gate*

We implement the proposal of [191] to realize a holonomic $\hat{X}(\theta)$ gate on a cat qubit. This gate relies on the observation that, applying a rotation $\hat{R}(\theta) = e^{i\theta\hat{a}^\dagger\hat{a}}$ on a superposition of well-separated coherent states, does not impact the phase of the superposition. On the opposite, doing the same operation on the superposition of $|0\rangle$ and $|1\rangle$ does. Following this property, the gate $\hat{X}(\theta)$ is realized by simply modulating the buffer drive amplitude $\epsilon_d(\alpha)$ (Fig. 5.12**a.**).

The memory state is first mapped onto the deflated manifold $\mathrm{span}(|0\rangle, |1\rangle)$, after which the buffer drive is immediately turned back on with an additional phase 2θ. This additional phase acts as a $\hat{R}(\theta)$ rotation while the memory is in the manifold $\mathrm{span}(|0\rangle, |1\rangle)$, which is then compensated by a final counter-rotation $\hat{R}(-\theta)$. This final rotation brings the memory back onto the initial code space while preserving the phase of the superposition. The evolution of the memory in phase space starting from $|\alpha\rangle$ is represented in Fig. 5.12**b**. Compared to the $\hat{Y}(\theta)$ gate, the memory does not remain for a prolonged time in the deflated manifold as the buffer drive is immediately turned back on. This limits the amount of time during which memory dephasing corrupts the logical information, which should yield better fidelities.

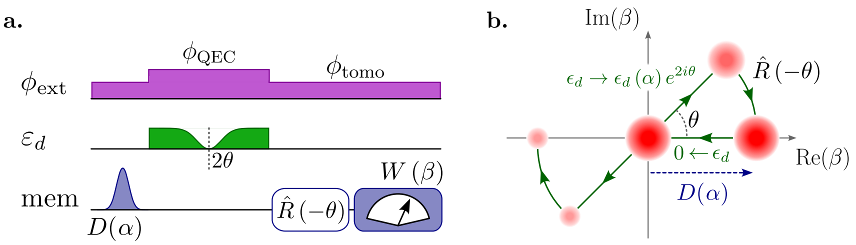

Figure 5.12: **a.** Pulse sequence used to prepare an initial state $|\alpha\rangle$ in the memory, apply the holonomic $\hat{X}(\theta)$ gate for an arbitrary angle θ, and measure the memory Wigner function. The Holonomic gate consists in the modulation of $\epsilon_d(\alpha)$ to deflate the cat state to span $(|0\rangle, |1\rangle)$, apply a virtual rotation of 2θ by changing the phase of the buffer drive, and re-inflate the cat back to the cat manifold. A final virtual rotation $\hat{R}(-\theta)$ is applied by adding a phase $-\theta$ to the memory displacement drive, which stabilizes the direction of the cat. **b.** Evolution in the memory phase space of a coherent state when applying the holonomic $\hat{X}(\theta)$ gate.

We describe the evolution of the joint memory & buffer system using the master equation[3]

$$\begin{aligned}\frac{d\hat{\rho}}{dt} = &-\frac{i}{\hbar}[\hat{H}(t), \hat{\rho}] + \mathcal{D}[\sqrt{\kappa_1}\hat{a}](\hat{\rho}) + \mathcal{D}[\sqrt{\kappa_\varphi^m}\hat{a}^\dagger\hat{a}](\hat{\rho}) \\ &+ \mathcal{D}[\sqrt{\kappa_b}\hat{b}](\hat{\rho}) + \mathcal{D}[\sqrt{\kappa_\varphi^b}\hat{b}^\dagger\hat{b}](\hat{\rho}),\end{aligned} \tag{5.33}$$

with the time-dependent Hamiltonian expressed as

$$\begin{aligned}\frac{\hat{H}(t)}{\hbar} = &-\frac{\chi_{\text{m,m}}}{2}\hat{a}^{\dagger 2}\hat{a}^2 - \frac{\chi_{\text{b,b}}}{2}\hat{b}^{\dagger 2}\hat{b}^2 - \chi_{\text{m,b}}\hat{a}^\dagger\hat{a}\,\hat{b}^\dagger\hat{b} \\ &+ g_2\hat{a}^2\hat{b}^\dagger + g_2^*\hat{a}^{\dagger 2}\hat{b} + \epsilon_d(t)\hat{b}^\dagger + \epsilon_d^*(t)\hat{b}.\end{aligned} \tag{5.34}$$

The values of the different parameters are summarized in Table. 4.1. To optimize the gate fidelity, we perform numerical simulations for various shapes of the buffer drive $\epsilon_d(t)$, while enforcing some conditions on the drive. First, because the gate starts and finishes in the cat manifold, this gives a first constraint on $\epsilon_d(t)$

$$|\epsilon_d(0)| = |\epsilon_d(T_{\text{tot}})| = |\epsilon_\alpha|, \tag{5.35}$$

---

[3] We do not adiabatically eliminate the buffer as, in order to optimize the gate, we are interested in the transition period between the manifolds span $(|\alpha\rangle, |-\alpha\rangle)$ and span $(|0\rangle, |1\rangle)$ during which the condition $8g_2\alpha < \kappa_b$ is not necessarily verified.

with T_{tot} the total duration of the gate and $|\epsilon_\alpha|$ the drive amplitude stabilizing a cat state of size $|\alpha|$. The second constraint comes from the necessity for the memory to transit through $\text{span}(|0\rangle, |1\rangle)$ in order to realize the desired population transfer. This can be mathematically expressed as

$$\exists\, \tau,\ 0 \leq \tau \leq T_{\text{tot}},\ \epsilon_d(\tau) = 0. \tag{5.36}$$

We choose $\tau = T_{\text{tot}}/2$ due to the symmetry between the deflation and re-inflation step of the gate. Furthermore, using the same symmetry argument, we impose that the evolution of $\epsilon_d(t)$ is symmetric around τ. Finally, we choose a Gaussian edge shape for the evolution of the buffer drive for $0 \leq t \leq \tau$. This choice is motivated by the observation that, while $\epsilon_d(t)$ needs to evolve on timescales longer than $\kappa_{\text{conf}}^{-1}$ in order for the gate to remain adiabatic, faster evolutions are allowed for large $|\alpha|$ at the beginning and end of the gate. The buffer drive is then parameterized as

$$\begin{aligned} \epsilon_d(t) =& \frac{\epsilon_\alpha}{1 - e^{-\tau^2/(2\sigma^2)}} \left(e^{-t^2/(2\sigma^2)} - e^{-\tau^2/(2\sigma^2)} \right) \text{ for } 0 \leq t \leq \tau, \\ & \frac{\epsilon_\alpha e^{2i\theta}}{1 - e^{-\tau^2/(2\sigma^2)}} \left(e^{-(2\tau - t)^2/(2\sigma^2)} - e^{-\tau^2/(2\sigma^2)} \right) \text{ for } \tau \leq t \leq 2\tau. \end{aligned} \tag{5.37}$$

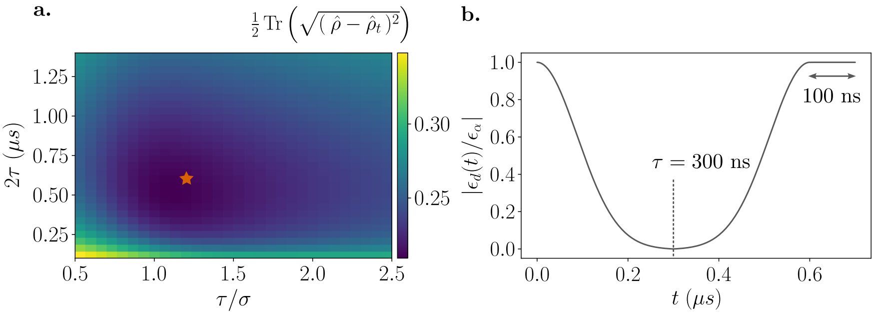

Figure 5.13: **a.** Evolution, as a function of τ and τ/σ, of the trace distance between the simulated density matrix after application of the gate and the ideal desired state. The star indicates the optimal parameters chosen for the following experiments. **b.** Evolution of $|\epsilon_d(t)|$ for the chosen parameters τ and σ. A final stabilization time of 100 ns is added after the gate to ensure the memory converges to the manifold $\text{span}(|\alpha\rangle, |-\alpha\rangle)$.

We optimize the parameters τ and σ of this pulse by simulating the evolution of the memory according to Eq. (5.33). Starting from $|\alpha\rangle$, we compare the simulated density matrix $\hat{\rho}$ after the gate for $\theta = \pi/2$ with the target $\hat{\rho}_t = \hat{X}\left(\pi/2\right)|\alpha\rangle\langle\alpha|\hat{X}^\dagger\left(\pi/2\right)$. The metric used to compare these two density matrices is the trace distance [72], defined as

$$T\left(\hat{\rho},\hat{\rho}_t\right) = \frac{1}{2}\mathrm{Tr}\left(\sqrt{\left(\hat{\rho}-\hat{\rho}_t\right)^2}\right) \tag{5.38}$$

The optimization shown in Fig. 5.13**a.** provides the parameters $\tau = 300$ ns and $\sigma = \tau/1.2 = 250$. The corresponding waveform for $|\epsilon_d(t)|$ is presented in Fig. 5.13**b.** and is used for the following measurements.

5.2.2.2 *Dynamic of the Holonomic gate*

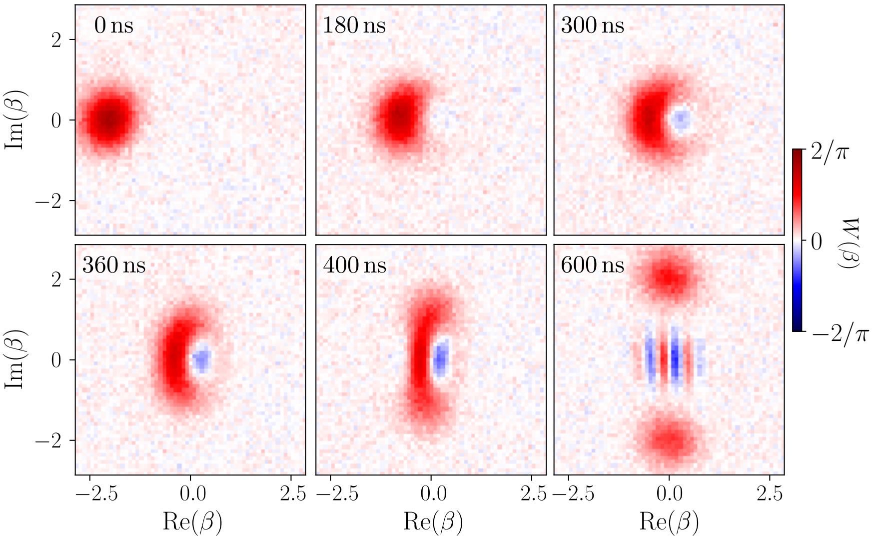

Figure 5.14: Measured evolution of the memory Wigner function, starting from the coherent state $|-2.27\rangle$, during the holonomic $\hat{X}\left(\pi/2\right)$ gate. The evolution of $\epsilon_d(t)$ is that shown in Fig. 5.13**b.**. The final rotation $\hat{R}(-\theta)$ is not applied to highlight the dynamic of the memory during the gate.

We experimentally realize the gate $\hat{X}\left(\pi/2\right)$ starting from the coherent state $|-\alpha\rangle$, $\alpha = 2.27$, without applying the final rotation $\hat{R}(-\theta)$ (see Fig. 5.12**a.**). The coherent state $|-\alpha\rangle$ is encoded by resonantly driving the memory at ϕ_{tomo} for 20 ns, effectively inducing the displacement $\hat{D}\left(-\alpha\right)$, after which the flux is immediately set to ϕ_{QEC} while driving the buffer with a drive amplitude $\epsilon_d(\alpha)$. The system is then left idle for 100 ns to ensure the memory converges to the manifold span $\left(|\alpha\rangle, |-\alpha\rangle\right)$, correcting for small miscalibration of the initial memory displacement. As $T_{\mathrm{X}} \sim 50\ \mu$s for $|\alpha| = 2.27$, we assume a perfect preparation of $|-\alpha\rangle$ before applying the gate.

We show in Fig. 5.14 the Wigner tomography of the memory for 6 different times during the gate. Between 0 ns and 300 ns, the memory adiabatically decays from the the coherent state $|-\alpha\rangle$ to the corresponding state $(|0\rangle - |1\rangle)/\sqrt{2}$ in the deflated manifold. After applying a phase shift $e^{i\pi}$, the buffer drive is slowly turned back on in 300 ns (Fig. 5.13**b.**) and the memory adiabatically evolves towards the state $\left(\left|e^{i\pi/2}\alpha\right\rangle - i\left|-e^{i\pi/2}\alpha\right\rangle\right)/\sqrt{2}$. This state would be brought back to $(|\alpha\rangle - i|-\alpha\rangle)/\sqrt{2}$ by a rotation $\hat{R}(-\pi/2)$, thus performing the desired $\hat{X}(\pi/2)$ gate.

5.2.2.3 *Fidelity of the gate*

We repeat the operation presented in Sec. 5.2.2.2 for varying values of θ and characterize the performance of the gate. Because we only performed the gate $\hat{X}(\theta)$ starting from the coherent state $|-\alpha\rangle$, we cannot use the formalism of the process χ matrix to characterize the gate fidelity[4]. Instead, we use the trace distance between the memory density matrix $\hat{\rho}$ estimated after the gate and $\hat{\rho}_t = \hat{X}(\pi/2)|-\alpha\rangle\langle-\alpha|\hat{X}^{\dagger}(\pi/2)$. The density matrix $\hat{\rho}$ is estimated from the measured Wigner function shown in Fig. 5.15**a.** using Maximum Likelihood Estimation (MLE). We impose that the density matrix belongs to the cat qubit manifold $\mathrm{span}(|\alpha\rangle, |-\alpha\rangle)$, with α being deduced from the position of the coherent states in the Wigner function.

The dependence of the trace distance with θ is shown in Fig. 5.15**b.**. A non-trivial evolution can be observed with a trace distance $T(\hat{\rho}, \hat{\rho}_t) \approx 0.18$ for $\theta = \pm\pi,\ 0$ and $T(\hat{\rho}, \hat{\rho}_t) \approx 0.23$ for $\theta = \pm\pi/2$. We attribute this degradation for $\theta = \pm\pi/2$ to phase-flip errors occurring during the re-inflation step of protocol and the final 100 ns of stabilization (see Fig. 5.13**b.**). Indeed, while for $\theta = \pm\pi,\ 0$ the memory ends up in the coherent states $|\pm\alpha\rangle$ which are unaffected by phase flip errors, the states $C_{\alpha}^{\pm i}$ do not benefit from the same protection and lose their coherence at a rate $\Gamma_{\mathrm{Z}} = 2\bar{n}\kappa_1$.

We simulate the evolution of the trace distance according to the master equation Eq. (5.33), with the optimized buffer drive amplitude shown in

---

[4] We actually expect the gate to perform the best when starting from $\left|C_{\alpha}^{+}\right\rangle$ and $\left|C_{\alpha}^{-}\right\rangle$ which are respectively mapped to $|0\rangle$ and $|1\rangle$. Both these states are unaffected by dephasing errors, the main source of decoherence in the manifold $\mathrm{span}(|0\rangle, |1\rangle)$, which isn't the case for other cardinal states of the Bloch sphere. The other error channel affecting the memory, single photon loss, would induce a decay $|1\rangle \rightarrow |0\rangle$ with a probability $p = 1 - e^{-t_{0/1}\kappa_1}$. There, $t_{0/1}$ is the time during which the memory transitions to the deflated manifold, estimated to $t_{0/1} \approx 200$ ns (see Fig. 5.13**b.**), which gives $\mathrm{p} = 0.003$.

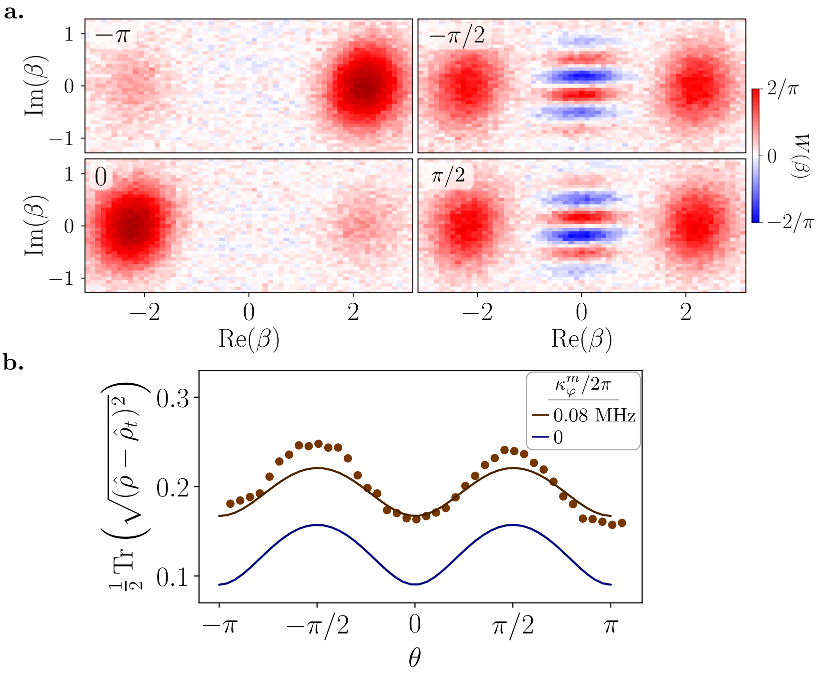

Figure 5.15: **a.** Measured Wigner function $W(\beta)$ after performing the gate $\hat{X}(\theta)$, starting from the coherent state $|-\alpha\rangle$. The angle θ corresponding to each Wigner function is indicated as an inset. **b.** Dots: Trace distance between the density matrices $\hat{\rho}$ estimated from the Wigner functions of **a.** and $\hat{\rho}_t = \hat{X}(\theta)|-\alpha\rangle\langle-\alpha|\hat{X}^\dagger(\theta)$. Lines: Simulated trace distance for $\kappa_\varphi^{\mathrm{m}}/2\pi = 0.08$ MHz (brown line) and $\kappa_\varphi^{\mathrm{m}}/2\pi = 0$ MHz (blue line).

Fig. 5.13**b**. Using the measured dephasing rate $\kappa_\varphi^{\mathrm{m}}/2\pi = 0.08$ MHz, we qualitatively reproduce the experimental results, the trace distance being slightly underestimated for $\theta = \pm\pi/2$. Additional simulations for $\kappa_\varphi^{\mathrm{m}}/2\pi = 0$ indicate that reducing to dephasing rate[5] could reduce the trace distance by ≈ 0.08 using the same pulse parameters. Note that, as the optimization of $\epsilon_d(t)$ was performed using the measured value of $\kappa_\varphi^{\mathrm{m}}$, it is not optimal for $\kappa_\varphi^{\mathrm{m}} = 0$.

We finally study the trajectory of the memory in the Bloch sphere of the cat qubit, shown in Fig. 5.16**a.**. It presents the desired rotation around the logical **x** axis, with $\langle\hat{\sigma}_{x,L}(\theta)\rangle$ showing no visible dependence on θ (Fig. 5.16**b.**). Its small mean value $\langle\hat{\sigma}_{x,L}\rangle = 0.02$ can be attributed to single-photon loss. Indeed, during a ≈ 200 ns spent in the manifold span $(|0\rangle, |1\rangle)$, single-photon

---

[5] For instance by ensuring $\phi_{\mathrm{QEC}} = \phi_{\mathrm{ext}}^{(\mathrm{sweet})}$ in future iterations of the Auto-cat.

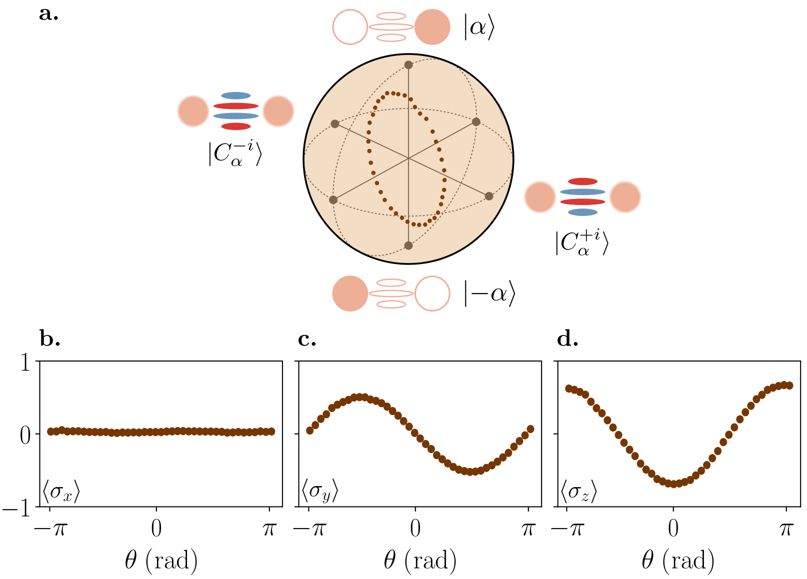

Figure 5.16: **a.** Trajectory of the cat qubit during the $\hat{X}(\theta)$ gate estimated from the Wigner functions of Fig. 5.15 **b.** Mean value of $\hat{\sigma}_{x,L}$ as a function of the parameter θ. **c.** Mean value of $\hat{\sigma}_{y,L}$ as a function of the parameter θ. **d.** Mean value of $\hat{\sigma}_{z,L}$ as a function of the parameter θ.

loss induces the decay $|1\rangle \rightarrow |0\rangle$ which increases the population of even Fock states once the state is mapped back onto the cat manifold. The two remaining quadratures $\langle\hat{\sigma}_{y,L}(\theta)\rangle$ and $\langle\hat{\sigma}_{z,L}(\theta)\rangle$ exhibit the expected oscillations (Fig. 5.16**c-d.**), with a phase shift of $\pi/2$ between the 2 curves. A small phase shift of 0.12 rad is observed, particularly noticeable in Fig. 5.16**d.** where $\langle\hat{\sigma}_{z,L}(\theta)\rangle$ is not symmetric around the axis $\theta = 0$. This can be explained with an additional detuning $\Delta_m \hat{a}^\dagger \hat{a}$, $\Delta_m/2\pi = 90$ kHz to the Hamiltonian of Eq. (5.34). This induces a rotation in the memory phase space when in the manifold $\mathrm{span}(|0\rangle, |1\rangle)$, with no impact when the 2-photon dissipation stabilizes $\mathrm{span}(|\alpha\rangle, |-\alpha\rangle)$ at a rate $\kappa_2 \gg \Delta_m$.

5.3 PREPARATION OF SQUEEZED CAT STATES

In this brief section, we shift our focus to the dynamics of the memory during its decay towards $\mathrm{span}(|0\rangle, |1\rangle)$ under two-photon dissipation. This particular evolution was already observed experimentally in Fig. 5.14, starting from the coherent state $|-\alpha\rangle$ where $\alpha = 2.27$. The observed evolution then corresponds to what is expected from a cavity losing pairs of photons to its environment under the loss operator $\sqrt{\kappa_2}\hat{a}^2$. The situation changes however for larger cat states where coherent states exhibit noticeable squeezing throughout the decay. Indeed, for cat states with $\alpha \gtrsim 2.5$, the system of memory & buffer is deep in the non-adiabatic regime where $8\,|g_2|\,\alpha \gg \kappa_b$, making it necessary to take the buffer dynamic into account.

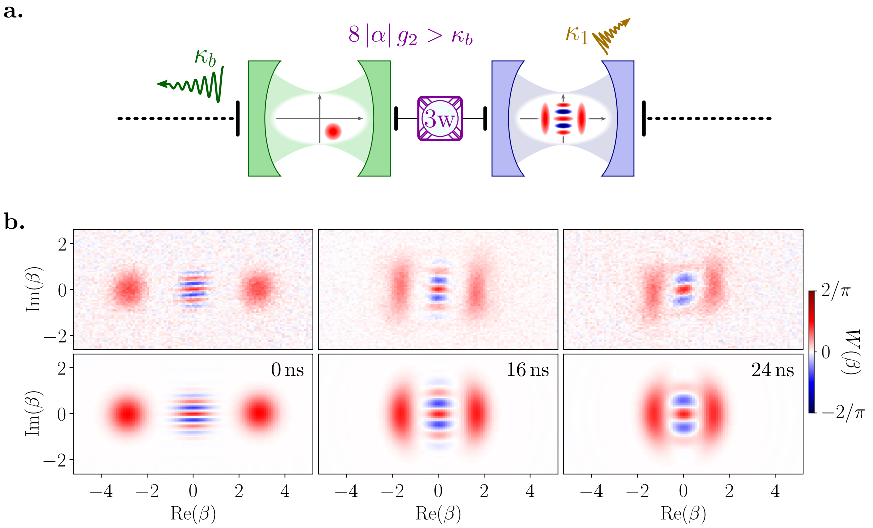

Figure 5.17: **a.** Impact of the two-photon loss on the memory and buffer mode. While the memory loses pairs of photons to the buffer at a rate $g_2\alpha^2$, the buffer cannot evacuate these photons quickly enough leading to an effective displacement $D(\gamma)$ of mode $\hat{b}$. This creates an effective squeezing Hamiltonian acting on the memory during its decay to the $\{|0\rangle, |1\rangle\}$ manifold. **b.** Wigner functions of the memory at 3 different times of its evolution towards the deflated manifold, starting from $|C_\alpha^+\rangle$. The data (top) are compared with numerical simulations made with no free parameters (bottom).

We characterize this process by looking at the impact of two-photon dissipation on $|C_\alpha^+\rangle$. After preparing the state $|C_\alpha^+\rangle$ in the memory, the drive $\epsilon_d(\alpha)$ is turned off while remaining at ϕ_{QEC}. After a varying time t, the memory state is then measured using the modified Wigner tomography sequence, with the resulting Wigner functions shown in Fig. 5.17**b.** for three different times. Initially, with the cavity in $|C_\alpha^+\rangle$ and the buffer in its ground state, the system is described by the Hamiltonian and loss operators of Eq. (5.33). As the memory releases photon pairs to the buffer, it can be described as an effective drive acting on mode $\hat{b}$, characterized by an amplitude $\langle g_2\hat{a}^2\rangle = g_2\alpha^2$ This drive, which should not have an impact on the buffer if $\kappa_b \gg 8g_2\alpha$, then displaces mode $\hat{b}$ to a coherent state $|\gamma\rangle$ whose amplitude is proportional to α^2 (Fig. 5.17**a**). In turn, the memory sees a squeezing Hamiltonian

$$\hat{H}_{\mathrm{m,eff}}/\hbar = g_2 \left\langle \hat{b} \right\rangle \hat{a}^{\dagger 2} + h.c, \tag{5.39}$$

which compresses the superposition of coherent states. As the memory evolves, it reaches a maximal compression at a time depending on the initial photon number, after which the buffer decays to vacuum suppressing the effective squeezing Hamiltonian. A maximal compression of 3.88 dB was observed after a time $t = 16$ ns, starting from a state $|C_\alpha^+\rangle$ where $\alpha = 2.9$ (Fig. 5.17**b**). We compare the evolution predicted by our theoretical model with the measured Wigner functions of the memory, which yields a good qualitative correspondence. While bigger compression is expected starting with a larger photon number, we experimentally observe that going to larger values of α leads to a deformation of the initial cat state (see Sec. 4.4.4.3), preventing the observation of larger maximal squeezing.

5.4 CHAPTER SUMMARY

In this chapter, we presented how the large 2-to-1 photon coupling of the Auto-cat can be leveraged to perform gates on the cat qubit, allowing full control of a single cat qubit. Using Zeno dynamics, with two-photon dissipation preventing leakage from the stabilized manifold while driving the memory, we demonstrate a $\hat{Z}$ and $\hat{Y}$ gate. While the $\hat{Y}$ gate has a relatively low fidelity, mainly due to the memory dephasing which induces decoherence during the gate, we perform a gate $\hat{Z}(\pi)$ with 96.5 % fidelity in 28 ns. This fidelity was achieved for a cat with $|\alpha|^2 = 9.3$, which increases the confinement rate $\kappa_{\mathrm{conf}} = 2\kappa_2|\alpha|^2$ and allows us to perform fast gates, thus limiting the impact of dissipation channels. We additionally implement a proposal from [191] and demonstrate a holonomic $\hat{X}$ gate, based on the collision of 2 coherent states. We observe the desired oscillations around the $\mathbf{x}$ axis of the logical Bloch sphere and a trace distance $T(\hat{\rho}, \hat{\rho}_t) \approx 0.2$ with the desired theoretical density matrix. This figure could be improved by operating closer to the memory sweet spot, thus decreasing the memory dephasing rate. Finally, we demonstrate how working deep in the non-adiabatic regime enables the preparation of squeezed cat states, reaching a maximal squeezing of 3.88 dB.

6

CONCLUSION AND PERSPECTIVES

In this thesis, we investigated the role of Quantum Error Correction in preserving the quantum information stored within superconducting circuits. By redundantly encoding this information across many physical qubits, thus defining a logical qubit, this approach ensures that errors impacting an isolated physical qubit can be detected and corrected without collapsing the state of the logical qubit. Various encoding schemes have been envisioned, with the CSS surface code emerging as a leading contender, notably investigated by industry giants like Google and IBM. However, the error threshold of this encoding remains relatively high, with no experiment reaching the break-even point so far. This motivates using an alternative encoding, capitalizing on noise biases within the physical qubits to increase the code's threshold. Such a code would be the XZZX surface code when the bias remains moderate, or a simple repetition code when the noise bias is sufficiently large so that either bit-flip or phase-flip errors can be neglected.

A promising qubit candidate showcasing the necessary noise bias is the cat qubit, which encodes information in the superposition of the coherent states $|\alpha\rangle$ and $|-\alpha\rangle$ of a superconducting cavity. The redundancy required for QEC is then provided by the infinite dimension of this Hilbert space, easing the hardware requirement of error-correcting codes by compactly encoding the quantum information into multi-photon states of a memory mode. When stabilized, using measurement-based feedback, Hamiltonian engineering, or dissipation engineering, these states exhibit an exponential suppression of bit-flip errors with $|\alpha|^2$ at the modest cost of a linear increase in the phase-flip rate. However, despite having observed this exponential suppression in dissipative cat qubits, the achieved bit-flip time and gate fidelities remained limited by the two-photon dissipation rate $\kappa_2/2\pi$ which did not exceed 200 kHz.

We improve on this figure by introducing the Auto-cat design, leveraging an autoparametric 3-wave mixing interaction to induce the desired dissipation. We measure a dissipation rate $\kappa_2/2\pi \approx 2$ MHz, which we exploit in order to improve on the usual parity measurement protocol. This alternative measurement method does not rely on the autoparametric approach and can be used whenever $\kappa_2 \gg \kappa_1$, which was previously achieved using a transmon mediating a 4-wave mixing interaction.

The cat qubit stabilized using the Auto-cat exhibits the expected exponential improvement of T_{X}, reaching $T_{\mathrm{X}} \approx 0.3$ s for $|\alpha|^2 \approx 20$ photons. Additionally, we harnessed the strong two-photon dissipation to perform fast gates, demonstrating a Holonomic $\hat{X}$ gate of an arbitrary angle θ in 600 ns. Furthermore, we execute a Zeno-blocked $\hat{Z}(\pi)$ gate with 96.5 % fidelity in 28 ns.

The natural evolution of this experiment as we look ahead, other than further improving this design so that $\phi_{\mathrm{QEC}} = \phi_{\mathrm{ext}}^{(\mathrm{sweet})}$ and increasing κ_2, is to correct for the remaining phase flip-errors. This could notably be done by using a repetition code of cat qubit, with several theoretical proposals exploring the performance of such a code. In the conclusion of this thesis, we present an alternative approach that employs frequency combs to preserve the parity of the memory mode. This project was the initial focus of my research during the first year of my PhD. Still, fabrication issues yielding poor transmon lifetimes prevented us from seeing the expected parity stabilization.

6.1 PARITY STABILIZATION

The states $|C_\alpha^+\rangle$ and $|C_\alpha^-\rangle$ of a two-component cat qubit each possess a distinct photon number parity, as evidenced by Eq. (3.46) which provides their expansion in the Fock basis. Phase-flip errors induced by single photon loss thus cannot be corrected by stabilizing a given photon number parity, and would for instance require the use of a repetition code of cat qubits. The situation changes however when considering four-component cat qubits. Here, stabilizing the manifold of even or odd Fock states protects the encoding against bit-flip errors, phase-flips being exponentially suppressed by an engineered dissipation. In this section, we first describe how the parity can be stabilized using measurement-based feedback or dissipation engineering, before explaining how this protection can be combined with a 4-photon dissipation to autonomously stabilize a fully protected logical qubit.

In measurement-based feedback, the parity of the memory is regularly measured after which a recovery operation is applied if any change in the parity is detected. To ensure the effectiveness of this method, the time interval between two parity measurements should verify $\tau \ll 1/\kappa_1$ so that no pairs of single photon loss can occur while remaining unnoticed. Alternatively, photon loss events can be corrected by engineering a dissipation whose operator is expressed as

$$\hat{\Pi} = \sum_k |2k\rangle \langle 2k-1| \,. \tag{6.1}$$

As represented in Fig. 6.1, this dissipation autonomously stabilizes the subspace of even Fock states, adding a photon wherever one is lost to the environment. Conversely, we can opt for an alternative dissipation choice that stabilizes the odd subspace by choosing $\hat{\Pi} = \sum_k |2k+1\rangle \langle 2k|$.

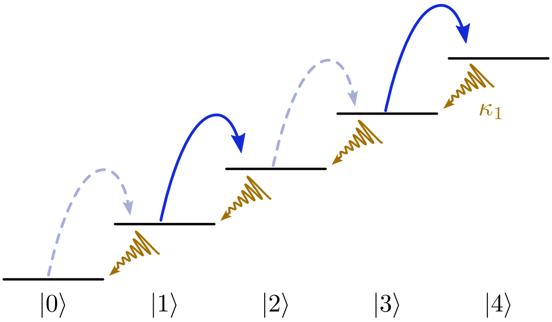

Figure 6.1: Stabilisation of even Fock states using the dissipation operator defined in Eq. (6.1). Whenever a photon is lost to the environment at a rate κ_1, a recovery operation is applied which adds a photon to the memory, bringing it back into the even Fock states manifold. Erroneous excitations from the even manifold due to the stabilization scheme are represented by the dashed blue arrows.

6.1.1 *Frequency combs to stabilize the parity of a memory*

Such a dissipation was experimentally demonstrated in [148, 198], using a transmon qubit dissipatively coupled to a memory and buffer modes (Fig. 6.2). When operated in the photon number resolved regime, two frequency combs can then be applied to the transmon which induce the desired dynamic. The first comb adds a photon to the memory whenever it initially contains an odd number of photons, simultaneously exciting the transmon to its second excited state $|f\rangle$. However, because information about the memory photon number is now encoded in the transmon's frequency, an unread measurement of the transmon by the environment would collapse the memory to the corresponding Fock state. This can be prevented by erasing this information, using a second frequency comb which transfers the excitation to a buffer mode. This lossy mode finally quickly decays at a rate κ_b through a transmission line. The effect of these frequency combs is represented in Fig. 6.3[1].

The Hamiltonian describing the system of Fig. 6.2 can be written as

---

[1] The pulse sequence used in [148] was different from the one proposed in this section. An unconditional π pulse was first used to excite the transmon to its first excited state $|e\rangle$ before a frequency comb induced the transition $|2n+1, e, 0\rangle \rightarrow |2n, g, 1\rangle$.

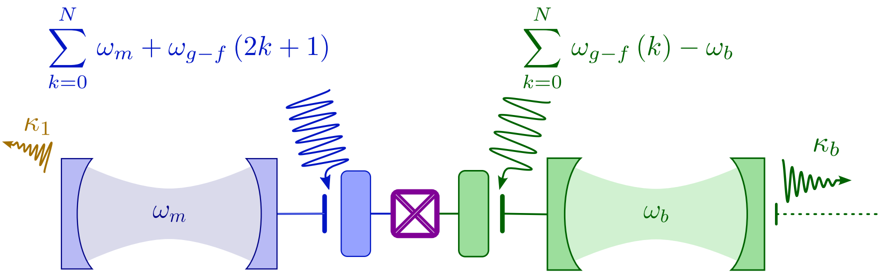

Figure 6.2: Scheme of the experiment. The memory (blue) is coupled to a lossy buffer mode (green) through a transmon qubit. Two frequency combs are applied which effectively induce the desired dissipation after adiabatically eliminating the buffer mode.

$$\frac{\hat{H}}{\hbar} = \omega_q \hat{q}^\dagger \hat{q} + \omega_m \hat{a}^\dagger \hat{a} + \omega_b \hat{b}^\dagger \hat{b} - \frac{E_j}{\hbar}\left(\cos\left(\hat{\varphi}\right) + \frac{\hat{\varphi}^2}{2}\right), \tag{6.2}$$

with $\hat{\varphi} = \varphi_q\left(\hat{q}^\dagger + \hat{q}\right) + \varphi_m\left(\hat{a}^\dagger + \hat{a}\right) + \varphi_b\left(\hat{b}^\dagger + \hat{b}\right)$. The modes $\hat{q}$, $\hat{m}$, and $\hat{b}$ respectively refer to the transmon, memory, and buffer modes. Similar to [148], the drives applied on the transmon qubit are taken into account through a modification of the transmon's operator

$$\hat{q} \rightarrow \hat{q} + \sum_j \xi_j e^{i\omega_j t}, \tag{6.3}$$

considering an ensemble of drives of amplitude ξ_j and frequency $\omega_j/2\pi$. Going into the rotating frame with the transformation $\hat{U}(t) = e^{i\left(\omega_q \hat{q}^\dagger \hat{q} + \omega_m \hat{a}^\dagger \hat{a} + \omega_b \hat{b}^\dagger \hat{b}\right)t}$, this Hamiltonian becomes

$$\begin{aligned}
\frac{\hat{H}'}{\hbar} &= -E_j\ \hat{U}(t)\left(\cos\left(\hat{\varphi}\right) + \frac{\hat{\varphi}^2}{2}\right)\hat{U}(t)^\dagger \\
&\approx -\frac{E_j}{4!}\ \hat{U}(t)\hat{\varphi}^4\hat{U}(t)^\dagger \\
&\approx -\frac{E_j}{4!}\left(\varphi_m\,\hat{a}^\dagger e^{i\omega_m t} + \varphi_b\,\hat{b}^\dagger e^{i\omega_b t} + \varphi_q\left(\hat{q}^\dagger e^{i\omega_q t} + \sum_j \xi_j e^{i\omega_j t}\right) + h.c.\right)^4 .
\end{aligned}$$

We expand this Hamiltonian as a function of $\hat{q}$, $\hat{m}$ and $\hat{b}$, restricting our analysis to terms surviving the Rotating Wave Approximation. The resulting self-Kerr and cross-Kerr couplings can then be expressed through the Hamiltonian

$$\begin{aligned}\hat{H}_{\text{Kerr}} =& -\frac{\chi_{m,m}}{2}\hat{a}^{\dagger\,2}\hat{a}^2 - \frac{\chi_{b,b}}{2}\hat{b}^{\dagger\,2}\hat{b}^2 - \frac{\chi_{q,q}}{2}\hat{q}^{\dagger\,2}\hat{q}^2 \\ &- \chi_{m,b}\,(\hat{a}^\dagger\hat{a})(\hat{b}^\dagger\hat{b}) - \chi_{q,m}\,(\hat{a}^\dagger\hat{a})(\hat{q}^\dagger\hat{q}) - \chi_{q,b}\,(\hat{q}^\dagger\hat{q})(\hat{b}^\dagger\hat{b}),\end{aligned} \tag{6.4}$$

with

$$\begin{aligned}&\hbar\,\chi_{m,m} = \frac{1}{2}E_J\varphi_m^4,\ \hbar\,\chi_{b,b} = \frac{1}{2}E_J\varphi_b^4,\ \hbar\,\chi_{q,q} = \frac{1}{2}E_J\varphi_q^4, \\ &\hbar\,\chi_{m,b} = E_J\varphi_m^2\varphi_b^2,\ \hbar\,\chi_{q,m} = E_J\varphi_m^2\varphi_q^2,\ \hbar\,\chi_{q,b} = E_J\varphi_q^2\varphi_b^2.\end{aligned} \tag{6.5}$$

Additionally, considering terms involving the drives applied on the transmon, a Stark-shift is observed where the frequency of each mode is shifted proportionally to the drive's energy

$$\hat{H}_{\text{Stark}} = \sum_{n\in\{m,\,b,\,q\}} -E_j\,\varphi_q^2\varphi_n^2\,\hat{n}^\dagger\hat{n}\sum_j|\xi_j|^2\,. \tag{6.6}$$

Finally, the impact of the two frequency combs is captured by the Hamiltonian

$$\begin{aligned}\hat{H}_{\text{Combs}} = -\frac{1}{4}E_j\Bigg(&\varphi_q^3\varphi_m\,\hat{q}^{\dagger 2}\hat{a}^\dagger e^{i(2\omega_q+\omega_m)t}\sum_j\xi_j^* e^{-i\omega_j t} \\ &+\varphi_q^3\varphi_b\,\hat{q}^2\hat{b}^\dagger e^{i(\omega_b-2\omega_q)t}\sum_j\xi_j e^{i\omega_j t}\Bigg) + h.c.\end{aligned} \tag{6.7}$$

The first term of this sum corresponds to the first desired transition, adding a photon to the memory while exciting the transmon to its second excited state. It is selected by the 1^{st} order RWA under the condition that a drive at ω_j is resonant with the transition frequency between $|2n-1,g,0\rangle$ and $|2n,f,0\rangle$[2]. These correspond to frequencies

$$\omega_j \in \{\omega_m + \omega_{g-f} - 4n\,\chi_{q,m}, n\in\mathbb{Z}\}\,, \tag{6.8}$$

represented by blue arrows in Fig. 6.3. Note that non-resonant transitions can still induce some erroneous population transfer despite being suppressed by the RWA. The second frequency comb is made of frequencies

---

[2] States are written using the convention:
$|\text{memory photon number, transmon state, buffer photon number}\rangle$

$$\omega_j \in \{\omega_{g-f} - 2n\,\chi_{q,m} - \omega_b, n \in \mathbb{Z}\}\,, \tag{6.9}$$

which are resonant with the transition frequency between $|n, f, 0\rangle$ and $|n, g, 1\rangle$ for all $n \geq 1$.

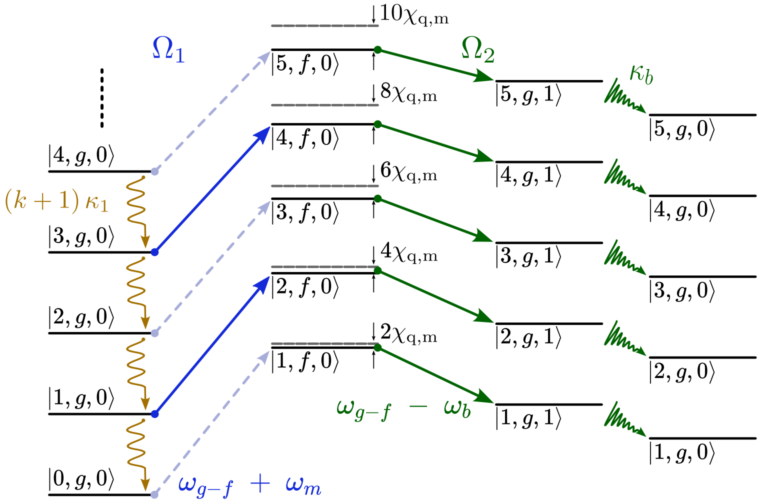

Figure 6.3: Effect of the two frequency combs Ω_1 and Ω_2. The first comb adds a photon to the memory mode when it initially contains an odd number of photons, while exciting the transmon to its second excited state $|f\rangle$. The second comb then transfers this excitation from the transmon to the buffer mode, preventing the environment from performing an unread measurement of the transmon's frequency. Finally, the buffer mode quickly decays at a rate κ_b through a transmission line.

6.1.2 *Reducing erroneous excitations of the memory*

The frequencies chosen for the second frequency comb might seem counter-intuitive at first, notably considering frequencies $\omega_j = \omega_{g-f} - 2(2n+1)\,\chi_{q,m} - \omega_b$ which induce transitions $|2n+1, f, 0\rangle \rightarrow |2n+1, g, 1\rangle$ unnecessary to stabilize the even manifold. Actually, these additional frequencies are added to the second frequency comb in order to mitigate erroneous excitations induced by the first comb, adding a photon while the memory is already in the manifold of even Fock states.

To understand the effect of these added frequencies, we consider the time evolution of $\Omega_1(t)$ and $\Omega_2(t)$ represented in Fig. 6.4. Because the Fourier transform of a frequency comb remains a comb, both these signals present sharp peaks regularly spaced in time. The corresponding period depends on the spacing between the frequencies of each comb as $T_{\Omega_1} = 2\pi/(4\chi_{q,m})$ for $\Omega_1(t)$ and $T_{\Omega_2} = 2\pi/(2\chi_{q,m})$ for $\Omega_2(t)$. The additional frequencies in the second comb allow us to double the period of $\Omega_2(t)$ compared to what is strictly necessary for our scheme, with two peaks of $\Omega_1(t)$ occurring in one period of the second frequency comb. This feature is particularly appealing when looking at the impact of $\Omega_1(t)$ on non-resonant states, corresponding to transitions $|2n, g, 0\rangle \rightarrow |2n+1, f, 0\rangle$. Indeed, a *kick/counter-kick* dynamic induced by non-resonant drives of the comb is observed which compensates for erroneous excitations of the memory before $\Omega_2(t)$ transfers this excitation to the buffer.

6.2 COUPLING THE PARITY STABILIZATION AND MULTI-PHOTONIC DISSIPATION

6.2.1 *Pulsing the multi-photonic dissipation*

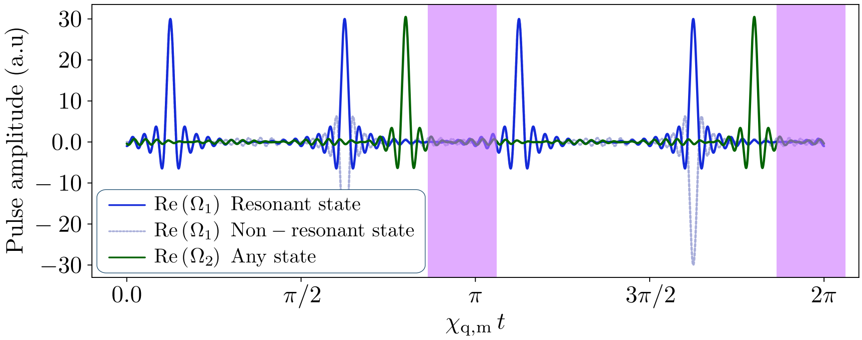

Figure 6.4: Time evolution of the drives $\Omega_1(t)$ and $\Omega_2(t)$ for 50 frequencies in the combs. $\Omega_1(t)$ is represented for resonant (blue) and non-resonant (dashed blue) states, the second frequency comb (green) is resonant with every transition. The purple regions correspond to time periods during which neither Ω_1 nor Ω_2 impact the memory. The two or four-photon dissipation can be activated during the purple time interval, regularly projecting the memory into the corresponding cat manifold without disturbing the parity stabilization.

Because this parity stabilization scheme relies on a dispersive coupling between the memory mode and an auxiliary transmon, it is fundamentally incompatible with the two-photon dissipation required to stabilize cat qubits.

The reason is similar to why the Wigner tomography cannot be performed at ϕ_{QEC} using the Auto-cat. The two-photon dissipation broadens the energy levels by κ_2 which then overlap in the regime $\kappa_2 \gg \chi_{q,m}$ (see Fig. 4.5**c.**), condition necessary to ensure that excitations of the transmon do not disturb the cat qubit stabilization. Fortunately, this issue can be easily solved by pulsing the two-photon dissipation during the dead times of the combs, represented by the purple regions in Fig. 6.4, using the fast flux line demonstrated in the Auto-cat experiment. As neither Ω_1 nor Ω_2 impact the memory during this period, the dispersive coupling can be inhibited by the two-photon dissipation without any detrimental effect on the parity stabilization.

A few conditions must be verified for this scheme to be effective. First, in order for the memory not to lose pairs of single photons during a period T_{Ω_1}, we require $\chi_{q,m} \gg \kappa_1$. Additionally, because the two-photon stabilization is only activated for a fraction of $1/\chi_{q,m}$, the rate κ_2 needs to be large enough so that the system is effectively projected onto the cat qubit manifold, yielding the condition $\kappa_2 \gg \chi_{q,m}$. Finally, the buffer linewidth κ_b needs to be large enough to ensure that photons are evacuated between two peaks of $\Omega_2(t)$, resulting in the condition $\kappa_b \gg \chi_{q,m}$.

6.2.2 *Extending the encoding to 4-component cat states*

The proposed scheme combining parity stabilization and two-photon dissipation does not actually stabilize a qubit but a single quantum state, $|C_\alpha^+\rangle$ if even Fock states are stabilized and $|C_\alpha^-\rangle$ otherwise. In order to stabilize a qubit, we slightly change the encoding and consider the 4-component cat qubit introduced in Sec. 3.3.3. Using four-photon dissipation described by the loss operator

$$\hat{L}_4 = \sqrt{\kappa_4}\left(\hat{a}^4 - \alpha^4\right), \tag{6.10}$$

superposition of $|\pm\alpha\rangle$ and $|\pm i\alpha\rangle$ are stabilized in the memory. Four distinct states can be defined from these coherent states, each having a distinct parity modulo 4. Choosing the states with a parity of 0 and 2 modulo 4 as the logical states of a qubit,

$$\begin{aligned}
|0_L\rangle &= \left|C_\alpha^{0 \bmod 4}\right\rangle = \mathcal{N}_0\left(|\alpha\rangle + |-\alpha\rangle + |i\alpha\rangle + |-i\alpha\rangle\right) \propto \sum_k \frac{\alpha^{4k}}{\sqrt{4k!}}\,|4k\rangle \\
|1_L\rangle &= \left|C_\alpha^{2 \bmod 4}\right\rangle = \mathcal{N}_2\left(|\alpha\rangle + |-\alpha\rangle - |i\alpha\rangle - |-i\alpha\rangle\right) \propto \sum_k \frac{\alpha^{4k+2}}{\sqrt{4k+2!}}\,|4k+2\rangle\,,
\end{aligned}$$

(6.11)

all states belonging to the code space $\mathcal{C}$ would have an even number of photons. The loss of a single photon would then map the qubit into an error manifold defined by

$$\begin{aligned}
|0_{\text{Error}}\rangle &= \left|C_\alpha^{3 \bmod 4}\right\rangle = \mathcal{N}_3\left(|\alpha\rangle - |-\alpha\rangle + i\,|i\alpha\rangle - i\,|-i\alpha\rangle\right) \propto \sum_k \frac{\alpha^{4k+3}}{\sqrt{4k+3!}}\,|4k+3\rangle \\
|1_{\text{Error}}\rangle &= \left|C_\alpha^{1 \bmod 4}\right\rangle = \mathcal{N}_1\left(|\alpha\rangle - |-\alpha\rangle - i\,|i\alpha\rangle + i\,|-i\alpha\rangle\right) \propto \sum_k \frac{\alpha^{4k+1}}{\sqrt{4k+1!}}\,|4k+1\rangle\,.
\end{aligned} \tag{6.12}$$

Such an error is corrected by the parity stabilization, adding a photon to the memory and bringing it back into the code space while preserving the qubit's logical information. This is the fully autonomous version of the measurement-based feedback experiment of [104]. Using the convention of Fig. 3.10**c.**, the phase-flip rate of the defined 4-component cat qubit would be exponentially suppressed with $|\alpha|$ by the four-photon dissipation, while the parity stabilization provides a first-order protection against bit-flip errors.

A four-photon dissipation has not been demonstrated yet, notably due to the difficulty of engineering a large rate κ_4 while keeping other non-linear terms under control. The Auto-cat design could be used for this task, being specifically designed to reach large dissipation rates. Ensuring the frequency-matching condition $\omega_b = 4\omega_m$ in future iterations of the device, a strong 4-to-1 photon coupling could be achieved with a buffer mode, yielding the desired four-photon dissipation after adiabatic elimination. Adding the already demonstrated parity stabilization [148, 198] should then lead to the stabilization of a fully protected cat qubit.

Part III

APPENDIX

a

APPENDIX: ROTATING WAVE APPROXIMATION

A.1 THE ROTATING WAVE APPROXIMATION

In this section, we consider a quantum system described by a Hamiltonian $\hat{H}_0$, driven by an external drive. Its dynamics is described by the Schrödinger equation [39, 199]

$$i\hbar \frac{\mathrm{d}}{\mathrm{d}t} \left|\Psi\right\rangle_t = \left(\hat{H}_0 + \sum_{k=1}^{m} u_k(t)\hat{H}_k\right) \left|\Psi\right\rangle_t , \tag{a.1}$$

with $\left|\Psi\right\rangle_t$ the state of the quantum system at time t and $\sum_{k=1}^{m} u_k(t)\hat{H}_k$ the Hamiltonian describing m independent control drives. Solving this equation to obtain the expression of $\left|\Psi\right\rangle_t$ is challenging, and in most cases actually proves impossible without relying on numerical methods. This is particularly problematic in the optic of having precise control of a qubit state. To tackle this issue, we simplify the previous Hamiltonian using the Rotating Frame Approximation (RWA), finding an approximate dynamics resembling that of the exact system.

For the sake of clarity, we consider the case of a single drive $m = 1$. Extending the following calculations to the case where $m > 1$ is straightforward as all operations are linear. Following the demonstration in [199], we first go to the interaction frame using the change of variables

$$\left|\Phi\right\rangle_t = e^{-i\hat{H}_0 t/\hbar} \left|\Psi\right\rangle_t . \tag{a.2}$$

In this new frame, the dynamics of the system is described by the equation

$$i\hbar \frac{\mathrm{d}}{\mathrm{d}t} \left|\Phi\right\rangle_t = u_1(t) e^{-i\hat{H}_0 t/\hbar} \hat{H}_1 e^{i\hat{H}_0 t/\hbar} \left|\Phi\right\rangle_t . \tag{a.3}$$

Assuming the time-dependent drive $u_1(t)$ to have a small amplitude compared to the frequency of the quantum system, and be almost-periodic [1], it can be written as

---

[1] An almost periodic function is a function of a real parameter $f(t)$ that can be written as a function $g(\omega_1 t, ..., \omega_r t)$, 2π-periodic in each of its arguments.

$$u_1(t) = \epsilon \sum_{j=1}^{r} \left(u_j e^{i\omega_j t} + u_j^* e^{-i\omega_j t} \right), \tag{a.4}$$

with $\epsilon > 0$ a small parameter and r the number of different frequencies ω_j. To simplify the notations we then introduce

$$\hat{K}(t) = \frac{u_1(t)}{\epsilon} e^{-i\hat{H}_0 t/\hbar} \hat{H}_1 e^{i\hat{H}_0 t/\hbar}. \tag{a.5}$$

This operator has an almost-periodic time dependence and can then be decomposed as

$$\hat{K}(t) = \left\langle \hat{K} \right\rangle + \frac{\mathrm{d}}{\mathrm{d}t} \hat{K}_{\mathrm{osc}}(t), \tag{a.6}$$

with $\left\langle \hat{K} \right\rangle = \lim_{T\to\infty} \int_0^t \hat{K}(t) \mathrm{d}t$ the mean value of the operator and $\hat{K}_{\mathrm{osc}}(t)$ the time integral of its oscillating part. Eq. (a.1) then reads

$$i\hbar \frac{\mathrm{d}}{\mathrm{d}t} \left|\Phi\right\rangle_t = \epsilon \left(\left\langle \hat{K} \right\rangle + \frac{\mathrm{d}}{\mathrm{d}t} \hat{K}_{\mathrm{osc}}(t) \right) \left|\Phi\right\rangle_t . \tag{a.7}$$

A.1.1 1^{st} *order*

The 1^{st} order approximation of the RWA consists in approximating Eq (a.7) by

$$i\hbar \frac{\mathrm{d}}{\mathrm{d}t} \left|\Phi_{\mathrm{rwa}}^{1^{st}}\right\rangle_t = \epsilon \left\langle \hat{K} \right\rangle \left|\Phi_{\mathrm{rwa}}^{1^{st}}\right\rangle_t . \tag{a.8}$$

Only valid on time intervals of length $O(1/\epsilon)$, this approximation can be physically understood as neglecting fast oscillating terms which average out to zero on reasonable timescales. It can be justified by changing to another frame using the transformation

$$\left|\chi\right\rangle_t = \left(\mathbb{1} - \epsilon \hat{K}_{\mathrm{osc}}(t) \right) \left|\Phi\right\rangle_t . \tag{a.9}$$

Note that despite the operator $\left(\mathbb{1} - \epsilon \hat{K}_{\mathrm{osc}}(t) \right)$ not being Hermitian, this transformation is valid for small ϵ as this operator is invertible

$$\left(\mathbb{1} - \epsilon\,\hat{K}_{\text{osc}}(t)\right)\left(\mathbb{1} + \epsilon\,\hat{K}_{\text{osc}}(t)\right) = \mathbb{1} + O\left(\epsilon^2\right).$$

The dynamics of $|\chi\rangle_t$ then reads

$$i\hbar\frac{\mathrm{d}}{\mathrm{d}t}|\chi\rangle_t = \epsilon\left(\left\langle\hat{K}\right\rangle + \epsilon\left[\left\langle\hat{K}\right\rangle, \hat{K}_{\text{osc}}(t)\right] - \epsilon\hat{K}_{\text{osc}}(t)\frac{\mathrm{d}}{\mathrm{d}t}\hat{K}_{\text{osc}}(t) + O\left(\epsilon^2\right)\right)|\chi\rangle_t. \tag{a.10}$$

The 1^{st} order RWA then simply consists in neglecting terms of order $O\left(\epsilon^2\right)$. Going back to the interaction frame we recover Eq (a.8), which can then be solved to give the approximate evolution of $\left|\Phi^{1^{st}}_{\text{rwa}}\right\rangle_t$.

A.1.2 2^{nd} *order*

To present the 2^{nd} order RWA, we start by introducing the 2 notations

$$\begin{aligned}\hat{K}_{\text{osc}}(t) &= \frac{\mathrm{d}}{\mathrm{d}t}\hat{E}_{\text{osc}}(t)\\ \hat{K}_{\text{osc}}(t)\frac{\mathrm{d}}{\mathrm{d}t}\hat{K}_{\text{osc}}(t) &= \left\langle\hat{F}\right\rangle + \frac{\mathrm{d}}{\mathrm{d}t}\hat{F}_{\text{osc}}(t).\end{aligned} \tag{a.11}$$

Eq. (a.10) can then be rewritten as

$$i\hbar\frac{\mathrm{d}}{\mathrm{d}t}|\chi\rangle_t = \epsilon\left(\left\langle\hat{K}\right\rangle + \epsilon\left\langle\hat{F}\right\rangle + \epsilon\frac{\mathrm{d}}{\mathrm{d}t}\left(\left[\left\langle\hat{K}\right\rangle, \hat{E}_{\text{osc}}(t)\right] - \hat{F}_{\text{osc}}(t)\right) + O\left(\epsilon^2\right)\right)|\chi\rangle_t. \tag{a.12}$$

Once again, the RWA consists in only considering the non-rotating terms of this Hamiltonian. Another change of frame, not performed here, shows the remaining oscillating terms correspond to corrections of order $O\left(\epsilon^3\right)$ in the dynamics. Once again going back to the interaction frame, the second-order approximation reads

$$i\hbar\frac{\mathrm{d}}{\mathrm{d}t}\left|\Phi^{2^{nd}}_{\text{rwa}}\right\rangle_t = \left(\epsilon\left\langle\hat{K}\right\rangle - \epsilon\left\langle\hat{F}\right\rangle\right)\left|\Phi^{2^{nd}}_{\text{rwa}}\right\rangle_t. \tag{a.13}$$

A.2 EXAMPLE OF A DRIVEN QUBIT

To give some intuition on the RWA, we show how it can be applied to the simple system of a qubit driven by a single external drive. This system is described in the laboratory frame by the Hamiltonian

$$\hat{H}_{\text{lab}}/\hbar = \frac{\omega_0}{2}\sigma_z + \frac{u_1}{2}\cos(\omega_1 t)\,\sigma_x, \tag{a.14}$$

corresponding to a situation with $m = r = 1$ previously. We go to the rotating frame associated with the drive frequency ω_1 doing the change of variable $|\Phi\rangle = e^{i\frac{\omega_1 t}{2\hbar}\sigma_z}|\Psi\rangle$. In this frame, the dynamics is governed by the Hamiltonian

$$\hat{H}_{\text{rot}}/\hbar = \frac{\Delta}{2}\sigma_z + \frac{u_1}{4}\left(\sigma_x + \cos(2\omega_1 t)\,\sigma_x - \sin(2\omega_1 t)\,\sigma_y\right), \tag{a.15}$$

with $\Delta = \omega_0 - \omega_1$ the detuning between the qubit and drive frequency. This detuning is taken to be 0 as the drive is usually resonant with the qubit frequency. The rotating wave approximation applies under the condition $u_1 \ll \omega_0$, in which case the rotating terms can be neglected and the qubit dynamic approximated to

$$i\hbar\frac{\mathrm{d}}{\mathrm{d}t}\left|\Phi^{1^{st}}_{\text{rwa}}\right\rangle_t = \frac{u_1}{4}\sigma_x\left|\Phi^{1^{st}}_{\text{rwa}}\right\rangle_t. \tag{a.16}$$

This corresponds to a situation where the qubit simply revolves around the **x** axis of the Bloch sphere. A comparison of the qubit trajectories, starting from its ground state, is shown in Fig. a.1 for $\omega_0/2\pi = 5$ GHz and $u_1/2\pi = 300$ MHz. We see that despite local deviations, the 1^{st} order RWA manages to capture the qubit dynamics. Note that in a typical superconducting experiment, $u_1/2\pi$ is of the order of a few MHz, and deviations from the 1^{st} order RWA are negligible.

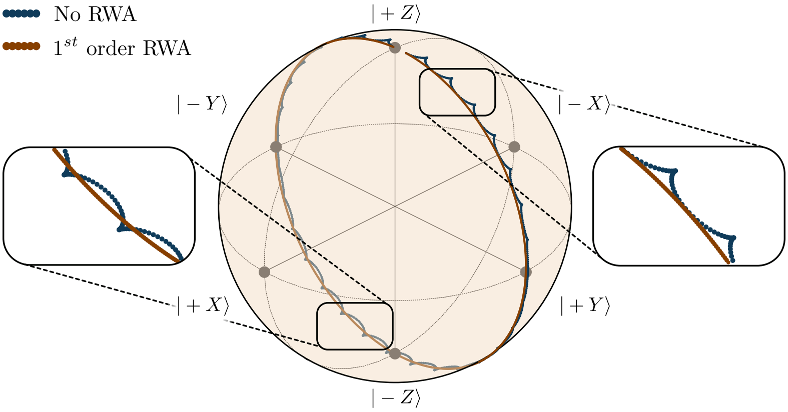

Figure a.1: Simulated evolution of a qubit state $|\Psi(t)\rangle$ driven by an external drive over 3ns, with no approximation (blue) and approximating the trajectory with 1^{st} order RWA (orange). The 2 insets show zoom on these 2 trajectories, highlighting the different behaviors occurring during the dynamic.

b

APPENDIX: FRIDGE CABLING

This appendix introduces the cabling used to measure the autoparametric cat, nicknamed the *Auto-cat*.

The transmon qubit, readout resonator, memory, and buffer modes are driven by pulses whose envelope is generated using an Arbitrary Waveform Generator (AWG), an OPX by Quantum Machine in this experiment. These pulses are respectively modulated at $\omega_{\mathrm{IF},q}/2\pi = 100\,\mathrm{MHz}$, $\omega_{\mathrm{IF},r}/2\pi = 75\,\mathrm{MHz}$, $\omega_{\mathrm{IF},m,\mathrm{tomo}}/2\pi = 40\,\mathrm{MHz}$, with the relations

$$\begin{aligned} \omega_{\mathrm{IF},m,\mathrm{QEC}} &= (\omega_{m,\mathrm{tomo}} + \omega_{\mathrm{IF},m,\mathrm{tomo}}) - \omega_{b,\mathrm{QEC}}/2 \\ \omega_{\mathrm{IF},b,\mathrm{QEC}} &= 2\omega_{\mathrm{IF},m,\mathrm{QEC}}. \end{aligned} \tag{b.1}$$

$\omega_{\mathrm{IF},m,\mathrm{tomo}}$ and $\omega_{\mathrm{IF},m,\mathrm{QEC}}$ are the modulation frequencies used to respectively drive the memory at ϕ_{tomo} or ϕ_{QEC}, $\omega_{m,\mathrm{tomo}}$ and $\omega_{b,\mathrm{QEC}}$ are the frequencies of the memory mode at ϕ_{tomo} and the buffer mode at ϕ_{QEC}. The above condition on $\omega_{\mathrm{IF},m,\mathrm{QEC}}$ and $\omega_{\mathrm{IF},b}$ ensures the phase stability of the encoded cat in the frame rotating at the memory frequency.

These signals are up-converted using single sideband mixers for the transmon qubit and readout resonator, and IQ mixers for the memory and buffer mode, with Radio Frequency signals generated by a 4-channel Anapico APUASYN20. The signals at frequencies ω_q, ω_r, and $\omega_{m,\mathrm{tomo}}/\omega_{m,\mathrm{QEC}}$ are all combined and then sent via the readout port of the device using a 6 GHz frequency diplexer. The memory drive subsequently goes through the transmon qubit, readout resonator, and its Purcell filter before reaching the memory cavity. Given this intricate path, employing a room-temperature amplifier is needed for achieving displacements $\hat{D}(\beta)$ where $\beta \geq 2$.

The signal driving the buffer mode at ω_b is sent through the buffer port of the device. It is combined with a DC tone directly generated by one DAC of the OPX using a 3 GHz frequency diplexer, facilitating a swift transition from ϕ_{tomo} to ϕ_{QEC}. We attempted to drive the memory through this port to bypass the previously described elements, but the protection from the symmetry of the non-linear coupler is excessively effective and prevented the achievement of large enough displacements.

The two reflected signals from the buffer and readout modes merge at the mixing chamber. The latter is first pre-amplified by a Travelling Wave Parametric Amplifier (TWPA) from Lincoln labs [200]. Further amplification is performed by a High Electron Mobility Transistor at the 4K stage, and then a room-temperature amplifier. Subsequently, the signal is down-converted using an image reject mixer, followed by filtering, amplification, and acquisition by an ADC of the OPX. With its capacity for real-time digitization and demodulation, the OPX allows for real-time feedback and implementation of the transmon qubit reset at the beginning of each pulse sequence. The complete setup is depicted in (Fig. b.1).

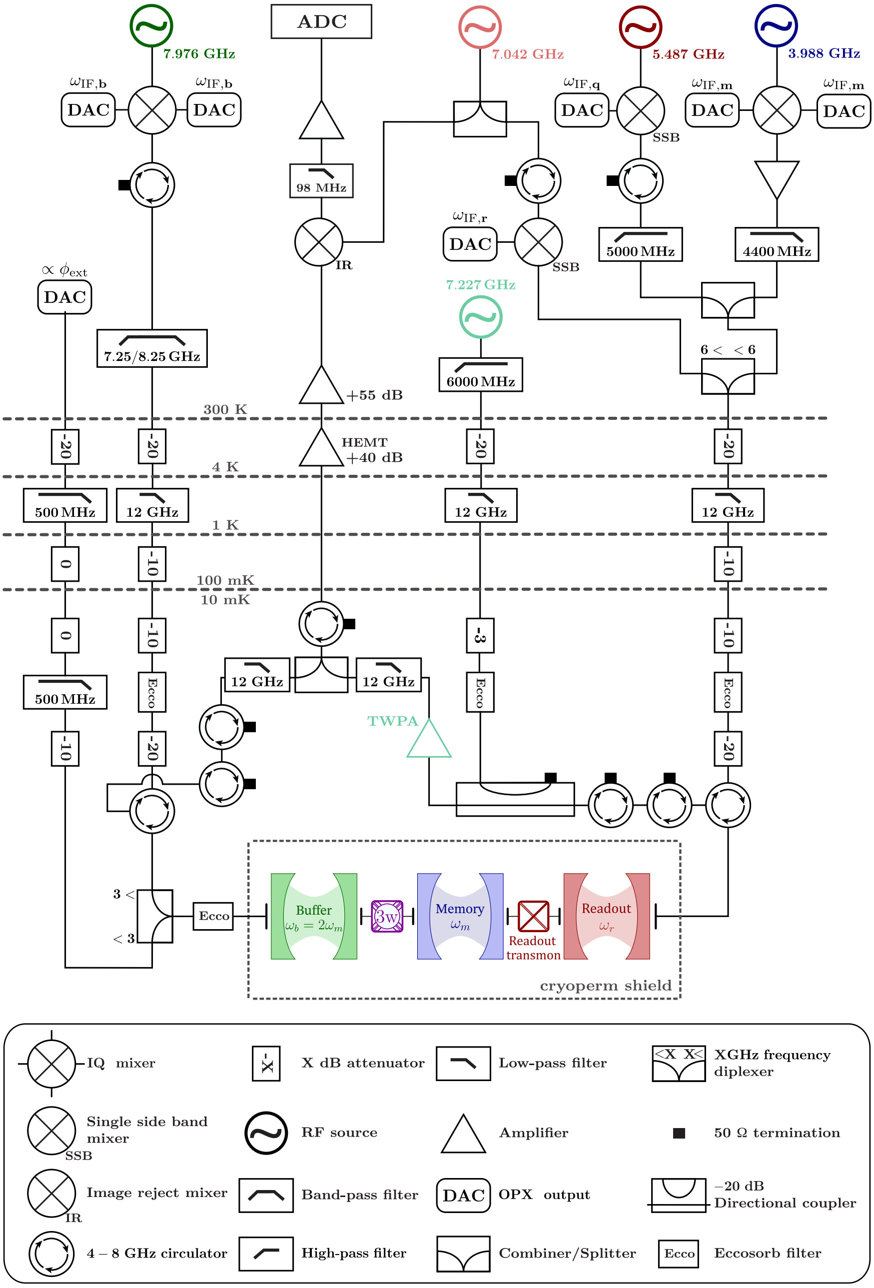

Figure b.1: Schematic of the setup. Each electromagnetic mode in the circuit is driven by an RF source detuned by the modulation frequency and whose color matches that of the corresponding mode.

C

APPENDIX: SAMPLE FABRICATION AT ENS DE LYON

We detail in this section the fabrication process developed at the ENS de Lyon, presenting both optical and electrical lithography techniques. These are used to create patterns or deposit structures on a thin layer of tantalum, sputtered onto a sapphire chip with typical dimensions of 9×8 mm. These chips are diced in the Nanolyon clean room from 2 inch wafers, and the sputtering is performed by the company StarCryo directly on these wafers following a piranha cleaning.

C.1 OPTICAL LITHOGRAPHY

Optical lithography is used to pattern structures directly onto the tantalum film, the smallest dimension of these structures typically being a few micrometers. This would for instance be suited for the fabrication of microwave resonators, capacitances, or inductances.

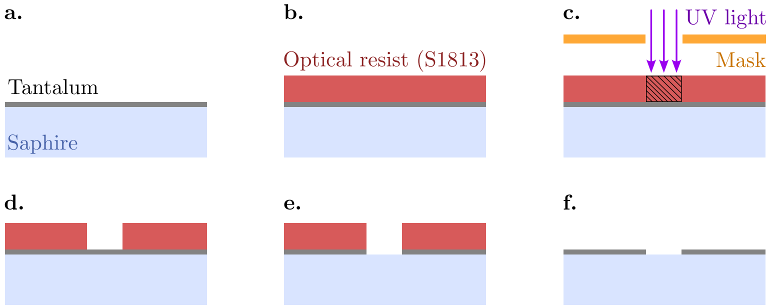

Figure c.1: Representation of the optical lithography process. **a.** The sample initially consists of a thin layer of tantalum sputtered on top of a sapphire substrate. **b.** A layer of optical resist is deposited on top of the tantalum.**c.** UV light is shined through a mask in order to expose the desired regions, breaking chains of polymers and weakening the degrading the photo-sensitive material. **d.** The sample is exposed to a developer, MF319 for the S1813 resist, which dissolves away the exposed regions. **e.** The exposed tantalum is etched. **f.** Finally, the resist is removed using a cleaning protocol.

An optical resist is first deposited on top of the tantalum layer, consisting of a light-sensitive organic material. The desired regions are then exposed to light, using either a LASER or a mask through which light is shined[1], after which a developer is applied to the surface. In the case of positive optical resists, the photo-sensitive material is degraded when exposed to light and the developer dissolves away the regions exposed to light. On the opposite, a negative resist is strengthened by light so that the developer only removes regions that were not exposed. The exposed regions of tantalum are then removed using a dry or wet etch, after which the resist is removed to reveal the patterned structure. This process is represented in Fig. c.1 in the case of a positive optical resist. In the following, I detail the recipe that I developed together with other Ph.D. students during the first months of this thesis.

c.1.1 *Cleaning*

Clean the sample in a beaker filled with NMP (also called PG remover). The beaker is placed in a sonicator for at least 30 min with the sonication activated. Rinse with IPA and dry the sample with nitrogen on a cleanroom wipe.

c.1.2 *Coating*

Take out the resist bottle from the fridge at least 15 min before spin-coating in order to consistently have the same viscosity. The bottle is kept in the fridge to avoid degradation of the resist. Dry the sample for at least 3 min on a hotplate at 115° C. Let it cool down for 1 min and spin of few drops of S1813 at 500 RPM for 5 s then 4000 RPM for 55 s, this should yield a resist thickness of $1.7 - 1.8\ \mu$m. Bake the resist at 115° C for 1 min in order to give it its structural integrity. From this point and until development, the sample should not be exposed to light. Cover the sample with aluminum of necessary.

c.1.3 *Exposure to light*

During this thesis, a Smart Print was used for the lithography which uses a projector to expose the resist. Mask are exported from GDS files to bitmap,

---

[1] This mask can be a physical mask as is standard in the industry, usually yielding the best precision, but requiring the fabrication of multiple chips so that the fabrication of the mask is made profitable. Alternatively, one could use a simple projector as was initially the case at the ENS, which provides more modularity at the cost of a degraded precision.

turning on or off the corresponding pixel. This allowed us to easily design new masks, the smallest feature allowed measuring ≈ 2 μm. The dose was not calibrated (the intensity of the emitted light was not measured) and an exposure time of 0.5 s was experimentally determined instead.

Because the regions exposed by the projector are much smaller than the dimensions of the chip, multiple expositions must be performed. The sample is moved between each exposition, leading to potential stitching issues. This issue was mitigated by having a small overlap of ≈ 2.5 μm between each exposition window, as slightly overexposed lines are less detrimental to the chip than a gap between two exposed regions.

c.1.4 *Development*

The resist is developed using MF319, taken straight from the fridge. Having a cold MF319 is useful to slow down the development, allowing for larger margin of errors from the experimentalist. The sample is emerged and smoothly agitated in the developer for 50s, then immediately rinsed in DI water for at least 30s in order to stop the development and dried with nitrogen.

c.1.5 *Etching*

The sample is etched using HF, emerging the sample and smoothly agitating for 19 s. The water is then abundantly rinsed with water and dried with nitrogen. Finally, after an inspection under a microscope to check if the etch was successful, the optical resist is removed using a bath of NMP in the sonicator at 60° C for at least 30 min.

c.2 FABRICATION OF THE JOSEPHSON JUNCTIONS

Josephson junctions have a typical dimension of 200×200 nm^2 and are therefore too small to be fabricated using optical lithography. Instead, a *scanning electron microscope* (SEM) is used with allows to reach a precision of ≈ 2 nm.

These junctions are fabricated using a Dolan bridge technique [201], which uses shadow evaporation to deposit two layers of aluminum separated by an insulating oxide layer. The wafer is covered by a bi-layer of resist polymethylglutarimide (PMGI) and PMMA, with the PMMA layer sitting on top of the PMGI. The pattern represented in Fig. c.2**a.** is exposed using the SEM, which degrades the electron-sensitive PMMA resist. The electron-

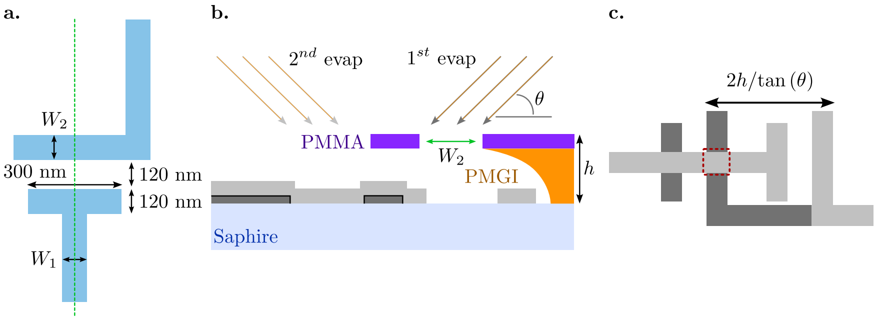

Figure c.2: **a.** Pattern exposed during the electrical lithography at the SEM. The widths W_1 and W_2 fix the dimensions of the resulting junction. The dimensions of the bridge are experimentally fixed to 300 nm and 120 nm in order to guarantee its structural integrity, notably preventing vibration modes from collapsing it. **b.** Cut along the green axis of **a.** showing the two step evaporation and the resulting evaporated aluminum. The first (dark grey) and second (light grey) layers are separated by an insulating barrier of AlOx (dark line), created by introducing O_2 to the evaporation chamber between the two aluminum evaporations. **c.** Top view of the resulting evaporated aluminum layers, the color scheme is consistent with **b**. The Josephson is indicated by the dashed red box, the separation between the two layers depends on the resin thickness and evaporation angle.

insensitive PMGI layer is not affected by this process. Development is then performed in two steps, first dissolving away the exposed PMMA layer and in a second time the PMGI. This creates the desired *bridge* of PMMA and an *undercut* in the PMGI shown in Fig. c.2**b**. aluminum is then evaporated at ±22° in a Plassys evaporator, with an oxidation step separating the two evaporations. This defines the Al/AlOx/Al structure of the Josephson junction. The area of the Josephson junction (red box in Fig. c.2**c.**) is fixed by the width of the two overlapping fingers W_1 and W_2, the thickness of the aluminum oxide being controlled by the duration of the oxidation process and the pressure of O_2. In the following, I detail the recipe that I developed together with other Ph.D. students during the first months of this thesis. A picture of the chip after developing the resists is shown in Fig. c.3**a.**, and an SEM image of a Josephson junction in Fig. c.3**b**.

C.2.1 *Cleaning*

The surface of the sample is thoroughly cleaned before depositing the resists in order to remove organic residues and limit the presence of two-level systems near the Josephson junctions. First, we perform a toluene-methanol-acetone-IPA (TAMI) cleaning where the sample is successively emerged in a beaker containing these four solvents, and placed in a sonicator at room temperature for 5 min each.

The sample is then cleaned in a piranha solution for 5 min (without agitation, the sample is lying at the bottom of the beaker), rinsed with DI water, and dried with nitrogen.

C.2.2 *Spin coating PMGI and PMMA*

We first deposit the PMGI at the surface of the sample. The chip is dried on a hotplate at 200° C for 5 min before cooling down for 2 min. A few drops of PMGI are then deposited at the surface and the chip is spin-coated at 500 RPM for 3 s then 2000 RPM for 60 s. This yields a layer thickness of $\approx$ 550 nm. The resist is then baked at 200° C for 5 min. Because we experienced issues regarding the adherence of the PMGI on the substrate, this was later increased to 210° C for 10 min.

A few drops of PMMA are then deposited and the chip spin coated at 500 RPM for 3 s then 4000 RPM for 60 s, yielding a thickness of $\approx$ 150 nm. The resin is then baked at 180° C for 15 min.

C.2.3 *Electronic lithography*

Before the electrical lithography, a thin layer of 10 nm of aluminum is evaporated at the surface of the non-conductive PMMA resist. This prevents electrons from accumulating in a localized spot of the resist, which could then deflect the electron beam.

The lithography is performed using a Zeiss Supra 55VP, the relevant parameters of the lithography being the tension of 30 keV, working distance of 7 mm, aperture of 7.5 μm, and dose of 350 μCμm^{-1}. This typically leads to a pixel size of 2×2 nm.

C.2.4 *Development*

The thin aluminum layer is removed using a bath of KOH. The duration of the dip depends on the concentration of the solution, a visible shift of color

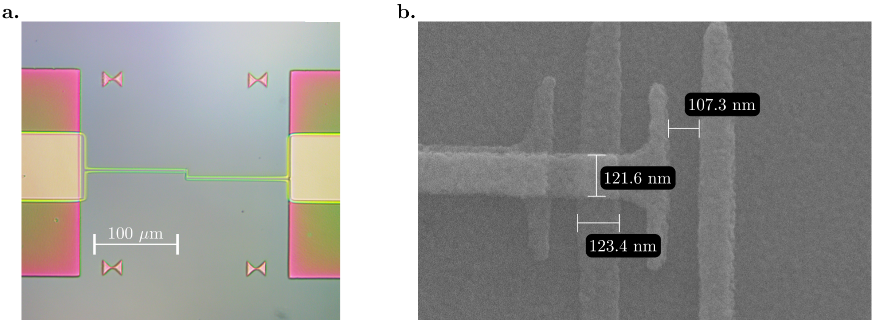

Figure c.3: **a.** Picture taken under microscope of the sample after the development of the PMMA and PMGI. The two pads on the side are made of tantalum, as the crosses that are used for the alignment during the electrical lithography. The blue background corresponds to exposed sapphire. The removed PMMA layer corresponds to the horizontal dark connecting the two pads, the green halo surrounding it being the PMGI undercut. **b.** SEM picture of a Josephson junction for a designed W_1 and W_2 of 120 nm. The structure of Fig. c.2**b.** can be easily recognized.

indicating that all aluminum has been removed and the PMMA is visible. The chip is then rinsed with DI water and dried with nitrogen.

PMMA is developed by emerging and gently stirring the chip in a solution of 1:3 in volume of MIBK/IPA for 60 s. The MIBK was diluted with IPA in order to slow down the development of the PMMA. Rinse in IPA for at least 20 s and dry with nitrogen. The PMGI is then developed with cold MF319 for 30 s, after which the sample is rinsed with DI water and blowdried with nitrogen.

C.2.5 *Aluminum evaporation*

The sample is placed in the load chamber of a Plassys MEB550S electron beam evaporator. First, in order to remove the tantalum oxide and have good contact between the tantalum and the deposited aluminum, argon milling is performed. Then, a first layer of 20 nm aluminum is deposited at a rate of 0.5 nm/s while the sample is tilted at 22°. 1 mbar of O_2 is then admitted to the chamber for 50 min which grows the AlOx layer. Finally, a second layer of 40 nm aluminum is evaporated at the same rate of 0.5 nm/s with a sample tilted at $-22°$.

c.2.6 *Lift-off*

The remaining resist is removed by placing the sample in a bath of NMP for about 1 hour at 60°. After this time, the layer of aluminum evaporated on top of the PMMA (now floating above the surface of the sample in the NMP), is dispersed by sonicating for a few seconds. The sample is finally rinsed one final time with DI water and blowdried with nitrogen.

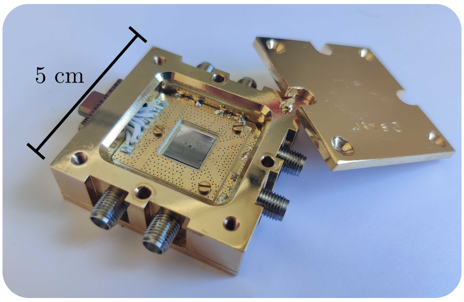

Figure c.4: Picture of the JAWS sample Holder, an Auto-cat chip is placed at the center. The sample Holder is connected inside the fridge using the outside SMA ports, and the chip is connected to the sample holder using wirebonds (not shown here, the chip is simply deposited at its corresponding location). Once the lid is put in place, a 3D cavity is defined around the chip which hosts harmonic modes. These are pushed to large frequencies ($\geq$ 15 GHz) by reducing the dimensions of the empty space surrounding the sample, ensuring they do not couple to modes of the chip.

If the room-temperature resistance of the Josephson junctions is satisfying, the sample is mounted using wirebounds to a PCD, placed in a sample holder, and mounted inside a dilution fridge where it will be measured. Otherwise, junctions are removed using a bath of KOH or aluminum etchant and the fabrication process is started again. The sample holder used is called a JAWS (Joint Assembly for the Wiring of Superconducting circuits), developed by Marius Villiers at ENS Paris, and is represented in Fig. c.4.

c.2.7 *Junction resistance*

The Josephson energy E_J of a junction can be deduced from its resistance using the Ambegaokar–Baratof relation, which links the normal state resistance of a junction at zero temperature $R(0)$ and the critical current $I_c = E_J/\varphi_0$ as

$$R(0) = \frac{\pi\Delta}{2eI_c}. \tag{c.1}$$

The parameter Δ is the superconducting gap, with $\Delta \approx 180\ \mu$eV for aluminum. The room temperature resistance $R(300\ \mathrm{K})$ is measured at a probe station after the fabrication, from which we deduce $R(0)$ that is typically $10-20\%$ larger than $R(300\ \mathrm{K})$. The room temperature resistance is proportional to $1/W_1$, $1/W_2$, and $\sqrt{P_0 t}$, with P_0 the oxidation pressure and t the time of oxidation. We calibrate the resistance of our junction by fixing P_0 and t to the parameters given in the recipe, W_2 to 120 nm, and sweep the value of W_1. The dependence of $R(300\ \mathrm{K})$ on W_1 is represented in Fig. c.5, from which the necessary width to reach an arbitrary resistance is deduced.

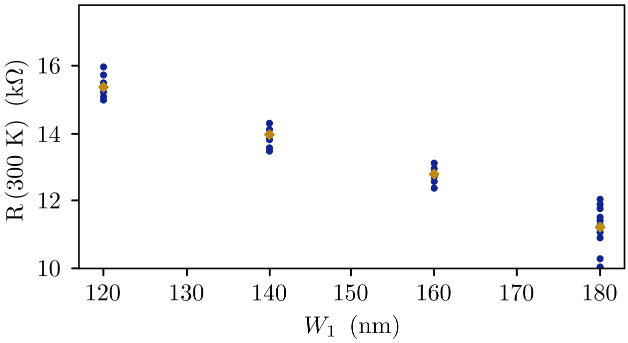

Figure c.5: Dependence of $R(300\ \mathrm{K})$ on the junction's width W_1. Average resistance values are indicated with an orange dot.

d

APPENDIX: SPECTROSCOPY OF THE BUFFER MODE

This appendix describes the spectroscopy introduced in Sec. 4.1.2 and used to reconstruct the evolution of the buffer frequency with the external flux. The desired value of ϕ_{ext} is first set using a DC pulse, after which an RF tone is sent to drive the buffer mode at ω_d. Looking at the signal reflection $r(\omega_d)$, the buffer frequency ω_b can be extracted for a particular flux. Repeating this experiment for different values of ϕ_{ext} gives the evolution of $\omega_b\left(\phi_{\text{ext}}\right)$.

The buffer drive is described in this experiment by a propagating field $\hat{b}_{in}(t)$, with the outgoing signal denoted as $\hat{b}_{out}(t)$. These two fields are linked by the input/output relation [162]

$$\sqrt{\kappa_{b,c}}\,\hat{b}[\omega] = \hat{b}_{in}[\omega] + \hat{b}_{out}[\omega], \tag{d.1}$$

with $\hat{b}[\omega]$, $\hat{b}_{in}[\omega]$ and $\hat{b}_{out}[\omega]$ the Fourier transform of $\hat{b}(t)$, $\hat{b}_{in}(t)$ and $\hat{b}_{out}(t)$[1]. Note that the buffer loss rate can be decomposed as $\kappa_b = \kappa_{b,i} + \kappa_{b,c}$. The first term $\kappa_{b,i}$ corresponds to the intrinsic loss of the buffer due to surface or radiative losses for instance, while $\kappa_{b,c}$ is the rate at which the buffer decays through the input line.

The evolution of the buffer field amplitude is given in the Heisenberg picture by the Langevin equation [202]

$$\frac{\partial}{\partial t}\hat{b}(t) = -\frac{i}{\hbar}\left[\hat{b}(t), \hat{H}\right] - \frac{\kappa_b}{2}\hat{b} + \sqrt{\kappa_{b,c}}\,\hat{b}_{in}(t), \tag{d.2}$$

which can alternatively be written in a time-reversed version

$$\frac{\partial}{\partial t}\hat{b}(t) = -\frac{i}{\hbar}\left[\hat{b}(t), \hat{H}\right] + \frac{\kappa_b}{2}\hat{b} - \sqrt{\kappa_{b,c}}\,\hat{b}_{out}(t). \tag{d.3}$$

In these equations, $\left[\hat{b}(t), \hat{H}\right]$ represents the natural Hamiltonian evolution of the mode and $\frac{\kappa_b}{2}\hat{b}$ the natural decay of the buffer. The last term $\sqrt{\kappa_{b,c}}\,\hat{b}_{in}(t)$ or $-\sqrt{\kappa_{b,c}}\,\hat{b}_{out}(t)$ originates from the interaction between the propagating modes of the input line and the buffer mode. To compute the reflection

---

[1] Beware of subtleties in taking this transform [162]

coefficient $r(\omega_d) = \left\langle \hat{b}_{in}[\omega_d] \right\rangle / \left\langle \hat{b}_{out}[\omega_d] \right\rangle$, we use the Langevin equation with the Hamiltonian

$$\hat{H}/\hbar = \omega_m \hat{a}^\dagger \hat{a} + \omega_b \hat{b}^\dagger \hat{b} + g_2^* \hat{a}^{\dagger 2} \hat{b} + g_2 \hat{a}^2 \hat{b}^\dagger. \tag{d.4}$$

The 2-to-1 coupling $g_2^* \hat{a}^{\dagger 2} \hat{b} + h.c$ depends on the external flux and is notably suppressed by the RWA (see Appendix. a) when $\omega_b \neq 2\omega_m$

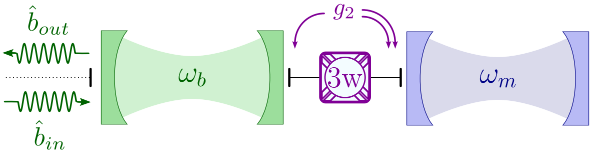

Figure d.1: Schematic of buffer spectroscopy measurement. A drive at ω_d described by the propagating field $\hat{b}_{in}$ is sent to the buffer through the input line, and the outgoing signal $\hat{b}_{out}$ is measured.

D.1 $\omega_b \neq 2\omega_m$, THE USUAL REFLECTION ON A CAVITY

When $\omega_b \neq 2\omega_m$, the two-to-one coupling Hamiltonian can be neglected, as well as the memory which no longer couples to the buffer mode. The Hamiltonian then reduces to

$$\hat{H}/\hbar = \omega_b \hat{b}^\dagger \hat{b}, \tag{d.5}$$

and the Langevin equation reads

$$\frac{\partial}{\partial t} \hat{b}(t) = -i\omega_b \hat{b}(t) - \frac{\kappa_b}{2} \hat{b} + \sqrt{\kappa_{b,c}}\, \hat{b}_{in}(t). \tag{d.6}$$

Going to the frequency space, this equation becomes

$$\left(-i\Delta + \frac{\kappa_b}{2}\right) \hat{b}[\omega] = \sqrt{\kappa_{b,c}}\, \hat{b}_{in}[\omega] \tag{d.7}$$

with $\Delta = \omega_d - \omega_b$. The state of this driven buffer is known to be a coherent state, which can be treated classically by replacing the operator $\hat{b}[\omega]$ by a complex amplitude $\beta[\omega]$. This yields

$$\left(-i\Delta + \frac{\kappa_b}{2}\right) \beta[\omega] = \sqrt{\kappa_{b,c}}\, \beta_{in}[\omega], \tag{d.8}$$

which finally gives the reflection coefficient using the input/output relation

$$\begin{aligned} r(\omega) &= \frac{\sqrt{\kappa_{b,c}}\,\beta}{\beta_{in}} - 1 \\ &= \frac{\kappa_{b,c} - \kappa_{b,i} + 2i\Delta}{\kappa_{b,c} + \kappa_{b,i} - 2i\Delta}. \end{aligned} \tag{d.9}$$

D.2 $\omega_b = 2\omega_m$, REFLECTION IN PRESENCE OF 2 PHOTON COUPLING

When the frequency matching condition of the Auto-cat is verified, the two-to-one photon coupling cannot be ignored and the full Hamiltonian of Eq. (d.4) must be considered. For simplicity, the intrinsic loss of the buffer and memory modes are neglected and the corresponding loss rates are written as κ_b and κ_m. The system is then described by 2 Langevin equations, respectively describing the evolution of the buffer and memory mode

$$\frac{\partial}{\partial t}\,\hat{a}(t) = -2ig_2^*\hat{a}(t)^\dagger\hat{b}(t) - i\omega_m\hat{a}(t) - \frac{\kappa_m}{2}\hat{a}(t) \tag{d.10a}$$

$$\frac{\partial}{\partial t}\,\hat{b}(t) = -ig_2\hat{a}(t)^2 - i\omega_b\hat{b}(t) - \frac{\kappa_b}{2}\hat{b} + \sqrt{\kappa_b}\,\hat{b}_{in}(t). \tag{d.10b}$$

Going to the frequency space through a Fourier transform, the Langevin equations become

$$\left(i\frac{\Delta}{2} - \frac{\kappa_m}{2}\right)\hat{a}[\omega] = 2ig_2^*\hat{a}[\omega]^\dagger\hat{b}[\omega] \tag{d.11a}$$

$$\left(i\Delta - \frac{\kappa_b}{2}\right)\beta[\omega] + \sqrt{\kappa_b}\,\hat{b}_{in}[\omega] = ig_2\hat{a}[\omega]^2. \tag{d.11b}$$

$\Delta = \omega_d - \omega_b$ keeps the same definition as in the previous section. Once again, knowing that the drive displaces the buffer mode to a coherent state, it can be treated classically and the operator $\hat{b}[\omega]$ replaced by a complex amplitude $\beta[\omega]$. The same reasoning cannot be applied to the memory mode however, whose state converges to a cat state

$$|\Psi_m\rangle = \mu\,|\alpha\rangle + \nu\,|-\alpha\rangle\,. \tag{d.12}$$

Here, the metastable solution corresponding to the memory remaining in its vacuum state is neglected. The complex coefficients μ and ν are normalized to unity $|\mu|^2 + |\nu|^2 = 1$, and the cat amplitude α is to be determined. An equation on $\alpha[\omega]$ is obtained by projecting Eq. (d.11) in the cat manifold $\langle\Psi_m| (...) |\Psi_m\rangle$, which yields

$$\beta[\omega] = \frac{1}{2g_2^*}\left(i\frac{\kappa_m}{2} + \frac{\Delta}{2}\right) e^{2i\arg(\alpha[\omega])} \tag{d.13a}$$

$$\alpha[\omega]^2 = \frac{i}{g_2}\left(\left(\frac{\kappa_b}{2} - i\Delta\right)\beta[\omega] - \sqrt{\kappa_b}\beta_{in}[\omega]\right). \tag{d.13b}$$

Note that we neglect $\langle\alpha|-\alpha\rangle \ll 1$ to find Eq. (d.13), which is valid for large α only. The photon number in the memory being proportional to the drive amplitude, this equation is then only valid for large drive amplitudes β_{in}. Furthermore, we can deduce from Eq. (d.13a) that the amplitude of the coherent field in the buffer is small at resonance, $\beta[\omega_b] \ll 1$, due to the large two-to-one coupling $|g_2| \gg \kappa_m$. The reflection coefficient is obtained from Eq. (d.13a) as

$$\begin{aligned} r(\omega) &= \frac{\sqrt{\kappa_b}\,\beta}{\beta_{in}} - 1 \\ &= \frac{\sqrt{\kappa_b}}{2g_2^*\beta_{in}}\left(i\frac{\kappa_m}{2} + \frac{\Delta}{2}\right) e^{2i\arg(\alpha[\omega])} - 1. \end{aligned} \tag{d.14}$$

For large drive amplitudes β_{in}, this coefficient becomes independent of ω, which is verified experimentally. The phase of the memory, $\arg(\alpha[\omega])$, is finally deduced from Eq. (d.13b) as

$$\arg(\alpha[\omega]) = \pm\frac{1}{2g_2}\left(\arg\left(\left(\frac{\kappa_b}{2} - i\Delta\right)\beta[\omega] - \sqrt{\kappa_b}\beta_{in}[\omega]\right) + \frac{\pi}{2}\right). \tag{d.15}$$

The phase of the reflected signal has a specific pattern at $\omega = \omega_b = 2\omega_m$. A 4π phase shift can be seen, corresponding to the sum of two 2π phase drops. A first phase drop comes from the term $\left(\frac{\kappa_b}{2} - i\Delta\right)$ in the argument of $\alpha[\omega]$, with a frequency width of κ_b. And inside this phase drop, another one occurs due to the term $\frac{1}{2}(i\kappa_m + \Delta)$, with a width given by κ_m.

D.3 EXPERIMENTAL RESULTS

The buffer mode's spectroscopy was performed at different external flux ϕ_{ext}, to characterize the evolution of $\omega_b(\phi_{\text{ext}})$. Additionally, this measurement provides a straightforward method to identify ϕ_{QEC} by observing the

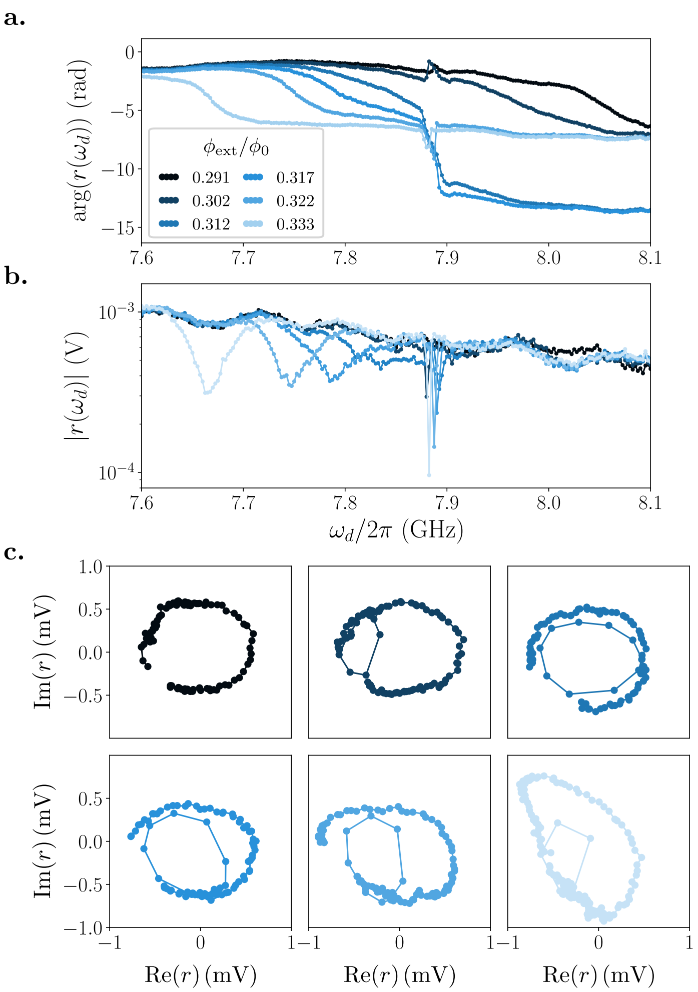

Figure d.2: **a.** Unwrapped phase of the reflected signal as a function of the drive frequency $\omega_d/2\pi$. The corresponding values of ϕ_{ext} are indicated in the inset. **b.** Amplitude of the reflected signal as a function of drive frequency. Same color code for the values of ϕ_{ext} as in **a.** **c.** Trajectories of $r(\omega_d)$ from which **a.** and **b.** are obtained.

transition between the two previously described regimes, as illustrated in Figure d.2.

Ramping up the external flux from $\phi_{\text{ext}} = 0.291\phi_0$ to $0.333\phi_0$, a clear difference can be seen at $\phi_{\text{ext}} \approx 0.312\phi_0$ where the frequency matching condition $\omega_b = 2\omega_m$ is verified. There, a 4π drop can be observed in the phase of the reflected signal, corresponding in Fig. d.2**c.iii** and **c.iv** to a trajectory circling twice around the point (0,0). Close to ϕ_{QEC}, the system is in an intermediate regime where the two-to-one photon interaction is only weakly suppressed by the 1^{st} order RWA. While this interaction still impacts the reflected signal as evidenced by the secondary loop visible in Fig. d.2**c.ii**, **c.v** and **c.vi**, it does not result in the characteristic 4π phase drop. Finally, for $\phi_{\text{ext}} = 0.291\phi_0$, the buffer is far detuned from the frequency $2\omega_m$ and the reflection coefficient $r(\omega_d)$ is well described by Eq. (d.9).

Regarding the buffer linewidth, a significant evolution can be observed in Fig. d.2**a** for varying external flux. We attribute this evolution to the interaction of the buffer with the microwave background or spurious modes of the device. For our simulations, the value of κ_b was determined at ϕ_{QEC} by decomposing the 4π phase drop into two distinct 2π phase drops occurring at the same frequency. These phase drops had respective widths of $\kappa_m/2\pi =$ 14 kHz (independently measured) and $\kappa_b/2\pi = 40$ MHz.

Part IV

BIBLIOGRAPHY

BIBLIOGRAPHY

[1] Haocun Yu et al. "Quantum correlations between light and the kilogram-mass mirrors of LIGO." In: *Nature* 583.7814 (2020), pp. 43–47 (Cited on page 1).

[2] *The Nobel Prize in Physics 1956.* 1956 (Cited on page 1).

[3] E Schrödinger. "Are There Quantum Jumps? Part II." In: *The British Journal for the Philosophy of Science* 3.11 (1952), pp. 233–242 (Cited on page 1).

[4] *The Nobel Prize in Physics 2012.* 2012 (Cited on page 1).

[5] J. S. Bell. "On the Einstein Podolsky Rosen paradox." In: *Physics Physique Fizika* 1 (3 Nov. 1964), pp. 195–200 (Cited on page 1).

[6] Alain Aspect, Jean Dalibard, and Gérard Roger. "Experimental Test of Bell's Inequalities Using Time- Varying Analyzers." In: *Physical Review Letters* 49 (25 June 1982), pp. 1804–1807 (Cited on page 1).

[7] Richard P. Feynman. "Simulating physics with computers." In: *International Journal of Theoretical Physics* 21.6 (1982), pp. 467–488 (Cited on page 2).

[8] Peter W Shor. "Polynomial-Time Algorithms for Prime Factorization and Discrete Logarithms on a Quantum Computer." In: *SIAM Journal on Computing* 26 (5 June 1997), pp. 1484–1509 (Cited on page 2).

[9] Lov K. Grover. "A Fast Quantum Mechanical Algorithm for Database Search." In: STOC '96 (1996), 212–219 (Cited on page 2).

[10] D DiVincenzo. "The Physical Implementation of Quantum Computation." In: *Fortschr. Phys.* 48 (9-11 2000), p. 771 (Cited on page 2).

[11] M. Saffman, T. G. Walker, and K. Mølmer. "Quantum information with Rydberg atoms." In: *Rev. Mod. Phys.* 82 (3 Aug. 2010), pp. 2313–2363 (Cited on page 3).

[12] H. Häffner, C.F. Roos, and R. Blatt. "Quantum computing with trapped ions." In: *Physics Reports* 469.4 (2008), pp. 155–203 (Cited on page 3).

[13] Daniel Loss and David P. DiVincenzo. "Quantum computation with quantum dots." In: *Phys. Rev. A* 57 (1 Jan. 1998), pp. 120–126 (Cited on page 3).

[14] David G. Cory, Amr F. Fahmy, and Timothy F. Havel. "Ensemble quantum computing by NMR spectroscopy." In: *Proceedings of the National Academy of Sciences* 94.5 (1997), pp. 1634–1639 (Cited on page 3).

[15] Neil A. Gershenfeld and Isaac L. Chuang. "Bulk Spin-Resonance Quantum Computation." In: *Science* 275.5298 (1997) (Cited on page 3).

[16] Slussarenko Sergei and J. Pryde Geoff. "Photonic quantum information processing: A concise review." In: *Applied Physics Review* (2019) (Cited on page 3).

[17] Han-Sen Zhong et al. "Quantum computational advantage using photons." In: *Science* 370.6523 (2020), pp. 1460–1463 (Cited on page 3).

[18] Katrina Barnes et al. "Assembly and coherent control of a register of nuclear spin qubits." In: *Nature Communications* 13.1 (2022), p. 2779 (Cited on page 3).

[19] Pengfei Wang et al. "Single ion qubit with estimated coherence time exceeding one hour." In: *Nature Communications* 12.1 (2021), p. 233 (Cited on page 3).

[20] J. Bardeen, L. N. Cooper, and J. R. Schrieffer. "Theory of Superconductivity." In: *Phys. Rev.* 108 (5 Dec. 1957), pp. 1175–1204 (Cited on pages 3, 45).

[21] John M Martinis, Michel H Devoret, and John Clarke. "Energy-level quantization in the zero-voltage state of a current-biased Josephson junction." In: *Physical Review Letters* 55 (15 1985), pp. 1543–1546 (Cited on page 3).

[22] John M. Martinis, Michel H. Devoret, and John Clarke. "Experimental tests for the quantum behavior of a macroscopic degree of freedom: The phase difference across a Josephson junction." In: *Phys. Rev. B* 35 (10 Apr. 1987), pp. 4682–4698 (Cited on page 3).

[23] B.D. Josephson. "Possible new effects in superconductive tunnelling." In: *Physics Letters* 1.7 (1962), pp. 251–253 (Cited on pages 3, 48).

[24] Morten Kjaergaard et al. "Superconducting Qubits: Current State of Play." In: *Annual Review of Condensed Matter Physics* 11.1 (2020), pp. 369–395 (Cited on page 4).

[25] Helin Zhang et al. "Universal Fast-Flux Control of a Coherent, Low-Frequency Qubit." In: *Physical Review X* 11.1 (Jan. 2021) (Cited on page 4).

[26] Chenlu Wang et al. "Towards practical quantum computers: transmon qubit with a lifetime approaching 0.5 milliseconds." In: *npj Quantum Information* 8.1 (Jan. 2022) (Cited on page 4).

[27] Aaron Somoroff et al. "Millisecond Coherence in a Superconducting Qubit." In: *Phys. Rev. Lett.* 130 (26 June 2023), p. 267001 (Cited on page 4).

[28] Ofir Milul et al. "A superconducting quantum memory with tens of milliseconds coherence time." In: (2023). arXiv: `2302.06442 [quant-ph]` (Cited on pages 4, 41, 104).

[29] A Wallraff et al. "Strong coupling of a single photon to a superconducting qubit using circuit quantum electrodynamics." In: *Nature* 431 (7005 2004), pp. 162–167 (Cited on page 5).

[30] Alexandre Blais et al. "Cavity quantum electrodynamics for superconducting electrical circuits: An architecture for quantum computation." In: *Phys. Rev. A* 69 (6 June 2004), p. 062320 (Cited on pages 5, 51).

[31] T. D. Ladd et al. "Quantum computers." In: *Nature* 464.7285 (2010), pp. 45–53 (Cited on page 5).

[32] Y Nakamura, Yu. A Pashkin, and J S Tsai. "Coherent control of macroscopic quantum states in a single-Cooper-pair box." In: *Nature* 398 (6730 June 1999), pp. 786–788 (Cited on pages 5, 20, 41).

[33] J Koch et al. "Charge-insensitive qubit design derived from the Cooper pair box." In: *Physical Review A* 76 (4 June 2007), p. 42319 (Cited on pages 5, 22, 49).

[34] Vladimir E Manucharyan et al. "Fluxonium: Single Cooper-Pair Circuit Free of Charge Offsets." In: *Science* 326 (5949 June 2009), pp. 113–116 (Cited on pages 5, 22).

[35] Leonid I. Glazman and Gianluigi Catelani. "Bogoliubov quasiparticles in superconducting qubits." In: *SciPost Phys. Lect. Notes* (2021), p. 31 (Cited on pages 5, 20).

[36] R. W. Hamming. "Error detecting and error correcting codes." In: *The Bell System Technical Journal* 29.2 (1950), pp. 147–160 (Cited on pages 5, 23).

[37] M. J. E. Golay. "Notes on digital coding." In: *Proc. IEEE* 37.657 (1949) (Cited on page 5).

[38] Claude Elwood Shannon. "A Mathematical Theory of Communication." In: *The Bell System Technical Journal* (1948), pp. 379–423 (Cited on page 5).

[39] E. Schrodinger. "Quantisierung als Eigenwertproblem." In: *Annalen der Physik* 384.4 (1926), pp. 361–376. eprint: `https://onlinelibrary.wiley.com/doi/pdf/10.1002/andp.19263840404` (Cited on pages 13, 60, 175).

[40] S Haroche and J Raimond. "Exploring the Quantum: Atoms, Cavities, and Photons." In: *Oxford Graduated Text* (June 2006), p. 616 (Cited on pages 13, 55, 60, 61, 97, 98).

[41] F. Bloch. "Generalized Theory of Relaxation." In: *Phys. Rev.* 105 (4 Feb. 1957), pp. 1206–1222 (Cited on page 15).

[42] A. G. Redfield. "On the Theory of Relaxation Processes." In: *IBM Journal of Research and Development* 1.1 (1957), pp. 19–31 (Cited on page 15).

[43] J. E. Tanner and E. O. Stejskal. "Restricted Self-Diffusion of Protons in Colloidal Systems by the Pulsed-Gradient, Spin-Echo Method." In: *J. Chem. Phys.* (Aug. 1968) (Cited on page 17).

[44] Jonas Bylander et al. "Noise spectroscopy through dynamical decoupling with a superconducting flux qubit." In: *Nature Physics* 7 (2011) (Cited on page 17).

[45] P. Krantz et al. "A quantum engineer's guide to superconducting qubits." In: *Applied Physics Reviews* 6.2 (June 2019) (Cited on pages 17, 19, 20).

[46] John M. Martinis et al. "Decoherence of a superconducting qubit due to bias noise." In: *Phys. Rev. B* 67 (9 Mar. 2003), p. 094510 (Cited on page 17).

[47] Jeremy Stevens. "Effect of the Environment on Fluxonium Qubits and Thermodynamics of Quantum Measurement." Theses. ENS de Lyon, 2021 (Cited on pages 17, 22, 45).

[48] William Oliver and Paul Welander. "Materials in superconducting quantum bits." In: *MRS Bulletin* 38 (Oct. 2013) (Cited on page 19).

[49] Irfan Siddiqi. "Engineering high-coherence superconducting qubits." In: *Nature Reviews Materials* 6 (2021), pp. 875 –891 (Cited on page 19).

[50] V Bouchiat et al. "Quantum coherence with a single Cooper pair." In: *Physica Scripta* T76 (June 1998), pp. 165–170 (Cited on page 20).

[51] P. Kumar et al. "Origin and Reduction of $1/f$ Magnetic Flux Noise in Superconducting Devices." In: *Phys. Rev. Appl.* 6 (4 Oct. 2016), p. 041001 (Cited on pages 20, 21).

[52] Jochen Braumüller et al. "Characterizing and Optimizing Qubit Coherence Based on SQUID Geometry." In: *Physical Review Applied* 13.5 (May 2020) (Cited on page 20).

[53] David A. Rower et al. "Evolution of $1/f$ Flux Noise in Superconducting Qubits with Weak Magnetic Fields." In: *Phys. Rev. Lett.* 130 (22 May 2023), p. 220602 (Cited on pages 20, 21).

[54] M. Houzet et al. "Photon-Assisted Charge-Parity Jumps in a Superconducting Qubit." In: *Phys. Rev. Lett.* 123 (10 Sept. 2019), p. 107704 (Cited on page 21).

[55] Matt McEwen et al. "Resolving catastrophic error bursts from cosmic rays in large arrays of superconducting qubits." In: *Nature Physics* 18.1 (Dec. 2021), pp. 107–111 (Cited on pages 21, 36).

[56] C. M. Quintana et al. "Characterization and reduction of microfabrication-induced decoherence in superconducting quantum circuits." In: *Applied Physics Letters* 105.6 (Aug. 2014) (Cited on page 21).

[57] Alexander P M Place et al. "New material platform for superconducting transmon qubits with coherence times exceeding 0.3 milliseconds." In: *Nature Communications* 12 (1 June 2021), p. 1779 (Cited on page 21).

[58] Archana Kamal et al. *Improved superconducting qubit coherence with high-temperature substrate annealing.* 2016. arXiv: `1606.09262 [cond-mat.mes-hall]` (Cited on page 21).

[59] Roger H. Koch, David P. DiVincenzo, and John Clarke. "Model for $1/f$ Flux Noise in SQUIDs and Qubits." In: *Phys. Rev. Lett.* 98 (26 June 2007), p. 267003 (Cited on page 21).

[60] S. M. Anton et al. "Magnetic Flux Noise in dc SQUIDs: Temperature and Geometry Dependence." In: *Phys. Rev. Lett.* 110 (14 Apr. 2013), p. 147002 (Cited on page 21).

[61] S Krinner et al. "Engineering cryogenic setups for 100-qubit scale superconducting circuit systems." In: *EPJ Quantum Technology* 6 (1 2019) (Cited on page 22).

[62] Galen C. O'Neil et al. "Measurement and modeling of a large-area normal-metal/insulator/superconductor refrigerator with improved cooling." In: *Phys. Rev. B* 85 (13 Apr. 2012), p. 134504 (Cited on page 22).

[63] O.-P. Saira et al. "Vanishing quasiparticle density in a hybrid Al/Cu/Al single-electron transistor." In: *Phys. Rev. B* 85 (1 Jan. 2012), p. 012504 (Cited on page 22).

[64] Arno Bargerbos et al. “Mitigation of Quasiparticle Loss in Superconducting Qubits by Phonon Scattering.” In: *Phys. Rev. Appl.* 19 (2 Feb. 2023), p. 024014 (Cited on page 22).

[65] Aaron Somoroff et al. “Millisecond Coherence in a Superconducting Qubit.” In: *Phys. Rev. Lett.* 130 (26 June 2023), p. 267001 (Cited on page 22).

[66] Alexei Kitaev. *Protected qubit based on a superconducting current mirror*. 2006. arXiv: `cond-mat/0609441 [cond-mat.mes-hall]` (Cited on page 22).

[67] András Gyenis et al. “Experimental Realization of a Protected Superconducting Circuit Derived from the 0–π Qubit.” In: *PRX Quantum* 2 (1 Mar. 2021), p. 010339 (Cited on page 22).

[68] Steven M. Girvin. “Introduction to quantum error correction and fault tolerance.” In: *SciPost Physics Lecture Notes* (June 2023) (Cited on page 25).

[69] W. K. Wootters and W. H. Zurek. “A single quantum cannot be cloned.” In: *Nature* 299.5886 (1982), pp. 802–803 (Cited on page 26).

[70] Jérémie Guillaud, Joachim Cohen, and Mazyar Mirrahimi. “Quantum computation with cat qubits.” In: *SciPost Physics Lecture Notes* 72 (June 2023), p. 72. arXiv: `2203.03222` (Cited on pages 27, 67).

[71] Emanuel Knill, Raymond Laflamme, and Lorenza Viola. “Theory of Quantum Error Correction for General Noise.” In: *Phys. Rev. Lett.* 84 (11 Mar. 2000), pp. 2525–2528 (Cited on page 27).

[72] M A Nielsen and I L Chuang. “Quantum Computation and Quantum Information.” In: *Book* (2000) (Cited on pages 27, 29, 142, 144, 156).

[73] Dave Bacon. “Operator quantum error-correcting subsystems for self-correcting quantum memories.” In: *Phys. Rev. A* 73 (1 Jan. 2006), p. 012340 (Cited on page 31).

[74] Panos Aliferis and Andrew W. Cross. “Subsystem Fault Tolerance with the Bacon-Shor Code.” In: *Phys. Rev. Lett.* 98 (22 May 2007), p. 220502 (Cited on page 33).

[75] Andrew W. Cross, David P. DiVincenzo, and Barbara M. Terhal. *A comparative code study for quantum fault-tolerance*. 2009. arXiv: `0711.1556 [quant-ph]` (Cited on page 33).

[76] John Napp and John Preskill. “Optimal Bacon-Shor codes.” In: *Quantum Information and Computation* 13 (Sept. 2012) (Cited on page 33).

[77] Austin G Fowler et al. "Surface codes: Towards practical large-scale quantum computation." In: *Physical Review A* 86 (3 June 2012), p. 32324 (Cited on pages 34, 35, 38).

[78] A. R. Calderbank and Peter W. Shor. "Good quantum error-correcting codes exist." In: *Phys. Rev. A* 54 (2 Aug. 1996), pp. 1098–1105 (Cited on page 33).

[79] A Steane. "Multiple-Particle Interference and Quantum Error Correction." In: *Proceedings of the Royal Society A: Mathematical, Physical and Engineering Sciences* 452 (1954 June 1996), pp. 2551–2577 (Cited on page 33).

[80] Jack Edmonds. "Maximum matching and a polyhedron with 0,1-vertices." In: *Journal of Research of the National Bureau of Standards Section B Mathematics and Mathematical Physics* (1965), p. 125 (Cited on page 35).

[81] Eric Dennis et al. "Topological quantum memory." In: *Journal of Mathematical Physics* 43.9 (Aug. 2002), pp. 4452–4505 (Cited on page 35).

[82] Sebastian Krinner et al. "Realizing repeated quantum error correction in a distance-three surface code." In: *Nature* 605 (7911 2022), pp. 669–674 (Cited on pages 36, 37).

[83] Joachim Cohen et al. "Reminiscence of Classical Chaos in Driven Transmons." In: *PRX Quantum* 4 (2 Apr. 2023), p. 020312 (Cited on page 36).

[84] Yulin Wu et al. "Strong Quantum Computational Advantage Using a Superconducting Quantum Processor." In: *Phys. Rev. Lett.* 127 (18 Oct. 2021), p. 180501 (Cited on page 36).

[85] Youwei Zhao et al. "Realization of an Error-Correcting Surface Code with Superconducting Qubits." In: *Phys. Rev. Lett.* 129 (3 July 2022), p. 030501 (Cited on page 36).

[86] Rajeev Acharya et al. "Suppressing quantum errors by scaling a surface code logical qubit." In: *Nature* 614.7949 (2023), pp. 676–681 (Cited on page 37).

[87] J. Pablo Bonilla Ataides et al. "The XZZX surface code." In: *Nature Communications* 12.1 (2021), p. 2172 (Cited on page 38).

[88] Jérémie Guillaud and Mazyar Mirrahimi. "Repetition Cat Qubits for Fault-Tolerant Quantum Computation." In: *Physical Review X* 9 (4 Dec. 2019), p. 41053 (Cited on pages 39, 40, 67, 75, 149).

[89] Andrew S. Darmawan et al. "Practical Quantum Error Correction with the XZZX Code and Kerr-Cat Qubits." In: *PRX Quantum* 2 (3 Sept. 2021), p. 030345 (Cited on page 40).

[90] Jé rémie Guillaud and Mazyar Mirrahimi. "Error rates and resource overheads of repetition cat qubits." In: *Physical Review A* 103.4 (Apr. 2021) (Cited on pages 40, 133).

[91] Samuel L Braunstein. "Quantum error correction for communication with linear optics." In: *Nature* 394 (6688 1998), pp. 47–49 (Cited on page 43).

[92] Atharv Joshi, Kyungjoo Noh, and Yvonne Y Gao. "Quantum information processing with bosonic qubits in circuit QED." In: *Quantum Science and Technology* 6 (3 2021), p. 033001 (Cited on pages 43, 63).

[93] H. Jeong and M. S. Kim. "Efficient quantum computation using coherent states." In: *Phys. Rev. A* 65 (4 Mar. 2002), p. 042305 (Cited on page 43).

[94] T. C. Ralph et al. "Quantum computation with optical coherent states." In: *Physical Review A* 68.4 (Oct. 2003), p. 042319. arXiv: `0306004 [quant-ph]` (Cited on page 43).

[95] Hyunseok Jeong and Timothy C. Ralph. "Schrödinger Cat States for Quantum Information Processing." In: *in Quantum Information with Continuous Variables of Atoms and Light (Imperial College Press)* (2007), pp. 159–179 (Cited on page 43).

[96] Marios H. Michael et al. "New Class of Quantum Error-Correcting Codes for a Bosonic Mode." In: *Phys. Rev. X* 6 (3 July 2016), p. 031006 (Cited on pages 43, 63).

[97] Daniel Gottesman, Alexei Kitaev, and John Preskill. "Encoding a qubit in an oscillator." In: *Physical Review A* 64 (1 June 2001), p. 12310 (Cited on pages 43, 65).

[98] A Grimm et al. "Stabilization and operation of a Kerr-cat qubit." In: *Nature* 584 (7820 2020), pp. 205–209 (Cited on pages 43, 71, 78).

[99] Nicholas E. Frattini et al. "The squeezed Kerr oscillator: spectral kissing and phase-flip robustness." In: (Sept. 2022) (Cited on pages 43, 71, 72, 78, 86).

[100] Z Leghtas et al. "Confining the state of light to a quantum manifold by engineered two-photon loss." In: *Science* 347.6224 (2015), pp. 853–857 (Cited on page 43).

[101] S Touzard et al. "Coherent Oscillations inside a Quantum Manifold Stabilized by Dissipation." In: *Physical Review X* 8 (2 June 2018), p. 21005 (Cited on pages 43, 76, 77, 86, 105, 113, 134).

[102] Raphaël Lescanne et al. "Exponential suppression of bit-flips in a qubit encoded in an oscillator." In: *Nature Physics* 16 (5 2020), pp. 509–513 (Cited on pages 43, 49, 75, 77, 86, 105, 113, 117, 121, 134, 147).

[103] Mazyar Mirrahimi et al. "Dynamically protected cat-qubits: a new paradigm for universal quantum computation." In: *New Journal of Physics* 16 (4 2014), p. 45014 (Cited on pages 43, 125).

[104] Nissim Ofek et al. "Extending the lifetime of a quantum bit with error correction in superconducting circuits." In: *Nature* 536 (7617 2016), pp. 441–445 (Cited on pages 43, 68, 70, 86, 171).

[105] Matthew Reagor et al. "Reaching 10 ms single photon lifetimes for superconducting aluminum cavities." In: *Applied Physics Letters* 102 (19 2013), p. 192604 (Cited on page 44).

[106] A. Romanenko and D. I. Schuster. "Understanding Quality Factor Degradation in Superconducting Niobium Cavities at Low Microwave Field Amplitudes." In: *Phys. Rev. Lett.* 119 (26 2017), p. 264801 (Cited on page 44).

[107] Alex Krasnok et al. "Advancements in Superconducting Microwave Cavities and Qubits for Quantum Information Systems." In: (2023). arXiv: `2304.09345 [quant-ph]` (Cited on page 45).

[108] S. Girvin. "Circuit QED: superconducting qubits coupled to microwave photons." In: *Oxford University Press* (2014) (Cited on pages 45, 48).

[109] Uri Vool and Michel Devoret. "Introduction to quantum electromagnetic circuits." In: vol. 45. 2017 (Cited on page 45).

[110] Stephen D. Bartlett et al. "Efficient Classical Simulation of Continuous Variable Quantum Information Processes." In: *Phys. Rev. Lett.* 88 (9 2002), p. 097904 (Cited on pages 47, 56).

[111] A. Mari and J. Eisert. "Positive Wigner Functions Render Classical Simulation of Quantum Computation Efficient." In: *Phys. Rev. Lett.* 109 (23 2012), p. 230503 (Cited on pages 47, 56).

[112] Wen-Long Ma et al. "Quantum control of bosonic modes with superconducting circuits." In: *Science Bulletin* 66.17 (2021), pp. 1789–1805 (Cited on page 49).

[113] Alec Eickbusch et al. "Fast universal control of an oscillator with weak dispersive coupling to a qubit." In: *Nature Physics* 18.12 (2022), pp. 1464–1469 (Cited on page 49).

[114] Asaf A. Diringer et al. "Conditional not displacement: fast multi-oscillator control with a single qubit." In: (2023). arXiv: `2301.09831 [quant-ph]` (Cited on pages 49, 115).

[115] R Dassonneville et al. "Dissipative Stabilization of Squeezing Beyond 3 dB in a Microwave Mode." In: *PRX Quantum* 2 (2 May 2021), p. 20323 (Cited on pages 49, 58).

[116] Xiaozhou Pan et al. "Protecting the Quantum Interference of Cat States by Phase-Space Compression." In: *Phys. Rev. X* 13 (2 Apr. 2023), p. 021004 (Cited on pages 49, 134).

[117] Z Leghtas et al. "Confining the state of light to a quantum manifold by engineered two-photon loss." In: *Science* 347 (6224 Feb. 2015). doi: 10.1126/science.aaa2085, pp. 853–857 (Cited on pages 49, 73, 76, 86, 105, 113).

[118] Antoine Essig. "Compteur de photon basé sur une mesure dispersive multiplexée." Theses. ENS de Lyon, 2021 (Cited on page 50).

[119] Alexandre Blais et al. "Circuit quantum electrodynamics." In: *Rev. Mod. Phys.* 93 (2 Mar. 2021), p. 025005 (Cited on page 51).

[120] E.T. Jaynes and F.W. Cummings. "Comparison of quantum and semiclassical radiation theories with application to the beam maser." In: *Proceedings of the IEEE* 51.1 (1963), pp. 89–109 (Cited on pages 51, 59).

[121] Mohamed Abdelhafez, David I. Schuster, and Jens Koch. "Gradient-based optimal control of open quantum systems using quantum trajectories and automatic differentiation." In: *Phys. Rev. A* 99 (5 May 2019), p. 052327 (Cited on page 53).

[122] T Walter et al. "Rapid High-Fidelity Single-Shot Dispersive Readout of Superconducting Qubits." In: *Physical Review Applied* 7 (5 June 2017), p. 54020 (Cited on page 54).

[123] Cristóbal Lledó et al. "Cloaking a qubit in a cavity." In: (2022). arXiv: `2211.05758 [quant-ph]` (Cited on page 54).

[124] Hai-Woong Lee. "Theory and application of the quantum phase-space distribution functions." In: *Physics Reports* 259.3 (1995), pp. 147–211 (Cited on page 54).

[125] William Case. "Wigner functions and Weyl transforms for pedestrians." In: *American Journal of Physics - AMER J PHYS* 76 (Oct. 2008) (Cited on page 54).

[126] Robin L. Hudson. "When is the wigner quasi-probability density nonnegative?" In: *Reports on Mathematical Physics* 6 (1974), pp. 249–252 (Cited on page 56).

[127] Francisco Soto and Pierre Claverie. "When is the Wigner function of multidimensional systems nonnegative?" In: *Journal of Mathematical Physics* 6 (1983) (Cited on page 56).

[128] Anatole Kenfack and Karol Życzkowski. "Negativity of the Wigner function as an indicator of non-classicality." In: *Journal of Optics B: Quantum and Semiclassical Optics* 6.10 (Aug. 2004), p. 396 (Cited on page 56).

[129] Abadie et.al. "Search for gravitational waves associated with the August 2006 timing glitch of the Vela pulsar." In: *Phys. Rev. D* 83 (4 Feb. 2011), p. 042001 (Cited on page 58).

[130] A. Bienfait et al. "Magnetic Resonance with Squeezed Microwaves." In: *Phys. Rev. X* 7 (4 Oct. 2017), p. 041011 (Cited on page 58).

[131] S. Kono et al. "Nonclassical Photon Number Distribution in a Superconducting Cavity under a Squeezed Drive." In: *Phys. Rev. Lett.* 119 (2 July 2017), p. 023602 (Cited on page 58).

[132] David S. Schlegel, Fabrizio Minganti, and Vincenzo Savona. "Quantum error correction using squeezed Schrödinger cat states." In: *Phys. Rev. A* 106 (2 Aug. 2022), p. 022431 (Cited on page 58).

[133] Timo Hillmann and Fernando Quijandría. "Quantum error correction with dissipatively stabilized squeezed-cat qubits." In: *Phys. Rev. A* 107 (3 2023), p. 032423 (Cited on pages 58, 134).

[134] Qian Xu et al. "Autonomous quantum error correction and fault-tolerant quantum computation with squeezed cat qubits." In: (Oct. 2022) (Cited on pages 58, 134).

[135] H.J. Groenewold. "On the principles of elementary quantum mechanics." In: *Physica* 12.7 (1946), pp. 405–460 (Cited on page 60).

[136] J. E. Moyal. "Quantum mechanics as a statistical theory." In: *Mathematical Proceedings of the Cambridge Philosophical Society* 45.1 (1949), 99–124 (Cited on page 60).

[137] Gerhard Kirchmair et al. "Observation of quantum state collapse and revival due to the single-photon Kerr effect." In: *Nature* 495 (7440 June 2013), pp. 205–209 (Cited on pages 62, 111).

[138] Shruti Puri et al. "Bias-preserving gates with stabilized cat qubits." In: *Science Advances* 6 (34 Apr. 2020). doi: 10.1126/sciadv.aay5901, eaay5901 (Cited on pages 62, 68, 139, 148).

[139] L Hu et al. "Quantum error correction and universal gate set operation on a binomial bosonic logical qubit." In: *Nature Physics* 15 (5 June 2019), pp. 503–508 (Cited on page 63).

[140] Zhongchu Ni et al. "Beating the break-even point with a discrete-variable-encoded logical qubit." In: *Nature* 616.7955 (2023), pp. 56–60 (Cited on pages 64, 70).

[141] Arne L Grimsmo, Joshua Combes, and Ben Q Baragiola. "Quantum Computing with Rotation-Symmetric Bosonic Codes." In: *Physical Review X* 10 (1 Mar. 2020), p. 11058 (Cited on pages 64, 86).

[142] C. Flühmann et al. "Encoding a qubit in a trapped-ion mechanical oscillator." In: *Nature* 566.7745 (2019), pp. 513–517 (Cited on page 66).

[143] P Campagne-Ibarcq et al. "Quantum error correction of a qubit encoded in grid states of an oscillator." In: *Nature* 584 (7821 2020), pp. 368–372 (Cited on page 66).

[144] V. V. Sivak et al. "Real-time quantum error correction beyond break-even." In: *Nature* 616.7955 (2023), pp. 50–55 (Cited on pages 66, 70).

[145] F. M. Le-regent et al. "High-performance repetition cat code using fast noisy operations." In: (2022) (Cited on pages 67, 75, 117, 125).

[146] Christopher Chamberland et al. "Building a Fault-Tolerant Quantum Computer Using Concatenated Cat Codes." In: *PRX Quantum* 3 (1 Feb. 2022), p. 10329 (Cited on pages 67, 75, 133, 136).

[147] Ronan Gautier, Mazyar Mirrahimi, and Alain Sarlette. "Designing High-Fidelity Gates for Dissipative Cat Qubits." In: (Mar. 2023) (Cited on pages 68, 137).

[148] Jeffrey M Gertler et al. "Protecting a bosonic qubit with autonomous quantum error correction." In: *Nature* 590 (7845 June 2021), pp. 243–248 (Cited on pages 68, 165, 166, 171).

[149] Victor V Albert et al. "Pair-cat codes: autonomous error-correction with low-order nonlinearity." In: *Quantum Science and Technology* 4 (3 June 2019), p. 035007 (Cited on page 68).

[150] Jeffrey M. Gertler et al. "Experimental Realization and Characterization of Stabilized Pair-Coherent States." In: *PRX Quantum* 4 (2 2023), p. 020319 (Cited on page 68).

[151] Ronan Gautier, Alain Sarlette, and Mazyar Mirrahimi. "Combined Dissipative and Hamiltonian Confinement of Cat Qubits." In: *PRX Quantum* 3 (2 June 2022), p. 20339 (Cited on pages 70, 133).

[152] Shruti Puri, Samuel Boutin, and Alexandre Blais. "Engineering the quantum states of light in a Kerr-nonlinear resonator by two-photon driving." In: *npj Quantum Information* 3 (1 2017), p. 18 (Cited on pages 71, 78).

[153] N E Frattini et al. "3-wave mixing Josephson dipole element." In: *Applied Physics Letters* 110 (22 June 2017), p. 222603 (Cited on page 71).

[154] Shruti Puri et al. "Stabilized Cat in a Driven Nonlinear Cavity: A Fault-Tolerant Error Syndrome Detector." In: *Phys. Rev. X* 9 (4 Oct. 2019), p. 041009 (Cited on page 71).

[155] R Azouit et al. "Towards generic adiabatic elimination for bipartite open quantum systems." In: *Quantum Science and Technology* 2.4 (Sept. 2017), p. 044011 (Cited on page 73).

[156] François-Marie Le Régent and Pierre Rouchon. "Adiabatic elimination for composite open quantum systems: Heisenberg formulation and numerical simulations." In: (2023). arXiv: `2303.05089 [quant-ph]` (Cited on page 73).

[157] C. Berdou et al. "One hundred second bit-flip time in a two-photon dissipative oscillator." In: (2022) (Cited on pages 75, 77, 86, 105, 113, 121, 130).

[158] Ulysse Réglade et al. "Quantum control of a cat-qubit with bit-flip times exceeding ten seconds." In: (2023). arXiv: `2307.06617 [quant-ph]` (Cited on pages 77, 86, 113, 131, 136, 137).

[159] Ferdinand Verhulst. In: *Acta Applicandae Mathematicae* 70.1/3 (2002), pp. 231–264 (Cited on page 77).

[160] B Yurke et al. "Observation of parametric amplification and deamplification in a Josephson parametric amplifier." In: *Physical Review A* 39 (1989), p. 2519 (Cited on page 77).

[161] T Yamamoto et al. "Flux-driven Josephson parametric amplifier." In: *Applied Physics Letters* 93 (4 June 2008), p. 42510 (Cited on pages 77, 78).

[162] Ananda Roy and Michel Devoret. "Introduction to parametric amplification of quantum signals with Josephson circuits." In: *Comptes Rendus Physique* 17 (7 June 2016), pp. 740–755 (Cited on pages 77, 193).

[163] C M Wilson et al. "Photon Generation in an Electromagnetic Cavity with a Time-Dependent Boundary." In: *Physical Review Letters* 105 (23 June 2010), p. 233907 (Cited on page 78).

[164] Waltraut Wustmann and Vitaly Shumeiko. "Parametric resonance in tunable superconducting cavities." In: *Physical Review B* 87.18 (May 2013), p. 184501. arXiv: `1302.3484` (Cited on page 78).

[165] Ida Maria Svensson et al. "Period multiplication in a parametrically driven superconducting resonator." In: *Applied Physics Letters* 113 (2 2018) (Cited on page 78).

[166] Daisuke Iyama et al. "Observation and manipulation of quantum interference in a superconducting Kerr parametric oscillator." In: *arXiv:2306.12299* (2023) (Cited on pages 78, 86).

[167] Yao Lu et al. "A high-fidelity microwave beamsplitter with a parity-protected converter." In: (Mar. 2023) (Cited on page 79).

[168] D Vion et al. "Manipulating the quantum state of an electrical circuit." In: *Science (New York, N.Y.)* 296 (5569 June 2002), pp. 886–889 (Cited on page 79).

[169] Nicolas Didier, Jérôme Bourassa, and Alexandre Blais. "Fast Quantum Nondemolition Readout by Parametric Modulation of Longitudinal Qubit-Oscillator Interaction." In: *Phys. Rev. Lett.* 115 (20 Nov. 2015), p. 203601 (Cited on page 79).

[170] Susanne Richer and David DiVincenzo. "Circuit design implementing longitudinal coupling: A scalable scheme for superconducting qubits." In: *Physical Review B* 93 (13 June 2016), p. 134501 (Cited on page 79).

[171] R. Dassonneville et al. "Fast High-Fidelity Quantum Nondemolition Qubit Readout via a Nonperturbative Cross-Kerr Coupling." In: *Phys. Rev. X* 10 (1 Feb. 2020), p. 011045 (Cited on page 79).

[172] A. Miano et al. "Hamiltonian extrema of an arbitrary flux-biased Josephson circuit." In: (Feb. 2023) (Cited on page 80).

[173] Luiz Davidovich. "Sub-Poissonian processes in quantum optics." In: *Reviews of Modern Physics* 68 (1 1996), pp. 127–173 (Cited on page 89).

[174] P Bertet et al. "Direct Measurement of the Wigner Function of a One-Photon Fock State in a Cavity." In: *Physical Review Letters* 89 (20 Oct. 2002), p. 200402 (Cited on pages 89, 97, 98).

[175] Brian Vlastakis et al. "Deterministically Encoding Quantum Information Using 100-Photon Schrodinger Cat States." In: *Science* 342 (6158 June 2013), pp. 607–610 (Cited on pages 89, 97).

[176] Antoine Marquet et al. *Autoparametric resonance extending the bit-flip time of a cat qubit up to 0.3 s.* 2023. arXiv: `2307.06761 [quant-ph]` (Cited on pages 89, 113).

[177] D M Pozar. *Microwave Engineering.* John Wiley & Sons, 1998 (Cited on page 90).

[178] R.N. Simons. "Coplanar Waveguide Circuits, Components, and Systems." In: *Wiley* (2004) (Cited on page 91).

[179] L G Lutterbach and L Davidovich. "Method for Direct Measurement of the Wigner Function in Cavity QED and Ion Traps." In: *Physical Review Letters* 78 (13 Mar. 1997), pp. 2547–2550 (Cited on page 97).

[180] Réouven Assouly. "Superconducting Quantum Node for Quantum Sensing." Theses. Ecole normale supérieure de lyon - ENS LYON, Dec. 2022 (Cited on pages 101, 102).

[181] Philippe Campagne-Ibarcq. "Measurement back action and feedback in superconducting circuits." In: *Ph.D thesis* (June 2015) (Cited on pages 101, 103).

[182] H D Simaan and R Loudon. "Quantum statistics of single-beam two-photon absorption." In: *Journal of Physics A: Mathematical and General* 8.4 (Apr. 1975), p. 539 (Cited on page 108).

[183] Volodymyr Sivak. "Quantum Error Correction Beyond Break-Even." In: *Ph.D thesis* (June 2022) (Cited on page 108).

[184] M Hofheinz et al. "Synthesizing arbitrary quantum states in a superconducting resonator." In: *Nature* 459 (7246 June 2009), p. 546 (Cited on page 110).

[185] Max Hofheinz et al. "Generation of Fock states in a superconducting quantum circuit." In: *Nature* 454.7202 (2008), pp. 310–314 (Cited on page 110).

[186] Reinhold Philip. "Controlling Error-Correctable Bosonic Qubits." PhD thesis. Yale University, 2019 (Cited on page 111).

[187] Joachim Cohen et al. "Reminiscence of Classical Chaos in Driven Transmons." In: *PRX Quantum* 4 (2 Apr. 2023), p. 020312 (Cited on page 123).

[188] Mostafa Khezri et al. "Measurement-Induced State Transitions in a Superconducting Qubit: Within the Rotating Wave Approximation." In: *arxiv:2212.05097* (2022) (Cited on page 123).

[189] Roland Ketzmerick and Waltraut Wustmann. “Statistical mechanics of Floquet systems with regular and chaotic states.” In: *Phys. Rev. E* 82 (2 Aug. 2010), p. 021114 (Cited on page 123).

[190] É lie Gouzien et al. “Performance Analysis of a Repetition Cat Code Architecture: Computing 256-bit Elliptic Curve Logarithm in 9 Hours with 126 133 Cat Qubits.” In: *Physical Review Letters* 131.4 (July 2023) (Cited on page 133).

[191] Victor V Albert et al. “Holonomic Quantum Control with Continuous Variable Systems.” In: *Physical Review Letters* 116 (14 Apr. 2016), p. 140502 (Cited on pages 133, 153, 161).

[192] J M Raimond et al. “Phase Space Tweezers for Tailoring Cavity Fields by Quantum Zeno Dynamics.” In: *Physical Review Letters* 105 (21 June 2010), p. 213601 (Cited on page 134).

[193] J M Raimond et al. “Quantum Zeno dynamics of a field in a cavity.” In: *Physical Review A* 86 (3 June 2012), p. 32120 (Cited on page 134).

[194] F. Schäfer et al. “Experimental realization of quantum zeno dynamics.” In: *Nature Communications* 5.1 (Jan. 2014), p. 3194 (Cited on page 134).

[195] Adrien Signoles et al. “Confined quantum Zeno dynamics of a watched atomic arrow.” In: *Nat Phys* 10 (10 June 2014), pp. 715–719 (Cited on page 134).

[196] L Bretheau et al. “Quantum dynamics of an electromagnetic mode that cannot have N photons.” In: *Science* 348 (2015), p. 776 (Cited on page 134).

[197] M. Mohseni, A. T. Rezakhani, and D. A. Lidar. “Quantum-process tomography: Resource analysis of different strategies.” In: *Phys. Rev. A* 77 (3 Mar. 2008), p. 032322 (Cited on page 142).

[198] Marina Kudra et al. “Experimental realization of deterministic and selective photon addition in a bosonic mode assisted by an ancillary qubit.” In: (2022). arXiv: `2212.12079 [quant-ph]` (Cited on pages 165, 171).

[199] Mazyar Mirrahimi and Pierre Rouchon. “Dynamics and Control of Open Quantum Systems.” In: *Lectures notes* (2021) (Cited on page 175).

[200] C Macklin et al. “A near – quantum-limited Josephson traveling-wave parametric amplifier.” In: *Science* 350 (September 2015), p. 307 (Cited on page 181).

[201] G. J. Dolan. “Offset masks for lift-off photoprocessing.” In: *Appl. Phys. Lett* (Sept. 1977) (Cited on page 187).

[202] C. W. Gardiner and M. J. Collett. “Input and output in damped quantum systems: Quantum stochastic differential equations and the master equation.” In: *Phys. Rev. A* 31 (6 June 1985), pp. 3761–3774 (Cited on page 193).